



MONASH University

**Novel Organic Salts as Corrosion Inhibitors
and Solid Electrolytes**

Alison Lishan Chong

BScAdv (with Honours)

A thesis submitted for the degree of Doctor of Philosophy at

Monash University in 2017

School of Chemistry

Supervised by Professor Douglas R. MacFarlane

and Professor Maria Forsyth

For my family, near and far.

COPYRIGHT NOTICE

© Alison Chong (2017).

I certify that I have made all reasonable efforts to secure copyright permissions for third-party content included in this thesis and have not knowingly added copyright content to my work without the owner's permission

ABSTRACT

This thesis focuses on the investigation of the properties and applications of ionic liquids (ILs) and organic salts featuring the imidazolinium cation – a relative of the imidazolium cation that is saturated at the C4-C5 bond. Following the successful development of task-specific ILs in the literature, such as those incorporating pharmaceutical ions or heavy-metal chelating agents, this work aimed to develop salts for specific use as corrosion inhibitors. Imidazolines are well-known corrosion inhibitors and this, coupled with their structural similarity to the ubiquitous imidazolium cation, made them an intriguing cation family to investigate.

Synthesis and physical characterisation of a number of novel protic salts with the 2-methylimidazolinium cation ($[2\text{-MeHImn}]^+$) were carried out. The subsequent study of these compounds can be divided into two distinct parts.

The first was an investigation of the corrosion inhibiting behaviour of 2-methylimidazolinium 4-hydroxycinnamate, $[2\text{-MeHImn}][4\text{-OHCin}]$, on mild steel, with a comparison to the corresponding imidazolium salt and investigation of the effects of concentration and pH. It was found that the combination of imidazolinium and cinnamate ions resulted in substantial improvements in inhibition relative to the component ions. It was proposed that this synergy arose due to the reactivity of $[4\text{-OHCin}]^-$ in the presence of $[2\text{-MeHImn}]^+$, that produced a more strongly protective film at the steel surface.

Further to this, a number of other novel compounds were investigated as potential inhibitors. A selection of alkylated, aprotic imidazolinium salts were synthesised and of these, 1,2,3-trimethylimidazolinium 4-hydroxycinnamate, $[\text{triMeImn}][4\text{-OHCin}]$, showed similar levels of inhibition to $[2\text{-MeHImn}][4\text{-OHCin}]$. Sugar acid anions were used as alternatives to $[4\text{-OHCin}]^-$ anion, however, they were found to be less effective when paired with $[2\text{-MeHImn}]^+$. These results confirmed the importance of the combination of imidazolinium and cinnamate for synergistic inhibition.

A parallel study was carried out, investigating the conductivity of protic imidazolinium and imidazolium triflate salts. A comparison of the analogous compounds found that both showed high conductivities, particularly as solids at room temperature. It was proposed that conduction may be due to transport of labile protons from the protic cations. These materials were considered as potential proton-conducting electrolytes and it was found that the solid-state conductivities could be substantially improved with the use of the component acid or base as dopants. The high conductivity of the samples was

largely attributed to the presence of a highly mobile phase within the solid, however, the imidazolium salt showed some evidence of proton hopping on the cation.

This work introduced a family of protic and aprotic imidazolinium salts, using a cation that has, up until this point, gone largely unnoticed in the IL community, despite the popularity of the closely related imidazolium cation. The synthesised salts showed promise for both corrosion inhibition and solid electrolyte applications.

PUBLICATIONS DURING ENROLMENT

A. L. Chong, M. Forsyth and D. R. MacFarlane, Novel Imidazolinium Ionic Liquids and Organic Salts, *Electrochimica Acta*, 2015, **159**, 219-226.

A. L. Chong, J. I. Mardel, D. R. MacFarlane, M. Forsyth and A. E. Somers, Synergistic Corrosion Inhibition of Mild Steel in Aqueous Chloride Solutions by an Imidazolinium Carboxylate Salt, *ACS Sustainable Chemistry & Engineering*, 2016, **4**, 1746-1755.

THESIS INCLUDING PUBLISHED WORKS DECLARATION

I hereby declare that this thesis contains no material which has been accepted for the award of any other degree or diploma at any university or equivalent institution and that, to the best of my knowledge and belief, this thesis contains no material previously published or written by another person, except where due reference is made in the text of the thesis.

This thesis includes two original papers published in peer reviewed journals and two chapters which have not been submitted for publication. The core theme of the thesis is the investigation of novel organic salts. The ideas, development and writing up of all the papers in the thesis were the principal responsibility of myself, the student, working within the School of Chemistry under the supervision of Professor Douglas MacFarlane.

The inclusion of co-authors reflects the fact that the work came from active collaboration between researchers and acknowledges input into team-based research.

In the case of chapters 2, 3.1, 4 and 5 my contribution to the work involved the following:

The majority of the experiments were designed and conducted by myself, with instrument training provided by members of the group. Corrosion testing methodology was refined in collaboration with Dr Anthony Somers and Prof Bruce Hinton. Dr Haijin Zhu provided assistance with instrument set-up and experimental methods for the solid-state NMR studies.

Thesis Chapter	Publication Title	Status	Nature and % of student contribution	Co-author name(s) Nature and % of Co-author's contribution*	Co-author(s), Monash student Y/N*
2	Novel Protic Imidazolinium Salts and Ionic Liquids	Published	Concept, experimental design, collecting and analysing data, primary author, 80 %	- Prof Maria Forsyth, concept, input into manuscript, 10 % - Prof Doug MacFarlane, concept, input into manuscript, 10 %	No
3.1	Synergistic Corrosion Inhibition of Mild Steel in Aqueous Chloride Solutions by an Imidazolinium Carboxylate Salt	Published	Concept, experimental design, collecting and analysing IR data, contributing author, 35 %	- Dr James Mardel, data analysis, 5 % - Prof Doug MacFarlane, input into manuscript, 5 % - Prof Maria Forsyth, concept, input into manuscript, 10 % - Dr Anthony Somers, concept, experimental design, collecting and analysing corrosion data, contributing author, 45 %	No

Thesis Chapter	Publication Title	Status	Nature and % of student contribution	Co-author name(s) Nature and % of Co-author's contribution*	Co-author(s), Monash student Y/N*
4	Protic sugar acid salts for the corrosion inhibition of mild steel	Not submitted	Concept, experimental design, collecting and analysing data, primary author, 85 %	- Prof Maria Forsyth, concept, input into manuscript, 10 % - Prof Doug MacFarlane, concept, 5 %	No
5	Enhancing solid state conductivity through acid and base doping of protic imidazolium and imidazolinium triflate salts	Not submitted	Concept, experimental design, collecting and analysing data, primary author, 70 %	- Dr Haijin Zhu, experimental design, data analysis, 7.5 % - Dr Katherine Nairn, data analysis, input into manuscript 7.5% - Prof Maria Forsyth, concept, input into manuscript, 7.5 % - Prof Doug MacFarlane, concept, input into manuscript, 7.5 %	No

I have not renumbered sections of submitted or published papers in order to generate a consistent presentation within the thesis.

Student signature: 

Date: 9/6/2017

The undersigned hereby certify that the above declaration correctly reflects the nature and extent of the student's and co-authors' contributions to this work. In instances where I am not the responsible author I have consulted with the responsible author to agree on the respective contributions of the authors.

Main Supervisor signature: 

Date: 9/6/2017

ACKNOWLEDGEMENTS

This thesis has by no means been a solo effort. Thanks first to my supervisors, Doug and Maria, for their guidance, advice and inspiration.

Next, I would like to recognise the knowledge and support of those that helped me with my research; Dr Anthony Somers, Professor Bruce Hinton, Dr Rainier Catubig and Mark for your corrosion expertise, and for every time one of you packed up my experiments; Dr Haijin Zhu, Dr Luke O'Dell, Dr Kate Nairn and Rossie, without whom I would know nothing about solid-state NMR spectroscopy; All the facilities staff in the School of Chemistry, chiefly Dr Finlay Shanks for TGA and IR, and Peter Nichols for NMR; Dr Vijay Ranganathan, the protic IL expert; my proof-readers who have helped me through this last hurdle; and finally Dr Peter Newman, without you there would be no functioning instruments in our labs.

To each and every person in the MacFarlane and Forsyth groups, those who've been there from the beginning, and those that have come along the way, you've been amazing colleagues, but more importantly, amazing friends. Mega, Ciaran and Gary – you've been there every day, through countless coffees and questions and long lunches. Aminah, Diogo, Colin, Zheng and all office-mates past and present – I'm sorry I never really figured out a quiet office voice. Raimund, Sonja and those whose time with us was brief – thank you for brightening up our labs. Dave, Matt, Bartek, Chun, Jenny and Derick – my weeks haven't been the same without trivia and kebabs. Tim, Matze, Lane, Shannon and the whole Deakin group – a huge thank you for every opened door, borrowed card and slice of cake when I came rushing in unannounced.

I'm also thankful to all manner of friends who have enriched my life over the last four years and longer. Amelia, Nick, Yuji and everyone else that didn't think Honours was enough – thank you for listening to every PhD-related complaint (and others, besides). To my friends elsewhere in the department – thanks for the hallway chats and borrowed things. Bec and Kat – why didn't one of you tell me this was a terrible idea before it was too late? Phoebe and Mercia – I don't think anyone could have asked for a better home than Club Nicholson.

None of this would have happened without Mel and Robin, the most supportive of parents, and Rosie, my favourite bro. And thanks to Indrek, for every wonderful distraction.

TABLE OF CONTENTS

1 INTRODUCTION	1
1.1 ORGANIC SALTS AND IONIC LIQUIDS	1
1.2 CORROSION PROCESSES ON IRON AND STEEL.....	2
1.2.1 <i>Electrochemical Principles of Corrosion</i>	2
1.2.2 <i>Passivation</i>	3
1.2.3 <i>Localised Corrosion and Chloride Attack</i>	5
1.2.4 <i>Protection Methods</i>	6
1.3 CORROSION INHIBITORS FOR STEEL	7
1.3.1 <i>Inhibition Mechanisms</i>	7
1.3.2 <i>Synergistic Effects</i>	10
1.3.3 <i>Dual-active Organic Inhibitors</i>	15
1.3.4 <i>Imidazoline Corrosion Inhibitors</i>	20
1.4 LIQUID AND SOLID ELECTROLYTES.....	21
1.4.1 <i>Exploring Physical Properties</i>	21
1.4.2 <i>Ionic Liquids as Electrolytes</i>	21
1.4.3 <i>Organic Ionic Plastic Crystals as Electrolytes</i>	23
1.5 AIMS	26
1.6 THESIS OUTLINE	27
1.7 REFERENCES	28
2 NOVEL IMIDAZOLINIUM SALTS AND IONIC LIQUIDS	33
2.1 NOVEL IMIDAZOLINIUM SALTS AND IONIC LIQUIDS.....	36
2.2 SUPPLEMENTARY INFORMATION	44
3 SYNERGISTIC CORROSION INHIBITION BY IMIDAZOLINIUM	
CINNAMATE SALTS.....	49
3.1 SYNERGISTIC CORROSION INHIBITION OF MILD STEEL IN AQUEOUS CHLORIDE SOLUTIONS BY AN IMIDAZOLINIUM CARBOXYLATE SALT	51
3.2 FURTHER INVESTIGATIONS.....	61
3.2.1 <i>Concentration Effects</i>	61
3.2.2 <i>Component Ion Effects</i>	64
3.2.3 <i>Alternative Cations</i>	65
3.2.4 <i>Inhibitor Reactivity</i>	68

3.3	ALKYLATED IMIDAZOLINIUMS	76
3.3.1	<i>Synthetic Routes</i>	76
3.3.2	<i>A Family of Alkylated Imidazolinium Cations</i>	78
3.4	CONCLUSIONS	80
3.5	EXPERIMENTAL METHODS	81
3.5.1	<i>Materials</i>	81
3.5.2	<i>Synthesis</i>	81
3.5.3	<i>Characterisation</i>	85
3.5.4	<i>Electrochemistry</i>	85
3.5.5	<i>Surface Analysis</i>	86
3.6	REFERENCES	86
4	PROTIC SUGAR ACID SALTS FOR THE CORROSION INHIBITION OF MILD STEEL	88
4.1	PROTIC SUGAR ACID SALTS FOR THE CORROSION INHIBITION OF MILD STEEL ...	89
4.2	SUPPLEMENTARY INFORMATION	105
5	SOLID-STATE CONDUCTIVITY IN PROTIC IMIDAZOLIUM AND IMIDAZOLINIUM SALTS	111
5.1	ENHANCING SOLID-STATE CONDUCTIVITY THROUGH ACID OR BASE DOPING OF PROTIC IMIDAZOLIUM AND IMIDAZOLINIUM TRIFLATE SALTS	114
5.2	SUPPLEMENTARY INFORMATION	137
6	CONCLUSIONS AND FUTURE WORK	145
6.1	CONCLUSIONS	145
6.2	FUTURE WORK	147
	BIBLIOGRAPHY	149

LIST OF TABLES

CHAPTER 1

<i>Table 1. A selection of organic inhibitor mixtures with synergistic corrosion inhibition effects on iron and steel.</i>	12
<i>Table 2. Dual-functional organic salts as corrosion inhibitors for steel.</i>	17

CHAPTER 2

<i>Table 1. Summary of thermal transitions.</i>	38
<i>Table 2. Density and thermal expansivity parameters for imidazolium ILs.</i>	39
<i>Table 3. Summary of average E_{corr} and i_{corr} and percentage efficiency values.</i>	41

CHAPTER 3

<i>Table 1. Corrosion current density (i_{corr}), corrosion potential (E_{corr}) and inhibitor efficiency.</i>	53
<i>Table 2. Pit analysis from optical profilometry at all conditions.</i>	56
<i>Table 3. Corrosion current density (i_{corr}), corrosion potential (E_{corr}), and inhibitor efficiency calculated from potentiodynamic polarisation.</i>	62
<i>Table 4. Pit analysis conducted by optical profilometry of coupons immersed for 24 h in 0.01 M NaCl plus inhibitor, with corrosion product removed.</i>	64
<i>Table 5. Comparison of shift in E_{corr} resulting from cathodic polarisation.</i>	71
<i>Table 6. Optimisation of reaction conditions for synthesis of [triMeImn][BF₄].</i>	77
<i>Table 7. Alkylated imidazolium salts synthesised by orthoester exchange.</i>	79

CHAPTER 4

<i>Table 1. Thermal transitions of glucuronate and galacturonate salts.</i>	95
<i>Table 2. Corrosion potential, E_{corr}, corrosion current density, i_{corr} and inhibition efficiency.</i>	96
<i>Table 3. Pit analysis from optical profilometry.</i>	100

CHAPTER 5

<i>Table 1. Entropies (ΔS) of transitions observed in [2-MeHIm][TfO] and [2-MeHImn][TfO].</i>	123
<i>Table 2. Activation energies for conductivity for [2-MeHIm][TfO] and [2-MeHImn][TfO] with highest doping level at 30 °C.</i>	126
<i>Table S1. Dopant level determined by titration with HCl or NaOH standard solutions.</i>	138

LIST OF FIGURES

CHAPTER 1

Figure 1. Pourbaix diagram for iron-water at 25 °C indicating presence of species with solubility of 10^{-6} M.....	4
Figure 2. Pitting corrosion on steel in an aqueous chloride environment.	5
Figure 3. Classification of corrosion inhibitors.	8
Figure 4. A comparison of the common ionic liquid cation methylimidazolium (left) and the general form of imidazolium (right).	20
Figure 5. Example of an oleic imidazoline corrosion inhibitor.	20
Figure 6. Common IL cations and anions for electrochemical applications.	22
Figure 7. Schematic representation of the Grotthuss mechanism, with the formation and cleavage of hydrogen bonds along a chain of water molecules resulting in the net movement of a proton.	23
Figure 8. The relationship between volume, conductivity and thermal behaviour with temperature for $[N_{2222}][DCA]$	24

CHAPTER 2

Figure 1. Hypothetical polarisation curve featuring anodic Fe dissolution and cathodic H_2 evolution.	35
Figure 1. A comparison of the common ionic liquid cation methylimidazolium and the general structure of the imidazolium cation.....	37
Figure 2. a) Reaction scheme for synthesis of 2-methylimidazolium acetate. b) The imidazolium and imidazolinium cations and accompanying anions studied.	38
Figure 3. TGA data for the salicylate and triflate salts.	39
Figure 4. Density of $[2\text{-MeHImn}]^+$ and $[2\text{-MeHIm}]^+$ ILs.	39
Figure 5. Arrhenius plot of viscosity of $[2\text{-MeHImn}]^+$ and $[2\text{-MeHIm}]^+$ ILs.	39
Figure 6. Arrhenius plot of conductivity of $[2\text{-MeHImn}]^+$ and $[2\text{-MeHIm}]^+$ ILs.....	40
Figure 7. Walden plot of $[2\text{-MeHImn}]^+$ and $[2\text{-MeHIm}]^+$ ILs.....	40
Figure 8. Possible Grotthuss-type mechanism for protonic charge transfer between $[2\text{-MeHImn}]^+$ cations to an unprotonated base, including transport of protons across the imidazolium face.	41
Figure 9. Electrochemical windows of $[2\text{-MeHImn}][Tf]$ and $[2\text{-MeHIm}][Tf]$ measured as 0.25M solutions in acetonitrile.....	41
Figure 10. Tafel plots of $[2\text{-MeHImn}]$ inhibitors at 4mM concentration in a 0.01 M NaCl aqueous solution compared with a control of 0.01 M NaCl solution in the absence of the inhibitor.	41

Figure 11. Optical images obtained after immersion of mild steel coupons in 4 mM [2-MeHImn][4-OHCin].	42
Figure S1. DSC traces of [2-MeHImn][Sal] showing initial melt, followed by a glass transition.	46
Figure S2. TGA of [2-MeHImn]+ carboxylate salts.	47
Figure S3. Titration of starting bases with 0.1 M HCl.	47
Figure S4. Comparison to individual ion components for [2-MeHImn][4-OHCin].	48
Figure S5. Optical images of steel coupons immersed in 4 mM solutions of component ion salts.	48

CHAPTER 3

Figure 1. Chemical structures of imidazolium and imidazolinium cations and cinnamate anion.	52
Figure 2. Tafel plots at: a) pH 8 showing affect of IL concentration; b) pH 8 comparing IL with separate salts; c) pH 2 showing affect of IL concentration and d) pH 2 comparing IL with separate salts.	53
Figure 3. Optical images of the surfaces of mild steel samples with corrosion product intact after immersion for 24 hours in a) 0.01M NaCl at pH 8; b) 0.01M NaCl and 4mM 2-MeHImn 4-OHCin at pH 8; c) 0.01M NaCl at pH 2; d) 0.01M NaCl and 4mM 2-MeHImn 4-OHCin at pH 2; e) 0.01M NaCl neutral and f) 0.01M NaCl and 4mM 2-MeHImn 4-OHCin neutral.	54
Figure 4. SEM images after corrosion product removal of the surfaces of mild steel samples immersed for 24 hours in a) 0.01M NaCl at pH 8; b) 0.01M NaCl and 4mM 2-MeHImn 4-OHCin at pH 8; c) 0.01M NaCl at pH 2; d) 0.01M NaCl and 4mM 2-MeHImn 4-OHCin at pH 2; e) 0.01M NaCl neutral and f) 0.01M NaCl and 4mM 2-MeHImn 4-OHCin neutral.	55
Figure 5. a) Optical profilometry image of pH 2 control sample; b) Typical profile across pH 2 control surface; c) Optical profilometry image of pH 2 inhibited sample; d) Typical profile across pH 2 inhibited surface.	56
Figure 6. IR spectra of 2-MeHImn 4-OHCin and component ion compounds.	57
Figure 7. IR spectrum of the steel surface after 48h immersion in 4mM 2-MeHImn 4-OHCin and 0.01M NaCl.	57
Figure 8. IR spectrum of the steel surface after 48h immersion in 4mM 2-MeHImn 4-OHCin and 0.01M NaCl at pH 2.	58
Figure 9. IR spectrum of the steel surface after 48h immersion in 4mM 2-MeHImn 4-OHCin and 0.01M NaCl at pH 8.	58
Figure 10. Polarisation curves for different concentrations of [2-MeHImn][4-OHCin].	62

Figure 11. Microscope images with corrosion product intact (x 0.8) and SEM images with corrosion product removed (x 1000) for coupons immersed for 24 h in 0.01 M NaCl and [2 MeHImn][4-OHCin] at varied concentration. a) and b) 4 mM; c) and d) 0.01 M; e) and f) 0.05 M; g) and h) control – no inhibitor.	63
Figure 12. Polarisation curve of 4 mM [2-MeHImn][Br] and 4 mM [Na][4-OHCin] component mixture.	65
Figure 13. Alternative cations; 2-methylimidazolium and 1,2,3-trimethylimidazolinium.	66
Figure 14. Polarisation curves of inhibitors with altered cations.	66
Figure 15. Microscope images with corrosion product intact (x 0.8) and SEM images with corrosion product removed (x 1000) for coupons immersed for 24 h in 0.01 M and 4 mM of inhibitor. a) and b) [2-MeHImn][4-OHCin]; c) and d) [2-MeHIm][4-OHCin]; e) and f) [triMeImn][4-OHCin]; g) and h) control – no inhibitor.	67
Figure 16. Comparison of OCP with and without 4 mM [2-MeHImn][4-OHCin] over a) 30 min and b) 24h.	69
Figure 17. Addition of inhibitor after 30 min OCP hold in 0.01 M NaCl. The inhibitor ennobled the electrode, but introduced instability in the OCP.	70
Figure 18. Starting the anodic polarisation from -50 mV vs. OCP resulted in a 53 mV shift in E_{corr} relative to E_{corr} at the end of the OCP hold (initial polarisation).	71
Figure 19. Electrochemical windows for [2-MeHImn][4-OHCin] and component ion salts.	72
Figure 20. Products obtained from the electrochemical reduction of cinnamic acid (l to r): β -phenylpropionic acid, $\beta\gamma$ -diphenyladipic acid, γ -truxillic acid.	73
Figure 21. IR spectrum of precipitate from electrolyte solution 0.05 M [2-MeHImn][4-OHCin] in 0.01 M NaCl.	74
Figure 22. Measurement of the anodic and cathodic arms separately resulted in an increased estimation of i_{corr}	75
Figure 23. Reaction scheme for synthesis of N-substituted 2-methylimidazolinium salts.	76
Figure 24. Reaction scheme for synthesis of 1,3-diethyl,2-methylimidazolinium iodide via lithiation and alkylation with iodoethane.	78
Figure 25. A selection of imidazolinium cations synthesised via the orthoester route (l to r): 1,2-dimethylimidazolinium, 1,2,3-trimethylimidazolinium, 1,3-diethyl, 2-methylimidazolinium and 1,3-bis(hydroxyethyl),2-methylimidazolinium.	78

CHAPTER 4

Figure 1. Selection of uronic acid anions and protic ammonium cations.	94
Figure 2. Polarisation curves for mild steel electrodes in neutral aqueous electrolytes with 0.01 M NaCl and 4 mM inhibitor.	96
Figure 3. Polarisation curves comparing effects of concentration on [2-MeHImn][Glu] inhibition.	97
Figure 4. Optical images (x 0.8) with corrosion product and SEM images (x 300) after removal of corrosion product of mild steel after immersion for 24 h in 0.01 M NaCl and a) and b) 4 mM [2-MeHImn][Glu]; c) and d) 0.01 M [2-MeHImn][Glu]; e) and f) 4 mM [2-MeHIm][Glu]; g) and h) 4 mM [2-MeHImn][Gal]; i and j) control – no inhibitor.	99
Figure 5. a) Optical profilometry image of 4 mM [2-MeHImn][Glu] sample; b) cross-section of surface depth across 4 mM [2-MeHImn][Glu] sample; c) optical profilometry image of 0.01 M NaCl control sample; d) cross-section of surface depth across 0.01 M NaCl control sample.	101
Figure S1. TGA curves for a) glucuronate salts and b) galacturonate salts.	109
Figure S2. SEM images (x 300) of corroded (left) and uncorroded (right) regions after removal of corrosion product from mild steel immersed for 24 h in 0.01 M NaCl and: a) and b) 4 mM [2-MeHImn][Glu]; c) and d) 10 mM [2-MeHImn][Glu]; e) and f) 4 mM [2-MeHIm][Glu]; g) and h) 4 mM [2-MeHImn][Gal]; i) and j) control – no inhibitor.	110

CHAPTER 5

Figure 1. Structure and TGA data for a) [2-MeHIm][TfO] and b) [2MeHImn][TfO] with acid or base doping.	121
Figure 2. DSC thermograms of [2-MeHImn][TfO] with acid or base doping into the pure salt (green trace, centre diagram).	122
Figure 3. DSC thermograms of [2-MeHIm][TfO] with acid or base doping into the pure salt (green trace, centre diagram).	122
Figure 4. Conductivity of the pure and doped a) [2-MeHIm][TfO] and b) [2-MeHImn][TfO] samples as a function of inverse temperature.	124
Figure 5. Dependence of conductivity of [2-MeHImn][TfO] and [2-MeHIm][TfO] on mole fraction of dopant at selected temperatures.	126
Figure 6. Static solid-state a) ^1H NMR and b) ^{19}F NMR spectra of [2-MeHIm][TfO] and [2 MeHImn][TfO] at selected temperatures.	128
Figure 7. Area fraction of narrow peaks, indicating mobile species in a) ^1H and b) ^{19}F static NMR.	130
Figure 8. Line widths for broad peaks in a) ^1H and b) ^{19}F static NMR.	131

Figure 9. Comparison of [2-MeHIm][TfO] and [2-MeHImn][TfO] a) ^1H cation diffusion coefficients; b) ^{19}F anion diffusion coefficients.	133
Figure 10. Comparison of diffusion coefficients for the C-H and N-H protons for [2 MeHIm][TfO] with TfOH or 2-MeIm doping.	134
Figure S1. Titrations of 2-MeImn and 2-MeIm with 0.1 M TfOH.	137
Figure S2. Titration of [2-MeHImn][TfO] + 4.1 mol% TfOH with 0.009 M NaOH.	137
Figure S3. Static solid-state ^1H NMR spectra of [2-MeHIm][TfO] with doping at selected temperatures.	139
Figure S4. Static solid-state ^{19}F NMR spectra of [2-MeHIm][TfO] with doping at selected temperatures.	139
Figure S5. Static solid-state ^1H NMR spectra of [2-MeHImn][TfO] with doping at selected temperatures.	140
Figure S6. Static solid-state ^{19}F NMR spectra of [2-MeHImn][TfO] with doping at selected temperatures.	140
Figure S7. Comparison of the narrow ^1H peaks for a) [2-MeHIm][TfO] and [2-MeHImn][TfO] with doping at 273 K; b) TfOH doped samples showing shift in N-H and TfOH peaks with increasing temperature.	141
Figure S8. Line fitting for [2-MeHImn][TfO] + 2.6 mol% 2-MeImn at 20 °C using dmfit software.	142
Figure S9. Comparison of cation and anion diffusion coefficients for a) [2-MeHIm][TfO] and b) [2-MeHImn][TfO] with TfOH and base doping.	143
Figure S10. Comparison of diffusion coefficients for C-H and N-H protons in [2-MeHImn] $^+$. The similarity in values suggests the protons in both environments diffuse together as part of the whole cation.	144

LIST OF ABBREVIATIONS

[2-MeHIm] ⁺	2-methylimidazolium
[2-MeHImn] ⁺	2-methylimidazolinium
[4-OHCin] ⁻	4-hydroxycinnamate
[Ac] ⁻	Acetate
[BF ₄] ⁻	Tetrafluoroborate
[C ₂ mim] ⁺	1-ethyl-3-methylimidazolium
[C ₃ MPyr] ⁺	1-propyl-1-methylpyrrolidinium
[C ₄ mpip] ⁺	<i>N</i> -butyl- <i>N</i> -methylpiperidinium
[DCA] ⁻	Dicyanamide
[diEtMeImn] ⁺	1,3-diethyl-2-methylimidazolinium
[diEtOHMeImn] ⁺	1,3-bis(hydroxyethyl)-2-methylimidazolinium
[diMeHImn] ⁺	1,2-dimethylimidazolinium
[For] ⁻	Formate
[FSI] ⁻	Bis(fluorosulfonyl)imide
[Gal] ⁻	Galacturonate
[Gen] ⁻	Gentisate
[Glu] ⁻	Glucuronate
[HBIm] ⁺	1-butylimidazolium
[HMIIm] ⁺	1-methylimidazolim
[HMPyr] ⁺	1-methylpyrrolidinium
[N ₁₂₂₄] ⁺	<i>N,N</i> -diethyl- <i>N</i> -methyl- <i>N</i> -butylammonium
[N ₄₄₄₄] ⁺	Tetraethylammonium
[NTf ₂] ⁻	Bis(trifluoromethylsulfonyl)imide
[PF ₆] ⁻	Hexafluorophosphate
[Sal] ⁻	Salicylate
[SCN] ⁻	Thiocyanate
[TfO] ⁻	Triflate (trifluoromethanesulfonate, NB. [TfO] ⁻ is used in published works)
[triMeImn] ⁺	1,2,3-trimethylimidazolinium
2-MeIm	2-methylimidazole
2-MeImn	2-methylimidazoline
2M2	Sodium 2-undecyl-1-ethanoate-imidazoline
ATR	Attenuated total reflectance
b.p.	Boiling point
Boc	<i>tert</i> -butoxycarbonyl
BTA	Benzotriazole

Bu	Butyl
CP	Calcium propionate
CSA	Chemical shift anisotropy
CTAB	Cetyltrimethylammonium bromide
<i>D</i>	Diffusion coefficient
D ₂ O	Deuterium oxide
DAP	2,6-diaminopyridine
DCM	Dichloromethane
DICHAN	Dicyclohexylammonium nitrite
DMSO	Dimethylsulfoxide
DSC	Differential scanning calorimetry
EAN	Ethylammonium nitrate
<i>E_a</i>	Activation energy
<i>E_{corr}</i>	Corrosion potential
EDTA	Ethylenediamine tetraamine
equiv.	Equivalent
ESI	Electrospray ionisation
Et	Ethyl
EtOAc	Ethyl acetate
EtOH	Ethanol
FID	Free induction decay
FTIR	Fourier transform infrared spectroscopy
<i>g</i>	Gas state
<i>G</i>	Magnetic field gradient
Hz	Hertz
<i>I</i>	NMR signal intensity
<i>i_{corr}</i>	Corrosion current density
IE	Inhibition efficiency
IL	Ionic Liquid
J	Joules
K	Degrees Kelvin
M	Molar
MAS	Magic Angle Spinning
Me	Methyl
MeCN	Acetonitrile
MeOH	Methanol
mol	mole
MS	Mass spectrometry

NMR	Nuclear magnetic resonance
OCP	Open circuit potential
OCV	Open circuit voltage
OIPC	Organic Ionic Plastic Crystal
P	Poise
PAA	Polyacrylamide
PEG	Polyethylene glycol
PEMFC	Proton exchange membrane fuel cells
PGSE	Pulsed-gradient spin echo
PGSTE	Pulsed-gradient stimulated echo
PP	Potentiodynamic polarisation
PPA	Phenylphosphate
ppm	Parts per million
QI	8-Quinolinol
R	Gas constant
RF	Radio frequency
S _a	Surface roughness
SB	Sodium benzoate
SCE	Saturated calomel electrode
SDS	Sodium dodecylsulfonate
SEM	Scanning electron microscopy
SG	Sodium gluconate
SO	Sodium oleate
SOP	Sodium octylmercaptopropionate
T	Temperature
TA	Tartaric acid
TBA	Tetrabutylammonium
TBP	tertiary butyl phosphonate
T _d	Decomposition temperature
temp.	Temperature
TfOH	Triflic acid (trifluoromethane sulfonic acid)
T _g	Glass transition
TGA	Thermogravimetric analysis
THF	Tetrahydrofuran
T _m	Melting temperature
TU	Thiourea
ν	IR vibrational stretch
V	Volts

Van	<i>iso</i> -Vanillin
VPI	Vapour phase inhibitor
VTF	Vogel-Fulcher-Tammann
α_v	Thermal expansivity
β_a	Anodic Tafel constant
β_c	Cathodic Tafel constant
γ	Gyromagnetic ratio
Δ	Diffusion time
δ	Gradient pulse length
ΔS_f	Entropy of fusion
η	Viscosity
η_a	Anodic overpotential
η_c	Cathodic overpotential
Λ	Molar conductivity
ρ	Density
σ	Conductivity
τ	Time between NMR gradient pulses

1 INTRODUCTION

1.1 Organic Salts and Ionic Liquids

Organic salts are compounds consisting of an anion and cation where at least one of the species is an organic ion. Salt formulations may be accessed as a consequence of a synthetic route, or employed to increase stability or alter solubility. The counter ion is often a simple halide or main group metal and does not play an active role in the reactivity of the compound.

Increasing interest in ionic liquids (ILs) has seen a shift in the perception of organic salts generally. ILs are a subset of organic salts that have low melting points, often stated as below 100 °C.¹ These liquids can have a range of highly advantageous physical and chemical properties such as high ionic conductivity, high thermal and electrochemical stability, non-flammability, negligible vapour pressure and excellent solvation.² This has led to exploration of ILs for use in diverse applications including batteries and electrochemical devices,³⁻⁵ synthetic solvents,^{1,6} CO₂ capture^{7,8} and biomass dissolution.⁹¹⁰ This work has greatly expanded the library of known organic salts, in particular those with both an organic anion and cation. As salts can be made from any combination of ions, the number of potential compounds is immense.

One of the greatest strengths of the IL platform is the ability to hand pick a formulation to obtain the desired properties for a given application. In recent years, there has been a shift in the focus of this tunability. While early research focused solely on modifying physical properties such as fluidity or electrochemical window, researchers are now designing task-specific ILs with properties targeted to their applications.¹¹ Instead of trying to fit traditional ILs to a given application, one can take an “active” compound and redesign it as an IL with enhanced functionality. Examples include ILs that have large aromatic functionality to stabilise radioactive waste, and dual-active pharmaceutical ILs that combine antimicrobials with analgesics.¹² In this thesis, a customising approach is

used to discover novel organic salts for use as corrosion inhibitors for steel in aqueous chloride environments.

1.2 Corrosion Processes on Iron and Steel

Metal alloys such as carbon steel have revolutionised modern construction and manufacturing; however, these materials are not stable when unprotected in the environment. Corrosion is the natural process of destruction of metals and alloys that returns the metal atoms to more stable compounds, akin to the minerals that they were originally extracted from. It is estimated that corrosion causes trillions of dollars of damage worldwide every year.¹³ With the heavy reliance of modern infrastructure on steel and other metals, constant monitoring and control are required to prevent the incursion of corrosive attack.

1.2.1 Electrochemical Principles of Corrosion

In chemical terms, corrosion is the degradation of metals through electrochemical processes. Typically two connected metal sites (often different areas of the same piece of metal) form the anode and cathode that, when linked by an electrolyte, complete an electrochemical cell.¹⁴

At the anodic site, the metal undergoes oxidation, as described in Equation 1.



Where z is a stable valence of a given metal, M . This process generates electrons which flow to the cathode where they are consumed by the reduction of a cathodic species (Equation 2).



The result is a spontaneous reaction with an overall loss of metal:



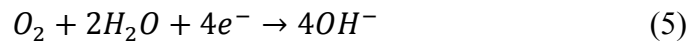
In steel, the predominant anodic reaction is the oxidation of Fe to ferrous (Fe^{2+}) or ferric (Fe^{3+}) ions, however, there is a wider range of cathodic processes that can take place. In acidic environments, the most common reaction is hydrogen reduction, the overall equation for which is:



Typically a proton is first adsorbed to the cathode before reacting with either another adsorbed species or another proton from solution to generate hydrogen gas. Iron is

vulnerable to this form of attack due to having a lower electrode potential than that of hydrogen.

In neutral and basic conditions, where protons are less readily available, oxygen gas reduction is a key cathodic process. This involves the conversion of dissolved O_2 gas to hydroxyl ions, the overall equation being:



A common pathway for this $4e^-$ process is through the formation of hydrogen peroxide.¹⁵

A number of other cathodic processes can take place, depending on the environment, including the reduction of water or oxidising agents such as nitric and sulfuric acid or the deposition of a more noble metal.¹⁶ Most corrosion processes, and protection methods, can be understood in terms of their effects on either the anodic or cathodic reactions and how readily they proceed.

1.2.2 Passivation

The reactions that take place are dependent on the environment, and factors such as the electrode potential, temperature and pH can determine which forms of iron will be thermodynamically favoured. For example, in the presence of water, iron can exist as soluble ferric or ferrous ions, or as a number of solid oxides and hydroxides, such as Fe_2O_3 . A useful way to graphically express this information is through Pourbaix diagrams. These phase diagrams represent the metal-ion-oxide equilibria with respect to electrode and pH at a given temperature and solute concentration.¹⁷ A Pourbaix diagram for iron in water at 25 °C is shown in Figure 1.

At very negative potentials, the metallic iron is cathodically protected and immune to corrosive attack. As the electrode potential is increased in neutral or acidic conditions, the iron is oxidised to soluble ferrous ions or, at very high potentials and low pH, soluble ferric ions, leading to corrosion of the metal. However, in alkaline or sufficiently anodic conditions, the iron forms ferrous compounds that are highly insoluble in aqueous solutions and precipitate at the surface. These precipitates, primarily Fe_2O_3 , form an adherent film that insulates the remaining metal from further reaction. This results in a domain of passivity, in which the iron resists corrosion despite the thermodynamic driving force for oxidation.

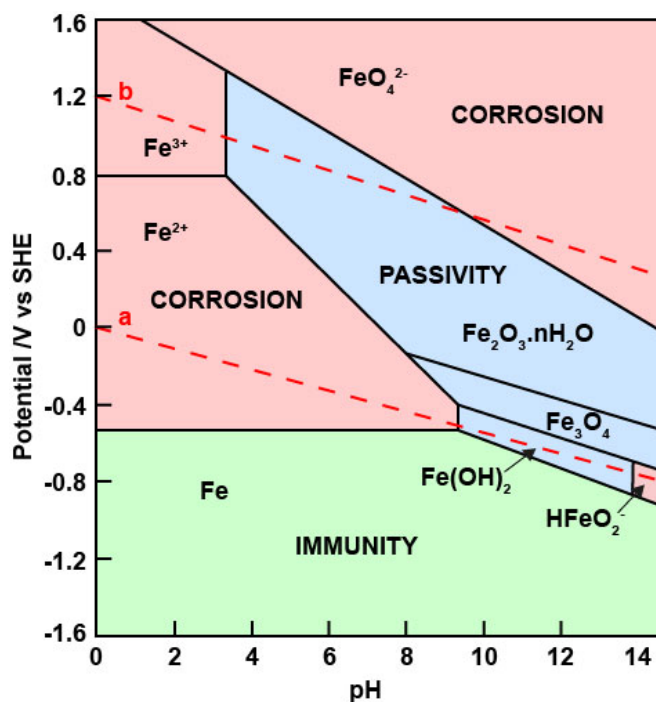


Figure 1. Pourbaix diagram for iron-water at 25 °C indicating presence of species with solubility of 10^{-6} M. Dashed lines indicate the stable region for water; below a) H₂O is reduced to H₂, above b) H₂O is oxidised to O₂. Green colouring indicates 'immune' Fe, with cathodic protection, red indicates regions of corrosion and blue indicates formation of a passivating oxide layer. Adapted from Ahmad.¹⁸

Although the metal may be operating in corrosive conditions, as would be the case for steel in a neutral aqueous environment, there are a number of ways of treating the iron to actively promote passivation. Most metals will naturally form a thin oxide layer when exposed to air, and there are a number of ways to bolster this film. Anodising is an electrolytic pre-treatment that can thicken such oxide layers by holding the metal at a sufficiently anodic potential. In iron in neutral conditions this process can lead to unstable, flaky films; however, the formation of more adherent films can occur if anodising is performed in the presence of nitric acid.¹⁶

Passive films do not have to be made up solely of iron oxides, but may also include other metal oxides or insoluble salts. As such, additives can be used to influence passivation. An important example of this is the alloying of chromium, nickel and other elements with iron to form stainless steel. The alloying elements help to form a stronger oxide film that greatly increases the range of passivity compared to that of pure iron. Chemical inhibitor additives can also be used to promote passivation *in situ*. This will be discussed further in section 1.3.1.

1.2.3 Localised Corrosion and Chloride Attack

Once a protective film is formed, it can remain stable, undergo complete dissolution to reactivate the surface, or break down at selected points. This partial failure of the film can lead to localised attacks such as crevice and pitting corrosion. Localised corrosion is one of the key methods of corrosion in steel, particularly alloyed steels such as stainless steel, which are designed to passivate as protection against general corrosion. Due to the random nature of localised corrosion, it can be much more difficult to engineer against than uniform corrosion, and is responsible for far more premature part failures.

Pitting corrosion can occur when dissolution begins at a defect or hole in the passive film (Figure 2). Initially both anodic and cathodic process can take place at the site. As the process continues, oxygen cannot readily diffuse to the area, and a differential aeration cell is established, with current passing between the oxygen-free local anode and the aerated cathodic area around the defect. As the soluble metal ions that are generated precipitate as hydroxides, they can form a loose shield of corrosion product that further restricts migration of oxygen into the pore. This precipitation also depletes the local hydroxide concentration, causing a rise in the H^+ concentration and drastic drop in pH. The processes become self-sustaining and result in a small anode/ large cathode situation, where the high currents generated from oxygen reduction across the large exposed surface are concentrated on the small anode area. Such high current densities result in substantial corrosion rates in the pit and can lead to rapid perforation or failure of a part.¹⁹

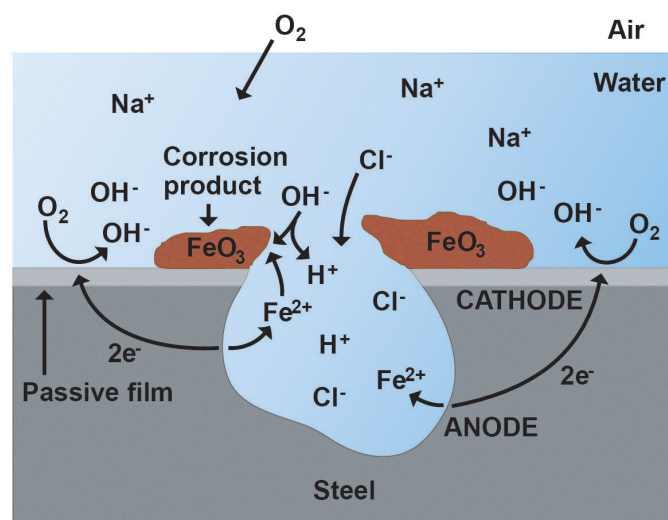


Figure 2. Pitting corrosion on steel in an aqueous chloride environment. Electrons flow from the anodic site inside the pit to cathodes at nearby passive areas. The corrosion products obscure the mouth of the pit and the solution inside becomes concentrated with H^+ and attracted Cl^- .

Localised corrosion is greatly enhanced by the presence of aggressive species such as chloride ions. A number of studies, dating from the 1960s have described models for the involvement of chloride and other species in initiating passivation breakdown.²⁰

Hoar et al.²¹ first suggested that chloride and other aggressive anions could access the metal surface by direct transfer through the passive layer, after which they can complex with the metal ions. This could be feasible due to the highly disordered structure of the oxide layer, with a high concentration of atomic defects. Others have suggested that mechanical defects in the passive film, such as fissures, are required for chloride ions to reach the surface.²² Once there, they can begin to form an unstable chloride film that competes with the passive film, causing it to break further. Adsorption mechanisms have also been proposed, whereby chloride at the surface of the passive film draws metal ions out of the oxide layer. This gradually thins out the passive layer, until a point where it is breached.²³

Once a pit has formed, the greater mobility of the chloride ions means that they dominate migration into the pores, in place of oxygen. From within the pore the chloride anions form complexes with metal ions that are rapidly hydrolysed, contributing to the increase in H^+ concentration (Figure 2). The subsequent drop in pH serves to attract further Cl^- ions. This behaviour results in highly acidic and chloride-rich solutions within the pits, even if the bulk solution is neutral and has low chloride concentrations. In such an environment, even stainless steel cannot remain passive, and rapid dissolution follows.

1.2.4 Protection Methods

Regardless of the specific processes, during spontaneous corrosion, the anodic and cathodic reactions must generate the same current. As such, protection methods can target one or both of the anodic and cathodic reactions in order to reduce the overall rate of corrosion. Some common methods include:

- Impressed current cathodic protection: Cathodic polarisation reduces the driving force for the anodic reaction by supplying an external source of electrons. Inaccessible structures such as underground pipelines and offshore drilling can be connected to power lines or external generators.
- Galvanic or sacrificial anode cathodic protection: The metal is coupled to a more reactive metal that takes over the anodic role and sacrificially dissolves. Carbon steel in soil or seawater can be successfully protected by contact with aluminium, zinc or magnesium.

- Chemical scavengers: Chemical compounds remove possible reactants from the environment to limit the rate of cathodic processes. The most common oxygen scavengers used in water at ambient temperatures are sulfites, such as sodium sulfite (Na_2SO_3), that react with dissolved O_2 to form sulfates.
- Metallic coatings: Corrosion-prone metals can be coated with a secondary metal or alloy that is more corrosion resistant. Often a more reactive metal is chosen so that it can provide galvanic protection at defects or breaks in the coating.
- Non-metallic coatings: Inert organic coatings such as glass, plastic, paints, or polymers can prevent access of moisture and corrosive species to metal, as well as insulate sites to prevent formation of an electrochemical cell.
- Inhibitors: Chemical compounds are added to the environment which help to create an *in situ* barrier at the exposed metal surface, either by promoting the formation of a passive film or by simply adsorbing to the surface.

Each of these methods has a number of advantages and disadvantages, and their use has to be considered as part of the design of a metallic structure. For example, impressed current protection provides good general protection, but is energy-intensive to maintain and may not protect against localised corrosion; and while paints and polymers are cheap coatings, they may not be stable in high temperature environments.^{16, 24}

1.3 Corrosion Inhibitors for Steel

1.3.1 Inhibition Mechanisms

When considering protection methods, chemical inhibitors are attractive due to their relatively low cost, and ease of use. Unlike many of the other methods, they do not require substantial infrastructure (needed for cathodic protection) and do not have to be administered at the time of installation (such as a metal or polymer coating), but can instead be added remedially or adjusted as required over the lifetime of the structure. Chemical inhibitors generally fall into three categories: species that target anodic sites, species that target cathodic sites, or species that adsorb indiscriminately across the whole surface (Figure 3).²⁵

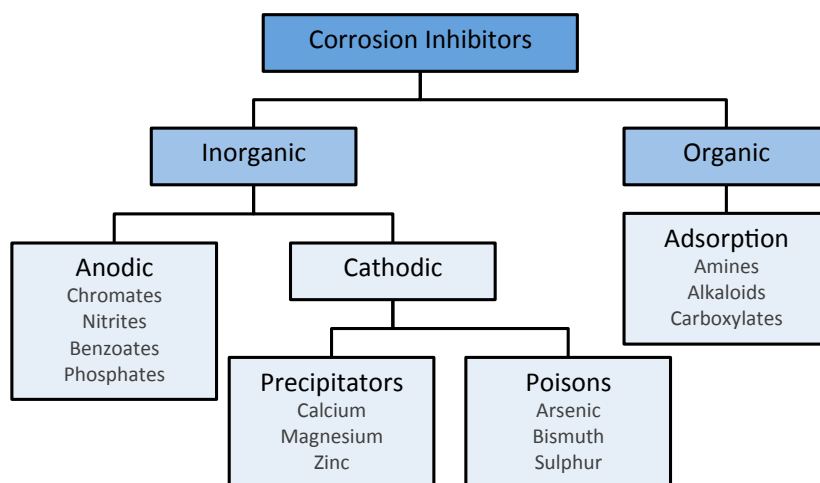


Figure 3. Classification of corrosion inhibitors.

Nitrite, NO_2^- , and chromate, CrO_4^{2-} , are two examples of oxidising agents that act as anodic inhibitors. These ions are attracted to positive metal ions in solution, and are thus targeted to the anodic sites. As gaps appear in the passivating layer, these anions migrate to the area and influence the equilibrium of iron states from the ferrous Fe^{2+} in favour of the ferric Fe^{3+} state. The ferric ions quickly precipitate into a stable film that repairs the original breakdown. The oxidising agent is in turn reduced via varied pathways to species such as ammonium or chromium oxide.¹⁶

Other passivating anodic inhibitors include anions of weak acids such as benzoates, silicates and orthophosphates. These anions are not oxidising agents, but can promote the formation of iron oxide films in the presence of oxygen. Some of these inhibitors can also act like adsorption inhibitors, as described below. By forming a surface film at the anodic sites, these compounds minimise dissolution of iron from the surface, hence slowing the anodic reaction.²⁶

A crucial disadvantage of anodic inhibitors is that they can cause extensive damage if used in insufficient quantities. If a pore opens up in the passive film and all of the inhibitor is already consumed, this small anode will support all the current for cathodic reactions taking place across a much larger surface area. This causes very high current densities and accelerates the formation of severe pits.²⁷

Inorganic cathodic inhibitors generally fall into two categories: precipitators and poisons. As the cathodic reactions proceed, they raise the pH of the local area, causing metal ions such as Ca^{2+} , Mg^{2+} and Zn^{2+} to precipitate out of solution as insoluble carbonates and hydroxides. This mineral 'scale' insulates the surface, preventing further cathodic reactions. Many natural waterways self-inhibit in this way, due to the formation

of scale from naturally occurring salts. When using this method, however, the pH of the system must be carefully controlled; if the pH is too high the rapidly precipitated hydroxides will be poorly-adherent and if it drops too low the metals will redissolve.²⁷

Cathodic poisons directly interfere with cathodic processes such as hydrogen evolution and oxygen reduction. Group 15 elements (arsenic, antimony, bismuth) and group 16 elements (sulfur, selenium) increase the energy barrier for H^+ adsorption and molecular hydrogen evolution, thus slowing the cathodic rate, and the overall rate of corrosion. One of the major dangers with this type of inhibition is that the atomic hydrogen trapped on the surface can diffuse into the steel, leading to embrittlement or hydrogen blisters.²⁷

Some species do not form precipitates or affect the formation of a passive film, but instead function merely by assembling at the metal surface to block the approach of species such as Cl^- and O_2 . These adsorption inhibitors are often organic molecules, characterised by the presence of heteroatoms such as nitrogen, sulfur or oxygen that either sustain charge or are highly polarised within the neutral molecule. It is through this functionality that the inhibitor binds to the surface, via physisorption (i.e. electrostatic charge attraction) or chemisorption (i.e. coordination of lone pairs to metal ions). As these species act by steric hindrance, they are traditionally quite bulky, with long alkyl chains or aromatic ring systems providing optimal surface coverage. These inhibitors generally adsorb across the whole surface, but may preferentially affect cathodes or anodes. It is not easy to predict trends in how individual chemical structures will inhibit. Common inhibitors of this type include amines, quinolones, alkaloids, sulfonates, formaldehyde, and thiourea.¹⁶

While the number of inhibitors to choose from is immense, it is important to select a formulation that is appropriate for the system. Their effectiveness is highly dependant on environmental factors such as temperature, pH, metal type and the presence of species such as water, oxygen or chloride. Inhibitors can be formulated as either solids or liquids, and can be added to a system continuously or in regular batches. They are generally used in low concentrations, particularly in flow-through systems, where the chemical cannot be recouped; however, higher inhibitor concentrations can be supported in circulating systems such as water cooling tanks.

Many of the highly effective inorganic inhibitors are falling out of use due to concerns about their toxicity and environmental impact. Chromates, nitrites and arsenates are among the compounds that are no longer considered safe for widespread use.²⁸ Trends have turned towards the use of organic inhibitors as potential green inhibitors that reduce environmental impact in both manufacturing and application.²⁹⁻³²

1.3.2 Synergistic Effects

One way for organic inhibitors to match the inhibition efficiency of toxic inorganic species is to take advantage of synergy between a mixture of inhibitors, and it is quite common for a protection regime to incorporate multiple inhibitors. Table 1 presents a selection of organic inhibitor mixtures that have been studied as corrosion inhibitors on iron and steel in aqueous environments. Different combinations of species have been shown to interact synergistically to inhibit corrosion. The inhibition mechanisms of each system are reported, as well as the inhibition efficiencies (calculated as a percentage decrease in i_{corr} relative to an uninhibited control).

A number of studies have observed synergistic increases in inhibition upon mixing of carboxylic acids or carbonyls with amines.³³⁻³⁶ Hackerman has suggested that this method is effective due to the ability of an ionic co-species to stabilise an adsorbed ion layer. Qiang et al.³³ and Rammelt et al.³⁴ described co-adsorption of species in such mixed inhibitors. Benzotriazole (BTA) was found to adsorb to the oxide layer on the surface, complementing the adsorption of sodium benzoate specifically at the anodic sites.³⁴ In acidic media, BTA adsorbed to the surface as a cation, enabling better adsorption of the anionic ethylenediamine tetraamine (EDTA) – iron complexes formed in solution.³⁵ Suzuki et al.³⁶ observed co-precipitation of iron complexes when using two neutral complexing molecules, where once again, one species acted preferentially at the anodic sites. The blending of these organic compounds resulted in inhibition efficiencies of over 90 %.

Due to their long alkyl chains, surfactants are a class of organic molecules that are attractive as corrosion inhibitors. While combining two surfactants, sodium dodecylsulfonate (SDS) and cetyltrimethylammonium bromide (CTAB) gave moderate efficiencies,³⁷ pairing a surfactant with a smaller organic inhibitor (i.e. gluconate³⁸, hexamethylenetetramine³⁹ or urea⁴⁰) was highly successful. In all cases inhibition was attributed to adsorption, resulting in cathodic or mixed inhibition. Hosseini et al.³⁹ did note, however, that if the concentrations of either additive were too low, the synergistic effects were lost. They proposed that this was due to the electrostatic interactions between compounds not favouring migration to the metal surface at low concentrations. Interestingly, when pairing a surfactant with tetramethylammonium iodide, the ability of the surfactant to adsorb to the surface was enhanced not by the amine but by the I⁻ ions.⁴¹ This is in line with the well-reported synergy between organic inhibitors and iodides.⁴²⁻⁴⁴ Umoren⁴⁵ has presented a study combining two polymers, with the hope that their bulky

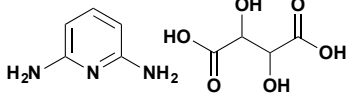
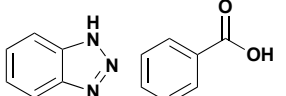
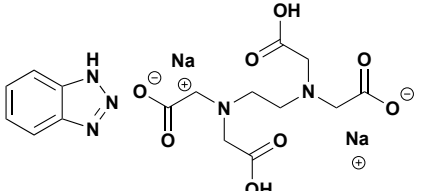
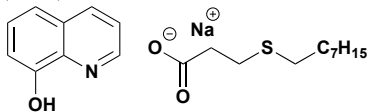
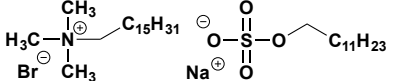
nature would provide good surface coverage. Moderate synergistic effects were observed upon blending, with a 1:3 ratio of PEG to PVP.

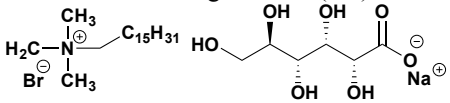
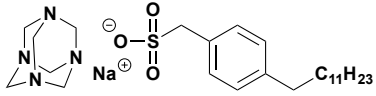
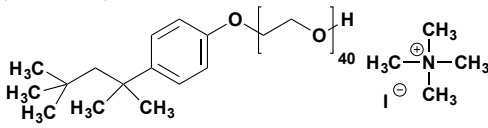
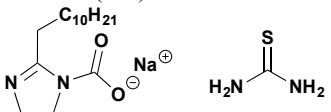
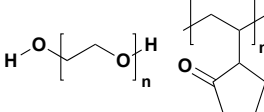
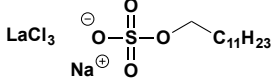
Organic – inorganic combinations have also been explored. Simple salts of rare earth metals were first investigated as corrosion inhibitors for steel in the late 1980s.⁴⁶ They act by precipitating as oxide and hydroxide films at the cathodic sites. Mu et al.⁴⁷ found that by pairing lanthanum (III) chloride, LaCl_3 , with SDS, mixed inhibition was observed. At the optimal composition, the addition of SDS increased the inhibition efficiency of LaCl_3 by over 70 %. Further studies by Li and coworkers found similar success with cerium (IV) chloride combined with surfactants and aromatic molecules.⁴⁸⁻⁵¹ They suggest that metal – organic complexes form in solution and are incorporated into the protective surface film.

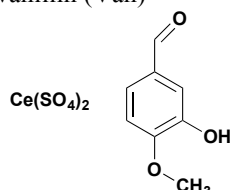
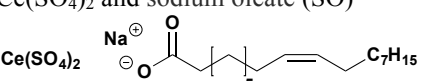
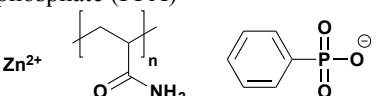
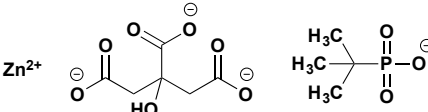
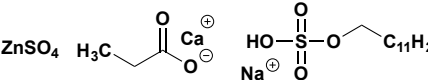
Another popular organic – inorganic combination is ternary zinc mixtures. Such inhibitor systems combine zinc sulfate, a successful cathodic precipitator, with a range of additives: polymers, surfactants, carboxylates, amino acids or phosphorous compounds.⁵²⁻⁵⁶ Alone, the Zn^{2+} accelerates corrosion and the organic components do not form adherent surface films.⁵⁶ A proposed mechanism suggests that the species can form complexes in solution that are attracted to the metal surface. Once at the anodic sites, Fe^{2+} displaces Zn^{2+} in the complexes and Zn^{2+} subsequently precipitates with hydroxide ions forming at the cathodes. This results in a mixed inhibitor system that is significantly more effective than any of the component parts.^{53, 56}

These examples of synergy rely on the use of multiple compounds in tandem. And in many of these cases, ionic inhibitors are added paired with a simple counter ion (Na^+ , Cl^- , Br^- , SO_4^{2-}). This ion is essentially a spectator and at best has no benefit, or in fact may be having an adverse effect. It can also be noted that many of the mechanisms presented rely on the ionisation of the organic compound in acidic solutions. This is where a dual active salt could be advantageous in moving towards greener systems. Salt inhibitors could be designed to incorporate two different inhibitors into the same compound, with an improvement in molecular efficiency. In a number of the described mixtures, the active components could be readily converted into a single salt

Table 1. A selection of organic inhibitor mixtures with synergistic corrosion inhibition effects on iron and steel. Efficiencies reported from polarisation data where available, or weight loss data.

Inhibitor	Substrate	Conditions	Concentration	Inhibition and remarks	Efficiency / %	Ref.
2,6-diaminopyridine (DAP) and tartaric acid (TA) 	Mild steel	0.5 M HCl	1 – 15 mM (2:1 DAP to TA)	Mixed inhibition Co-adsorption to surface	75 – 93	33
Benzotriazole (BTA) and sodium benzoate (SB) 	Mild steel	Aqueous	0.1M SB and BTA	Mixed inhibition Adsorption SB blocks pores in passive film, BTA adsorbs to oxide film		34
BTA and ethylenediamine tetraacetic acid disodium (EDTA) 	Cold rolled steel	0.1 M HCl	10 – 50 mg/L EDTA 8 – 10 mg/L BTA	Mixed inhibition, predominantly anodic BTA adsorption enables anionic Fe-EDTA complex adsorption through electrostatic interaction	74 – 93	35
8-quinolinol (QI) and sodium octylmercaptopropionate (SOP) 	Iron	0.5 Na ₂ SO ₄	0.1 – 3 mM SOP and QI	Precipitate film formation SOP-Fe ³⁺ precipitates at anodes QI chelates with Fe ²⁺ in oxide film	0 – 98	36
Cetyltrimethyl ammonium bromide (CTAB) and sodium dodecyl sulfate (SDS) 	Mild steel	3.5 wt% NaCl	0.005 – 0.1 M SDS and CTAB (10:90 mixtures)	Mixed inhibition Adsorption	40 – 61	37

Inhibitor	Substrate	Conditions	Concentration	Inhibition and remarks	Efficiency / %	Ref.
CTAB and sodium gluconate (SG) 	Galvanised steel	3 % NaCl	0.01 mM CTAB, 1 mM SG	Cathodic inhibition Adsorption	94	38
Hexamethylenetetramine (HA) and sodium dodecylbenzenesulfonate (SDBS) 	Mild steel	0.5 M H ₂ SO ₄	25 – 300 ppm HA, 200 ppm SDBS	Physical adsorption	57 – 94	39
TRITON-X-405 and tetramethylammonium iodide (C ₄ H ₁₂ N I) 	Stainless steel	2 M H ₂ SO ₄	0.0001 – 0.1 mM TRITON-X-405, 1 mM C ₄ H ₁₂ N I	Surfactant adsorption, in synergy with I ⁻	98 – 99	41
Sodium 2-undecyl-1-ethanoate-imidazoline (2M2), thiourea (TU) 	Carbon steel	3 wt% NaCl	20 – 800 mg/L (2M2), 100 mg/L TU	Mixed inhibition, Surface adsorption from multiple sites on 2M2 head group	94 – 97	40
Polyethylene glycol (PEG), polyvinylpyrrolidone (PVP) 	Mild steel	0.5 M H ₂ SO ₄	0.1 mM PEG and PVP	Physical adsorption	76	45
Lanthanum (III) chloride (LaCl ₃) and SDS 	Mild steel	2 M HCl	20 – 180 ppm LaCl ₃ , 80 ppm SDS	Adsorption of La-SDS complex	> 90	47

Inhibitor	Substrate	Conditions	Concentration	Inhibition and remarks	Efficiency / %	Ref.
Cerium (IV) sulfate tetrahydrate, $\text{Ce}(\text{SO}_4)_2$ and <i>iso</i> -vanillin (Van) 	Cold-rolled steel	1 M H_2SO_4	400 mg/L $\text{Ce}(\text{SO}_4)_2$, 100 mg/L Van	Mixed inhibition Adsorption of Van followed by precipitation of Ce-Van complex	95	48
$\text{Ce}(\text{SO}_4)_2$ and sodium oleate (SO) 	Cold rolled steel	3 M H_3PO_4	0.4 – 2 mM $\text{Ce}(\text{SO}_4)_2$ and SO	Mixed inhibition Precipitation of Ce-SO complex	71 – 93	51
Zinc (Zn^{2+}), polyacrylamide (PAA) and phenyl phosphate (PPA) 	Mild steel	60 ppm NaCl	50 ppm Zn^{2+} , 50 ppm PAA, 300 ppm PPA	Mixed inhibition Adsorption and precipitation of Zn complexes	4 – 95	52
Zn^{2+} , citrate and tertiary butyl phosphonate (TBP) 	Carbon steel	Aqueous	50 ppm Zn^{2+} , 25 – 200 ppm citrate, 50 – 150 ppm TBP	Mixed inhibition, predominantly cathodic Protective film of $\text{Zn}(\text{OH})_2$ and Fe-TBP-citrate complexes	43 – 96	53
Zinc (ZnSO_4), SDS and calcium propionate (CP) 	Carbon steel	Aqueous	50 ppm ZnSO_4 , 50 – 330 ppm SDS, 10 – 125 ppm CP	Complex formation with Zn, transmetalates to Fe complexes + $\text{Zn}(\text{OH})_2$ to make film	41 – 99	54

1.3.3 Dual-active Organic Inhibitors

Some dual-active salt inhibitors have been reported and used in the past, and many show similar structural traits to the inhibitor mixtures in Table 1. A selection of dual-functional organic salt corrosion inhibitors for steel is presented in Table 2.

A large number of vapour phase inhibitors (VPI) are dual-active salts. VPIs are chemicals used to inhibit corrosion on metals exposed to air. They are commonly a temporary inhibition solution, and often used for protecting machined parts during transport. Due to the requirement for the compound to volatilise, traditional inorganic salts are not suitable. Instead many examples feature an alkylammonium cation with nitrite or carboxylate anions.^{57, 58} Due to incomplete proton transfer in these salts, the neutral acids and bases can vapourise and then condense on the metal surface. One of the most common VPIs is dicyclohexylammonium nitrite (DICHAN). This salt is thought to have a mixed inhibitor effect by forming a protective film on exposed steel surfaces.^{59, 60} As nitrites are increasingly being replaced due to their toxicity,²⁷ carboxylates have become a more attractive counter anion. When testing a selection of VPIs in aqueous solutions, Rammelt et al.^{61, 62} found that using more weakly coordinating anions, such as benzoate, was advantageous, as they could dissociate more readily than stronger anions such as nitrite, and migrate to the passive film defects.

Du et al.⁶³ showed that more heavily functionalised amines could also be used in salt forms. Seter et al.^{64, 65} also described a more complex salt formation, with the combination of the surfactant cetyltrimethyl ammonium (CTA) and antimicrobial anion, nalidixate. This produced a salt that was both corrosion inhibiting and biocidal.

Extensive research has been carried out synthesising combined rare-earth carboxylates to take advantage of their different inhibitor actions.⁶⁶ The first reported study found that of a selection of rare-earth carboxylates, cerium (III) salicylate, $\text{Ce}(\text{Sal})_3$, showed the greatest reduction in corrosion of mild steel in aqueous chloride conditions.⁶⁷ Subsequent screening of a range of rare-earth metals and aromatic carboxylate ligands revealed similar synergism, particularly in the case of lanthanum (III) cinnamates.⁶⁸ Studies of the speciation of these compounds in solution determined that the organic ligand plays an important role in suppressing the anodic reaction, since when used alone the rare-earth chlorides tend towards cathodic inhibition.⁶⁹⁻⁷¹ By administering the species as a combined salt, it is possible to take advantage of the synergistic speciation without introducing additional aggressive ions such as Cl^- and SO_4^- , as is the case when the rare-earth metal and coordinating species are added individually to the electrolyte.⁴⁷⁻⁵¹

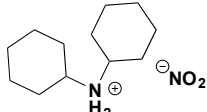
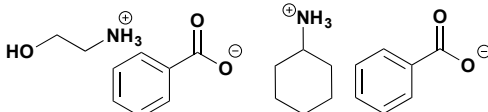
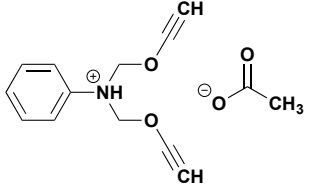
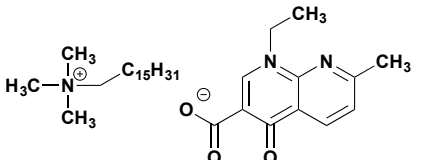
The final class of organic salts presented in Table 2 are ILs. Verma et al.²⁹ recently compiled a comprehensive list of IL corrosion inhibitors which showed that many studies focus only on the cation, paired with a halide anion. This discussion presents examples of key dual-active compounds that feature more varied anions. By far the most popular cation investigated for corrosion inhibitors is imidazolium. Many studies have used well-known ILs featuring 1-alkyl,3-methylimidazolium cations and anions such as halides, tetrafluoroborate (BF_4^-), hexafluorophosphate (PF_6^-) and dicyanamide (DCA^-).⁷²⁻⁷⁷ Some more creative uses of imidazoliums include the synthesis of dibenzyl-substituted^{78, 79} and vinyl-substituted⁸⁰⁻⁸² cations. Other IL cations that were investigated include pyrrolidiniums⁸³ and quaternary ammoniums.^{82, 84, 85} Many of these ILs employ longer aliphatic chains than typical for other applications. Increasing the cation chain length up to C10-C18 was found to improve inhibition by increasing lipophilicity; however, beyond this, performance decreased.^{75, 80} Atta et al.⁸² found that saturated octadecylammonium tosylate performed marginally better than the mono-unsaturated oleylammonium salt.

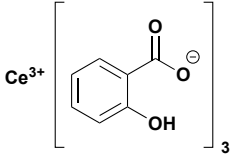
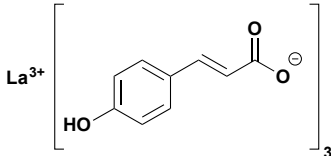
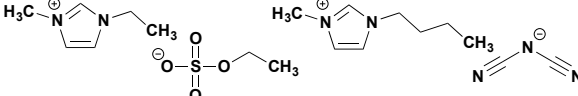
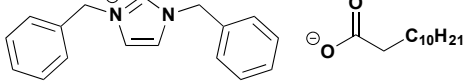
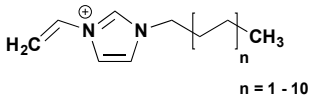
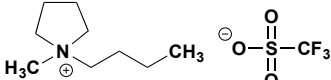
Just as for the inhibitor mixtures, many of the ammonium cations were paired with carboxylate anions. Ortega et al.⁸⁶ found that increasing the carboxylate size improved inhibition, while dicarboxylate species were also investigated.⁸⁴ Amino acids have also been employed as anions, as these are both cheap and environmentally benign.^{85, 87} Kowasari et al.⁸⁵ showed particularly high inhibition efficiencies with tetrabutylammonium (TBA) methioninate in 1 M HCl. This was attributed to selective adsorption of TBA at the cathodes and methioninate at the anodes. Adsorption resulting in mixed inhibition was the primary mechanism suggested for most of the ILs, which is consistent with observations for organic inhibitors generally.

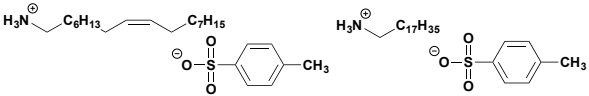
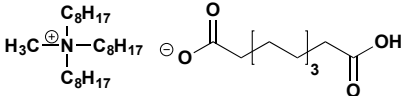
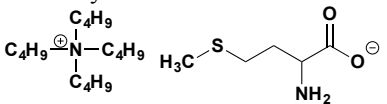
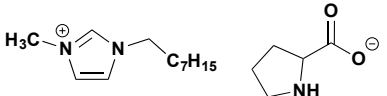
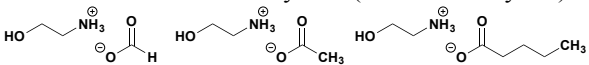
Some of the salts presented in Table 2 deliberately exploit the differing inhibition mechanisms of their components to enhance synergy. This was the case especially for the VPIs and rare-earth complexes. However, many IL studies, as with most inhibitor studies, investigated unique cation structures, but fell back on pairing these with simple halide counter ions.

This thesis explores the opportunities for targeted organic salts, using prior knowledge of effective compounds to create synergistic inhibitors. This work was inspired by the concepts of task-specific and dual-active ILs adopted by the IL community,¹¹ and this frame of reference informed the search for an appropriate inhibiting cation.

Table 2. Dual-functional organic salts as corrosion inhibitors for steel. Efficiencies reported from polarisation data where available.

Inhibitor	Substrate	Conditions	Concentration	Inhibition and remarks	Efficiency / %	Ref.
Dicyclohexylammonium nitrite (DICHAN) 	Carbon steel	Vapour phase, 20 days at 100% relative humidity (RH)		Mixed inhibition	98	59
Ethanolammonium benzoate Cyclohexyl-ammonium benzoate 	Mild steel	Aqueous	0.01 M	Anodic inhibition Passive film formation at neutral and basic pH Not stable at low pH		61, 62
1,3-dipropynoxymethylamine acetate 	Iron	0.5 M H ₂ SO ₄	5 – 60 ppm	Anodic inhibition Electrostatic adsorption Synergy with chloride	81 – 94	63
Cetrimonium nalidixate 	Mild steel	0.01M NaCl	0.01 mM – 1 mM	Anodic inhibition Nalidixate adsorbed to surface Antimicrobial	10 – 60	64

Inhibitor	Substrate	Conditions	Concentration	Inhibition and remarks	Efficiency / %	Ref.
Cerium (III) salicylate 	Mild steel	0.1 M NaCl	100 – 5000 ppm	Mixed inhibition, salicylate anodic and Ce ³⁺ cathodic Adsorption of mixed metal-salicylate film		67, 70
Lanthanum (III) 4-hydroxycinnamate 	Mild steel	0.1M NaCl	50 – 200 ppm	Mixed inhibition La(4-OHCin) ₃ dominates at high pH, ions dissociate at low pH	77 – 98	68, 71
1-ethyl,3-methylimidazolium ethylsulfate, 1-butyl,2-methylimidazolium dicyanamide 	Mild steel	1 M HCl	100 – 500 ppm	Mixed inhibition, predominantly cathodic Physical and chemical adsorption	68 – 93	73
1,3-dibenzylimidazolium dodecanoate 	API 5LX52 steel	1 M HCl 1 M H ₂ SO ₄	25 – 100 ppm	Mixed inhibition Adsorption Strong surface attachment in HCl	26 – 88 (HCl) 10 – 30 (H ₂ SO ₄)	78
1-vinyl-3-alkylimidazolium hexafluorophosphate 	Carbon steel	1 M H ₂ SO ₄	10 – 100 ppm	Mixed inhibition Maximum effect at C12 chain	68 – 96	80
N-butyl, methylpyrrolidinium triflate 	Mild steel	3.5 % NaCl	50 – 800 ppm	Adsorption Antibacterial	78 – 80	83

Inhibitor	Substrate	Conditions	Concentration	Inhibition and remarks	Efficiency / %	Ref.
Octadecylammonium tosylate, oleylammonium tosylate 	Steel	1M HCl	0.023 – 0.34 mM	Mixed inhibition Saturated chain slightly better performance	91 – 98	82
Trioctyl,methylammonium dodecanedioate 	API 5LX52 steel	Well production water	10 – 100 ppm	Mixed inhibition Adsorption	15 – 86	84
Tetrabutylammonium methioninate 	Mild steel	1 M HCl	$1.3 \times 10^{-5} - 1.6 \times 10^{-3}$ M	Mixed inhibition, predominantly anodic Electrostatic interaction with iron TBA at cathode and methioninate at anode	88 – 95	85
1-Octyl-3-methylimidazolium prolinat 	Mild steel	0.5 M H ₂ SO ₄	0.5 – 10 mM	Mixed inhibition, predominantly cathodic Both ions exist as cations at low pH, adsorbed to cathodic sites	38 – 73	87
Ethanolammonium carboxylates (formate – butyrate) 	API X70 steel	Aqueous	50 wt%	Anodic inhibition Adsorption Better with increased anion chain length but desorbs over time		86

1.3.4 Imidazoline Corrosion Inhibitors

Imidazolines are an obvious choice in the context of the ubiquity of methylimidazolium cations in the IL field. The core ring structure bears a striking resemblance to imidazolium, with the only difference being saturation of the C4-C5 position at the back of the ring. Despite these similarities, imidazolinium cations have not been widely studied in IL synthesis.

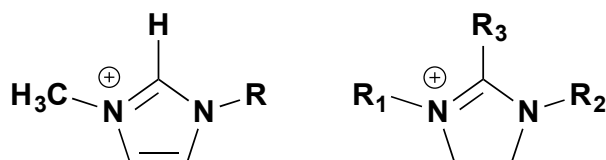


Figure 4. A comparison of the common ionic liquid cation methylimidazolium (left) and the general form of imidazolinium (right).

This amine is, however, a commercially used corrosion inhibitor. They are most commonly used as additives in oil pipelines.⁸⁸⁻⁹⁰ Commercial imidazolines typically feature a long aliphatic chain in the C2 position (R₃ in Figure 4). This tail is commonly a fatty acid residue such as oleic or palmitic acid. Molecules also feature pendant groups in one or both of R₁ and R₂ that incorporate hydroxyl or amine functionality (Figure 5).⁸⁸⁻⁹² Imidazolines have been used as neutral and cationic species, or, with a carboxylate pendant group, can be amphoteric.^{44, 90, 93}

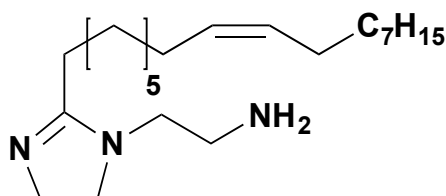


Figure 5. Example of an oleic imidazoline corrosion inhibitor.⁸⁹

A number of computational studies have modelled the imidazoline interaction with iron oxide surfaces to elucidate a mechanism. It is proposed that the polar head group binds strongly to Fe²⁺ in the oxide layer, displacing water from the surface. This creates a self-assembled monolayer with the C2 alkyl chains interacting via van der Waals forces to create a hydrophobic barrier that obstructs the approach of water and aggressive ions.⁹⁴⁻⁹⁶ Improvements in inhibition were predicted for increases in C2 alkyl chain length⁹⁶ and the use of carboxylate pendant groups.⁹⁵

There has been one example in the literature of such cations being paired with $[\text{BF}_4]^-$ to create ILs.⁹⁷ These ILs showed inhibition efficiencies of over 90 % in acidic aqueous conditions. However, the $[\text{BF}_4]^-$ anion does not make a substantial contribution to the inhibition, and the potential for breakdown to highly corrosive HF makes it a poor choice from an environmental perspective.^{98, 99}

The corrosion inhibitor literature is dominated by the use of fatty acid imidazolines. This thesis proposes to study smaller imidazolium salts that are more akin in structure to alkylmethylimidazoliums and to pair these with corrosion-inhibiting anions.

1.4 Liquid and Solid Electrolytes

1.4.1 Exploring Physical Properties

As the family of organic salts and ILs expands to tackle a growing number of applications, it is important to maintain our understanding of the properties these compounds possess. While ILs are often broadly characterised as all being green, non-volatile or electrochemically stable, in truth the vast combinations of ions mean that ILs can have a wide range of properties. Despite advances in computational screening,¹⁰⁰⁻¹⁰³ it is still difficult to predict how novel structures will impact an IL's properties and so it is important within our group to fully characterise new ILs. This can include thermal properties, such as melting points and decomposition temperatures, as well as transport properties such as viscosity and conductivity. These properties can be indicators of whether novel salt formulations will be suited to different applications. In this thesis it was also of interest to compare new imidazolium salts with their imidazolium analogues to assess the impact of the structural changes to the ring.

Routine physical characterisation of compounds synthesised during this work revealed that some of the novel organic salts showed promising conductivity behaviour, in both the liquid and solid states. This highlighted the possibility for their use as electrolyte materials. The following is a brief overview of the types of ILs and organic salts used in these applications.

1.4.2 Ionic Liquids as Electrolytes

Due to the ionic nature of salts, ILs have intrinsic ionic conductivity and this has led them to be widely considered as alternative electrolytes to molecular solvents in electrochemical devices such as batteries. ILs can possess attractive properties such as high thermal and electrochemical stability, non-volatility and non-flammability that can

overcome many of the problems associated with traditional organic solvent-based systems.^{3, 5}

The archetypal ionic liquid for electrochemical applications is 1-ethyl-3-methylimidazolium bis(trifluoromethylsulfonyl)imide, [C₂mim][NTf₂]. The combination of bulky, asymmetric cation and charge-diffuse anion results in a fluid liquid that freezes at -12 °C and shows no sign of decomposition or vaporisation until over 300 °C.³ The vast majority of electrochemical studies have focused on this family of ILs and a particular selection of other ions as shown in Figure 6.⁵ Cations are commonly cyclic or quaternary ammoniums with short alkyl substituents (less than C₄), while the anions encourage charge delocalisation.

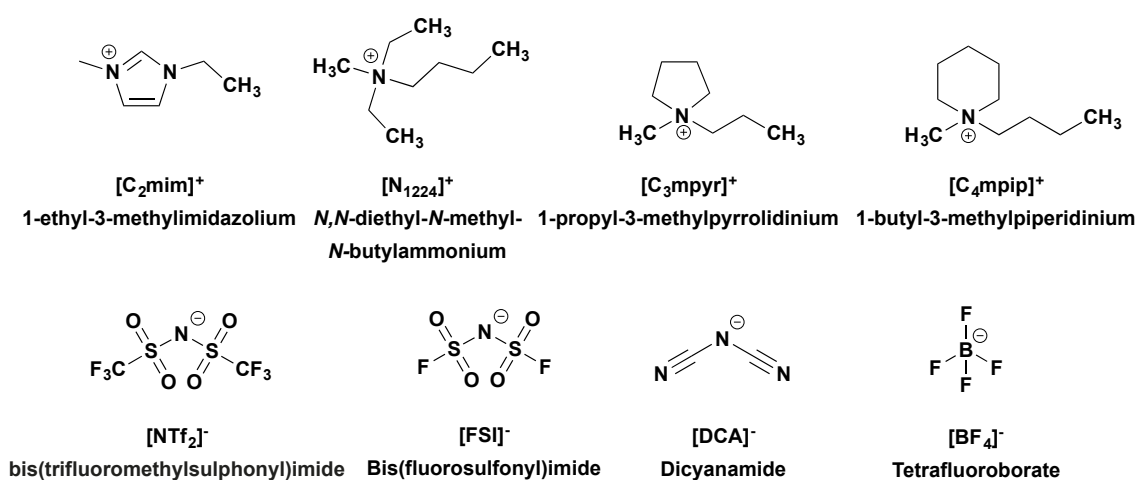


Figure 6. Common IL cations and anions for electrochemical applications.⁵

Initial interest in this field started with the demonstration of good stability of ammonium [NTf₂]⁻ ILs for lithium electrochemistry.^{104, 105} Subsequent research has focused on optimising aspects such as lithium-ion solubility,¹⁰⁶ electrolyte stability,^{107, 108} viscosity and rate capabilities,¹⁰⁹ and interfacial interactions.^{4, 110}

Research has also moved beyond lithium batteries. Studies have tried to develop ILs that can improve the energy density and efficiency of battery systems with other metals such as sodium,¹¹¹⁻¹¹³ magnesium¹¹⁴⁻¹¹⁸ and zinc.¹¹⁹⁻¹²¹ ILs have also been doped with redox couples for use in dye-sensitised solar cells¹²²⁻¹²⁵ and thermoelectrochemical cells.¹²⁶⁻¹²⁹

While the majority of studies have focused on ILs incorporating quaternary cations as shown in Figure 6, there has been increasing interest in the use of protic ILs, in which the cation features an available proton.¹³⁰ An advantage of such systems is that they can be synthesised directly through neutralisation of a Brønsted acid and base. This removes then

need for multi-step quaternisation and anion metathesis reactions, making for a more atom-efficient, and often much cheaper synthesis. There is also evidence that protic ILs can be less toxic and more readily biodegradable than their aprotic counterparts, reducing their potential environmental impact.¹³¹

In fact the first room temperature IL, as described by Walden¹³² in 1914, was ethylammonium nitrate (EAN), which is a protic IL. The electrochemical properties of EAN have been investigated, and as an electrolyte it supports reversible reduction of a variety of metal ions. Subsequent work on protic ILs in the electrochemistry field has focused on their use as electrolytes in capacitor,¹³³⁻¹³⁵ water splitting¹³⁶ and fuel cell applications.^{137, 138}

A key feature of these electrolytes is the inherent presence of a mobile species, in the form of an available proton on the cation. A possible means of proton transport through these materials is a Grotthuss-type mechanism. First proposed by Grotthuss in 1806¹³⁹ (although not established as it is understood today until much later^{140, 141}) this mechanism is typically used to describe proton conductivity through water. A proton is transferred between oxygen atoms on adjacent water molecules, starting a chain of concurrent formation and cleavage of hydrogen bonds. This results in the net transport of a proton, with minimal molecular movement (Figure 7). This proton hopping allows for much faster transport than possible through diffusion alone. It has been proposed that protic ILs can exhibit similar proton-hopping behaviour, allowing for high levels of proton conductivity.¹³⁸

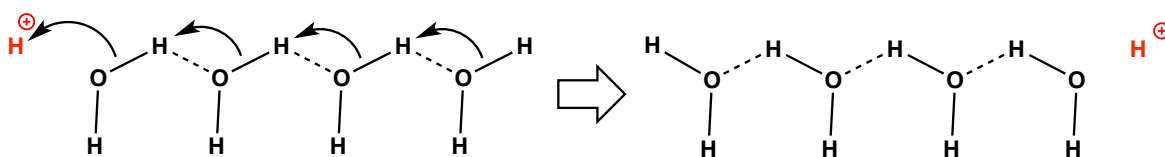


Figure 7. Schematic representation of the Grotthuss mechanism, with the formation and cleavage of hydrogen bonds along a chain of water molecules resulting in the net movement of a proton.

1.4.3 Organic Ionic Plastic Crystals as Electrolytes

Many combinations of typical IL ions form plastic crystalline phases, in which one or both of the ions retain some degree of rotational motion within the solid lattice. As with more commonly known liquid crystals, plastic crystals can be considered as intermediate phases between truly crystalline solid and liquid phases. In both cases there is a combination of order and disorder in the structures, however, where as liquid crystals only exhibit short-range order and can flow, the strong long-range order maintained in plastic

crystals means that they do not possess liquid properties, but are instead soft solids.^{142, 143} These differences in structure can be readily observed in the differing X-ray diffraction patterns; plastic crystals will give sharp diffraction patterns, while liquid crystals will only show broad peaks, or no coherent diffraction.^{144, 145} Organic salts that exhibit plastic crystalline behaviour are referred to as organic ionic plastic crystals (OIPCs).

As electrolytes, OIPCs are advantageous in comparison to ILs, because of their solid nature at room temperature. This could simplify cell packaging and substantially reduce the risk of leaks. In comparison to other solid electrolytes, such as conducting polymers and ceramics, OIPCs show high ion transport and mechanical flexibility.¹⁴³ Similarly to ILs, OIPCs are often also safer than their molecular plastic crystal counterparts due to being non-volatile and non-flammable.

An example of an OIPC is tetraethylammonium dicyanamide ($[N_{2222}][DCA]$, Figure 8). This material displays a low-temperature crystalline phase (phase II) and a highly conductive room-temperature plastic phase (phase I), prior to melting at 54 °C.¹⁴⁶ The volume of the solid increases substantially across the solid – solid transition, but by a much smaller amount across the melt. The change in entropy for the melt is also only 4 $Jmol^{-1}K^{-1}$, amongst the lowest observed for this type of material. It is suggested that this is partially due to the structure of the solid being very similar to that of the melt. The conductivity also correlates to thermal behaviour, with increases observed at both the solid – solid transition and the solid – melt transition. This strongly implies that the molecular processes that cause the phase changes are also responsible for the ionic conductivity.

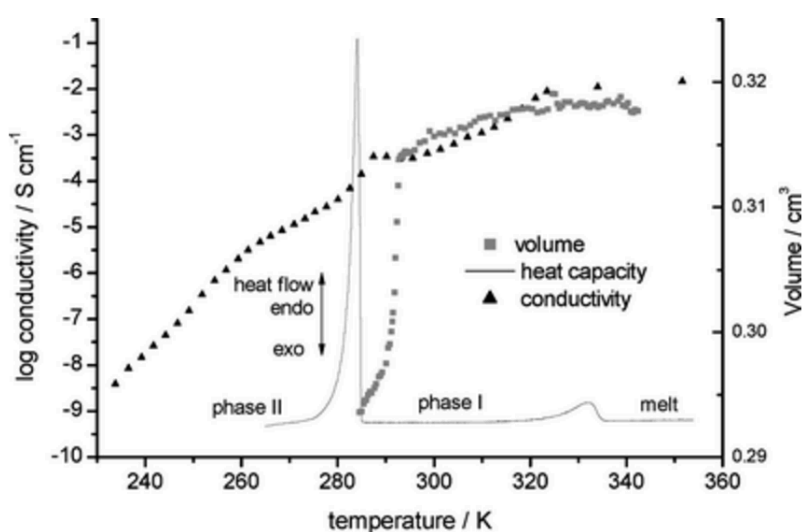


Figure 8. The relationship between volume, conductivity and thermal behaviour with temperature for $[N_{2222}][DCA]$. Reproduced from ref. 143 with permission from the Royal Society of Chemistry.¹⁴³

A number of different techniques can be employed to explore the motions of the ions in the plastic phases. Solid-state NMR spectroscopy is a valuable tool in this respect. Analysing the spectral linewidths can give an understanding of the degree of mobility, and overlaying peaks can indicate the presence of species with differing mobilities. Where single crystals of the OIPCs could be obtained, previous work in our group has used the structural information obtained from the crystal structure to calculate NMR linewidths associated with predicted molecular motions.^{145, 147} Comparing these to the experimentally obtained linewidths allowed Jin et al.¹⁴⁵ to propose increasing motions for the ions through the four solid phases of an OIPC; from rotation of methyl groups at low temperatures, through to tumbling and ion diffusion. Raman spectroscopy has also been used to identify the rotational motion in $[C_1\text{mpyr}][\text{SCN}]$, due to the high sensitivity of the vibrational modes of the thiocyanate anion to the coordinating environment.¹⁴⁸

It has been proposed that the molecular motions and their related conduction mechanisms are linked to the presence of vacancies and lattice defects in the crystal. Physical changes such as increasing volume are an indication that the number of lattice defects is higher in plastic phases than it is in regular crystal structures. Positron annihilation lifetime spectroscopy was used to probe the size of defects in $[C_1\text{mpyr}][\text{NTf}_2]$ and $[C_2\text{mpyr}][\text{NTf}_2]$ and it was found that conductivity strongly correlated with changes in the defect volumes.¹⁴⁹

Cooper and Angell¹⁵⁰ first suggested the use of OIPCs as electrolytes in their study of a double salt featuring a blend of LiBF_4 and a quaternary ammonium tetrafluoroborate OIPC. The addition of dopants such as lithium ions has been shown to increase the conductivity by over two orders of magnitude, but can also have a complex effect on the behaviour of the plastic phases. Adebahr et al.¹⁵¹ suggested that decreases in the transition temperatures of a pyrrolidinium OIPC upon doping indicated that the Li^+ ions were fully incorporated in the solid matrix and were improving mobility by introducing further vacancies. Molecular dynamics simulations supported this theory, finding that in $[\text{N}_{1111}][\text{DCA}]$, the plastic phase was the most sensitive to Li^+ doping. The Li^+ ions formed clusters with the $[\text{DCA}]^-$ anions which created more free volume elsewhere in the structure, facilitating diffusion of the other species.¹⁵² A contrasting theory suggests that coordination of available anions in the OIPC with the Li^+ ions generates a separate liquid phase that is distributed within the solid matrix.¹⁵³ *In situ* magnetic resonance imaging of an operating lithium metal cell confirmed liquefaction at the electrode interface as Li^+ ions were discharged into the OIPC.¹⁵⁴

The first reported lithium-ion batteries with $[\text{NTf}_2]^-$ -based OIPC electrolytes showed poor cathodic stability, which limited the choice of negative electrodes.¹⁵⁵ However, since then there have been improvements in operation of both pure¹⁵⁶ and hybrid electrolyte batteries.¹⁵⁷ OIPCs have also been investigated for use in other devices such as dye-sensitised solar cells¹⁵⁸⁻¹⁶¹ and supercapacitors.¹⁶²

For the high-conductivity organic salts synthesised in this thesis, the application for OIPCs that is of particular interest is proton exchange membrane fuel cells (PEMFCs). These fuel cells generate electricity through the recombination of hydrogen and oxygen at the cathode to form water. The H_2 and O_2 gas supplies must be kept separate, so that recombination can only occur when H^+ ions generated at the anode migrate to the cathode.^{163, 164} This requires the use of an electrolyte membrane that has fast, selective proton transport.

While the majority of OIPCs must be doped with Li^+ and other electrolyte species, protic OIPCs can show intrinsic H^+ transport. This is achieved through the use of cationrs that have an available proton, similar to those seen in protic ILs. Zhu et al.^{165, 166} and Chen et al.¹⁶⁷ synthesised protic OIPCs featuring guanidinium, while other studies have incorporated aromatic amines such as imidazolium and triazolium.^{144, 168, 169} The counter anion must be weakly coordinating to enable free movement of the proton within the matrix. This is achieved through the use of anions with charge-delocalising sulfonate groups and charge-withdrawing fluorine groups.

The intrinsic conductivities of these compounds can be increased through the addition of protons as dopants. This has been achieved through the addition of excess amount of the anion source. Zhu et al.¹⁶⁵ showed a several orders of magnitude increase in conductivity up to 10^{-3} Scm^{-1} upon the addition of TfOH to guanidinium triflate. Acid doping has also been applied to aprotic OIPCs and molecular plastic crystals in order to increase proton transport.^{170, 171}

The desired mechanism for proton transport in these systems is Grotthuss-type proton hopping. While this is supported by computational studies^{172, 173}, experimental evidence has suggested that the high conductivities may also be due to the formation of liquid-type phases, as observed with Li^+ ion doping.^{165, 166, 174}

1.5 Aims

This introduction has provided an insight into the state of corrosion inhibitors and highlighted a possible new approach to discovering effective, yet environmentally friendly

compounds. Taking cues from recent work on ILs, there is a gap in the research in which the dual-active nature of organic salts can be exploited by combining cationic and anionic organic inhibitors.

In IL research there is also a tendency to rely on the same few familiar cations and anions, despite the limitless potential for new salt combinations. This work hopes to enlarge the library of documented ILs by focusing on the highly underutilised imidazolinium family.

The main aims of this thesis were to:

- Synthesise novel dual-active salts based on the imidazolinium cation and carboxylate anions.
- Investigate the corrosion inhibition efficiency of these salts and determine the mechanism of any synergistic effects.
- Study the physical and transport properties of the salts and contrast with analogous imidazolium salts to understand the impact of differences in structure.

1.6 Thesis Outline

This thesis is arranged as follows:

Chapter 2 describes the synthesis of a novel family of protic salts featuring the [2-MeHImn]⁺ cation. For those salts that were found to be ILs, the physical properties were compared to the analogous imidazolium salts. Preliminary investigations identified promising corrosion inhibitor and electrolyte behaviour in some of the salts.

Chapters 3 and 4 further explore the corrosion inhibition of a key compound, [2-MeHImn][4-OHCin], focusing on the synergistic relationship between the two ions. Chapter 3 investigated the influence of changing parameters such as pH and inhibitor concentration as well as the effects of modifying the cation structure. In Chapter 4, [2-MeHImn]⁺ was paired with different anions, based on uronic acids.

Chapter 5 presents the work of a parallel study pursuing the promising electrolyte behaviour of [2-MeHImn][TfO] and its imidazolium analogue. The phase behaviour and solid-state conductivity of these salts was investigated, with insights into the mechanisms provided by solid-state NMR study.

Chapter 6, Conclusions and future work, draws together the key findings from the research and suggests directions for further study.

1.7 References

1. P. Wasserscheid and T. Welton, in *Ionic Liquids in Synthesis*, Wiley-VCH, Weinheim, 2008.
2. M. Deetlefs, K. R. Seddon and M. Shara, *Phys. Chem. Chem. Phys.*, 2006, **8**, 642-649.
3. M. Armand, F. Endres, D. R. MacFarlane, H. Ohno and B. Scrosati, *Nat. Mat.*, 2009, **8**, 621-629.
4. D. R. MacFarlane, M. Forsyth, P. C. Howlett, J. M. Pringle, J. Sun, G. Annat, W. Neil and E. I. Izgorodina, *Acc. Chem. Res.*, 2007, **40**, 1165-1173.
5. D. R. MacFarlane, N. Tachikawa, M. Forsyth, J. M. Pringle, P. C. Howlett, G. D. Elliott, J. H. Davis, M. Watanabe, P. Simon and C. A. Angell, *Energ. Environ. Sci.*, 2014, **7**, 232-250.
6. T. Welton, *Chem. Rev.*, 1999, **99**, 2071-2084.
7. D. M. D'Alessandro, B. Smit and J. R. Long, *Angew. Chem. Int. Ed.*, 2010, **49**, 6058-6082.
8. M. Ramdin, T. W. de Loos and T. J. H. Vlucht, *Ind. Eng. Chem. Res.*, 2012, **51**, 8149-8177.
9. A. Brandt, J. Grasvik, J. P. Hallett and T. Welton, *Green Chem.*, 2013, **15**, 550-583.
10. P. Mäki-Arvela, I. Anugwom, P. Virtanen, R. Sjöholm and J. P. Mikkola, *Ind. Crops Prod.*, 2010, **32**, 175-201.
11. W. L. Hough, M. Smiglak, H. Rodriguez, R. P. Swatloski, S. K. Spear, D. T. Daly, J. Pernak, J. E. Grisel, R. D. Carliss, M. D. Soutullo, J. J. H. Davis and R. D. Rogers, *New J. Chem.*, 2007, **31**, 1429-1436.
12. J. L. Shamshina, P. S. Barber and R. D. Rogers, *Expert Opin. Drug Deliv.*, 2013, 1-15.
13. G. Schmitt, M. Schütze, G. F. Hays, W. Burns, E.-H. Han, A. Pourbaix and G. Jacobson, *Global Needs for Knowledge Dissemination, Research, and Development in Materials Deterioration and Corrosion Control*, The World Corrosion Organization, 2009.
14. R. G. Kelly, J. R. Scully, D. Shoesmith and R. G. Buchheit, *Electrochemical Techniques in Corrosion Science and Engineering*, Marcel Dekker, New York, 2002.
15. V. Jovancicevic and J. O. M. Bockris, *J. Electrochem. Soc.*, 1986, **133**, 1797-1807.
16. J. M. West, *Electrodeposition and corrosion processes*, Van Nostrand Reinhold, London, 1965.
17. M. Pourbaix, *Atlas of electrochemical equilibria in aqueous solutions*, 2nd edn., National Association of Corrosion Engineers, Houston, Tex, 1974.
18. Z. Ahmad, in *Principles of Corrosion Engineering and Corrosion Control*, Butterworth-Heinemann, Oxford, 2006, pp. 9-56.
19. U. Evans and B. F. Brown, *Localised corrosion*, National Association of Corrosion Engineers, Houston, Tex, 1974.
20. H.-H. Strehblow, in *Corrosion Mechanisms in Theory and Practice*, ed. P. Marcus, Marcel Dekker, New York, 2nd edn., 2002, vol. 17.
21. T. P. Hoar, D. C. Mears and G. P. Rothwell, *Corros. Sci.*, 1965, **5**, 279-289.
22. N. Sato, *Electrochim. Acta*, 1971, **16**, 1683-1692.
23. T. P. Hoar and W. R. Jacob, *Nature*, 1967, **216**, 1299-1301.
24. D. A. Jones, *Principles and Prevention of Corrosion*, Prentice-Hall, New Jersey, 1996.
25. S. Papavinasam, in *Uhlig's Corrosion Handbook*, ed. R. W. Revie, John Wiley & Sons, Inc., New Jersey, 2011, pp. 1021-1032.
26. V. S. Sastri, in *Green Corrosion Inhibitors*, John Wiley & Sons, Inc., 2011, pp. 167-211.
27. P. R. Roberge, in *Handbook of Corrosion Engineering, Second Edition*, McGraw Hill Professional, Access Engineering, New York, 2012.
28. S. Wilbur, H. Abadin, M. Fay, D. Yu, B. Tencza, L. Ingerman, J. Klotzbach and S. James, Toxicological Profile for Chromium, US Department of Public Health and Human Services, Atlanta, 2012.
29. C. Verma, E. E. Ebenso and M. A. Quraishi, *J. Mol. Liq.*, 2017, **233**, 403-414.
30. G. B. Deacon, P. C. Junk, M. Forsyth and W. W. Lee, *Chem. Aust.*, 2008, **75**, 18-21.
31. R. L. Twite and G. P. Bierwagen, *Prog. Org. Coat.*, 1998, **33**, 91-100.
32. J. Sinko, *Prog. Org. Coat.*, 2001, **42**, 267-282.
33. Y. Qiang, L. Guo, S. Zhang, W. Li, S. Yu and J. Tan, *Sci. Rep.*, 2016, **6**, 33305.
34. U. Rammelt, S. Koehler and G. Reinhard, *Corros. Sci.*, 2008, **50**, 1659-1663.
35. Q. Qu, S. Jiang, W. Bai and L. Li, *Electrochim. Acta*, 2007, **52**, 6811-6820.

36. T. Suzuki, H. Nishihara and K. Aramaki, *Corros. Sci.*, 1996, **38**, 1223-1234.
37. S. Javadian, A. Yousefi and J. Neshati, *Appl. Surf. Sci.*, 2013, **285**, Part B, 674-681.
38. M. A. Azaroual, E. F. El Harrak, R. Touir, A. Rochdi and M. E. Touhami, *J. Mol. Liq.*, 2016, **220**, 549-557.
39. M. Hosseini, S. F. L. Mertens and M. R. Arshadi, *Corros. Sci.*, 2003, **45**, 1473-1489.
40. P. C. Okafor, C. B. Liu, X. Liu, Y. G. Zheng, F. Wang, C. Y. Liu and F. Wang, *J. Solid State Electrochem.*, 2010, **14**, 1367-1376.
41. R. Fuchs-Godec and M. G. Pavlović, *Corros. Sci.*, 2012, **58**, 192-201.
42. E. E. Oguzie, Y. Li and F. H. Wang, *J. Colloid Interface Sci.*, 2007, **310**, 90-98.
43. M. Bouklah, B. Hammouti, A. Aouniti, M. Benkaddour and A. Bouyanzer, *Appl. Surf. Sci.*, 2006, **252**, 6236-6242.
44. P. C. Okafor and Y. Zheng, *Corros. Sci.*, 2009, **51**, 850-859.
45. S. A. Umoren, *J. Appl. Polym. Sci.*, 2011, **119**, 2072-2084.
46. J. de Damborenea, A. Conde and M. A. Arenas, in *Rare Earth-Based Corrosion Inhibitors*, Woodhead Publishing, Cambridge, 2014, pp. 84-116.
47. G. N. Mu, T. P. Zhao, M. Liu and T. Gu, *Corrosion*, 1996, **52**, 853-856.
48. X. Li, S. Deng, G. Mu and Q. Qu, *Mater. Lett.*, 2007, **61**, 2514-2517.
49. X. Li, S. Deng, H. Fu, G. Mu and N. Zhao, *Appl. Surf. Sci.*, 2008, **254**, 5574-5586.
50. X. Li, S. Deng, H. Fu and G. Mu, *Corros. Sci.*, 2009, **51**, 2639-2651.
51. X. Li, S. Deng, H. Fu and G. Mu, *Corros. Sci.*, 2010, **52**, 1167-1178.
52. S. Rajendran, B. V. Apparao and N. Palaniswamy, *Electrochim. Acta*, 1998, **44**, 533-537.
53. P. Narmada, M. V. Rao, G. Venkatachari and B. V. A. Rao, *Anti Corros. Method. M.*, 2006, **53**, 310-314.
54. A. Leema Rose, A. Peter Pascal Regis, S. Rajendran, A. Krishnaveni and F. R. Selvarani, *Arab. J. Sci. Eng.*, 2012, **37**, 1313-1325.
55. B. Rao, M. Rao, S. Rao and B. Sreedhar, *J. Surf. Eng. Mater. Adv. Technol.*, 2013, **3**, 28-42.
56. M. Prabakaran, S. Ramesh, V. Periasamy and B. Sreedhar, *Res. Chem. Intermed.*, 2015, **41**, 4649-4671.
57. D. M. Bastidas, E. Cano and E. M. Mora, *Anti Corros. Method. M.*, 2005, **52**, 71-77.
58. E. Vuorinen and W. Skinner, *Br. Corros. J.*, 2002, **37**, 159-160.
59. J. M. Bastidas, E. M. Mora and S. Feliu, *Mater. Corros.*, 1990, **41**, 343-347.
60. J. M. Bastidas and E. M. Mora, *Can. Metall. Q.*, 1998, **37**, 57-65.
61. U. Rammelt, S. Koehler and G. Reinhard, *Corrosion*, 2011, **67**, 1-7.
62. U. Rammelt, S. Koehler and G. Reinhard, *Corros. Sci.*, 2009, **51**, 921-925.
63. T. Du, J. Chen and D. Cao, *Br. Corros. J.*, 2000, **35**, 229-231.
64. M. Seter, M. J. Thomson, A. Chong, D. R. MacFarlane and M. Forsyth, *Aust. J. Chem.*, 2013, **66**, 921-929.
65. M. Seter, M. J. Thomson, J. Stoimenovski, D. R. MacFarlane and M. Forsyth, *Chem. Commun.*, 2012, **48**, 5983-5985.
66. T. Markley, F. Blin, M. Forsyth and B. Hinton, in *Rare Earth-Based Corrosion Inhibitors*, Woodhead Publishing, Cambridge, 2014, pp. 117-142.
67. M. Forsyth, K. Wilson, T. Behrsing, C. Forsyth, G. B. Deacon and A. Phanasgaonkar, *Corrosion*, 2002, **58**, 953-960.
68. F. Blin, S. G. Leary, K. Wilson, G. B. Deacon, P. C. Junk and M. Forsyth, *J. Appl. Electrochem.*, 2004, **34**, 591-599.
69. F. Blin, S. G. Leary, G. B. Deacon, P. C. Junk and M. Forsyth, *Corros. Sci.*, 2006, **48**, 404-419.
70. M. Forsyth, C. M. Forsyth, K. Wilson, T. Behrsing and G. B. Deacon, *Corros. Sci.*, 2002, **44**, 2651-2656.
71. M. Seter, B. Hinton and M. Forsyth, *J. Electrochem. Soc.*, 2012, **159**, C181-C189.
72. Y. Sasikumar, A. S. Adekunle, L. O. Olasunkanmi, I. Bahadur, R. Baskar, M. M. Kabanda, I. B. Obot and E. E. Ebenso, *J. Mol. Liq.*, 2015, **211**, 105-118.
73. S. Yesudass, Lukman O. Olasunkanmi, I. Bahadur, M. M. Kabanda, I. B. Obot and Eno E. Ebenso, *J. Taiwan. Inst. Chem. Eng.*, 2016, **64**, 252-268.

74. A. Acidi, M. Hasib-ur-Rahman, F. Larachi and A. Abbaci, *Korean J. Chem. Eng.*, 2014, **31**, 1043-1048.
75. A. Yousefi, S. Javadian, N. Dalir, J. Kakemam and J. Akbari, *RSC Adv.*, 2015, **5**, 11697-11713.
76. D. Yang, M. Zhang, J. Zheng and H. Castaneda, *RSC Adv.*, 2015, **5**, 95160-95170.
77. L. C. Murulana, A. K. Singh, S. K. Shukla, M. M. Kabanda and E. E. Ebenso, *Ind. Eng. Chem. Res.*, 2012, **51**, 13282-13299.
78. I. Lozano, E. Mazario, C. O. Olivares-Xometl, N. V. Likhanova and P. Herrasti, *Mater. Chem. Phys.*, 2014, **147**, 191-197.
79. M. Messali and M. A. M. Asiri, *J. Mater. Environ. Sci.*, 2013, **4**, 770-785.
80. N. V. Likhanova, O. Olivares-Xometl, D. Guzmán-Lucero, M. A. Domínguez-Aguilar, N. Nava, M. Corrales-Luna and M. C. Mendoza, *Int. J. Electrochem. Sci.*, 2011, **6**, 4514-4536.
81. D. Guzmán-Lucero, O. Olivares-Xometl, R. Martínez-Palou, N. V. Likhanova, M. A. Domínguez-Aguilar and V. Garibay-Febles, *Ind. Eng. Chem. Res.*, 2011, **50**, 7129-7140.
82. A. Atta, G. El-Mahdy, H. Al-Lohedan and A. Ezzat, *Molecules*, 2015, **20**, 11131.
83. A. M. El-Shamy, K. Zakaria, M. A. Abbas and S. Zein El Abedin, *J. Mol. Liq.*, 2015, **211**, 363-369.
84. M. Ontiveros-Rosales, O. Olivares-Xometl, N. V. Likhanova, I. V. Lijanova, D. Guzman-Lucero and M. Del Consuelo Mendoza-Herrera, *Res. Chem. Intermed.*, 2017, **43**, 641-660.
85. E. Kowsari, S. Y. Arman, M. H. Shahini, H. Zandi, A. Ehsani, R. Naderi, A. P. Hanza and M. Mehdipour, *Corros. Sci.*, 2016, **112**, 73-85.
86. M. R. Ortega Vega, S. R. Kunst, J. A. T. da Silva, S. Mattedi and C. de Fraga Malfatti, *Corros. Eng. Sci. Techn.*, 2015, **50**, 547-558.
87. X. Zheng, S. Zhang, M. Gong and W. Li, *Ind. Eng. Chem. Res.*, 2014, **53**, 16349-16358.
88. J. Maddox, *USA Pat.*, 3629104, 1973.
89. A. J. McMahon, *Colloids Surf.*, 1991, **59**, 187-208.
90. D. Bajpai and V. K. Tyagi, *J. Oleo Sci.*, 2006, **55**, 319-329.
91. A. Edwards, C. Osborne, S. Webster, D. Klenerman, M. Joseph, P. Ostovar and M. Doyle, *Corros. Sci.*, 1994, **36**, 315-325.
92. I. Aiad, A. A. Hafiz, M. Y. El-Awady and A. O. Habib, *J. Surfactants Deterg.*, 2010, **13**, 247-254.
93. F.-l. Fei, J. Hu, J.-x. Wei, Q.-j. Yu and Z.-s. Chen, *Constr. Build. Mater.*, 2014, **70**, 43-53.
94. S. Ramachandran, B.-L. Tsai, M. Blanco, H. Chen, Y. Tang and W. A. Goddard, *Langmuir*, 1996, **12**, 6419-6428.
95. J. Zhang, G. Qiao, S. Hu, Y. Yan, Z. Ren and L. Yu, *Corros. Sci.*, 2011, **53**, 147-152.
96. S. Ramachandran and V. Jovancicevic, *Corros. Sci.*, 1999, **55**, 259 - 267.
97. S. Shi, P. Yi, C. Cao, X. Wang, J. Su and J. Liu, *CIESC Journal*, 2005, **56**, 1112-1119.
98. C. A. Wamser, *J. Am. Chem. Soc.*, 1948, **70**, 1209-1215.
99. M. G. Freire, C. M. S. S. Neves, I. M. Marrucho, J. A. P. Coutinho and A. M. Fernandes, *J. Phys. Chem. A*, 2010, **114**, 3744-3749.
100. E. I. Izgorodina, J. Rigby and D. R. MacFarlane, *Chem. Commun.*, 2012, **48**, 1493-1495.
101. K. E. Gutowski, J. D. Holbrey, R. D. Rogers and D. A. Dixon, *J. Phys. Chem. B*, 2005, **109**, 23196-23208.
102. E. J. Maginn, *J. Phys.: Condens. Matter*, 2009, **21**, 373101.
103. E. I. Izgorodina, Z. L. Seeger, D. L. A. Scarborough and S. Y. S. Tan, *Chem. Rev.*, 2017, **117**, 6696-6754.
104. M. Hajime, Y. Masahiro, T. Kazumi, N. Masakatsu, K. Yukiko and M. Yoshinori, *Chem. Lett.*, 2000, **29**, 922-923.
105. A. I. Bhatt, I. May, V. A. Volkovich, M. E. Hetherington, B. Lewin, R. C. Thied and N. Ertok, *J. Chem. Soc., Dalton Trans.*, 2002, 4532-4534.
106. Z. P. Rosol, N. J. German and S. M. Gross, *Green Chem.*, 2009, **11**, 1453-1457.
107. M. Egashira, M. Tanaka-Nakagawa, I. Watanabe, S. Okada and J.-i. Yamaki, *J. Power Sources*, 2006, **160**, 1387-1390.
108. G. H. Lane, *Electrochim. Acta*, 2012, **83**, 513-528.
109. H. Matsumoto, H. Sakaebe, K. Tatsumi, M. Kikuta, E. Ishiko and M. Kono, *J. Power Sources*, 2006, **160**, 1308-1313.

110. A. Basile, A. I. Bhatt and A. P. O'Mullane, *Nat. Commun.*, 2016, **7**, ncomms11794.
111. S. Seki, Y. Kobayashi, H. Miyashiro, Y. Ohno, A. Usami, Y. Mita, N. Kihira, M. Watanabe and N. Terada, *J. Phys. Chem. B*, 2006, **110**, 10228-10230.
112. S. A. Mohd Noor, P. C. Howlett, D. R. MacFarlane and M. Forsyth, *Electrochim. Acta*, 2013, **114**, 766-771.
113. D. Monti, E. Jónsson, M. R. Palacín and P. Johansson, *J. Power Sources*, 2014, **245**, 630-636.
114. Y. NuLi, J. Yang and R. Wu, *Electrochem. Commun.*, 2005, **7**, 1105-1110.
115. N. Yoshimoto, M. Matsumoto, M. Egashia and M. Morita, *J. Power Sources*, 2010, **195**, 2096-2098.
116. T. Khoo, A. Somers, A. A. J. Torriero, D. R. MacFarlane, P. C. Howlett and M. Forsyth, *Electrochim. Acta*, 2013, **87**, 701-708.
117. T. Khoo, P. C. Howlett, M. Tsagouria, D. R. MacFarlane and M. Forsyth, *Electrochim. Acta*, 2011, **58**, 583-588.
118. R. Mohtadi, O. Tutusaus and F. Mizuno, *USA Pat.*, US 9455473 B1, 2016.
119. C. C. Ho, J. W. Evans and P. K. Wright, *J. Micromech. Microeng.*, 2010, **20**, 104009.
120. M. Kar, B. Winther-Jensen, M. Armand, T. J. Simons, O. Winther-Jensen, M. Forsyth and D. R. MacFarlane, *Electrochim. Acta*, 2016, **188**, 461-471.
121. Z. Liu, P. Bertram and F. Endres, *J. Solid State Electrochem.*, 2017, 1-7.
122. Y. Bai, J. Zhang, Y. Wang, M. Zhang and P. Wang, *Langmuir*, 2011, **27**, 4749-4755.
123. J.-D. Decoppet, S. B. Khan, M. S. A. Al-Ghamdi, B. G. Alhogbi, A. M. Asiri, S. M. Zakeeruddin and M. Grätzel, *Energy Technol.*, 2017, **5**, 321-326.
124. H. H. Lin, J. D. Peng, V. Suryanarayanan, D. Velayutham and K. C. Ho, *J. Power Sources*, 2016, **311**, 167-174.
125. P. Wang, S. M. Zakeeruddin, J.-E. Moser and M. Grätzel, *J. Phys. Chem. B*, 2003, **107**, 13280-13285.
126. J. J. Black, T. Murphy, R. Atkin, A. Dolan and L. Aldous, *Phys. Chem. Chem. Phys.*, 2016, **18**, 20768-20777.
127. E. H. B. Anari, M. Romano, W. Teh, J. Black, E. Jiang, J. Chen, T. To, J. Panchompoo and L. Aldous, *Chem. Commun.*, 2016, **52**, 745-748.
128. T. J. Abraham, D. R. MacFarlane and J. M. Pringle, *Energ. Environ. Sci*, 2013, **6**, 2639-2645.
129. T. Migita, N. Tachikawa, Y. Katayama and T. Miura, *Electrochemistry*, 2009, **77**, 639-641.
130. T. L. Greaves and C. J. Drummond, *Chem. Rev.*, 2008, **108**, 206-237.
131. B. Peric, J. Sierra, E. Martí, R. Cruañas, M. A. Garau, J. Arning, U. Bottin-Weber and S. Stolte, *J. Hazard. Mater.*, 2013, **261**, 99-105.
132. P. Walden, *Bull. Acad. Imp. Sci. Saint-Petersbourg*, 1914, 405-422.
133. L. Mayrand-Provencher, S. Lin, D. Lazzarini and D. Rochefort, *J. Power Sources*, 2010, **195**, 5114-5121.
134. A. Brandt, J. Pires, M. Anouti and A. Balducci, *Electrochim. Acta*, 2013, **108**, 226-231.
135. L. Timperman, P. Skowron, A. Boisset, H. Galiano, D. Lemordant, E. Frackowiak, F. Beguin and M. Anouti, *Phys. Chem. Chem. Phys.*, 2012, **14**, 8199-8207.
136. A. Izgorodin, E. Izgorodina and D. R. MacFarlane, *Energ. Environ. Sci*, 2012, **5**, 9496-9501.
137. M. S. Miran, T. Yasuda, M. A. B. H. Susan, K. Dokko and M. Watanabe, *J. Phys. Chem. C*, 2014, **118**, 27631-27639.
138. T. Yasuda and M. Watanabe, *MRS Bull.*, 2013, **38**, 560-566.
139. C. J. T. Grotthuss, *Ann. Chim. - Sci. Mat.*, 1806, **58**, 54-73.
140. H. Danneel, *Z. Elektrochem. Angew. P.*, 1905, **11**, 249-252.
141. S. Cukierman, *Biochim. Biophys. Acta Bioenergetics*, 2006, **1757**, 876-885.
142. K. Binnemans, *Chem. Rev.*, 2005, **105**, 4148-4204.
143. J. M. Pringle, P. C. Howlett, D. R. MacFarlane and M. Forsyth, *J. Mater. Chem.*, 2010, **20**, 2056-2062.
144. J. Luo, A. H. Jensen, N. R. Brooks, J. Sniekers, M. Knipper, D. Aili, Q. Li, B. Vanroy, M. Wubbenhorst, F. Yan, L. Van Meervelt, Z. Shao, J. Fang, Z.-H. Luo, D. E. De Vos, K. Binnemans and J. Fransaer, *Energ. Environ. Sci*, 2015, **8**, 1276-1291.

145. L. Jin, K. M. Nairn, C. M. Forsyth, A. J. Seeber, D. R. MacFarlane, P. C. Howlett, M. Forsyth and J. M. Pringle, *J. Am. Chem. Soc.*, 2012, **134**, 9688-9697.
146. G. Annat, J. Adebahr, I. R. McKinnon, D. R. MacFarlane and M. Forsyth, *Solid State Ionics*, 2007, **178**, 1065-1071.
147. A. J. Seeber, M. Forsyth, C. M. Forsyth, S. A. Forsyth, G. Annat and D. R. MacFarlane, *Phys. Chem. Chem. Phys.*, 2003, **5**, 2692-2698.
148. J. Adebahr, M. Grimsley, N. M. Rocher, D. R. MacFarlane and M. Forsyth, *Solid State Ionics*, 2008, **178**, 1798-1803.
149. S. J. Pas, J. Huang, M. Forsyth, D. R. MacFarlane and A. J. Hill, *J. Chem. Phys.*, 2005, **122**, 064704.
150. E. I. Cooper and C. A. Angell, *Solid State Ionics*, 1986, **18**, 570-576.
151. J. Adebahr, A. J. Seeber, D. R. MacFarlane and M. Forsyth, *J. Phys. Chem. B*, 2005, **109**, 20087-20092.
152. L. Jin, S. de Leeuw, M. V. Koudriachova, J. M. Pringle, P. C. Howlett, F. Chen and M. Forsyth, *Phys. Chem. Chem. Phys.*, 2013, **15**, 19570-19574.
153. W. A. Henderson, D. M. Seo, Q. Zhou, P. D. Boyle, J.-H. Shin, H. C. De Long, P. C. Trulove and S. Passerini, *Adv. Energy Mat.*, 2012, **2**, 1343-1350.
154. K. Romanenko, L. Jin, P. Howlett and M. Forsyth, *Chem. Mater.*, 2016, **28**, 2844-2851.
155. Y. Abu-Lebdeh, A. Abouimrane, P.-J. Alarco and M. Armand, *J. Power Sources*, 2006, **154**, 255-261.
156. X. Y. Zhao, J. L. Wang, H. Luo, H. R. Yao, C. Y. Ouyang and L. Z. Zhang, *J. Zhejiang Univ. Sci. A*, 2016, **17**, 155-162.
157. P. C. Howlett, F. Ponzio, J. Fang, T. Lin, L. Jin, N. Iranipour and J. Efthimiadis, *Phys. Chem. Chem. Phys.*, 2013, **15**, 13784-13789.
158. S. Li, L. Qiu, C. Shi, X. Chen and F. Yan, *Adv. Mater.*, 2014, **26**, 1266-1271.
159. P. Wang, Q. Dai, S. M. Zakeeruddin, M. Forsyth, D. R. MacFarlane and M. Grätzel, *J. Am. Chem. Soc.*, 2004, **126**, 13590-13591.
160. V. Armel, M. Forsyth, D. R. MacFarlane and J. M. Pringle, *Energ. Environ. Sci*, 2011, **4**, 2234-2239.
161. J. M. Pringle and V. Armel, *Int. Rev. Phys. Chem.*, 2011, **30**, 371-407.
162. R. Taniki, K. Matsumoto, T. Nohira and R. Hagiwara, *J. Power Sources*, 2014, **245**, 758-763.
163. S. J. Peighambardoust, S. Rowshanzamir and M. Amjadi, *Int. J. Hydrogen Energy*, 2010, **35**, 9349-9384.
164. V. M. Vishnyakov, *Vacuum*, 2006, **80**, 1053-1065.
165. H. Zhu, U. A. Rana, V. Ranganathan, L. Jin, L. A. O'Dell, D. R. MacFarlane and M. Forsyth, *J. Mater. Chem. A*, 2014, **2**, 681-691.
166. H. Zhu, D. MacFarlane and M. Forsyth, *J. Phys. Chem. C*, 2014, **118**, 28520-28526.
167. X. Chen, H. Tang, T. Putzeys, J. Sniekers, M. Wubbenhorst, K. Binnemans, J. Fransaer, D. E. De Vos, Q. Li and J. Luo, *J. Mater. Chem. A*, 2016, **4**, 12241-12252.
168. J. Luo, O. Conrad and I. F. J. Vankelecom, *J. Mater. Chem. A*, 2013, **1**, 2238-2247.
169. V. Tricoli, G. Orsini and M. Anselmi, *Phys. Chem. Chem. Phys.*, 2012, **14**, 10979-10986.
170. S. Long, P. C. Howlett, D. R. MacFarlane and M. Forsyth, *Solid State Ionics*, 2006, **177**, 647-652.
171. U. A. Rana, R. Vijayaraghavan, D. R. MacFarlane and M. Forsyth, *Chem. Commun.*, 2011, **47**, 6401-6403.
172. A. Mondal and S. Balasubramanian, *J. Phys. Chem. C*, 2016, **120**, 22903-22909.
173. J. Thisuwan and K. Sagarik, *RSC Adv.*, 2014, **4**, 61992-62008.
174. J. Rao, R. Vijayaraghavan, F. Chen, H. Zhu, P. C. Howlett, D. R. MacFarlane and M. Forsyth, *Chem. Commun.*, 2016.

2 NOVEL IMIDAZOLINIUM SALTS AND IONIC LIQUIDS

This chapter is a paper titled “Novel imidazolinium salts and ionic liquids” that was published in *Electrochimica Acta* in 2015. The paper serves as an introduction to the imidazolinium cation; the common theme running throughout the thesis. It details the one-pot synthesis of a selection of protic salts featuring the 2-methylimidazolinium cation, paired with a selection of anions recognised for either their corrosion inhibiting or ionic liquid-forming properties. Because the majority of these salts have been synthesised for the first time, it was important to investigate their properties, both as potential ILs and as potential corrosion inhibitors.

One of the most obvious properties required for an IL is that it be a liquid, specifically that it should melt below 100 °C. To this end, differential scanning calorimetry (DSC) and also thermogravimetric analysis (TGA, for thermal decomposition) were among the first techniques used to characterise the synthesised ILs. DSC can identify the temperatures and energy changes involved in thermal transitions, not just between crystalline solid and liquid, but also solid – solid transitions or glass transitions that cannot always be observed by the naked eye.

Measurements of physical properties were carried out on those salts that were found to be liquid over a suitable range. This included measurement of the density, viscosity and conductivity. Many studies have tried to elucidate links between the observed properties of ILs and their structure and ionic nature. In this work such comparisons were made with the aid of a Walden plot. Developed by Angell and co-workers,^{1, 2} this logarithmic plot visualises the inverse relationship between viscosity and molar conductivity, and is a useful way to qualitatively compare the ionic strength or ionicity between ILs. The data is plotted relative to an ideal line, derived from data for 0.01 M KCl, where complete ion separation is assumed. ILs can then be classified into broad groups based on where they sit

on the plot: ‘good’ ionic liquids that show predominately individual ion transport, with high conductivity and fluidity, ‘poor’ ionic liquids that sit far below the ideal line, or ‘super’ ionic liquids that sit above the reference line due to additional conduction mechanisms. Using this method provided an interesting comparison between the imidazolium IL, [2-MeHImn][TfO] and its imidazolium analogue, [2-MeHIm][TfO].

This chapter also screened some of the novel salts for corrosion inhibition efficacy. Electrochemical methods, such as potentiodynamic polarisation, are useful for quickly assessing corrosion rates and obtaining information about the inhibition mechanisms.

When corroding naturally in solution, the cathodic and anodic processes occur simultaneously, with a common current density, i_{corr} , and corrosion potential, E_{corr} . If the surface is externally polarised such that a negative overpotential, η_c , is applied relative to E_{corr} , excess electrons are supplied to the surface and the cathodic process dominates. Conversely, if a positive overpotential, η_a , is applied, the anodic reaction takes place. The relationship between η and i is described by the Tafel equation; for anodic polarisation,

$$\eta_a = \beta_a \log i_a / i_0 \quad (6)$$

or cathodic polarisation,

$$\eta_c = \beta_c \log i_c / i_0 \quad (7)$$

where i_0 is the current density at the respective half-cell electrode potentials. β_a and β_c are known as Tafel constants.³

Based on these equations, plotting $\log(i)$ as a function of potential results in slopes with a gradient of β_a or β_c originating from E_{corr} . Experimentally, such polarisation curves show asymptotic behaviour near E_{corr} , however, extrapolating the linear cathodic and anodic regions to E_{corr} will give i_{corr} . This value is proportional to the rate of corrosion.⁴ Figure 1 shows a hypothetical Tafel plot for a corrosion process featuring Fe dissolution and H₂ evolution.

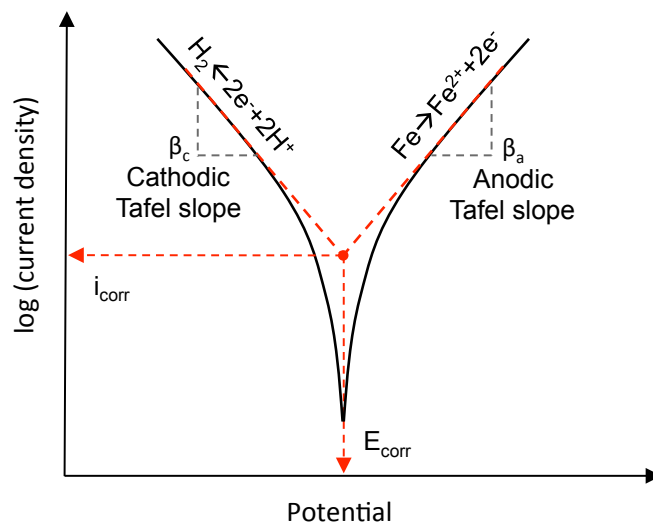


Figure 1. Hypothetical polarisation curve featuring anodic Fe dissolution and cathodic H₂ evolution. i_{corr} is determined by extrapolating the linear Tafel slopes to E_{corr} .

Potentiodynamic polarisation was used in this paper to compare the effects of different anions on the corrosion inhibition of the imidazolium salts on mild steel in aqueous chloride solutions. This method was also used extensively throughout the subsequent investigations of imidazolium corrosion inhibitors in Chapter 3 and Chapter 4.

1. W. Xu, E. I. Cooper and C. A. Angell, *J. Phys. Chem. B*, 2003, **107**, 6170-6178.
2. M. Yoshizawa, W. Xu and C. A. Angell, *J. Am. Chem. Soc.*, 2003, **125**, 15411-15419.
3. M. Stern and A. L. Geary, *J. Electrochem. Soc.*, 1957, **104**, 56-63.
4. R. G. Kelly, J. R. Scully, D. Shoesmith and R. G. Buchheit, *Electrochemical Techniques in Corrosion Science and Engineering*, Marcel Dekker, New York, 2002.

2.1 Novel Imidazolinium Salts and Ionic Liquids

Electrochimica Acta 159 (2015) 219–226



Contents lists available at ScienceDirect

Electrochimica Acta

journal homepage: www.elsevier.com/locate/electacta

Novel imidazolinium ionic liquids and organic salts

Alison L. Chong^a, Maria Forsyth^b, Douglas R. MacFarlane^{a,*}^aSchool of Chemistry, Monash University, Clayton, Victoria 3800, Australia^bInstitute for Frontier Materials, Deakin University, Burwood, Victoria 3125, Australia

ARTICLE INFO

Article history:

Received 8 January 2015

Accepted 28 January 2015

Available online 29 January 2015

Keywords:

Imidazolinium Ionic Liquids

Physical Properties

Conductivity

Electrochemical Stability

Corrosion Inhibition

ABSTRACT

The preparation and physical properties of a novel family of ionic liquids and organic salts based on the imidazolinium cation are described, and compared with their imidazolium analogues in some cases. Ionic liquids were obtained with the triflate, formate and salicylate anions, while > 100 °C melting points were observed with acetate and several other benzoate derivatives. The triflate salt was less ion-conductive than the corresponding imidazolium salt, but less so than expected on the basis of its viscosity, suggesting a contribution from proton conductivity. The electrochemical window of the imidazolinium was slightly extended in the reductive direction, due to the lower proton activity produced by the cation in this case. Imidazolinium salts are also known to exhibit anti-corrosion properties and hence a preliminary study of this property is also reported; 2-methylimidazolinium 4-hydroxycinnamate was found to show strong anodic corrosion inhibition on mild steel.

© 2015 Elsevier Ltd. All rights reserved.

1. Introduction

As a class of materials, ionic liquids (ILs) are generally classified as salts with melting points below 100 °C [1]. Due to the vast number of cations and anions that can be combined to form ILs, they can have greatly varying properties and, as such, ionic liquid research spans a broad range of fields. This includes, but is not limited to, investigation of their use in electrochemical devices [2] and as “green” solvents [3].

Recently this has begun to include development of ILs for use in corrosion protection of metals. Corrosion is an insidious problem that annually causes trillions of dollars' worth of damage worldwide [4]. While a variety of corrosion inhibitors exist, many, such as the extremely effective chromates, are highly toxic [5]. Ionic liquids are being sought that could provide “greener” alternatives for use on a range of metals. One approach is to use ionic liquid pre-treatments to form passivating films on the metal surface. This is particularly useful for protection of reactive metals such as magnesium and aluminium [6]. To date this work has focused predominantly on phosphonium based ILs [7,8].

A number of publications have also investigated the use of ionic liquids as additive chemical inhibitors, with a particular focus towards protecting steel in acidic environments, a common industrial condition. A range of imidazolium cations have been

tested, including traditional alkyl methylimidazoliums [9,10] and novel substituted cations [11,12], as well as other cations such as pyridinium [12] and pyridazinium [13].

Most of these examples rely on the use of conventional ILs, despite one of the greatest strengths of the IL platform being the ability in principle to design a compound or a formulation for a given application. In recent years, there has been a shift in the focus of this tuneability. Initial investigations into ILs looked to alter physical properties such as viscosity and thermal stability. Eventually this evolved to tailoring not only the physical properties, but the chemical properties as well, to develop ILs that were chiral [14,15] or strong coordinating solvents [16]. The “third generation” of ILs, as proposed by Rogers and coworkers [17] introduced the idea of manipulating their biological properties. This concept does not, however, have to be limited to pursuing pharmaceutical compounds, but rather can be seen as a shift in the way component ions are chosen. Instead of trying to fit traditional ILs to a given application, one can take an “active” compound and redesign it as an IL with enhanced functionality for a range of applications where bio-activity, or biocompatibility is important. In some of our previous work [18,19] we have shown how ionic liquids and salts developed this way can tackle the insidious problem of microbially induced corrosion, by combining known antibacterial agent ions with corrosion inhibiting counter ions.

From our continued investigation of such compounds we present here a novel family of task-oriented organic salts and ionic liquids featuring the 2-methylimidazolinium [2-MeHImn]⁺ cation. We describe a range of salts of this cation, some in particular

* Corresponding author.

E-mail address: douglas.macfarlane@monash.edu (D.R. MacFarlane).

targeted towards use as corrosion inhibitors. Imidazolines and their salts, some of which are liquids, are known and used in a number of industries, notably as corrosion inhibitors, particularly in oil pipelines [20,21]. The compounds often feature lengthy fatty-acid functional groups and in those cases can be classified as cationic surfactants [20–22]. As can be seen in Fig. 1, imidazolium cations are closely related to the more broadly recognised imidazolium cations, with the only difference to the core ring being the saturation of the C4–C5 double bond. Despite this similarity, the imidazolium cation has not been widely explored in the IL context (for any application) and thus it appears to offer a promising avenue for new IL chemistry. Thus we present here a number of novel ionic liquids and organic salts based on this cation and investigate their properties including an initial investigation of their corrosion inhibition activity.

2. Experimental

2.1. Materials

All chemicals were purchased from Sigma and were >98% pure. They were used without further purification. Methanol was distilled from sodium metal and stored over 4 Å molecular sieves, acetonitrile and dichloromethane were dried over 4 Å molecular sieves.

2.2. Synthetic Methods

2.2.1. Synthesis of 2-methylimidazolium acetate

Triethylorthoacetate (10.5 mL, 53 mmol) and acetic acid (3.1 mL, 53 mmol) were added to a flask of acetonitrile. Ethylenediamine (3.4 mL, 50 mmol) was added slowly via a dropping funnel, resulting in formation of a white precipitate. The mixture was heated to reflux and stirred under N₂ for 2 h, causing dissolution of the precipitate. The solvent was removed by rotary evaporation, with further drying under high vacuum to give a pale yellow solid (6.50 g, 90%). ¹H NMR (400 MHz, DMSO-*d*₆) δ (ppm): 1.67 (s, 3H, CH₃), 2.07 (s, 3H, CH₃), 3.73 (unresolved d, 4H, 2x CH₂). ¹³C NMR (400 MHz, DMSO-*d*₆) δ (ppm): 12.75 (CH₃), 25.13 (CH₃), 45.17 (2x CH₂), 169.01 (N–C=N), 177.90 (C=O). Mass spectrum: ES⁺ m/z 85.0 [2-MeHIm]⁺; ES[−] m/z 58.9 [Ac][−].

2.2.2. Synthesis of 2-methylimidazolium triflate

2-methylimidazole (1.6 g, 20 mmol) was dissolved in acetonitrile. Triflic acid (3.3 g, 22 mmol, diluted in acetonitrile) was added slowly and the mixture stirred at room temperature under nitrogen for 3 h. The solvent was removed via rotary evaporation and the product dried under high vacuum at 60 °C to yield a pale pink solid (4.6 g, 98%). ¹H NMR (400 MHz, DMSO-*d*₆) δ (ppm): 2.07 (s, 3H, CH₃), 3.73 (unresolved d, 4H, 2x CH₂). ¹³C NMR (400 MHz, DMSO-*d*₆) δ (ppm): 11.16 (CH₃), 118.70 (2x CH), 144.29 (N–C=N). ¹⁹F NMR (400 MHz, DMSO-*d*₆) δ (ppm): 77.77. Mass spectrum: ES⁺ m/z 83.1 [2-MeHIm]⁺, 315.1 [2[2-MeHIm]⁺[Tf][−]]; ES[−] m/z 148.9 [Tf][−], 380.9 [2-MeHIm]⁺2[Tf][−].

Synthesis of further compounds contained in the supplementary information.

2.3. Analysis

The purity of the samples was determined using NMR and mass spectrometry. NMR spectra were recorded in DMSO-*d*₆ (Merck) using a Bruker Avance 400 (9.4 T magnet) operating at 400 MHz. Low resolution ESI mass spectra were recorded on a Micromass Platform II QMS with a cone voltage of 35 V, using methanol as the mobile phase.

The ILs were dried thoroughly under high vacuum prior to physical property measurements and the presence of water was not detected during characterisation of these samples (ie. TGA). Karl Fischer titration was found to be an inaccurate means of testing the water content of the samples as the ILs reacted in the titration vessel.

Differential scanning calorimetry was carried out using a Perkin Elmer DSC 8000 with liquid nitrogen cryo cooler. Scans were run at a heating/cooling rate of 10 °C/min over a temperature range of −80 to 250 °C. Transition temperatures were reported using the peak maximum of the thermal transition.

Thermogravimetric analysis was undertaken on a Mettler Toledo TGA/DSC 1 STARe System. Samples were heated at 10 °C/min over a temperature range of 25 to 450 °C.

Density measurements were performed using an Anton Paar DMA 5000 Density Meter. This meter uses the 'oscillating U-tube principle' to determine density. Viscosity measurements were undertaken using an Anton Paar Lovis 2000 M microviscometer. This instrument uses the falling ball technique. Measurements were taken from 90 °C until the materials solidified. The conductivity was evaluated using AC impedance spectroscopy over a range of 20 Hz to 1 MHz. Measurements were carried out using a Hewlett Packard 4284 LCR meter. Resistance values for conductivity calculations were taken to be the data point closest to the x-axis on the impedance plot.

Cyclic voltammetry was carried out using a multi-channel potentiostat (VMP2, Princeton Applied Research). Samples were dissolved in acetonitrile and used as the electrolyte in a three-electrode system with platinum working and counter electrodes and a non-aqueous Ag/Ag⁺ reference. Measurements were carried out at a scan rate 20 mV s^{−1}.

For the potentiodynamic polarisation experiments AS1020 steel electrodes (composition: 0.26% C, 0.45% Mn, 0.14% Cr, 0.19% Si, 0.18% Al, 0.35% other, and balance Fe) with a 1.0 cm diameter (0.78 cm²) set in epoxy resin were used. They were abraded with silicon carbide paper to P4000 grit from P320 grit. The electrodes were washed with distilled water, dried and stored in a desiccator under vacuum. Potentiodynamic polarisation experiments were carried out half an hour after electrode preparation.

The test solutions were prepared by dissolving the appropriate masses of each compound in 1 L of 0.01 M sodium chloride solution (made with milliQ water) to make concentrations of 4 mM. The pH of these solutions ranged from 5.9–7.0.

All polarisation experiments were carried out in an open-to-air, standard three-electrode system consisting of a saturated calomel reference electrode (SCE), a titanium mesh counter electrode, and the working electrode with 150 mL of test solution as the electrolyte. The cell assembly was located in a Faraday cage to prevent electrical interference.

After immersion the open circuit potential (OCP) was monitored for 30 minutes, and then the potentiodynamic polarisation experiment was carried out at a scanning rate of 0.167 mV s^{−1}. The scans started at 100 mV more negative than E_{corr} and continued through E_{corr} for a range of 400 mV in the positive direction. Measurements were carried out in triplicate. All electrochemical

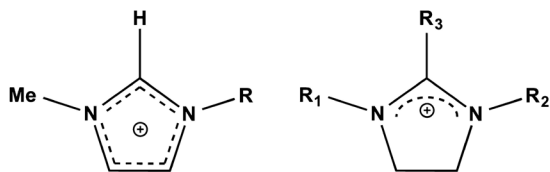


Fig. 1. A comparison of the common ionic liquid cation methylimidazolium and the general structure of the imidazolium cation.

measurements were conducted using a Princeton Applied Research VMP2 multichannel potentiostat. The i_{corr} values were calculated using Tafel extrapolation methods. Where anodic and cathodic curves were near linear and symmetrical within ± 20 mV from E_{corr} , both Tafel slopes were extrapolated until the lines intersected at E_{corr} .

Steel coupons (1.0 cm² AS1020 steel coupons set in epoxy resin) were prepared in the same way as the electrodes for the immersion experiments. The coupons were immersed in 4 mM solutions of inhibitor in 0.01 M NaCl for 24 hours or 7 days. The coupons were observed using a Leica MZ6 optical microscope at a magnification of 0.68x.

3. Results and Discussion

3.1. Synthesis

[2-MeHImn]⁺ salts were synthesised in a one-pot synthesis from ethylenediamine, triethylorthoacetate and the desired acid, following a method established by Cornia et al. [23] (Fig. 2a). The selection of anions is shown in Fig. 2b, focusing on carboxylates, with corrosion applications in mind. A number of equivalent 2-methylimidazolium ([2-MeHIm]⁺) salts were also synthesised for comparison.

3.2. Physical Properties

Differential scanning calorimetry (DSC) was used to determine the thermal behaviour of the materials. As can be seen in Table 1, the melting points of the [2-MeHImn]⁺ carboxylate salts increase with the size of the anion, such that [2-MeHImn][For] is an ionic liquid, melting at 75 °C, while the acetate and gentisate salts fall just outside the 100 °C threshold. [2-MeHImn][4-OHCin] decomposes from 128 °C.

An exception to this trend is salicylic acid, which has the lowest melting point of all the carboxylate salts, despite being similar in size and structure to gentisic acid. In addition, after the initial melt at 70 °C, no crystallisation event was observed on cooling. Instead, a glass transition appeared at -23 °C. This indicates that at the scan rate of the experiment (10 °C/min), the compound behaves as a supercooled liquid (Supplementary Fig. S1).

Comparing imidazolium and imidazolinium salts of the same anion, the [2-MeHIm][Sal] exhibits the same supercooling

Table 1
Summary of thermal transitions.

Sample	T_m /°C	T_g /°C
[2-MeHImn][For]	75	-
[2-MeHImn][Ac]	101	-
[2-MeHImn][Sal]	70	-23
[2-MeHImn][Gen]	105	-
[2-MeHImn][4-OHCin]	128 (d)	-
[2-MeHImn][Tf]	50	-62
[2-MeHIm][Sal]	104	-13
[2-MeHIm][Tf]	48 ^a	-

^a Melt is the final transition following two solid-solid transitions at 10 °C and 29 °C.

behaviour as [2-MeHIm][Sal], with a similar T_g , but melts 34 °C higher. In the case of the triflate ILs, [2-MeHImn][Tf] shows relatively easy glass formation upon cooling with crystallisation only occurring with heating to 8 °C. On the other hand, the imidazolium salt shows polymorphic behaviour, with two solid-solid phase transitions; such solid-solid phase transitions are suggestive of plastic crystal phase formation as observed in other organic salt families [24,25]. This behaviour has not been investigated further at this stage.

The thermal stability of the salts and ILs was assessed using thermogravimetric analysis (TGA). Fig. 3 shows that both [2-MeHImn][Tf] and [2-MeHImn][Sal] are more stable than the neutral base. In comparison to the imidazolium salt, [2-MeHImn][Sal] showed a slight increase in degradation temperature. In contrast, [2-MeHImn][Tf] was slightly less stable than [2-MeHIm][Tf], although both these ILs were substantially more stable than the salicylates. These results suggest that the imidazolium cation has a similar thermal stability to the equivalent imidazolium, and that the observed differences are predominantly dictated by the anion. TGA data for the remaining carboxylates can be found in the supplementary information (Fig. S2).

Both the 2-methylimidazoline and 2-methylimidazole bases were titrated against HCl to determine the pK_a (Fig. S3). The pK_a of 2-methylimidazole was found to be 8.0 ± 0.2 , which is in agreement with the literature [26]. 2-methylimidazoline was shown to be more basic, with a pK_a of 10.6 ± 0.2 . This difference likely arises due to the change in the electronic structure of the molecules. In the imidazole, the lone pair on the available nitrogen contributes to the aromaticity of the ring. Upon saturation of the C4 and C5 carbons, however, aromaticity is lost and the lone pair

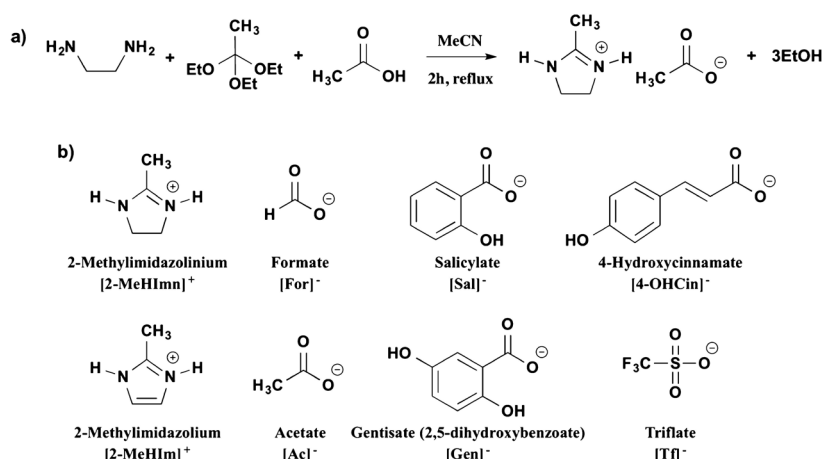


Fig. 2. (a) Reaction scheme for synthesis of 2-methylimidazolium acetate [23]. (b) The imidazolium and imidazolinium cations and accompanying anions studied.

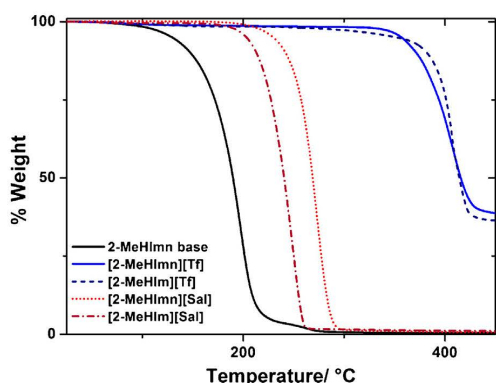


Fig. 3. TGA data for the salicylate and triflate salts.

becomes more available for protonation. Because of the increased basicity of the imidazoline, there will be a larger ΔpK_a and mixtures with weak acids (such as some of the benzoate derivatives used) are more likely to undergo proton transfer and form ILs and salts.

Density, viscosity and conductivity data were obtained for the two triflate ILs and [2-MeHImn][Sal] as these were the samples that were liquid over the optimum temperature range (50–90 °C). Fig. 4 shows the densities of the chosen ILs with respect to temperature. The triflate ILs have much higher densities than [2-MeHImn][Sal], indicating that the influence of the anion is greater; because the triflate anion features heavier elements (fluorine and sulphur) than salicylate, the density is significantly increased. Comparing the two triflates, [2-MeHImn][Tf] has the higher density, and the density decreases more slowly with increasing temperature.

This difference in slope can be quantified by linearly fitting the data to Eq. (1). This was achieved with correlation coefficients greater than 0.999. The fitting parameters are shown in Table 2. The lesser temperature dependence of the density of [2-MeHImn][Tf] (dp/dT) is shown by the less negative b parameter compared to [2-MeHImn][Sal].

$$\rho = \alpha + bT \quad (1)$$

Due to the inversely proportional relationship of density to volume, this parameter can be used to calculate the thermal expansivity (α_V) of the material from:

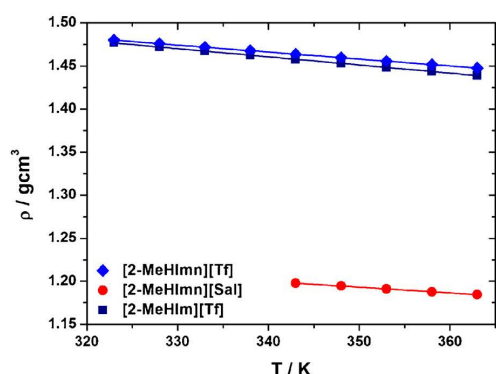


Fig. 4. Density of [2-MeHImn]⁺ and [2-MeHImn]⁺ ILs.

Table 2

Density and thermal expansivity parameters for imidazolium ILs.

Sample	a/gcm^{-3}	$b/10^{-4}$ $\text{gcm}^{-3}\text{K}^{-1}$	R^2	α_V/K^{-1}
[2-MeHImn][Sal]	1.426 ± 0.001	-6.64 ± 0.03	0.9999	0.560 ± 0.002
[2-MeHImn][Tf]	1.7416 ± 0.0008	-8.10 ± 0.02	0.9999	0.554 ± 0.001
[2-MeHImn][Tf]	1.7827 ± 0.0006	-9.47 ± 0.02	1.0000	0.6454 ± 0.0005

$$\alpha_V = \frac{1}{V} \frac{\partial V}{\partial T} \quad (2)$$

[2-MeHImn][Tf] has the larger α_V value (Table 2) compared to the two imidazolium salts. This quantity can be linked back to the concept of liquid fragility [27,28]. Larger thermal expansivity suggests that the liquid is more labile and allow expansion of the material. Thus it appears that the imidazolium salts are less fragile, perhaps because of the less diffuse nature of the charge on the cation. It is interesting to note that both the [2-MeHImn]⁺ ILs have very similar α_V values despite their differing densities.

Fig. 5 shows an Arrhenius plot of the viscosity of the ILs. [2-MeHImn][Tf] was found to be much less viscous than the [2-MeHImn]⁺ ILs. Interestingly, while [2-MeHImn][Sal] and [2-MeHImn][Tf] have similar viscosities at lower temperatures, they deviate at higher temperatures; the viscosity of [2-MeHImn][Sal] decreases more quickly as the temperature is increased.

An Arrhenius plot of the conductivity is shown in Fig. 6. As expected based on the viscosities, [2-MeHImn][Sal] exhibits the lowest conductivity, while [2-MeHImn][Tf], the most fluid of the samples, shows the highest conductivity.

Typically viscosity and conductivity data plotted in this manner can be fitted to the Vogel-Fulcher-Tammann (VFT) equation, $\sigma = \sigma_0 \exp\left[\frac{-B}{T-T_0}\right]$ where σ_0 , B and T_0 are constants. Such an equation curves exponentially towards an asymptote at $T=T_0$. T_0 is often found to be approximately 20 °C below the T_g . At temperatures far from this asymptote the VFT equation becomes linear. The lack of curvature in the data presented in Figs. 5 and 6 suggests that the temperatures involved are quite far from this asymptote, and hence the T_g of the ILs. Indeed T_g for those systems that were able to be vitrified (Table 1) was well below 0 °C and as low as -62 °C for [2-MeHImn][Tf].

Constructing a plot based on the Walden rule provides an approximate method for assessing the ionicity of ionic liquids. The Walden rule (Eq. (3)) empirically relates the molar conductivity (Λ) of a material to its viscosity (η) with a temperature dependent

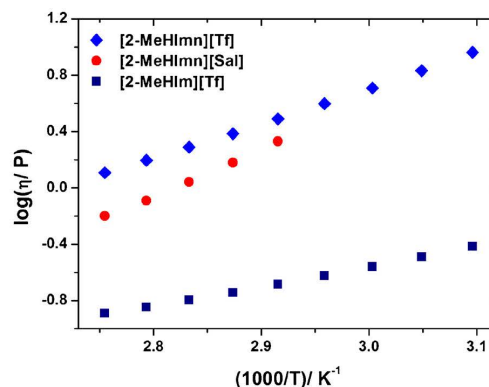


Fig. 5. Arrhenius plot of viscosity of [2-MeHImn]⁺ and [2-MeHImn]⁺ ILs.

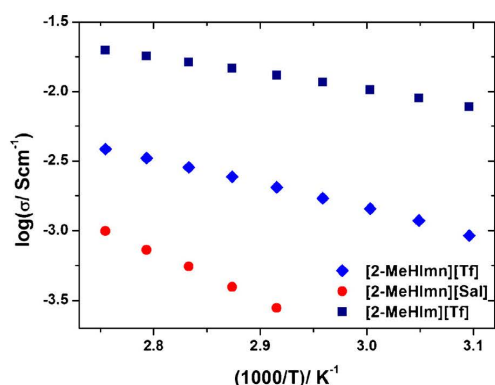


Fig. 6. Arrhenius plot of conductivity of [2-MeHlmn]⁺ and [2-MeHlm]⁺ ILs.

constant, C .

$$\Lambda \eta = C \quad (3)$$

On the resulting plot ($\log \Lambda$ vs $\log 1/\eta$) a sample can be compared to dilute aqueous KCl solution data which is often considered as an ideal case in which the anions and cations are able to move independently. Often ion association, or lack of proton transfer, within an IL causes it to fall below the KCl line on the plot, however liquids that lie within an order of magnitude of the ideal line (as represented by the 10% KCl line) are generally considered to be “good” ILs [29,30]. In Fig. 7 it can be seen that all three ILs fall above this 10% line.

While [2-MeHlm][Tf] sits within the typical region for an imidazolium ionic liquid [31–33], [2-MeHlmn][Tf] sits slightly above the KCl line, an indication that it may be showing “superionic” behaviour, i.e. that the molar conductivity is higher than predicted on the basis of the Walden rule. Such materials fall towards the top-left corner of the Walden plot [32]. Although [2-MeHlmn][Tf] showed higher viscosity than [2-MeHlm][Tf], the corresponding difference in conductivity was not as great. One possible reason for this apparent gain in conductivity is the presence of additional proton transfer mechanisms, potentially including a Grotthuss-type mechanism whereby a protonic charge in a system can effectively cross a series of hydrogen bonds between molecules without large-scale movement of the cations, hence moving through the material faster than conventional

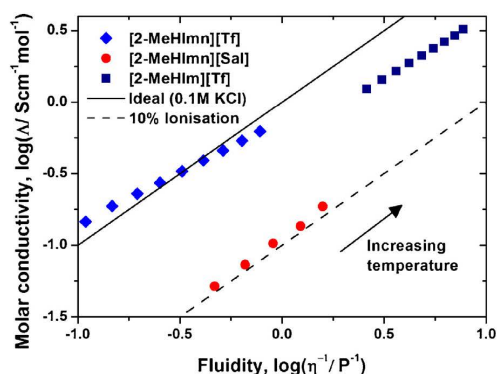


Fig. 7. Walden plot of [2-MeHlmn]⁺ and [2-MeHlm]⁺ ILs.

diffusion would allow [34]. A schematic of such a mechanism is shown in Fig. 8.

When comparing the two imidazolium samples, it can be observed that, while [2-MeHlmn][Sal] has a similar fluidity to the triflate IL, the conductivity is significantly lower, such that [2-MeHlmn][Sal] sits in the region of the “10% ionisation” line. While triflate only weakly bonds to cations, the salicylate anion can participate in multiple hydrogen bonding modes with the cation, producing ion pairs and clusters. Such ion pairing lessens the availability of the ions to participate in transport mechanisms, hence resulting in a lower conductivity. Lack of complete proton transfer [29] is also a potential issue in this case since the ΔpK_a is < 8 . However, we have shown previously [35,36] that when the IL has additional H-bonding functionality as in this case, proton transfer is typically more “aqueous-like” such that a ΔpK_a of this magnitude is more than sufficient to ensure strong proton transfer.

It can be noted that the [2-MeHlmn][Tf] data does not have the same slope as the ideal KCl line, but veers away from it at high temperatures. In such situations the fractional Walden rule can be used to describe the data, with the introduction of an exponential component, γ . This parameter is a value between zero and unity that represents the slope of any data set in the $\log \Lambda$ vs $\log 1/\eta$ plot [32].

$$\Lambda \eta^\gamma = C' \quad (4)$$

Experimentally, γ is typically found to be 0.8 ± 0.1 [37]. [2-MeHlm][Tf] was found to have a γ value of 0.873 ± 0.004 . [2-MeHlmn][Tf] has a noticeably shallower slope, with $\gamma = 0.729 \pm 0.005$. This is consistent with the influence of additional proton conduction effects such as the Grotthuss mechanism. The contribution of proton hopping is greatest at lower temperatures, when diffusion is limited, however the effect is less noticeable as the temperature is increased and the material becomes more mobile [32,38]. As such, it can be observed that [2-MeHlmn][Tf] actually drops below the ideal KCl line and begins to approach the [2-MeHlm][Tf] line as the temperature rises. In comparison, [2-MeHlmn][Sal] has a larger γ value, of 1.04 ± 0.03 . Potentially, with increasing temperature, the effects causing the low molar conductivity of the IL (ion pairing or incomplete proton transfer) are reduced; for example one might expect the entropy change in the ion pairing equilibrium to drive a shift towards less ion pairing at higher temperatures.

Fig. 9 shows a comparison of the electrochemical windows of the triflate ILs in acetonitrile. While the compounds both begin to oxidise just before 2 V vs SCE, presumably due to the oxidation of the triflate ion, [2-MeHlmn][Tf] is the more reductively stable, resulting in a larger electrochemical window of ~ 2.4 V. The reductive reaction in both cases is expected to be proton reduction. This gain in reductive stability may be due to the greater ΔpK_a of the imidazolium IL in comparison to [2-MeHlm][Tf], the proton site on the 2-MeHlmn being of lower energy (more stable). The electrochemical windows of the carboxylate salts vary depending on the stability of the anion; ~ 1.3 V for [2-MeHlm][Ac], increasing to ~ 3 V for [2-MeHlmn][4-OHCin] where the carboxylate is stabilised by the aromatic ring structure.

3.3. Corrosion Inhibiting Properties of Imidazolium Salts

3.3.1. Short term electrochemical measurements

Potentiodynamic polarisation (PP) experiments were undertaken to determine the corrosion inhibiting ability of the benzoate-derived compounds. Measurements were carried out on mild steel working electrodes (AS1020, 0.26 w% C), in a standard three-electrode cell with a SCE reference and titanium mesh counter

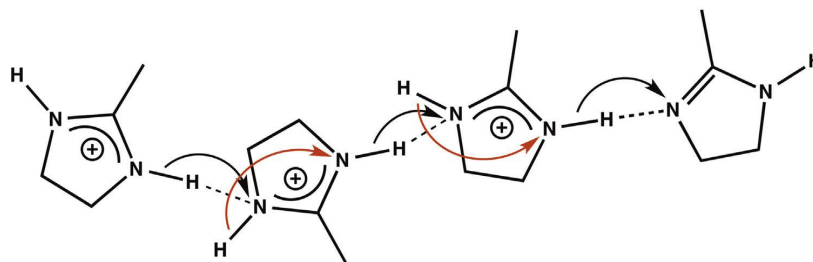


Fig. 8. Possible Grothuss-type mechanism for protonic charge transfer between [2-MeHImn]⁺ cations to an unprotonated base, including transport of protons across the imidazolinium face.

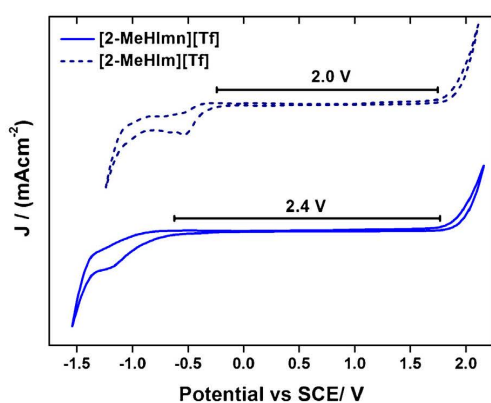


Fig. 9. Electrochemical windows of [2-MeHImn][Tf] and [2-MeHIm][Tf] measured as 0.25 M solutions in acetonitrile. The [2-MeHImn]⁺ cation shows improved reductive stability.

electrode. The electrolyte consisted of the designated inhibitor dissolved in 0.01 M NaCl. The resulting Tafel curves are shown in Fig. 10. These curves were fitted to calculate the corrosion potential (E_{corr}) and the corrosion current density (i_{corr}), a parameter that is indicative of the overall rate of corrosion (Table 3). The percentage inhibition efficiency of each sample was calculated based on improvement in the lowering of i_{corr} relative to the control as shown in Eq. (5)

$$\% \text{eff} = \frac{i_{\text{corr}}(\text{control}) - i_{\text{corr}}(\text{inhibitor})}{i_{\text{corr}}(\text{control})} \quad (5)$$

In addition to the new IL compounds investigated, for comparison we have examined the corrosion inhibiting properties of the individual ionic species of the IL by using the same concentration of the sodium salt of the anion (in the case of 4-hydroxycinnamate) or the bromide salt of the imidazolinium cation.

Table 3
Summary of average E_{corr} and i_{corr} and percentage efficiency values.

Solution	$E_{\text{corr}}/\text{mV}$	$i_{\text{corr}}/\mu\text{Acm}^{-2}$	% Efficiency
0.01 M NaCl (control)	-584 ± 9	2.4 ± 0.2	–
4 mM [2-MeHImn][Sal]	-499 ± 11	2.13 ± 0.02	13
4 mM [2-MeHImn][Gen]	-528 ± 3	1.2 ± 0.1	49
4 mM [2-MeHImn][4-OHCin]	-289 ± 9	0.4 ± 0.2	84
4 mM Na[4-OHCin]	-401 ± 12	1.3 ± 0.1	47
4 mM [2-MeHImn][Br]	-430 ± 10	2.5 ± 0.2	–4

Table 3 compares the three benzoate salts at a concentration of 4 mM (= 889–993 ppm). It can be seen that each of the salts has a favourable impact upon the corrosion behaviour, with the drop in i_{corr} indicating that the rate of corrosion was reduced relative to the control. However, the 4-hydroxycinnamate based imidazolinium compound has the most dramatic effect, decreasing the i_{corr} by a factor of 6 compared with the aqueous NaCl control and shifting the E_{corr} value by 300 mV to more anodic potentials. Cinnamate compounds have been previously shown to act as good inhibitors and show synergy with respect to inhibition efficiency when combined with rare earth metals [39] and even the sodium salt alone shows some degree of inhibition. Thus the greater inhibiting effect of [2-MeHImn][4-OHCin] was not completely unexpected. On the other hand, the synergy observed for this compound, when the 4-hydroxycinnamate is combined with the imidazolinium cation, is quite dramatic; the imidazolinium cation alone shows no inhibition at the same concentrations (Fig. S4).

The shift of the average E_{corr} of [2-MeHImn][4-OHCin] to more anodic potentials, and the decrease in the anodic currents relative to the control, indicate that the salt acts as a powerful anodic inhibitor. Such compounds reduce the anodic metal dissolution reaction by interacting with active sites, for example where the native oxide film has been breached by an aggressive solution, forming a barrier to further attack from Cl^- . A possible mechanism for this could involve reaction of the carboxylate group with iron on the surface of the steel. Due to the relatively high pK_a of the imidazoline, the cation may remain associated with the anion even in dilute solutions. This could provide extra blocking of the surface,

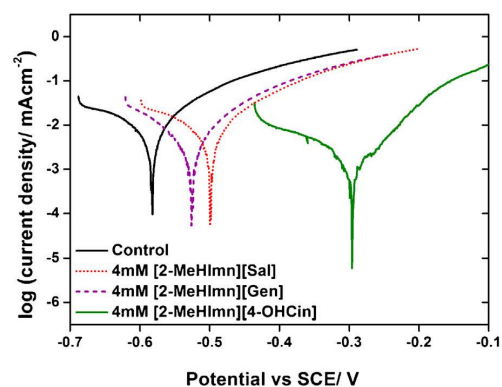


Fig. 10. Tafel plots of [2-MeHImn] inhibitors at 4 mM concentration in a 0.01 M NaCl aqueous solution compared with a control of 0.01 M NaCl solution in the absence of the inhibitor.

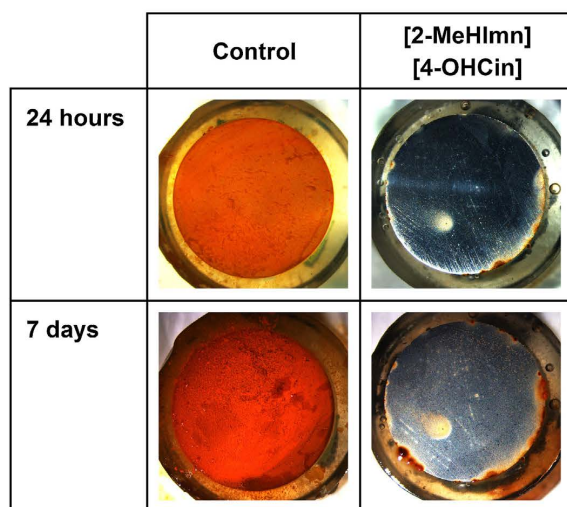


Fig. 11. Optical images obtained after immersion of mild steel coupons in 4 mM [2-MeHImn][4-OHCin]. The complete set of images is reproduced, in colour, in Fig. S5.

resulting in the observed synergy in comparison to [Na][4-OHCin]. Further surface characterisation is being undertaken to confirm this hypothesis.

In contrast, the cathodic currents do not appear to vary greatly from those of the controls, suggesting that this compound does not influence the cathodic reaction, which at the pHs involved will be oxygen reduction. Further improvements in the corrosion inhibition may be possible by introduction of alkyl or polar substituents to the imidazolium ring.

3.3.2. Longer term exposure in aggressive chloride contaminated aqueous solutions

The rate of corrosion was also assessed visually upon longer term immersion as the polarisation studies are only an indication of corrosion susceptibility at relatively short times. Mild steel coupons were immersed in 4 mM solutions of [2-MeHImn][4-OHCin], [2-MeHImn][Br] and [Na][4-OHCin] in 0.01 M NaCl and observed under a microscope after 24 hours and again after seven days (Fig. 11). After 24 h there is a significant difference between the [2-MeHImn][4-OHCin] and the control coupons. While the control has undergone general corrosion across the entire steel surface and is covered in corrosion product, the coupon immersed in [2-MeHImn][4-OHCin] displays only localised corrosion at a small number of sites, in particular at the epoxy interface. While both the [2-MeHImn][Br] and [Na][4-OHCin] solutions have visually decreased the extent of corrosion relative to the control (Fig. S5), there is significantly more corrosion product than observed for [2-MeHImn][4-OHCin] consistent with the polarisation data discussed above. Furthermore, after seven days the [2-MeHImn][4-OHCin] sample still exhibits only limited corrosion, indicating the long term stability of the inhibiting film that forms in the presence of this salt. Future work will use advanced surface characterisation techniques to investigate the nature of this inhibiting surface film to understand how the synergy arises for this compound. New compounds having a dual active role combining antimicrobial and corrosion inhibition based on imidazolium cations are currently being investigated and will be described in a future paper.

4. Conclusions

A series of ILs and organic salts with the [2-MeHImn]⁺ cation were synthesised via a facile one-pot reaction. Depending upon the nature of the anion in the salts, these materials were found to have interesting physical properties such as facile ion transport, as well as demonstrating synergistic corrosion inhibition on mild steel. The imidazolium cation shows promise as the basis of a new class of ILs. However, more work is required, both to better understand the potential scope of their properties and to broaden the range of materials in this family of salts.

Acknowledgements

A. Chong acknowledges her Australian Postgraduate Award and Professors MacFarlane and Forsyth are grateful to the Australian Research Council for support via the Australian Laureate Fellowship program.

Appendix A. Supplementary data

Supplementary data associated with this article can be found, in the online version, at <http://dx.doi.org/10.1016/j.electacta.2015.01.180>.

References

- [1] P. Wasserscheid, T. Welton, *Ionic Liquids in Synthesis*, Wiley-VCH, Weinheim, 2008.
- [2] F. Endres, D. MacFarlane, A. Abbott, *Electrodeposition from Ionic liquids*, Wiley-VCH, Weinheim, 2008.
- [3] R. Rogers, K.R. Seddon, *Ionic Liquids: Industrial Applications for Green Chemistry ACS Symposium Series 818*, American Chemical Society, Washington, DC, 2002.
- [4] G. Schmitt, M. Schütze, G.F. Hays, W. Burns, E.-H. Han, A. Pourbaix, G. Jacobson, (Eds.), *The World Corrosion Organization*, 2009.
- [5] S. Wilbur, H. Abadin, M. Fay, D. Yu, B. Tencza, L. Ingerman, J. Klotzbach, S. James, (Eds.), *US Department of Public Health and Human Services*, Atlanta, 2012.
- [6] P. Huang, J.-A. Latham, D.R. MacFarlane, P.C. Howlett, M. Forsyth, *Electrochim. Acta* 110 (2013) 501–510.
- [7] P.C. Howlett, T. Khoo, G. Mooketsi, J. Efthimiadis, M. MacFarlane, D.R. Forsyth, *Electrochim. Acta* 55 (2010) 2377–2383.
- [8] J. Efthimiadis, W.C. Neil, A. Bunter, P.C. Howlett, B.R. Hinton, D.R. MacFarlane, M. Forsyth, *ACS Appl. Mater. Interfaces* 2 (2010) 1317–1323.
- [9] S.K. Shukla, L.C. Murulana, E.E. Ebenso, *Int. J. Electrochem. Sci.* 6 (2011) 4286–4295.
- [10] M. Gong, C. Jiang, X. Zheng, X. Zeng, X. Lin, *Adv. Mater. Res.* 476–478 (2012) 1434–1440.
- [11] N.V. Likhanova, O. Olivares-Xometl, D. Guzman-Lucero, M.A. Dominguez-Aguilar, N. Nava, M. Corrales-Luna, M.C. Mendoza, *Int. J. Electrochem. Sci.* 6 (2011) 4514–4536.
- [12] M.A.M. Ibrahim, M. Messali, Z. Moussa, A.Y. Alzahrani, S.N. Alamry, B. Hammouti, *Port. Electrochim. Acta* 29 (2011) 375–389.
- [13] A.S. Ben, *Int. J. Electrochem. Sci.* 8 (2013) 10788–10804.
- [14] J. Ding, D.W. Armstrong, *Chirality* 17 (2005) 281–292.
- [15] M.J. Earle, P.B. McCormac, K.R. Seddon, *Green Chem.* 1 (1999) 23–25.
- [16] T. Welton, *Chem. Rev.* 99 (1999) 2071–2084.
- [17] W.L. Hough, M. Smiglak, H. Rodriguez, R.P. Swatloski, S.K. Spear, D.T. Daly, J. Pernak, J.E. Grisel, R.D. Carliss, M.D. Soutullo, J.J.H. Davis, R.D. Rogers, *New J. Chem.* 31 (2007) 1429–1436.
- [18] M. Seter, M.J. Thomson, A. Chong, D.R. MacFarlane, M. Forsyth, *Aust. J. Chem.* 66 (2013) 921–929.
- [19] M. Seter, M.J. Thomson, J. Stoimenovski, D.R. MacFarlane, M. Forsyth, *Chem. Commun.* 48 (2012) 5983–5985.
- [20] S. Shi, P. Yi, C. Cao, X. Wang, J. Su, J. Liu, *CIESC Journal* 56 (2005) 1112–1119.
- [21] D. Bajpai, V.K. Tyagi, *J. Oleo Sci.* 55 (2006) 319–329.
- [22] I. Aiad, A.A. Hafiz, M.Y. El-Awady, A.O. Habib, *J. Surfactants Deterg.* 13 (2010) 247–254.
- [23] A. Cornia, F. Felluga, V. Frenna, F. Ghelfi, A.F. Parsons, M. Pattarozzi, F. Roncaglia, D. Spinelli, *Tetrahedron* 68 (2012) 5863–5881.
- [24] D.R. MacFarlane, P. Meakin, N. Amini, M. Forsyth, *J. Phys.: Condens. Matter* 13 (2001) 8257.
- [25] M. Yoshizawa-Fujita, K. Fujita, M. Forsyth, D.R. MacFarlane, *Electrochem. Commun.* 9 (2007) 1202–1205.
- [26] B. Lenarcik, P. Ojczenasz, *J. Heterocycl. Chem.* 39 (2002) 287–290.
- [27] C.A. Angell, *Chem. Rev.* 102 (2002) 2627–2650.
- [28] M.S. Elsaesser, I. Kohl, E. Mayer, T. Loerting, *J. Phys. Chem. B* 111 (2007) 8038–8044.

- [29] M. Yoshizawa, W. Xu, C.A. Angell, *J. Am. Chem. Soc.* 125 (2003) 15411–15419.
- [30] M. Kar, B. Winther-Jensen, M. Forsyth, D.R. MacFarlane, *Phys. Chem. Chem. Phys.* 15 (2013) 7191–7197.
- [31] D.R. MacFarlane, M. Forsyth, E.I. Izgorodina, A.P. Abbott, K. Annat, G. Fraser, *Phys. Chem. Chem. Phys.* 11 (2009) 4962–4967.
- [32] W. Xu, E.I. Cooper, C.A. Angell, *J. Phys. Chem.* 107 (2003) 6170–6178.
- [33] C. Schreiner, S. Zugmann, R. Hartl, H.J. Gores, *J. Chem. Eng. Data* 55 (2009) 1784–1788.
- [34] C.J.T. Grotthuss, *Ann. Chim. - Sci. Mat.* 58 (1806) 54–73.
- [35] J.I. Stoimenovski, I. Ekaterina, D.R. MacFarlane, *Phys. Chem. Chem. Phys.* 12 (2010) 10341–10347.
- [36] J. Stoimenovski, P.M. Dean, E.I. Izgorodina, D.R. MacFarlane, *Faraday Discuss.* 154 (2012) .
- [37] S.A. Mohd Noor, P.C. Howlett, D.R. MacFarlane, M. Forsyth, *Electrochim. Acta* 114 (2013) 766–771.
- [38] M. McLin, C.A. Angell, *J. Phys. Chem.* 92 (1988) 2083–2086.
- [39] F. Blin, S.G. Leary, G.B. Deacon, P.C. Junk, M. Forsyth, *Corros. Sci.* 48 (2006) 404–419.

2.2 Supplementary Information

Synthesis

Synthesis of 2-methylimidazolinium formate

Triethylorthoacetate (10.5 mL, 53 mmol), formic acid (2.0 mL, 53 mmol) and ethylenediamine (3.4 mL, 50 mmol) were combined as described for [2-MeHImn][Ac] to yield a pale yellow, hygroscopic solid (6.0 g, 92 %). ^1H NMR (400 MHz, DMSO-*d*6) δ (ppm): 2.07 (s, 3H, CH₃), 3.73 (unresolved d, 4H, 2x CH₂). ^{13}C NMR (400 MHz, DMSO-*d*6) δ (ppm): 12.72 (CH₃), 45.11 (2x CH₂), 168.57 (C=O), 169.04 (N-C=N). Mass spectrum: ES⁺ m/z 85.1 [2-MeHImn]⁺; ES⁻ m/z 44.9 [For]⁻.

Synthesis of 2-methylimidazolinium salicylate

Triethylorthoacetate (5.9 mL, 32 mmol), salicylic acid (4.42 g, 32 mmol) and ethylenediamine (2.0 mL, 30 mmol) were combined in a 2:1 acetonitrile/methanol solution as described for [2-MeHImn][Ac] to yield a pale pink solid (6.6 g 99 %). ^1H NMR (400 MHz, DMSO-*d*6) δ (ppm): 2.18 (s, 3H, CH₃), 3.80 (unresolved d, 4H, 2x CH₂), 6.63 – 6.69 (m, 2H, 2x aromatic CH), 7.17 – 7.22 (m, 1H, aromatic CH), 7.68 – 7.71 (dd, J = 7.6, 2.0, 1H, aromatic CH), (s (broad), 2H, 2x NH). ^{13}C NMR (400 MHz, DMSO-*d*6) δ (ppm): 11.99 (CH₃), 45.22 (2x CH₂), 115.94 (aromatic), 116.55 (aromatic), 119.33 (4° aromatic), 130.01 (aromatic), 132.00 (aromatic), 162.37 (4° aromatic), 168.03 (N-C=N), 171.98 (C=O). Mass spectrum: ES⁺ m/z 85.1 [2-MeHImn]⁺; ES⁻ m/z 93.0 [C₆H₄OH]⁻, 137.0 [Sal]⁻.

Synthesis of 2-methylimidazolinium gentisate

Triethylorthoacetate (5.9 mL, 32 mmol), gentisic acid (4.93 g, 32 mmol) and ethylenediamine (2.0 mL, 30 mmol) were combined in a 2:1 acetonitrile/methanol solution as described for [2-MeHImn][Ac] to yield a pale brown solid (7.1 g, 99%). ^1H NMR (400 MHz, DMSO-*d*6) δ (ppm): 1.31 (s, 3H, CH₃), 3.00 (s, 4H, 2x CH₂), 5.96 – 5.98 (d, J = 8.8, 1H, aromatic CH), 6.10 – 6.13 (dd, J = 8.8, 3.1, 1H, aromatic CH), 6.42 – 6.43 (d, J = 3.1, 1H, aromatic CH). ^{13}C NMR (400 MHz, DMSO-*d*6) δ (ppm): 12.76 (CH₃), 45.16 (2x CH₂), 116.56 (aromatic), 117.40 (aromatic), 121.27b(aromatic), 154.97 (4° aromatic), 169.08 (N-C=N), 173.35 (C=O). Mass spectrum: ES⁺ m/z 85.1 [2-MeHImn]⁺; ES⁻ m/z 109.0 [C₆H₃(OH)₂]⁻, 153.0 [Sal]⁻.

Synthesis of 2-methylimidazolium 4-hydroxycinnamate

Triethylorthoacetate (5.9 mL, 32 mmol), 4-hydroxycinnamic acid (4.93 g, 32 mmol) and ethylenediamine (2.0 mL, 30 mmol) were combined in a 1:1 acetonitrile/methanol solution as described for [2-MeHImn][Ac] to yield a pale brown solid. (7.4 g, 100 %). ¹H NMR (400 MHz, DMSO-*d*6) δ (ppm): 2.03 (s, 3H, CH₃), 3.63 (unresolved d, 4H, 2x CH₂), 6.20 – 6.24 (d, *J* = 16.0, 1H, CH=CH), 6.75 – 6.77 (d, *J* = 8.6, 2H, 2x aromatic CH), 7.20 – 7.24 (d, *J* = 16.0, 1H, CH=CH), 7.33 – 7.35 (d, *J* = 8.6, 2H, 2x aromatic CH). ¹³C NMR (400 MHz, DMSO-*d*6) δ (ppm): 12.91 (CH₃), 46.09 (2x CH₂), 115.94 (2x aromatic), 121.76 (C=C), 126.24 (4° aromatic), 129.00 (2x aromatic), 139.27 (C=C), 158.96 (4° aromatic), 166.46 (N-C=N), 169.98 (C=O). Mass spectrum: ES⁺ *m/z* 85.1 [2-MeHImn]⁺; ES⁻ *m/z* 119.0 [C₆H₄CCHOH]⁻, 163.0 [4-OHCin]⁻.

Synthesis of 2-methylimidazolium triflate

Triethylorthoacetate (4.0 mL, 22 mmol), triflic acid (3.3 g, 22 mmol) and ethylenediamine (1.3 mL, 20 mmol) were combined in acetonitrile as described for [2-MeHImn][Ac] to yield an amorphous, hygroscopic solid (4.5 g, 95 %). ¹H NMR (400 MHz, DMSO-*d*6) δ (ppm): 2.14 (s, 3H, CH₃), 3.79 (unresolved d, 4H, 2x CH₂). ¹³C NMR (400 MHz, DMSO-*d*6) δ (ppm): 12.09 (CH₃), 44.23 (2x CH₂), 168.10 (N-C=N). ¹⁹F NMR (400 MHz, DMSO-*d*6) δ (ppm): 77.76. Mass spectrum: ES⁺ *m/z* 85.1 [2-MeHImn]⁺, 319.1 2[2-MeHImn]⁺[TfO]⁻; ES⁻ *m/z* 148.9 [TfO]⁻, 383.0 [2-MeHImn]⁺2[TfO]⁻.

Synthesis of 2-methylimidazolium bromide

Triethylorthoacetate (7.9 mL, 43 mmol), Hydrobromic acid (47% in H₂O, 4.9 mL, 43 mmol) and ethylenediamine (1.3 mL, 20 mmol) were combined in acetonitrile as described for [2-MeHImn][Ac] to yield a pale yellow precipitate (6.5 g, 98 %). The product was further purified by aqueous extraction from DCM. ¹H NMR (400 MHz, DMSO-*d*6) δ (ppm): 1.84 (s, 3H, CH₃), 2.82 (s, 4H, 2x CH₂). ¹³C NMR (400 MHz, DMSO-*d*6) δ (ppm): 22.77 (CH₃), 36.81 (2x CH₂), 174.36 (N-C=N) Mass spectrum: ES⁺ *m/z* 85.0 [2-MeHImn]⁺; ES⁻ *m/z* 78.9 [Br]⁻.

Synthesis of 2-methylimidazolium salicylate

A solution of salicylic acid (4.4g, 32 mmol) dissolved in methanol was added slowly to 2-methylimidazole (2.5g, 30 mmol, dissolved in methanol). The resulting orange solution was stirred at room temperature for 2h. The solvent was removed via rotary evaporation and the product dried under high vacuum at 60°C to yield a pale pink solid (6.5 g, 98 %). ¹H NMR (400 MHz, DMSO-*d*6) δ (ppm): 2.07 (s, 3H, CH₃), 3.73

(unresolved d, 4H, 2x CH₂). ¹³C NMR (400 MHz, DMSO-*d*₆) δ (ppm): 11.68 (CH₃), 48.73 (2x CH), 116.24 (aromatic), 117.08 (aromatic), 119.23 (4° aromatic), 130.21 (aromatic), 132.66 (aromatic), 144.15 (N-C=N), 162.32 (4° aromatic), 172.11 (C=O). Mass spectrum: ES⁺ m/z 83.1 [2-Meimidazolium]⁺; ES⁻ m/z 93.0 [C₆H₅OH]⁻, 137.0 [Sal]⁻.

Synthesis of sodium 4-hydroxycinnamate

A solution of NaOH (0.73 g, 18 mmol) in methanol was added slowly to 4-hydrocinnamic acid (3.0 g, 18 mmol, dissolved in methanol). The mixture was stirred at room temperature for 2h and the solvent removed to yield an off-white solid (3.4 g, 100 %). ¹H NMR (400 MHz, DMSO-*d*₆) δ (ppm): 6.14 – 6.18 (d, *J* = 16.0, 1H, CH=CH) 6.71 – 6.73 (d, *J* = 8.4, 2H, 2x aromatic CH), 7.00 – 7.03 (d, *J* = 16.0, 1H, CH=CH), 7.26 – 7.28 (d, *J* = 8.4, 2H, 2x aromatic CH). ¹³C NMR (400 MHz, DMSO-*d*₆) δ (ppm): 115.65 (2x aromatic), 121.38 (C=C), 128.43 (2x aromatic), 136.13 (C=C), 158.05 (4° aromatic). Mass spectrum: ES⁺ m/z 23.0 [Na]⁺, 209.1 2[Na]⁺[4-OHCin]⁻; ES⁻ m/z 119.2 [C₆H₄CCHOH]⁻, 163.2 [4-OHCin]⁻.

Physical Properties

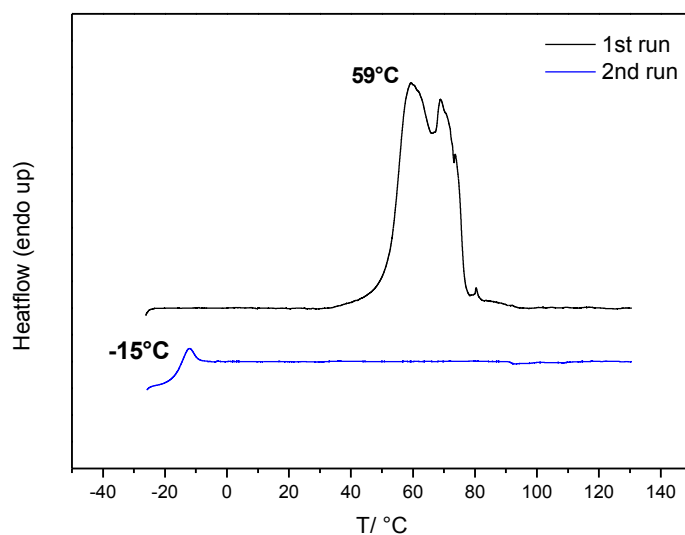


Figure S1. DSC traces of [2-MeHImn][Sal] showing initial melt, followed by a glass transition.

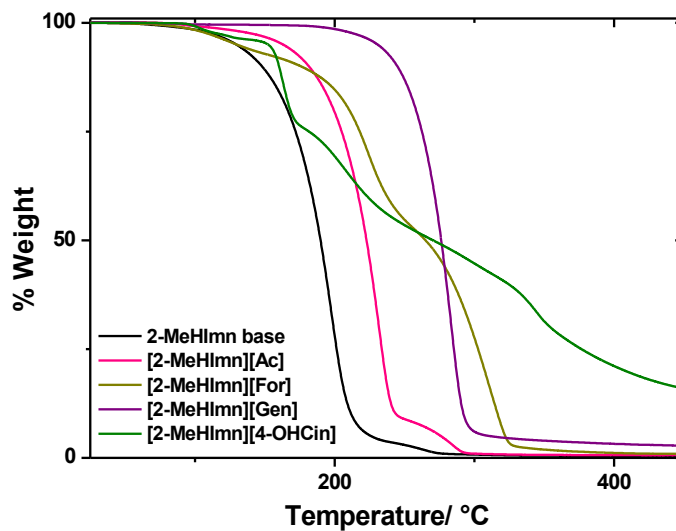


Figure S2. TGA of [2-MeHlmn]⁺ carboxylate salts.

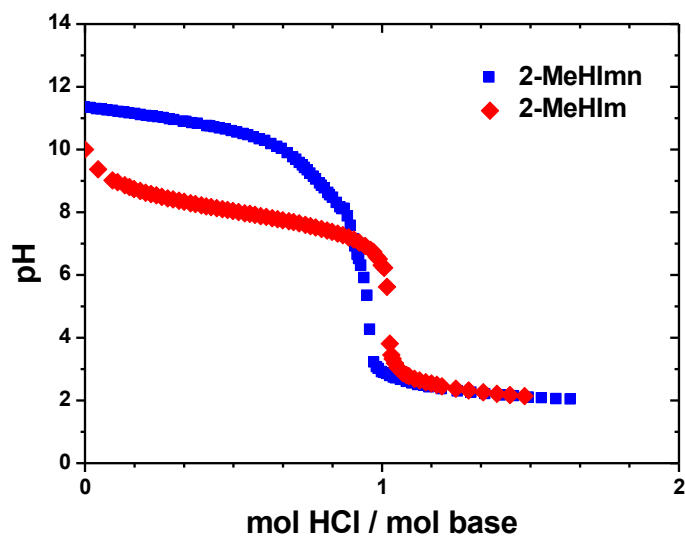


Figure S3. Titration of starting bases with 0.1 M HCl.

Comparison to Component Ions

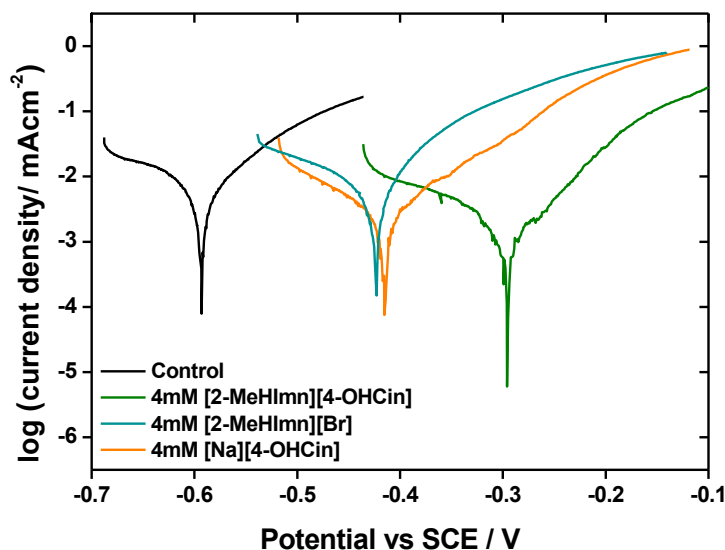


Figure S4. Comparison to individual ion components for [2-MeHImn][4-OHCin].

Figure S4 shows a comparison of [2-MeHImn][4-OHCin] with the individual component ions; the bromide salt of [2-MeHImn]⁺ and the sodium salt of the cinnamate. Comparing the two 4-hydroxycinnamate salts, it can be seen that the sodium salt has a lessened inhibitory effect, with both a higher i_{corr} and less pronounced shift in E_{corr} . This suggests that the observed behaviour of the imidazolium salt is not only due to the presence of the cinnamate anion but also the cation. However, despite a sizable shift in E_{corr} , the [2-MeHImn]⁺ cation on its own did not show any significant change in i_{corr} from the control. Thus this demonstrates a synergy in the dual-active IL, as its corrosion inhibiting performance is greater than the sum of the two active components.



Figure S5. Optical images of steel coupons immersed in 4 mM solutions of component ion salts.

3 SYNERGISTIC CORROSION INHIBITION BY IMIDAZOLINIUM CINNAMATE SALTS

Fostering synergy between inhibitor species is a key motivator for developing combined salts such as 2-methylimidazolinium 4-hydroxycinnamate, [2-MeHImn][4-OHCin]. It is important to understand the nature of the synergistic relationship between the ions and the conditions within which they operate. Electrochemical and surface analysis techniques have been employed to investigate the effects of conditions such as concentration and pH on the inhibitive action of [2-MeHImn][4-OHCin].

In addition to electrochemical determination of the corrosion rate, long-term immersion testing is a key diagnostic tool. By allowing the system to corrode naturally over a period of time, we can observe the longer-term inhibitor behaviour and gain insights into the mechanisms of corrosion that are not immediately obvious in the electrochemical tests. In this thesis, the primary means of analysing the surface after an immersion test were scanning electron microscopy (SEM) and optical profilometry.

SEM is a simple way to get a detailed view of the morphology of a surface. An electron beam is focused on the sample, and the secondary electrons emitted from collisions between the beam electrons and sample atoms are collected. The detected electrons can be spatially resolved to give a highly magnified image of the surface topography, with sub-nanometre resolution. In corrosion studies, this technique can be used to gain an understanding of how corrosion deposits or protective films form on the surface and, after the corrosion product is selectively etched off, where the underlying metal has been attacked. Based on the element-specific nature of the interactions between the electrons and sample atoms, SEM can also be used to map sample composition.

3D optical profilometry is another non-destructive surface analysis technique. Making use of the wave superposition principle, optical profilometers detect the

interference pattern between a light beam split between a reference mirror and the sample to accurately determine the height profile. This is a highly useful instrument for analysing pits formed on an immersion sample. Based on the 2D height profile it is possible to determine the number of pits formed and their dimensions, as well as information about the overall surface roughness that is a good indication of the extent of general corrosion.

Infrared (IR) spectroscopy was used to characterise the surface film formed on the mild steel during exposure to the inhibitor. Most intramolecular vibrations, such as the stretching of a C=O bond, occur at frequencies within the IR range of the electromagnetic spectrum. By collecting an absorption spectrum, it is possible to see which wavelengths are absorbed by a sample and in some cases, to assign these to specific functional group vibrations. As the vibrational frequencies are sensitive to the surrounding molecule, IR spectroscopy can provide a ‘fingerprint’ of a compound. This study used attenuated total reflectance (ATR) IR spectroscopy, a technique that allows direct measurement of a sample with no further preparation. Spectra of the coupon surfaces following immersion were collected and compared to a spectrum of the inhibitor compound to identify the species present and any changes in the bonding environments within the compounds.

Used in combination, SEM, optical profilometry and IR spectroscopy techniques can provide valuable information about the corrosion processes taking place at the metal surface, and highlight the role of the inhibitor.

It was also of interest to investigate the scope of the inhibitor’s synergy; would another cyclic amine, or a different imidazolinium cation produce the same effect as [2-MeHImn]⁺ when paired with [4-OHCin]⁻? With this in mind, corrosion tests were carried out in the presence of the analogous imidazolium salt, 2-methylimidazolium 4-hydroxycinnamate ([2-MeHIm][4-OHCin]). In addition, a selection of modified 2-methylimidazolium cations were synthesised and the methylated salt, [triMeImn][4-OHCin], was used as an inhibitor.

This chapter is presented as follows. Section 3.1 is a paper entitled “Synergistic Corrosion Inhibition of Mild Steel in Aqueous Chloride Solutions by an Imidazolinium Carboxylate Salt” that was published in ACS Sustainable Chemistry and Engineering in 2016. It explores the behaviour of [2-MeHImn][4-OHCin] as an inhibitor under varied pH conditions, and includes an IR study of the adsorbed surface species. Section 3.2 expands upon the work in the paper, to probe the synergistic relationship specific to the imidazolinium 4-hydroxycinnamate salts. Following this, Section 3.3 discusses the synthesis of novel alkylated imidazolinium salts derived from [2-MeHImn]⁺.

3.1 Synergistic Corrosion Inhibition of Mild Steel in Aqueous Chloride Solutions by an Imidazolinium Carboxylate Salt

ACS
Sustainable
Chemistry & Engineering

Research Article

pubs.acs.org/journal/ascecg

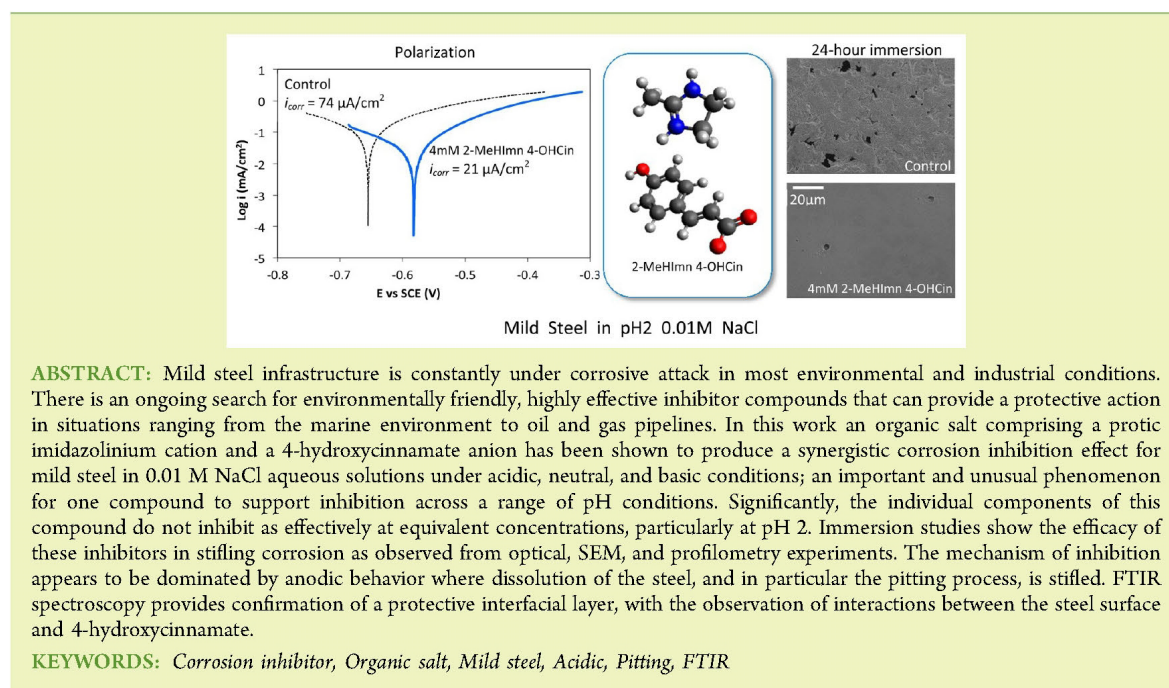
Synergistic Corrosion Inhibition of Mild Steel in Aqueous Chloride Solutions by an Imidazolinium Carboxylate Salt

Alison L. Chong,[†] James I. Mardel,[‡] Douglas R. MacFarlane,[†] Maria Forsyth,[§] and Anthony E. Somers^{*,§}

[†]School of Chemistry, Monash University, Box 23, Clayton, Victoria 3800, Australia

[‡]CSIRO Manufacturing, Private Bag 10, Clayton, Victoria 3169, Australia

[§]Institute for Frontier Materials, Deakin University, Locked Bag 20000, Geelong, Victoria 3220, Australia



INTRODUCTION

Due to its relatively high strength, low cost, and widespread availability, large infrastructure items such as storage tanks and pipelines use mild steel extensively.¹ There is a desire to maximize the lifetimes of such expensive items, with one of the main causes of degradation being corrosion, particularly in aggressive media such as acidic environments. A variety of approaches are used to minimize corrosion, with inhibitors being one of the cheapest methods; corrosion inhibitors can be incorporated into paint coatings or added to water tanks, pipeline streams, etc. Generally, inhibitors form passive or almost impermeable films on the metal surface to reduce the rate of corrosion.^{1,2}

For decades chromate based inhibitors have been known as the most effective chemical method for controlling corrosion in a variety of metallic systems, repressing both the anodic and cathodic reactions.² The extreme toxic nature of hexavalent chromium, however, has resulted in the need for safer alternatives.^{2–4} Other inorganic compounds containing metal

ions, such as zinc, magnesium, and rare earth metals, have proven effective as corrosion inhibitors. These metallic ions generally inhibit by reacting with the hydroxides produced at the cathodes to form an almost impermeable, adherent coating at these sites.^{5–7} At relatively high concentrations, naturally occurring organic compounds based on carboxylates, such as salicylate and cinnamate, have also been shown to be efficient corrosion inhibitors. These compounds adsorb or react at the surface to form a barrier, often at the anodic sites.^{9,10} In an effort to replicate the ability of chromates to suppress both the anodic and cathodic reactions, various combinations of these inorganic and organic compounds have also been extensively investigated in the past decade in the form of mixtures of components as well as integrated compounds such as rare earth carboxylates.^{5,9,11–14} In many cases such combinations have

Received: December 16, 2015

Revised: January 9, 2016

Published: January 12, 2016

been shown to produce a synergistic effect. This synergy is proposed to be due to these compounds not only having both components available in solution, but specifically the presence of particular complexation and speciation (ie. not just the individual dissolved components) at the sites of corrosion that leads to a unique protective film.^{5,9,15}

Such synergy, however, is not always utilized in commercial situations, with many organic salts containing one active ion and a simple counterion such as a halide or sodium. In such cases, the counterion is merely a spectator, with no active role. One subset of organic salts is ionic liquids (ILs) and these low-melting salts are increasingly being investigated for a wide range of applications, including corrosion inhibition. A limited range of traditional ILs, predominantly imidazolium based, have been investigated as potential corrosion inhibitors. With some exceptions,^{16–18} the IL has generally been chosen based on the properties of the cation, which has then been combined with a simple, inactive anion such as Br[−] or Cl[−].^{19–23} However, due to the vast array of possible combinations of cations and anions available (>10⁶) one of the proposed advantages of ILs is the ability to select both the anion and cation to have useful properties for a particular application. It is this feature of ILs and organic salts generally that could be exploited to find new organic inhibitors, ideally with synergistic effects; the aim would be to select biologically safe anions and cations to produce a salt that could approach the performance of chromates, while being environmentally benign.

We have recently reported on the synthesis of such a family of ILs and organic salts that target dual activity by incorporating both anions and cations that have shown prior evidence of effective inhibition.²⁴ These salts were based on the imidazolium cation—a relative of the fatty imidazolines that are commercially employed as corrosion inhibitors, commonly in oil pipelines^{25–27}—with carboxylate anions. Imidazolium salts are also used as fabric softeners and in other surfactant applications, and while some act as biocides, many are also readily biodegradable.^{25,28,29} The imidazolium structure is similar to imidazolium, the only difference being saturation of the C4–C5 double bond on the core ring of the imidazolium, as shown in Figure 1.

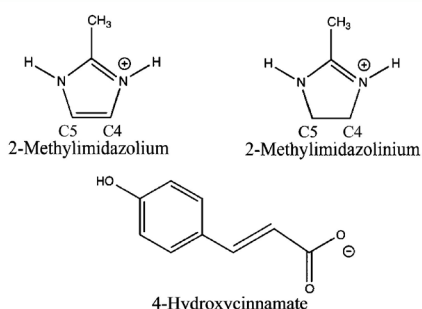


Figure 1. Chemical structures of imidazolium and imidazolium cations and the cinnamate anion.

Despite this similarity, imidazolium ionic liquids have not been extensively studied. The protic imidazolium cation was combined with a selection of biologically safe carboxylate anions that have previously shown promise as corrosion inhibitors.^{30,31} Preliminary corrosion studies conducted on mild steel in neutral conditions and a 0.01 M NaCl solution

found 2-methylimidazolium 4-hydroxycinnamate (2-Me-HImn 4-OHCin) was the most effective inhibitor, showing a strong anodic effect.

While corrosion inhibition in aggressive environments such as low pH is important, even in near neutral conditions the local pH on the surface of a metal component may vary from highly acidic (for example in the bottom of a pit or an occluded corrosion cell) to more basic (at the site of cathodic reactions just outside an occluded cell). Thus, it is important for a given compound to preferably have inhibition activity in a range of pH environments. In this work, we report the influence of pH on the corrosion inhibiting performance of the 2-Me-HImn 4-OHCin organic salt for AS1020 mild steel in chloride environments. The inhibition performance of the individual components of this salt, namely the salts 2-methylimidazolium bromide (2-Me-HImn Br) and sodium 4-hydroxycinnamate (Na 4-OHCin), were also investigated to establish the effect of each ion in isolation and to determine if there is a synergy in combining the imidazolium and cinnamate ions in a single compound. After immersion in the inhibited chloride containing solutions ATR-FTIR was used to probe the chemical nature of the surface film.

EXPERIMENTAL SECTION

Materials. Chong et al. reported the synthesis of 2-Me-HImn 4-OHCin, 2-Me-HImn Br, and Na 4-OHCin.²⁴ Mild steel AS1020 (composition: 0.26% C, 0.45% Mn, 0.14% Cr, 0.19% Si, 0.18% Al, 0.35% other, balance Fe) was used for electrochemical and immersion experiments. The mild steel was prepared to a P4000 grit finish, rinsed with distilled water, blown dry with nitrogen gas, and then placed in a vacuum desiccator for 30 min. Test solutions contained 0.01 M NaCl prepared with Milli-Q water, to which 1 or 4 mM of the organic salts were added. The pH of these “neutral” solutions ranged from 6.5 to 7.0. For the solutions at pH 2 and pH 8, hydrochloric acid or sodium hydroxide were added to these base solutions until the respective pH was achieved.

Electrochemical Testing. A Bio-Logic VMP3 multichannel potentiostat was used for the potentiodynamic polarization experiments. An open-to-air three-electrode cell was used, with a 1 cm diameter mild steel working electrode (WE), a counter electrode (CE) of titanium mesh, and a saturated calomel reference electrode; the latter was used with a Luggin capillary to minimize IR drops at the WE surface. The electrodes were placed in 150 mL of electrolyte and the open circuit voltage (OCV) was monitored for 30 min before performing the potentiodynamic polarization scan. The scan rate was 0.167 mV/s, and the scan range was from 150 mV below the OCV to 250 mV more positive than the OCV, with three measurements for each condition. The scans were performed in one sweep, meaning that there is the possibility that the cathodic polarization may cause local pH changes that could effect the results. This was minimized by limiting the cathodic polarization to 150 mV below the OCV. The corrosion current (i_{corr}) and corrosion potential (E_{corr}) were extracted from the Tafel plots. For the Tafel extrapolation, E_{corr} was initially identified by inspection and linear fits of the curve made between 25 and 50 mV either side of this E_{corr} . While the curves did not exhibit a linear region over one decade of current, as is usually required for an accurate Tafel extrapolation, they were somewhat linear over the 25–50 mV range either side of E_{corr} ; only slight adjustments from this 25–50 mV fitting range were required to ensure the fit matched the curve and the Tafel slopes intersected at the observed E_{corr} . From the i_{corr} values, inhibitor efficiencies (IE) were calculated according to eq 1:

$$\text{IE} \% = \frac{i_{\text{corr}}(\text{control}) - i_{\text{corr}}(\text{inhibitor})}{i_{\text{corr}}(\text{control})} \times 100 \quad (1)$$

Immersion Tests. Immersion tests were conducted over 24 h in 0.01 M NaCl control solution and in control solution plus 4 mM of

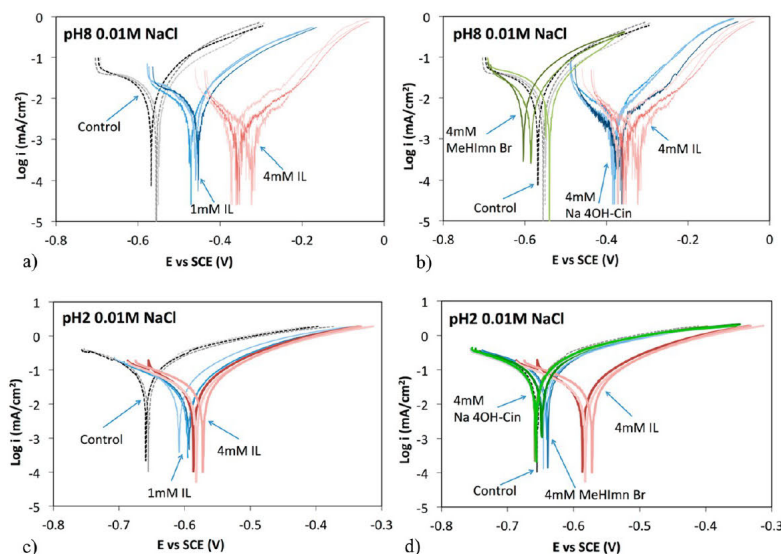


Figure 2. Tafel plots at (a) pH 8 showing effect of IL concentration; (b) pH 8 comparing IL with separate salts; (c) pH 2 showing effect of IL concentration; and (d) pH 2 comparing IL with separate salts. Replicate measurements using different electrodes are shown for each condition.

Table 1. Corrosion Current Density (i_{corr}), Corrosion Potential (E_{corr}), and Inhibitor Efficiency

	control 0.01 M NaCl	2-MeHImn 4-OHCin 1 mM	2-MeHImn 4-OHCin 4 mM	Na 4-OHCin 4 mM	2-MeHImn Br 4 mM
pH 8					
E_{corr} (mV)	-557 ± 11	-464 ± 12	-346 ± 27	-388 ± 3	-575 ± 33
i_{corr} ($\mu\text{A}/\text{cm}^2$)	10.1 ± 0.5	5.3 ± 0.3	1.5 ± 0.3	2.8 ± 1.3	10.0 ± 1.9
IE (%)		47	86	72	0
pH 2					
E_{corr} (mV)	-654 ± 2	-599 ± 8	-578 ± 9	-654 ± 4	-642 ± 3
i_{corr} ($\mu\text{A}/\text{cm}^2$)	74.4 ± 6.6	25.0 ± 4.9	20.6 ± 2.4	65.5 ± 4.6	64.7 ± 2.1
IE (%)		66	72	12	13
Neutral^a					
E_{corr} (mV)	-584 ± 9		-289 ± 9	-401 ± 12	-430 ± 10
i_{corr} ($\mu\text{A}/\text{cm}^2$)	2.4 ± 0.2		0.4 ± 0.2	1.3 ± 0.1	2.5 ± 0.2
IE (%)			84	47	-4

^aNeutral results taken from ref 24.

the appropriate salt to determine longer-term performance of the inhibitor compound. A 1 cm diameter mild steel sample mounted in epoxy was polished to P4000 grit, rinsed with distilled water, and blown dry with nitrogen. It was then placed in a vacuum desiccator for 30 min before being immersed in 60 mL of solution that was covered to minimize evaporation. After 24 h, the samples were photographed in solution, then removed from solution, rinsed with distilled water, and blown dry with nitrogen gas. The samples then had the corrosion product removed from the surface by immersion in a solution containing hydrochloric acid and hexamethylene tetramine, as detailed in ASTM G1-03 (2011).³² The surfaces were then observed with SEM and optical profilometry.

For SEM analysis a JEOL NeoScope JCM-5000 benchtop scanning electron microscope was used at an accelerating voltage of 10 kV. Three-dimensional (3D) surface profilometry was performed on a Bruker Contour GT-K1 3D optical microscope on immersion samples that had the corrosion product removed. Using the image analysis software, Vision 64, the number of pits deeper than 1 μm was detected for each of the $630 \times 470 \mu\text{m}$ scans. Two representative areas for each sample were recorded and the number of pits per square mm were calculated. The average pit depth, maximum pit depth, and the surface roughness, S_a (S_a is analogous to R_a but calculated from a 3D surface scan as opposed to a 2D line scan) were also calculated.

FTIR Spectroscopy. Infrared spectra were obtained for steel samples prepared as above with immersion for 48 h. Spectra of the surface films were obtained via diamond crystal ATR FTIR using a PerkinElmer Frontier. Sixteen scans were coadded at a resolution of 4 cm^{-1} . As a reference, spectra of the 2-MeHImn 4-OHCin, 2-MeHImn Br, and Na 4-OHCin powders were also obtained, as well as a sample of the inhibitor complexed to Fe(III). This was prepared by the addition of excess FeCl_3 to an aqueous solution of 2-MeHImn 4-OHCin. The water was evaporated from the resulting slurry overnight to leave a solid.

RESULTS AND DISCUSSION

Potentiodynamic Polarization. Figure 2 shows the Tafel plots for the samples tested at a pH of 8 and 2, while Table 1 shows the corrosion potential (E_{corr}), corrosion currents (i_{corr}), and the inhibitor efficiency extracted from the Tafel plots for all the conditions measured here.

Figure 2 and Table 1 show that, under all conditions, 2-MeHImn 4-OHCin at 4 mM significantly reduces the corrosion current density of the mild steel, with inhibition efficiencies of 86%, 72%, and 84% at pH 8, 2, and neutral, respectively. For

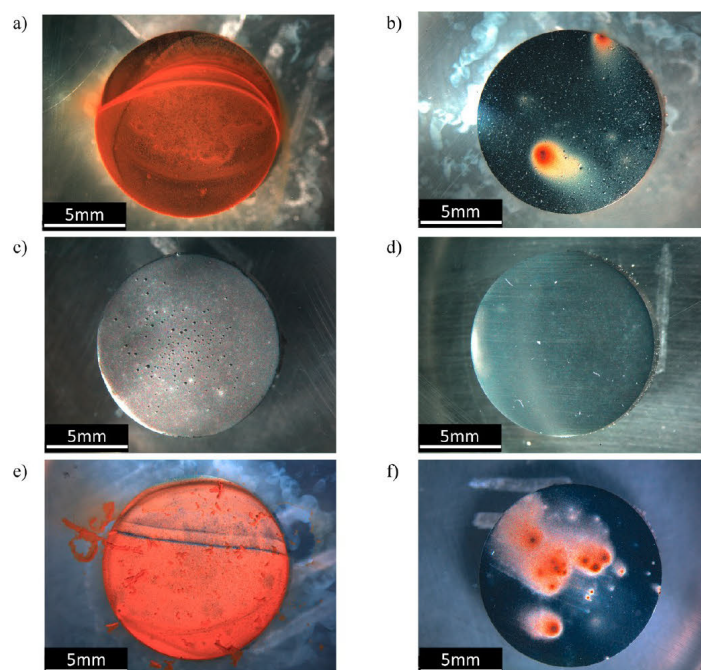


Figure 3. Optical images of the surfaces of mild steel samples with corrosion product intact after immersion for 24 h in (a) 0.01 M NaCl at pH 8; (b) 0.01 M NaCl and 4 mM 2-MeHImn 4-OHCin at pH 8; (c) 0.01 M NaCl at pH 2; (d) 0.01 M NaCl and 4 mM 2-MeHImn 4-OHCin at pH 2; (e) 0.01 M NaCl neutral; and (f) 0.01 M NaCl and 4 mM 2-MeHImn 4-OHCin neutral. Samples were imaged in solution.

each condition, however, it is clear that different mechanisms of protection are occurring.

At a pH of 8, Figure 2a and b and Table 1 show that both the 2-MeHImn 4-OHCin compound and Na 4OH-Cin salt at 4 mM concentration significantly reduce the corrosion process in comparison to the control sample, while the 2-MeHImn Br salt showed little affect at this concentration. The 2-MeHImn 4-OHCin shifted the E_{corr} toward more anodic potentials, from -557 mV for the control to -346 mV with an inhibitor efficiency of 86%, while the sodium salt shifted the E_{corr} almost as far, to -388 mV and had an inhibitor efficiency of 72%. Interestingly, the bromide salt displayed no inhibitor efficiency. These results suggest that, at pH 8, the 4OH-Cin plays the major role in reducing corrosion, although the 2-MeHImn compound consistently shifted to more positive potentials with evidence of a breakdown potential at even more positive potentials compared with the sodium salt. Furthermore, the 2-MeHImn 4-OHCin had a higher efficiency than the Na salt, 86% vs 72%, suggesting that the imidazolium ion does contribute to the corrosion current density reduction, even at a pH of 8. The 4 mM 2-MeHImn 4-OHCin and 4 mM Na 4-OHCin measurements show significant current fluctuations, particularly either side of E_{corr} . This type of fluctuation is consistent with metastable pitting, in which there is a constant breakdown and repair of a passive film.³³ Characterization of the mild steel surfaces following immersion in the various solutions is detailed below confirming this behavior.

In the pH 2 solution the 2-MeHImn 4-OHCin compound also results in a major reduction of corrosion in comparison to the control, while the sodium and bromide salts show little inhibiting effect. At this pH the cinnamate anion will be protonated to form the acid. This can be expected to be the

active species, in conjunction with the imidazolium cation, working synergistically to protect the mild steel surface. From Figure 2c and d it is apparent that the 2-MeHImn 4-OHCin compound causes a shift of E_{corr} toward more anodic potentials, from -654 mV for the control to -578 mV, while the bromide salt causes a very slight anodic shift to -642 mV. Interestingly, in this case the sodium salt that had a marked affect at a pH of 8 has little affect, with an inhibitor efficiency of 12% and no shift in E_{corr} ; thus the protonated 4-OHCin alone does not appear to offer any protection under these conditions. The inhibitor efficiency for the 2-MeHImn Br salt was 13%, while for the 2-MeHImn 4-OHCin it was 72%.

In the previously reported²⁴ neutral condition, 2-MeHImn 4-OHCin displayed an inhibitor efficiency of 84% and caused E_{corr} to shift from -584 to -289 mV. The reported inhibitor efficiencies for 2-MeHImn Br and Na 4-OHCin were -4% and 47% , respectively. Interestingly, similar to the results here at a pH of 8, the sodium salt had some affect, while the bromide salt had none. While not as obvious as the case at pH 2, the 2-MeHImn 4-OHCin still markedly out performed the two separate salts, again showing the synergy that exists when these ions are both present.

Likewise, synergistic effects on corrosion reduction have been reported when rare earth metals have been combined with carboxylates for corrosion inhibition of mild steel.⁵ This synergy was suggested to be due to speciation of the component ions that exist in solution which presented at the surface of the metal in a way that led to the formation of a complex surface film which was thin and adherent and offered superior protection to either component alone. This prior work clearly showed that if the solution conditions were such as to have the individual solvated species in solution, rather than the

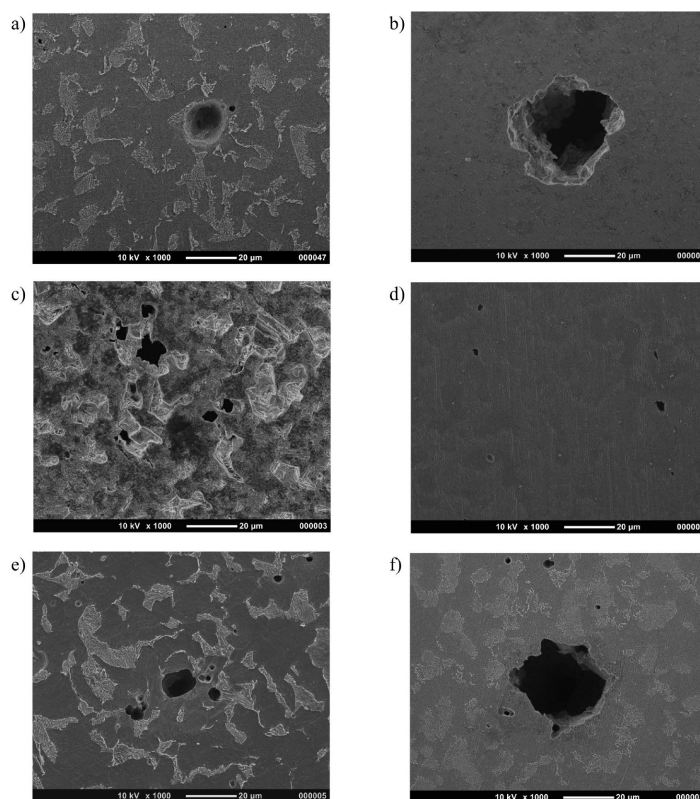


Figure 4. SEM images after corrosion product removal of the surfaces of mild steel samples immersed for 24 h in (a) 0.01 M NaCl at pH 8; (b) 0.01 M NaCl and 4 mM 2-MeHImn 4-OHCin at pH 8; (c) 0.01 M NaCl at pH 2; (d) 0.01 M NaCl and 4 mM 2-MeHImn 4-OHCin at pH 2; (e) 0.01 M NaCl neutral; and (f) 0.01 M NaCl and 4 mM 2-MeHImn 4-OHCin neutral.

complexed ions, the inhibition was significantly reduced. Further investigations will be conducted to determine if a similar effect may also be operating here, whereby the interaction between the 2-MeHImn cation and the 4-OHCin anion leads to species that react on the steel surface to form a more protective barrier. Interestingly, the species, and thus inhibition efficiency, depend on pH.

Immersion Tests. Since the electrochemical measurements detailed above were taken 30 min after the mild steel was immersed in the solutions, it gives a very short-term indication of the corrosion behavior. Additionally, the electrochemical methods give little information on the corrosion mechanism occurring, e.g. general vs pitting corrosion. To investigate the longer-term efficiency and the mechanism of corrosion, 24-h immersion tests were conducted. Mild steel samples were immersed in solutions containing 0.01 M NaCl and 4 mM 2-MeHImn 4-OHCin at pH 8, 2, and neutral conditions. As a comparison, mild steel samples were also immersed in control solutions containing only 0.01 M NaCl at each pH condition.

At the end of 24 h an optical microscope was used to image the samples while still immersed; these are shown in Figure 3. At a pH of 8, Figure 3a and b shows much less corrosion product but still some local attack on the sample in the inhibitor containing solution. At a pH of 2 Figure 3c shows many bubbles on the sample in the control solution. This is due to hydrogen gas evolution, according to the typical reaction of mild steel in acidic conditions:



Figure 3d shows the sample immersed at pH 2 with inhibitor added. This image does not have any bubbles visible, suggesting a marked reduction in the rate of reaction 2 and a relatively pristine surface after immersion with little corrosive attack despite the acidic conditions. The samples immersed in the neutral condition (Figure 3e and f) show a similar trend to those at a pH of 8, the inhibited solution showing much less corrosion product but still signs of localized attack.

Following the immersion, the corrosion products were removed and SEM images taken, Figure 4a and b show typical areas of the samples immersed in the control and inhibited solutions respectively at a pH of 8. It can be seen that there is much less general attack and fewer pits on the sample that was in the 2-MeHImn 4-OHCin solution, however one large pit over the whole examined surface was found.

Surface images of the samples immersed at a pH of 2 are shown in Figure 4c and d. Here a reduction in both the amount of general corrosion and severity of pitting can be seen for the 2-MeHImn 4-OHCin exposed sample as opposed to the sample immersed in the control solution alone.

Under neutral conditions, shown in Figure 4e and f, the control sample, Figure 4e, shows signs of extensive general corrosion and pitting, while the sample with 2-MeHImn 4-OHCin added to solution shows less general corrosion, but

some small pitting and one large pit (the only large pit on the entire surface), as shown in Figure 4f.

Profilometry. Following removal of the corrosion product, 3D surface profilometry was also performed on all of the mild steel samples immersed in the 0.01 M NaCl solutions at pH 8, 2, and neutral, with and without 4 mM of 2-MeHImn 4-OHCin. Table 2 shows the number of pits per square

Table 2. Pit Analysis from Optical Profilometry at All Conditions

solution	pits/mm ^{2a}	average pit depth (μm)	maximum pit depth (μm)	surface roughness, S_a (μm)
pH 8 inhibitor	3.0	30	40	0.045
pH 8 control	23.6	5.6	36	0.154
pH 2 inhibitor	0			0.069
pH 2 control	845	3.1	45	0.295
neutral inhibitor	1.7	29	29	0.114
neutral control	40	16	173	0.141

^aPits >1 μm deep were counted.

millimeter, along with the average pit depth, maximum pit depth, and the surface roughness, S_a , for each immersion condition. For each of the mild steel samples immersed in solutions that contained 4 mM of the 2-MeHImn 4-OHCin, the number of pits detected is much lower. This effect is particularly so at a pH of 2, where there were no pits greater than 1 μm deep detected in the inhibited solution, while there were 845 pits/mm² in the solution without inhibitor.

While the inhibited samples showed much less pitting under all conditions, in the neutral condition and at a pH 8 there were still some deep pits present. In the neutral solution the inhibited sample had a maximum pit depth of 29 μm , while the neutral control sample had a maximum pit depth of 173 μm . At a pH of 8 the inhibited solution had a maximum pit depth of 40 μm and the control sample 36 μm . Additionally, while the inhibited solutions at neutral and pH 8 reduced the number of pits, the average pit depth increased. This suggests that, while the compound is good at reducing pits, once a pit has established the compound is not as efficient at reducing its growth. This mixed ability to stop the pitting confirms that the current fluctuations seen for the polarization tests at a pH of 8 and the neutral condition are due to metastable pitting. At the neutral condition and at a pH 8, passive film breakdown and repair stops the formation of the majority of pits; however, as seen in the SEM and profilometry results, some stable pitting may still occur and lead to a few deeper pits. At a pH of 2, however, even though the control shows extensive pitting, with a pit density of 845 pits/mm², as can be seen in the SEM image, Figure 4c, and the 3D profilometer image, Figure 5a, the inhibitor is so effective at stifling pit growth, that there are no pits greater than 1 μm . The polarization scans in Figure 2c and d are also very stable at a pH of 2, suggesting that in this condition, unlike at neutral and pH 8, the inhibitor results in the formation of a stable passive film that protects the surface from pit initiation and growth.

From Table 2, the inhibited solutions also all show a lower surface roughness, S_a . While the reduction in pitting may account for some of this reduction in roughness, the SEM images show that there is also less general corrosion on all of the samples that were immersed in solutions containing inhibitor.

While the polarization tests were carried out after 30 min, the immersion test results were taken after 24 h. The SEM images

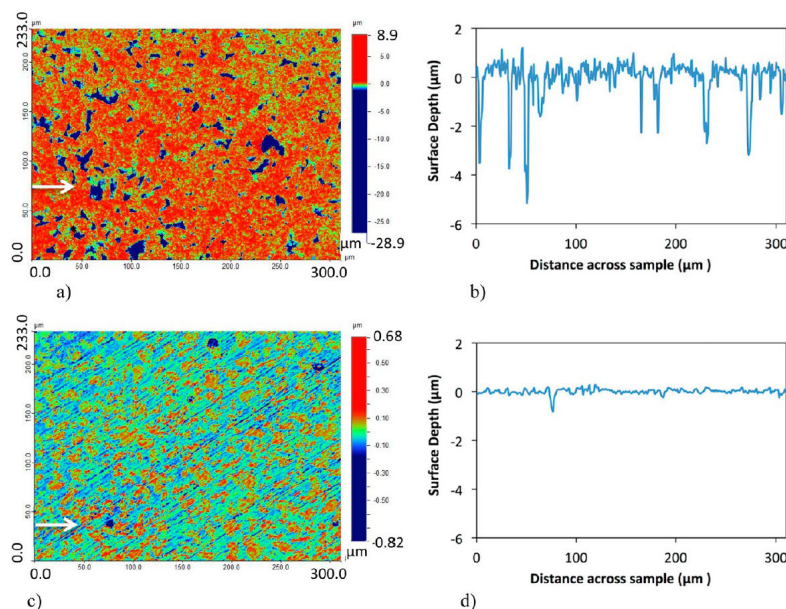


Figure 5. (a) Optical profilometry image of pH 2 control sample. (b) Typical profile across pH 2 control surface. (c) Optical profilometry image of pH 2 inhibited sample. (d) Typical profile across pH 2 inhibited surface. White arrows show where surface depth profile is taken from.

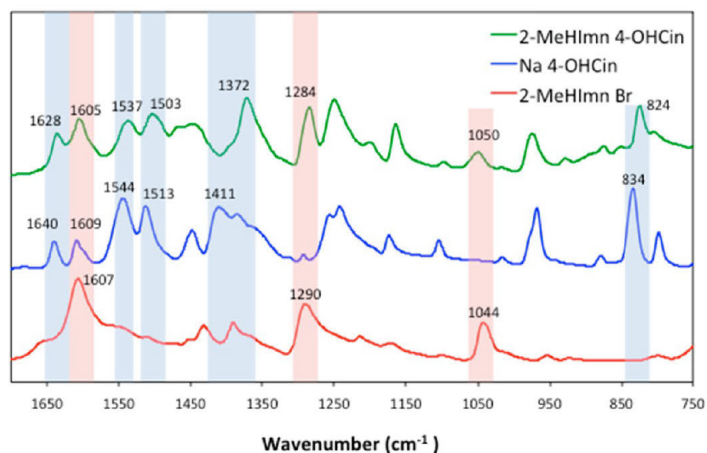


Figure 6. IR spectra of 2-MeHImn 4-OHCin and component ion compounds.

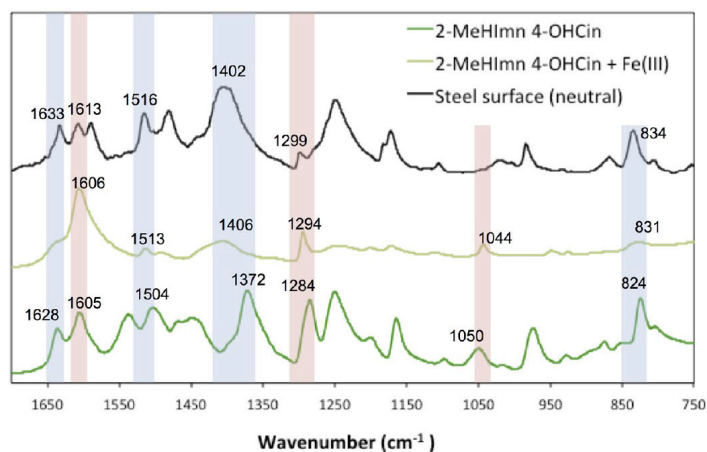


Figure 7. IR spectrum of the steel surface after 48 h immersion in 4 mM 2-MeHImn 4-OHCin and 0.01 M NaCl.

and profilometry results show that, over this longer period the differences between the surfaces of the mild steel in the control solution and in the 2-MeHImn 4-OHCin solution show a more marked difference in performance than the polarization tests were able to discriminate. This suggests that, as a corrosion inhibitor, the 2-MeHImn 4-OHCin performs even better over longer times. This is particularly so at a pH of 2, where the corrosion current density of the inhibited sample, measured after 30 min, was higher than that of the neutral or alkaline samples, but after 24 h of immersion the sample at pH2 shows the least amount of pitting and general corrosion. It has previously been shown for carboxylate type inhibitors that cathodic inhibition takes longer to take effect and, since the polarization results here show an anodic inhibition after 30 min, over 24 h the cathodic inhibition may contribute to the reduction in corrosion.^{30,31}

FTIR. The potentiodynamic polarization measurements and the immersion studies discussed above indicate that the inhibitor compound is forming a protective layer on the surface of the steel that blocks the approach of aggressive species such as chloride and oxygen and suppresses pitting. One

way to detect the presence of such a layer is through the use of infrared spectroscopy.

Steel samples were immersed in 0.01 M NaCl solutions with 4 mM 2-MeHImn 4-OHCin at pH 2, 8, and neutral for 48 h before being dried with nitrogen and analyzed by ATR FTIR. Powders of the inhibitor and component compounds were analyzed for comparison.

Figure 6 shows the IR spectra obtained for the 2-MeHImn 4-OHCin, Na 4-OHCin, and 2-MeHImn Br powders. There were a number of bands seen in the inhibitor compound that can be attributed to vibrations from both the anion and cation.

The IR spectrum for Na 4-OHCin was in good agreement with bands reported for the same compound by Świsłocka et al.³⁴ and a number of these can be seen in the 2-MeHImn 4-OHCin spectrum. The bands caused by stretching of the carboxylate group in the cinnamate were present, although the symmetric stretch was shifted to lower wavenumbers when paired with the 2-MeHImn⁺ cation rather than Na⁺ (from 1411 to 1372 cm⁻¹).

Due to its symmetry and smaller size, there are fewer strong vibrational modes in the cation and some of these were

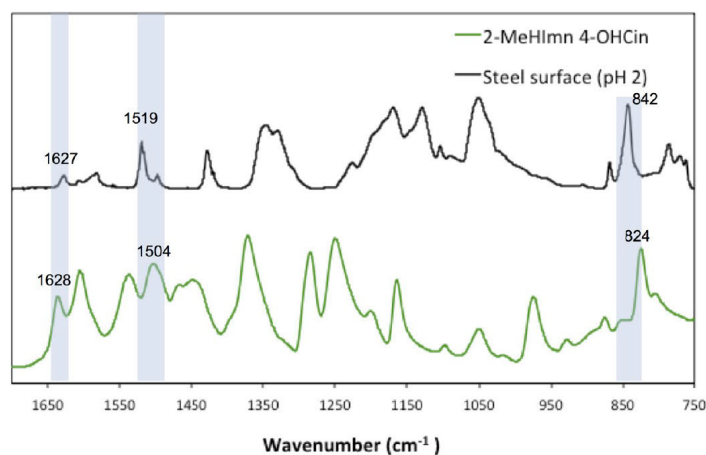


Figure 8. IR spectrum of the steel surface after 48 h immersion in 4 mM 2-MeHImn 4-OHCin and 0.01 M NaCl at pH 2.

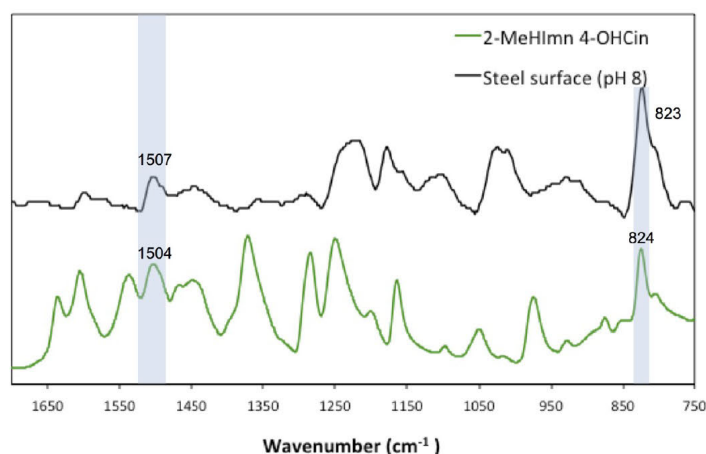


Figure 9. IR spectrum of the steel surface after 48 h immersion in 4 mM 2-MeHImn 4-OHCin and 0.01 M NaCl at pH 8.

obscured in the 2-MeHImn 4-OHCin spectrum, but bands can be seen at 1284 and 1050 cm^{-1} .

One band of interest falls at 1605 cm^{-1} in 2-MeHImn 4-OHCin. This appears quite strongly and can be seen to be a result of overlapping of vibrations from both ions. In Na 4-OHCin this band can be attributed to stretching of the aromatic carbons, and it is approximately the same strength as the neighboring band at 1634 cm^{-1} caused by the presence of the alkene. The strongest band in the 2-MeHImn Br spectrum also appears in this region. As such, in the combined spectrum the band at 1605 cm^{-1} is stronger than the one at 1628 cm^{-1} .

Figure 7 shows the spectrum obtained from the surface of the coupon immersed in neutral inhibitor solution with 0.01 M NaCl. A number of the bands in the steel sample, such as the C=C stretch at 1633 cm^{-1} , and aromatic bands at 1516 cm^{-1} ($\nu(\text{C}=\text{C}_{\text{ar}})$) and 834 cm^{-1} ($\nu(\text{C}-\text{H}_{\text{ar}})$) confirmed that the anion was present in a layer on the steel surface. A significant reduction of the bands associated with the 2-MeHImn⁺ cation at 1605, 1284, and 1050 cm^{-1} was observed, meaning that the cation could not be easily detected in the surface layer of the coupon although a weak band at 1299 cm^{-1} could be an indication of its presence.

While many bands appeared at similar wavenumbers, there appears to be shifting in the position of the symmetric carboxylate stretch compared to the pure inhibitor (from 1372 to 1402 cm^{-1}), suggesting that, on the steel surface, the carboxylate was no longer bound to the 2-MeHImn cation alone. The bands instead showed a very good correlation to those observed when 2-MeHImn 4-OHCin was complexed to Fe (III), achieved by adding FeCl_3 in excess to a solution of 2-MeHImn 4-OHCin. This indicates that 4-OHCin⁻ is adsorbed (or deposited) on the surface of the steel through interaction of the carboxylate group with the Fe(III) ions. This could be either Fe(III) in the oxide surface film or through reaction with any Fe(III) ions that result from the corrosion processes on the steel surface in solution. These observations are consistent with results obtained by Blin et al.¹⁰ during a study of rare earth cinnamate interactions with steel substrates.

As seen in Figure 8, the presence of an organic surface layer was also confirmed on a steel sample immersed in 4 mM inhibitor solution at pH 2. Once again key bands from the cation were not clearly observed, but bands at 1627, 1519, and 842 cm^{-1} could be seen, indicating the presence of 4-OHCin⁻ in the surface layer. Interestingly, the surface film here is much

more protective and often this reflects thinner, more compact films that may be difficult to detect spectroscopically.

Similarly, for immersion in the pH 8 4 mM 2-MeHImn 4-OHCin and 0.01 M NaCl solution there was evidence of aromatic $\nu(\text{C}=\text{C}_{\text{ar}})$ and $\nu(\text{C}-\text{H}_{\text{ar}})$ peaks in the IR spectrum, as displayed in Figure 9, that indicated the presence of 4-OHCin on the surface of the steel, although the signal response was very weak. It is possible that, as with at pH 2, at pH 8 a thinner film was being formed, leading to limitations in detection using ATR FTIR.

Analysis of the IR spectra of the steel coupons provides support for the electrochemical results that suggest the formation of a protective thin layer on the surface. It was observed that the cinnamate anion attached to the steel surface, potentially through interaction between the carboxylate moiety and the iron. There was, however, no clear evidence of the imidazolium cation bands on the steel surface. This is in part due to the smaller number of vibrations in the molecule, as well as their placement at wavenumbers that coincide with vibrations in the anion. It may be possible that the cation is present in the surface layer, albeit in smaller amounts that are not readily detected by ATR, or that it is left behind when the coupon is removed from the test solution. In such a situation the imidazolium could still be enhancing the formation of the surface layer by assisting transport of the cinnamate to the surface where it can interact with the iron while not being incorporated into the layer itself.

All characterization to date has shown a significant improvement in inhibition when the combined inhibitor was employed, rather than the sodium cinnamate salt, particularly at pH 2. This suggests that the attachment of the cinnamate alone is not providing the full amount of protection and that a synergistic effect is taking place in solution. Further elucidation of the nature of this relationship, and the role of the imidazolium is required to fully understand the mechanism of this inhibitor and thereby to design even more protective systems.

CONCLUSION

Previous work has shown that the 2-MeHImn 4-OHCin salt was a highly effective inhibitor on mild steel in neutral chloride conditions. Here it has been shown that this environmentally friendly compound remains highly active at pH 2 and 8, both of which are common environments in which corrosion protection is required. At elevated pH, the inhibition was driven by the anion, and the solution of Na 4-OHCin provided a comparable level of protection. At low pH, even though both the components were largely ineffective on their own, the combined salt still had an inhibition efficiency of 72%, as determined from short-term polarization measurements, indicating a strong synergy between the two ionic species under these conditions. SEM and optical profiling of mild steel samples immersed under various pH conditions supported the short-term electrochemical measurements and showed even more dramatic inhibition and stifling of both pitting and general corrosion. Across the pH range tested, the incorporation of 4 mM 2-MeHImn 4-OHCin into the immersion solution resulted in better preservation of the surface.

AUTHOR INFORMATION

Corresponding Author

*Mailing address: Institute for Frontier Materials, Deakin University, 221 Burwood Hwy, Burwood 3125, Victoria, Australia. E-mail: asomers@deakin.edu.au.

Funding

Professors M.F. and D.M. are grateful to the Australian Research Council for their Australian Laureate Fellowships.

Notes

The authors declare no competing financial interest.

REFERENCES

- (1) Mattsson, E. *Basic Corrosion Technology for Scientists and Engineers*, 2nd ed.; Institute of Materials, IOM Communications: London, 2001.
- (2) Sinko, J. Challenges of chromate inhibitor pigments replacement in organic coatings. *Prog. Org. Coat.* **2001**, *42* (3–4), 267–282.
- (3) Guertin, J. Toxicity and Health Effects of Chromium (All Oxidation States). In *Chromium(VI) Handbook*; CRC Press: 2004; pp 215–234.
- (4) Behrsing, T.; Deacon, G. B.; Junk, P. C. 1–The chemistry of rare earth metals, compounds, and corrosion inhibitors. In *Rare Earth-Based Corrosion Inhibitors*; Forsyth, M., Hinton, B., Eds.; Woodhead Publishing: 2014; pp 1–37.
- (5) Forsyth, M.; Seter, M.; Hinton, B.; Deacon, G.; Junk, P. New 'Green' Corrosion Inhibitors Based on Rare Earth Compounds. *Aust. J. Chem.* **2013**, *64* (6), 812–819.
- (6) Naderi, R.; Mahdavian, M.; Attar, M. M. Electrochemical behavior of organic and inorganic complexes of Zn(II) as corrosion inhibitors for mild steel: Solution phase study. *Electrochim. Acta* **2009**, *54* (27), 6892–6895.
- (7) Hinton, B. R. W.; Wilson, L. The corrosion inhibition of zinc with cerous chloride. *Corros. Sci.* **1989**, *29* (8), 967–975 977–985.
- (8) Dariva, C. G.; Galio, A. F. Corrosion Inhibitors—Principles, Mechanisms and Applications. In *Developments in Corrosion Protection*; Aliofkhaezai, M., Ed.; InTech: 2014; pp 365–379.
- (9) Forsyth, M.; Forsyth, C. M.; Wilson, K.; Behrsing, T.; Deacon, G. B. ATR characterisation of synergistic corrosion inhibition of mild steel surfaces by cerium salicylate. *Corros. Sci.* **2002**, *44* (11), 2651–2656.
- (10) Blin, F.; Leary, S. G.; Deacon, G. B.; Junk, P. C.; Forsyth, M. *Corros. Sci.* **2006**, *48* (2), 404–419.
- (11) Deacon, G. B.; Junk, P. C.; Forsyth, M.; Leeb, W. W. From chromates to rare earth carboxylates: a greener take on corrosion inhibition. *Chem. Aust.* **2008**, *75* (9), 18–21.
- (12) Ramezanzadeh, B.; Raiesi, E.; Mahdavian, M. *Int. J. Adhes. Adhes.* **2015**, *63*, 166–176.
- (13) Javadian, S.; Yousefi, A.; Neshati, J. Synergistic effect of mixed cationic and anionic surfactants on the corrosion inhibitor behavior of mild steel in 3.5% NaCl. *Appl. Surf. Sci.* **2013**, *285* (Part B), 674–681.
- (14) Amoozadeh, S. M.; Mahdavian, M. Synergistic Inhibition Effect of Zinc Acetylacetonate and Benzothiazole in Epoxy Coating on the Corrosion of Mild Steel. *J. Mater. Eng. Perform.* **2015**, *24* (6), 2464–2472.
- (15) Seter, M.; Hinton, B.; Forsyth, M. Understanding speciation of lanthanum 4-hydroxy cinnamate and its impact on the corrosion inhibition mechanism for AS1020 steel. *J. Electrochem. Soc.* **2012**, *159* (4), C181–C189.
- (16) Zheng, X.; Zhang, S.; Gong, M.; Li, W. Experimental and Theoretical Study on the Corrosion Inhibition of Mild Steel by 1-Octyl-3-methylimidazolium I-Proline in Sulfuric Acid Solution. *Ind. Eng. Chem. Res.* **2014**, *53* (42), 16349–16358.
- (17) Olivares-Xometl, O.; López-Aguilar, C.; Herrasti-González, P.; Likhanova, N. V.; Lijanova, I.; Martínez-Palou, R.; Rivera-Márquez, J. A. Adsorption and Corrosion Inhibition Performance by Three New Ionic Liquids on API 5L X52 Steel Surface in Acid Media. *Ind. Eng. Chem. Res.* **2014**, *53* (23), 9534–9543.

- (18) Lozano, I.; Mazario, E.; Olivares-Xometl, C. O.; Likhonova, N. V.; Herrasti, P. Corrosion behaviour of API 5LX52 steel in HCl and H₂SO₄ media in the presence of 1,3-dibencilimidazolium acetate and 1,3-dibencilimidazolium dodecanoate ionic liquids as inhibitors. *Mater. Chem. Phys.* **2014**, *147* (1–2), 191–197.
- (19) Likhonova, N. V.; Olivares-Xometl, O.; Guzmán-Lucero, D.; Domínguez-Aguilar, M. A.; Nava, N.; Corrales-Luna, M.; Mendoza, M. C. Corrosion inhibition of carbon steel in acidic environment by imidazolium ionic liquids containing vinyl-hexafluorophosphate as anion. *Int. J. Electrochem. Sci.* **2011**, *6* (10), 4514–4536.
- (20) Kowsari, E.; Payami, M.; Amini, R.; Ramezanzadeh, B.; Javanbakht, M. Task-specific ionic liquid as a new green inhibitor of mild steel corrosion. *Appl. Surf. Sci.* **2014**, *289* (0), 478–486.
- (21) Acidi, A.; Hasib-ur-Rahman, M.; Larachi, F.; Abbaci, A. Ionic liquids [EMIM][BF₄], [EMIM][Otf] and [BMIM][Otf] as corrosion inhibitors for CO₂ capture applications. *Korean J. Chem. Eng.* **2014**, *31* (6), 1043–1048.
- (22) Yousefi, A.; Javadian, S.; Dalir, N.; Kakemam, J.; Akbari, J. Imidazolium-based ionic liquids as modulators of corrosion inhibition of SDS on mild steel in hydrochloric acid solutions: experimental and theoretical studies. *RSC Adv.* **2015**, *5* (16), 11697–11713.
- (23) Zheng, X.; Zhang, S.; Li, W.; Gong, M.; Yin, L. Experimental and theoretical studies of two imidazolium-based ionic liquids as inhibitors for mild steel in sulfuric acid solution. *Corros. Sci.* **2015**, *95* (0), 168–179.
- (24) Chong, A. L.; Forsyth, M.; MacFarlane, D. R. Novel imidazolium ionic liquids and organic salts. *Electrochim. Acta* **2015**, *159* (0), 219–226.
- (25) Bajpai, D.; Tyagi, V. K. Fatty Imidazolines: Chemistry, Synthesis, Properties and Their Industrial Applications. *J. Oleo Sci.* **2006**, *55* (7), 319–329.
- (26) Arduengo, A. J.; Krafczyk, R.; Schmutzler, R.; Craig, H. A.; Goerlich, J. R.; Marshall, W. J.; Unverzagt, M. *Tetrahedron* **1999**, *55* (51), 14523–14534.
- (27) McMahon, A. J. The mechanism of action of an oleic imidazoline based corrosion inhibitor for oilfield use. *Colloids Surf.* **1991**, *59* (C), 187–208.
- (28) Tyagi, R.; Tyagi, V. K.; Pandey, S. K. Imidazoline and Its Derivatives: An Overview. *J. Oleo Sci.* **2007**, *56* (5), 211–222.
- (29) Garcia, M. T.; Campos, E.; Marsal, A.; Ribosa, I. Fate and effects of amphoteric surfactants in the aquatic environment. *Environ. Int.* **2008**, *34* (7), 1001–1005.
- (30) Forsyth, M.; Wilson, K.; Behrsing, T.; Forsyth, C.; Deacon, G. B.; Phanasoankar, A. Effectiveness of rare-earth metal compounds as corrosion inhibitors for steel. *Corrosion* **2002**, *58* (11), 953–960.
- (31) Blin, F.; Leary, S. G.; Wilson, K.; Deacon, G. B.; Junk, P. C.; Forsyth, M. Corrosion mitigation of mild steel by new rare earth cinnamate compounds. *J. Appl. Electrochem.* **2004**, *34* (6), 591–599.
- (32) *Standard Practice for Preparing, Cleaning, and Evaluating Corrosion Test Specimens*; ASTM International: West Conshohocken, PA, 2011; Vol. G1-03.
- (33) Cheng, Y. F.; Luo, J. L. Metastable pitting of carbon steel under potentiostatic control. *J. Electrochem. Soc.* **1999**, *146* (3), 970–976.
- (34) Świsłocka, R.; Kowczyk-Sadowy, M.; Kalinowska, M.; Lewandowski, W. Spectroscopic (FT-IR, FT-Raman, ¹H and ¹³C NMR) and theoretical studies of p-coumaric acid and alkali metal p-coumarates. *Spectroscopy* **2012**, *27* (1), 35–48.

3.2 Further Investigations

This section provides details of additional experiments that further explore the synergy observed between the imidazolinium and cinnamate species. It should be noted that due to changes in the testing procedure, including the use of a new batch of steel, direct comparison cannot be made to the results in Section 2.2 and Section 3.1. The relevant experiments were repeated with the new electrodes and the corrosion potential (E_{corr}), corrosion current density (i_{corr}) and the inhibition efficiency (%IE) are presented in Table 3. All measurements were carried out at the ‘as made’ neutral pH.

3.2.1 Concentration Effects

Section 3.1 showed that at concentrations as low as 1 mM, [2-MeHIImn][4-OHCin] halved i_{corr} compared to the control. Figure 10 shows the impact on polarisation of increasing the concentration. An increase in the inhibitor concentration to 0.01 M caused a modest anodic shift and very little reduction of i_{corr} (Table 3). There was, however, a noticeable reduction in the anodic currents. The steep slope of the anodic arm in the 4 mM [2-MeHIImn][4-OHCin] sample suggests that the corrosion potential is closely followed by the breakdown pitting potential, E_{pit} .¹ At this potential, there is a rapid increase in current density, signifying the breakdown of a passive film and the onset of pitting corrosion. Increasing the inhibitor concentration to 0.01 M anodically shifted this onset by 50 mV, indicating that the surface has become more resistant to pitting.

Increasing the inhibitor concentration to five times this amount had a considerable impact on efficacy; i_{corr} was reduced by over an order of magnitude, resulting in an inhibition efficiency of 99.5 %. This was also accompanied by a substantial ennoblement of E_{pit} to an anodic overpotential of 200 mV from E_{corr} . Hence, the steel is well-protected under anodic conditions; for example, under at -100 mV vs. SCE, the currents generated in the 0.05 M sample were four orders of magnitude lower than at the 4 mM concentration.

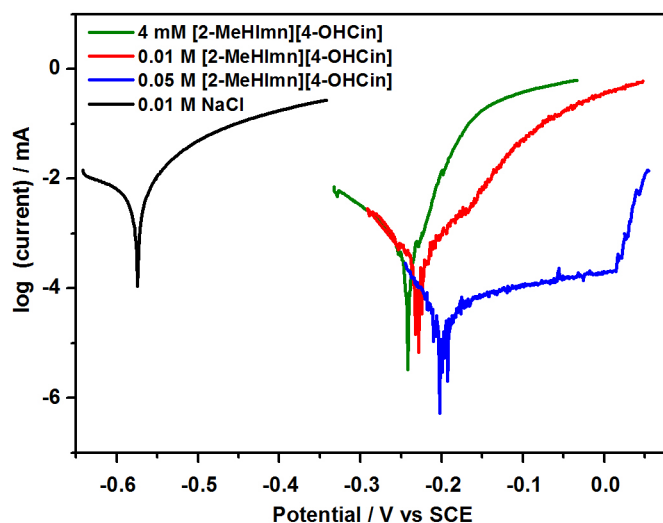


Figure 10. Polarisation curves for different concentrations of [2-MeHImn][4-OHCin]. Increasing the inhibitor concentration to 0.05 M drastically reduced the anodic currents.

Table 3. Corrosion current density (i_{corr}), corrosion potential (E_{corr}), and inhibitor efficiency calculated from potentiodynamic polarisation.

Inhibitor	$E_{\text{corr}} / \text{mV}$	$i_{\text{corr}} / \text{mAcm}^{-2}$	% IE
0.01 M NaCl control	-571 ± 5	2.2 ± 0.3	-
4 mM [Na][4-OHCin]	-277 ± 3	0.50 ± 0.06	77
4 mM [2-MeHImn][4-OHCin]	-240 ± 2	0.23 ± 0.07	89
0.01 M [2-MeHImn][4-OHCin]	-225 ± 3	0.17 ± 0.07	92
0.05 M [2-MeHImn][4-OHCin]	-197 ± 4	0.011 ± 0.005	99.5
4 mM [2-MeHImn]+[Na][4-OHCin]	-330 ± 20	0.5 ± 0.2	79
4 mM [2-MeHIm][4-OHCin]	-268 ± 7	1.6 ± 0.4	29
4 mM [triMeImn][4-OHCin]	-228 ± 2	0.26 ± 0.09	88

The behaviour observed in the polarisation measurements was confirmed by coupon immersion tests. Figure 11 shows optical microscopy and SEM images of steel coupons after exposure to 0.01 M NaCl and inhibitor for 24 h. The 0.01 M [2-MeHImn][4-OHCin] sample (Figure 11c and d) showed similar levels of pitting to the 4 mM sample (Figure 11a and b). Large regions of the coupon were protected, but a number of significant pits formed. This behaviour is consistent with a study of localised corrosion by Tan et al.² Using a multi-electrode array, they were able to map the current density across a mild steel surface. It was found that an imidazoline inhibitor showed a tendency towards forming a small number of major anodes, causing highly concentrated anodic dissolution.

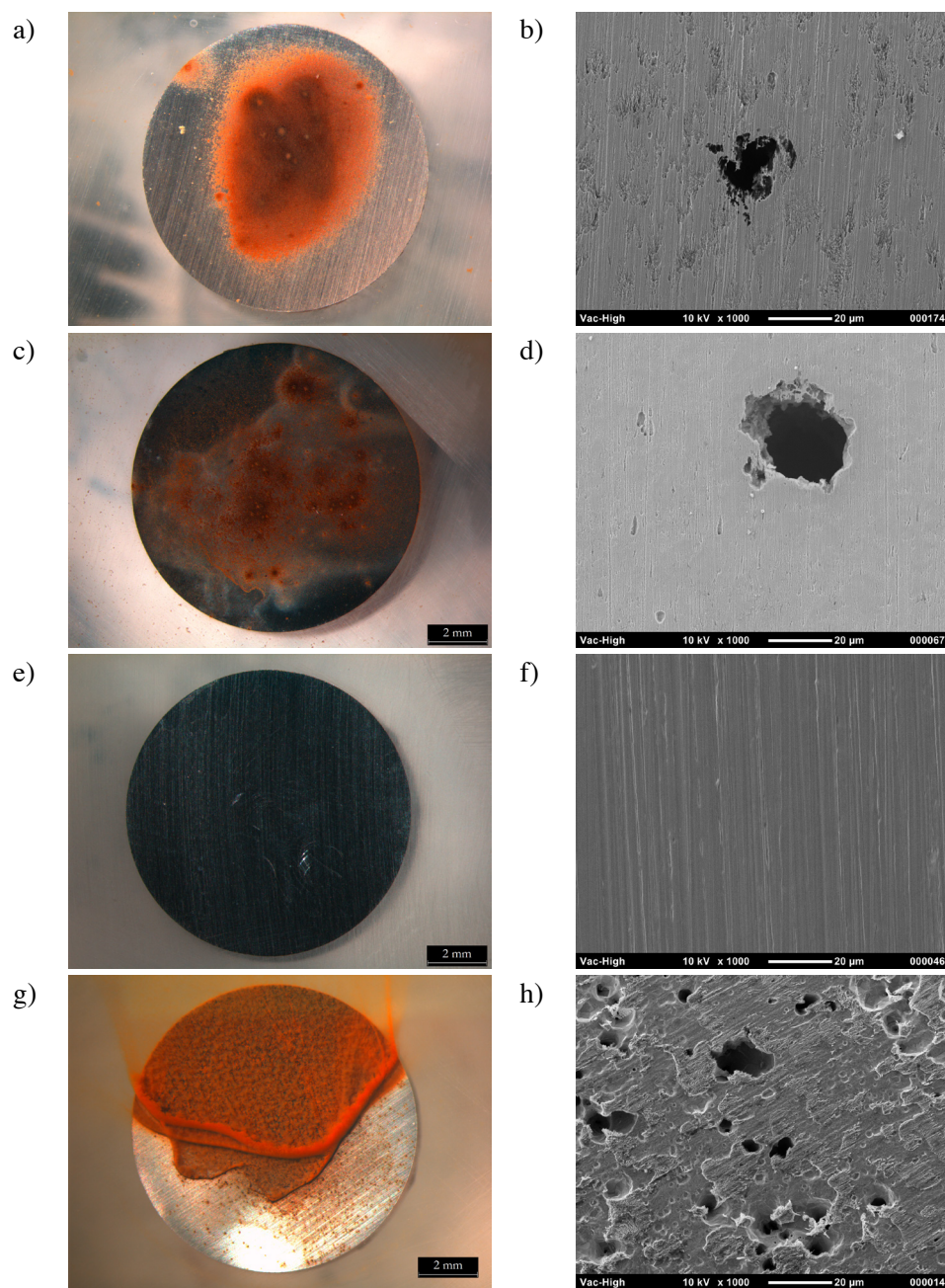


Figure 11. Microscope images with corrosion product intact (x 0.8) and SEM images with corrosion product removed (x 1000) for coupons immersed for 24 h in 0.01 M NaCl and [2-MeHImn][4-OHCin] at varied concentration. a) and b) 4 mM; c) and d) 0.01 M; e) and f) 0.05 M; g) and h) control – no inhibitor.

Pit analysis of the optical profilometry data revealed that although the number of pits observed on the 0.01 M sample was similar to the 4 mM sample, the depth of these pits was substantially reduced, as was the surface roughness (Table 4). This was consistent with the increased pitting corrosion resistance suggested by the polarisation results.

Table 4. Pit analysis conducted by optical profilometry of coupons immersed for 24 h in 0.01 M NaCl plus inhibitor, with corrosion product removed.

Inhibitor	Pits / mm ²	Average pit depth / μm	Maximum pit depth / μm	Surface roughness / μm
As polished steel	0	-	-	0.081 \pm 0.013
0.01 M NaCl control	350 \pm 80	7.8 \pm 0.8	36	0.42 \pm 0.03
4 mM [2-MeHImn][4-OHCin]	3 \pm 3	24 \pm 28	82	0.20 \pm 0.04
0.01 M [2-MeHImn][4-OHCin]	5 \pm 3	7 \pm 4	19	0.108 \pm 0.015
0.05 M [2-MeHImn][4-OHCin]	0	-	-	0.107 \pm 0.010
4 mM [2-MeHIm][4-OHCin]	12 \pm 10	9 \pm 5	74	0.18 \pm 0.06
4 mM [triMeImn][4-OHCin]	4 \pm 5	8 \pm 4	54	0.15 \pm 0.02

In contrast, the 0.05 M sample showed no evidence of corrosion across the entire surface. The 0.05 M test was continued for 7 days of immersion, after which the level of inhibition was maintained. It is clear that increasing the concentration of [2-MeHImn][4-OHCin] can provide excellent protection of mild steel from corrosion in chloride environments. It should be noted that 0.05 M corresponds to a concentration of 1.2 wt%, which, while high, is within the range of concentrations used commercially.³

3.2.2 Component Ion Effects

The previous work demonstrated that the combined inhibitor [2-MeHImn][4-OHCin] functions more effectively than salts of the individual ions, [2-MeHImn][Br] and [Na][4-OHCin].^{4,5} However, it was not clear how the species would behave together in solution if they were added as isolated compounds. Addition of the pure acid and base directly to the electrolyte (with the hope of forming the synergistic species *in situ*) was not possible due to the poor solubility of 4-OHCinH in water.

Figure 12 shows the polarisation curve after 30 minutes immersion of mild steel in 0.01M NaCl solution containing [2-MeHImn][Br] and [Na][4-OHCin], to give the equivalent of 4 mM active compound. While the mixture shows a clear positive shift in potential compared to the control, it is not as strong an anodic inhibitor as the combined salt. The i_{corr} of 0.5 mAcm⁻² was in fact closer to that observed for 4 mM [Na][4-OHCin] alone (Table 3). The poorer performance of the mixture of salts shows that there is a benefit in synthesising dual-active inhibitor salts, rather than just mixing components *in*

situ. This result supports the hypothesis that a synergistic species is formed at the steel surface in the presence of the mixed inhibitor. Additional solutes (i.e. Na^+ and Br^-) may disrupt the formation of this species by changing the ion interactions in solution, resulting in inhibition solely by adsorption of $[\text{4-OHCin}]^-$ to the steel.

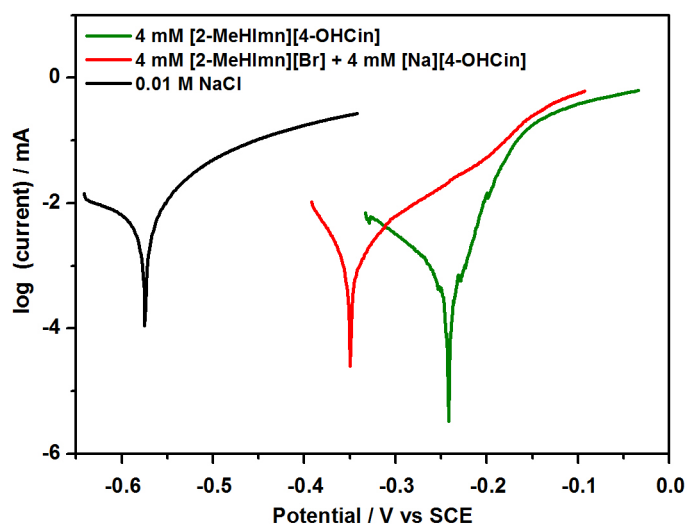


Figure 12. Polarisation curve of 4 mM [2-MeHImn][Br] and 4 mM [Na][4-OHCin] component mixture. The mixture provides poorer inhibition than the combined [2-MeHImn][4-OHCin] salt at the same concentration.

3.2.3 Alternative Cations

The polarisation curves in Figure 14 display the effects of altering the cation on the inhibitive action. The analogous imidazolium cation, $[\text{2-MeHIm}]^+$ (structure shown in Figure 13) does not display the same synergistic effects as $[\text{2-MeHImn}]^+$, and instead has a detrimental impact on the corrosion currents. The 4 mM $[\text{2-MeHIm}][\text{4-OHCin}]$ electrolyte caused E_{corr} to shift to -268 mV, which was not quite as large a shift as 4 mM $[\text{Na}][\text{4-OHCin}]$ displayed, however, i_{corr} remained three times larger than that of the sodium salt and almost 7 times higher than that of 4 mM $[\text{2-MeHImn}][\text{4-OHCin}]$ (Table 3). This drastic reduction in efficiency suggests that the imidazolium either acts as a corrosive species in solution, or in some way prevents $[\text{4-OHCin}]^-$ from adhering to the surface. This result is unusual given the large number of studies that have used similar concentrations of imidazolium salts (often ILs) as successful inhibitors.⁶⁻⁹

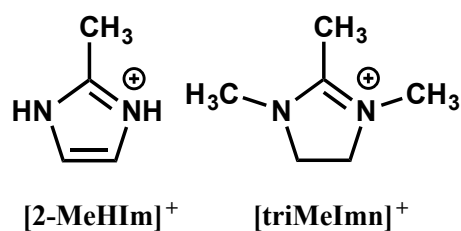


Figure 13. Alternative cations; 2-methylimidazolium and 1,2,3-trimethylimidazolium.

For the polarisation curve displayed in Figure 14, E_{pit} is close to E_{corr} . Hence, E_{pit} in the 4 mM [2-MeHIm][4-OHCin] solution is also 50 mV more negative than in the presence of 4 mM [2-MeHImn][4-OHCin], indicating that [2-MeHIm][4-OHCin] is not as effective at preventing the onset of pitting.

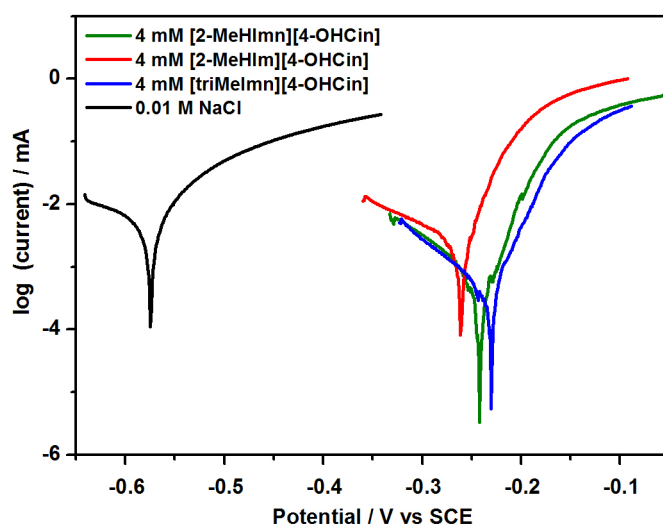


Figure 14. Polarisation curves of inhibitors with altered cations.

An increase in pitting was observed in the optical microscopy and SEM images of a coupon immersed for 24 h in 4 mM [2-MeHIm][4-OHCin] (Figure 15 c and d). The entire surface showed evidence of corrosion, suggesting that imidazolium does not concentrate the number of anodic regions to the same extent as imidazolium. In addition to a number of large pits, there was extensive coverage of shallow pits with diameters less than 5 μm . Pit analysis supported the SEM findings, as the data showed an increase in the number of pits and a decrease in average pit depth, although the maximum pit depth was still substantial.

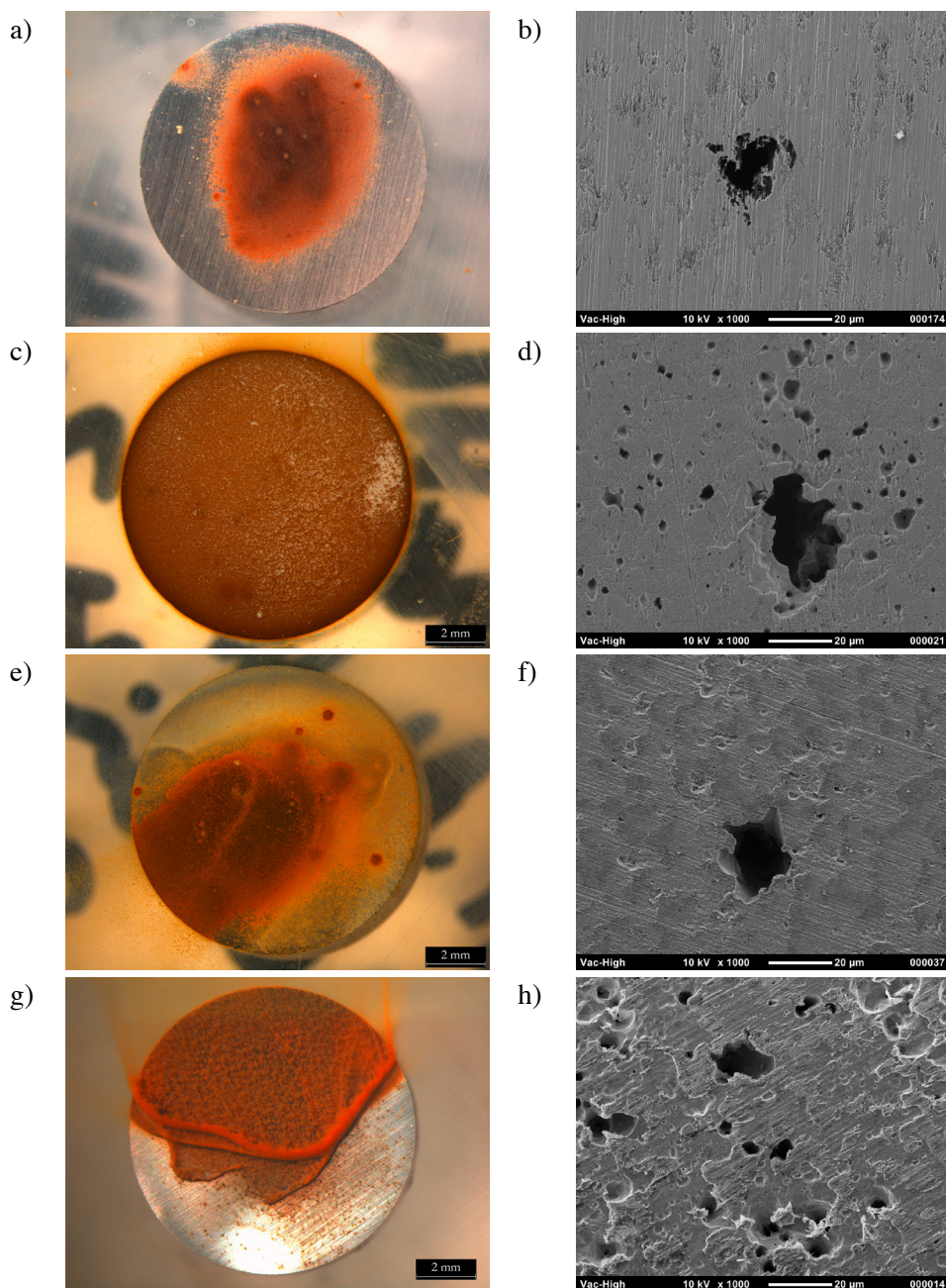


Figure 15. Microscope images with corrosion product intact (x 0.8) and SEM images with corrosion product removed (x 1000) for coupons immersed for 24 h in 0.01 M and 4 mM of inhibitor. a) and b) [2-MeHImn][4-OHCin]; c) and d) [2-MeHIm][4-OHCin]; e) and f) [triMeImn][4-OHCin]; g) and h) control – no inhibitor.

The efficacy of an aprotic imidazolinium cation was also investigated. Modifying the cation was of interest for two reasons. Generally, it has been shown that increasing the substituent chain lengths on species improves inhibition.⁶ This is most likely due to the longer chains on adsorbed inhibitors providing more coverage to prevent aggressive species approaching the surface. More specific to this system, alkylating the N positions on the cation could give an indication of the role, if any, of available protons in the inhibition mechanism.

1,2,3-trimethylimidazolium 4-hydroxycinnamate, [triMeImn][4-OHCin] (Figure 13), was synthesised using a similar method as described in Section 2.2. The synthesis of this, and other compounds, is described in more detail in Section 3.3. Although this cation does not feature long alkyl chains or additional functional groups, such as in the commercially used imidazoline inhibitors,¹⁰⁻¹² it does provide an aprotic analogue to [2-MeHImn]⁺.

The polarisation curves obtained from 4 mM [triMeImn][4-OHCin] were very similar to 4 mM [2-MeHImn][4-OHCin] (Figure 14 and Table 3). A slight anodic shift was observed, but i_{corr} was unchanged and the anodic and cathodic arms were also comparable. After immersion for 24 h, the steel surface showed very similar morphology to the 4 mM [2-MeHImn][4-OHCin] sample (Figure 15e and f). Once again, a small number of large pits were observed, while the majority of the surface showed little general corrosion. Pit analysis suggested that there was some reduction in the severity of the pits.

The similarities in behaviour of the protic and aprotic imidazoliums are a strong indication that the inhibition mechanism is not reliant on the availability of labile protons on the nitrogens. This helps to confirm that [2-MeHImn]⁺ is not acting as an oxygen scavenger, like some other primary and secondary amines such as hydrazine, hexamine or phenylenediamine.^{3, 13} This conclusion is supported by the predominantly anodic effects of the inhibitors and the inefficacy of [2-MeHImn]⁺ on its own. To observe any positive effects from alkylating the imidazoline ring, longer substituents would be required.

3.2.4 Inhibitor Reactivity

In carrying out the polarisation experiments, it became apparent that this inhibitor system was electrochemically reactive. An example of this is the large amount of spiking observed in the curves, particularly in the varied pH and high concentration measurements. While this was initially attributed to metastable pit formation, it seems likely that there is a further explanation.

The reactivity is most obvious in the open circuit potential (OCP) hold at the beginning of each measurement. Prior to polarisation, each electrode was held at rest for 30 min, with no current or potential applied, to equilibrate the cell. In Figure 16a, it can be seen that during this time the OCP in the control solution dropped gradually before reaching a plateau, however, the 4 mM [2-MeHImn][4-OHCin] sample underwent random jumps in potential, without appearing to stabilise. Typically, the formation of pits would result in a sudden drop in OCP, followed by a gradual recovery if the passive film can

repair and shutdown the pitting process. This is the opposite of what was observed in this case. The impact of experimental set-up effects such as issues with the electrodes, luggin capillary or potentiostat were discounted.

Holding the electrode at OCP for a longer time did not improve the stability. Although there appears to be a steady average OCP in Figure 16b, substantial jumps are observed over the whole 24 h period, up to 80 mV at a time. This suggests that there was sustained activity at the electrode surface.

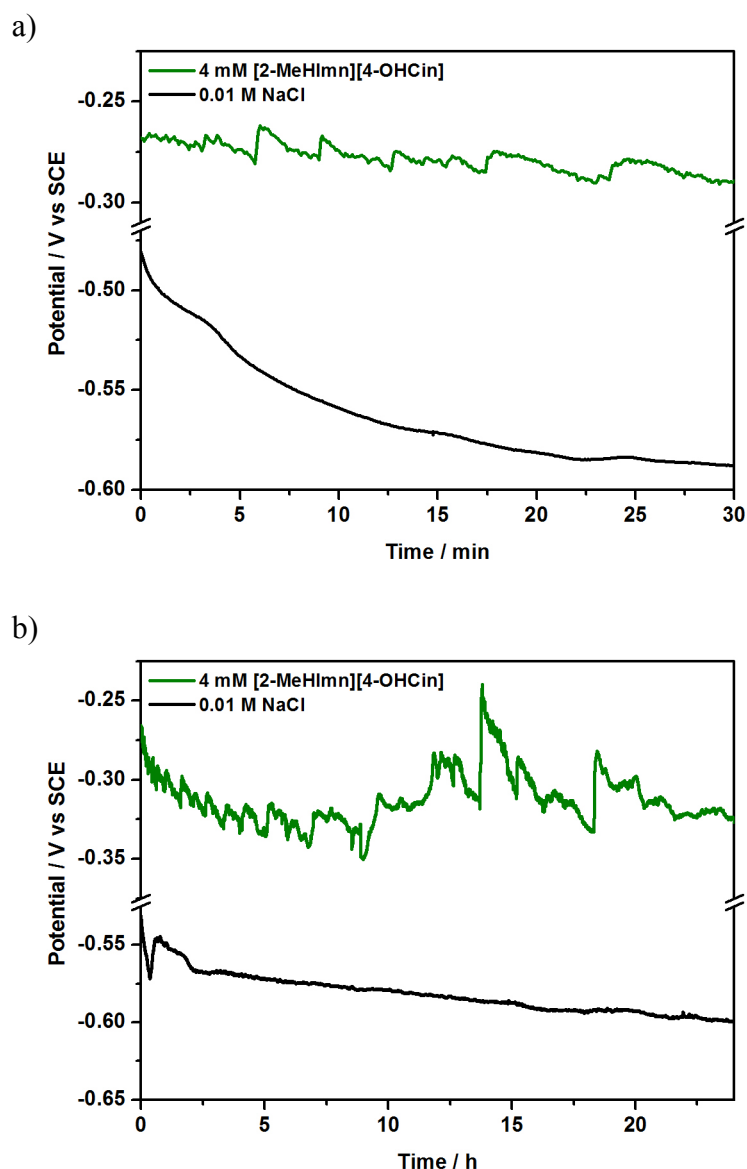


Figure 16. Comparison of OCP with and without 4 mM [2-MeHImn][4-OHCin] over a) 30 min and b) 24h. The inhibitor caused a substantial increase in OCP instability.

Figure 17 demonstrates the effect of adding the inhibitor after the electrode has already been exposed to the corroding solution. The cell was setup with 60 mL of 0.01 M

NaCl and the OCP measured for 30 min. After this 40 mL of 10 mM [2-MeHImn][4-OHCin] was added to give a total concentration of 4 mM [2-MeHImn][4-OHCin]. Addition of the inhibitor caused an instantaneous ennoblement of the electrode, showing that the compound remains active after corrosion products have begun to form on the surface. This is important for applications where inhibitors are used as periodic additives to systems where corrosion processes may already be taking place. The inhibitor also introduced instability to the OCP, confirming that the phenomenon is related to activity of the compound.

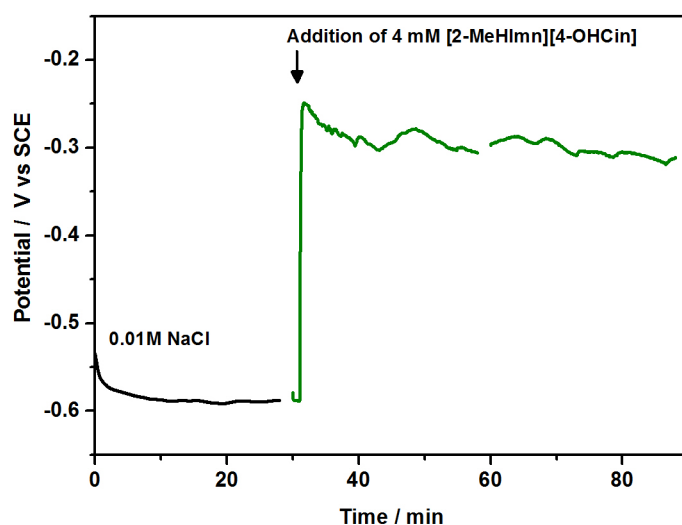


Figure 17. Addition of inhibitor after 30 min OCP hold in 0.01 M NaCl. The inhibitor ennobled the electrode, but introduced instability in the OCP.

A second irregularity was observed in the polarisation experiments. In all measurements, after the OCP hold, the potential was increased at a decade / min in the anodic direction, starting at -50 mV from OCP. It was observed, however, that in some cases this cathodic polarisation was altering E_{corr} , causing it to shift to more anodic potentials than expected. An example of this shift is shown in Figure 18. An initial polarisation (-10 mV to +10 mV vs. OCP), was carried out directly after the OCP hold to give an indication of the state of the electrode. Following this, the full anodic polarisation from -50 mV was carried out. It can be seen that E_{corr} is shifted 53 mV in the anodic direction.

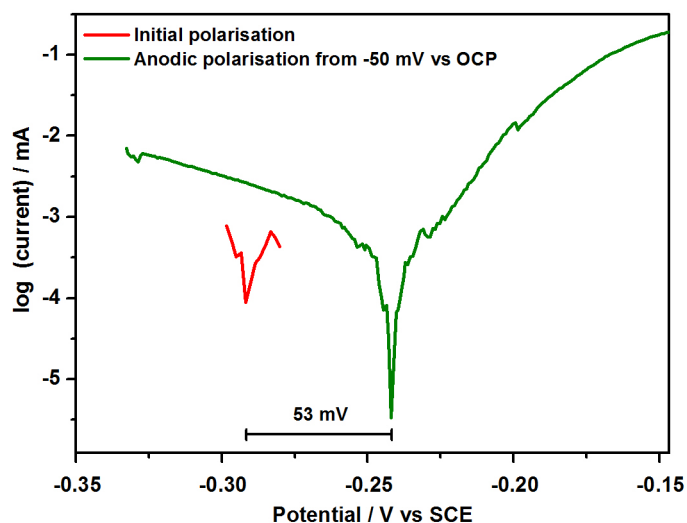


Figure 18. Starting the anodic polarisation from -50 mV vs. OCP resulted in a 53 mV shift in E_{corr} relative to E_{corr} at the end of the OCP hold (initial polarisation).

Table 5 presents a summary of the shift in E_{corr} (ΔE_{corr}) that was observed between the first and second polarisation steps for each inhibitor. At a concentration of 4 mM, the combined imidazolinium cinnamate inhibitors were disproportionately more affected than the other samples. 4 mM [2-MeHIm][4-OHCin] and the control showed a moderate ΔE_{corr} and there was no significant difference observed for 4 mM [Na][4-OHCin].

Table 5. Comparison of shift in E_{corr} resulting from cathodic polarisation.

Inhibitor	Initial E_{corr} / mV	Final E_{corr} / mV	ΔE_{corr} / mV
0.01 M NaCl control	-588 ± 4	-571 ± 5	17
4 mM [Na][4-OHCin]	-280 ± 40	-277 ± 3	-3
4 mM [2-MeHImn][4-OHCin]	-293 ± 5	-240 ± 2	53
0.01 mM [2-MeHImn][4-OHCin]	-240 ± 20	-225 ± 3	15
0.05 mM [2-MeHImn][4-OHCin]	-195 ± 4	-197 ± 4	-2
4 mM [2-MeHIm][4-OHCin]	-300 ± 30	-268 ± 7	32
4 mM [triMeImn][4-OHCin]	-268 ± 9	-228 ± 2	40
4 mM [2-MeHImn][4-OHCin] (24 h OCP)	-326 ± 2	-333 ± 3	-7
0.01 M NaCl + 4 mM [2-MeHImn] [4-OHCin] added after 30 min OPC	-310 ± 7	-303 ± 10	7

Interestingly, increasing the concentration of [2-MeHImn][4-OHCin] reduced the cathodic overpotential effect, such that in 0.05 M [2-MeHImn][4-OHCin], there was no significant difference between the initial and final E_{corr} values. Holding the OCP for 24 h and adding the inhibitor after exposure to the corroding solution also had the same effect on the E_{corr} values.

Competing redox reactions are a common cause of errors when using polarisation methods to determine corrosion behaviour.¹ It is possible that such a reaction is the source of the irregularities with the imidazolium cinnamate compounds, as well as the source of the synergistic effects.

The electrochemical windows of [2-MeHImn][4-OHCin] and its component ions were measured to assess the stability of the compounds. Platinum wire working and counter electrodes and an aqueous Ag/Ag^+ reference were placed in a cell with degassed 0.01 M aqueous salt solutions. The resulting voltammograms are shown in Figure 19. All three salts were stable to the limit of water reduction at -1 V vs. SCE. Both [4-OHCin]⁻ salts were stable to the positive aqueous limit (water oxidation) as well. [2-MeHImn][Br] showed reduced oxidative stability, due to oxidation of the bromide from 500 mV. There was, however, a small reduction process in [Na][4-OHCin] and [2-MeHImn][4-OHCin] with an onset around -200 mV. This could be the process taking place at the steel interface in the corrosion measurements.

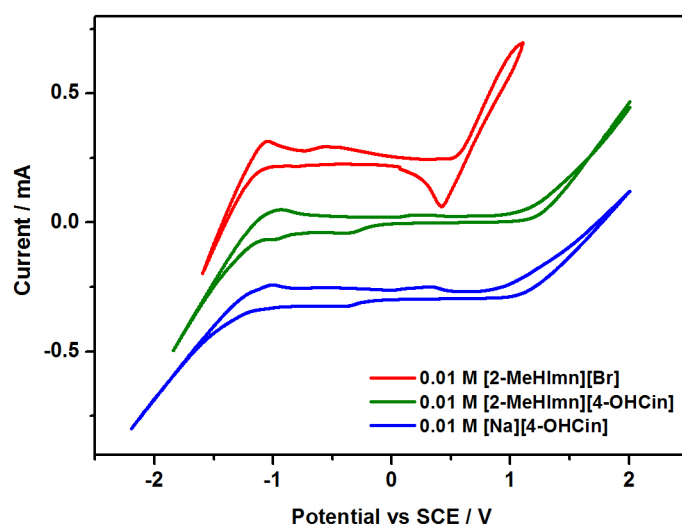


Figure 19. Electrochemical windows for [2-MeHImn][4-OHCin] and component ion salts. Potential was measured vs. Ag/Ag^+ but has been adjusted to vs. SCE for comparison to polarisation data.

A number of different studies have shown the electrochemical reduction of cinnamic acids and related compounds. The double bond is broken to yield the saturated carboxylic acid, hydrodimers, cycloaddition products or polymeric products (Figure 20).¹⁴⁻¹⁸ The suggested mechanism for dimerisation involves the formation of a radical species that subsequently reacts with another acid molecule. This can be induced electrochemically or photochemically.¹⁸

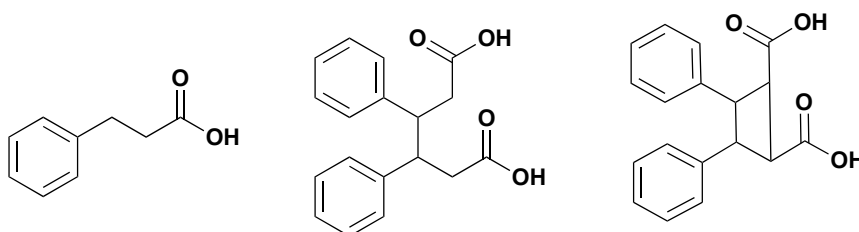


Figure 20. Products obtained from the electrochemical reduction of cinnamic acid (l to r): β -phenylpropionic acid, β - γ -diphenyladipic acid, γ -truxillic acid.

While the conditions required to reduce the acid in appreciable yields are more aggressive than those in this study, there is precedent for this reaction to take place on steel¹⁸ and in the presence of amines.¹⁹ In the present system, imidazoline-assisted reduction of the cinnamate could take place, resulting in a dimeric or polymeric species such as in Figure 20. It is possible that this process also takes place in solution, in the absence of an electrochemical driving force. If allowed to sit for a period of weeks, a fibrous precipitate forms in the combined inhibitor solutions that cannot be redissolved with heating or sonication (Figure 21). IR spectroscopy of the precipitate showed many of the same bands as the [2-MeHImn][4-OHCin] powder, indicating that the same species are present. Bands at 1606 cm^{-1} and 1286 cm^{-1} indicated the presence of the imidazolinium cation. The bands attributed to the cinnamate were also present, including the C=C stretch at 1633 cm^{-1} . This indicates that the bulk of the material did not significantly chemically change, however the appearance of additional bands between $800 - 1100\text{ cm}^{-1}$ and a shoulder on the band at 1250 cm^{-1} could suggest some other species were also present.

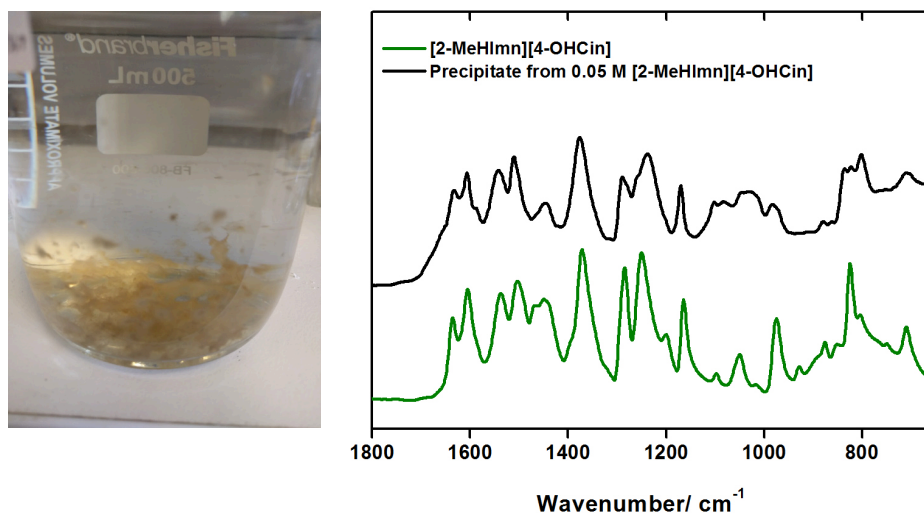


Figure 21. IR spectrum of precipitate from electrolyte solution 0.05 M [2-MeHImn][4-OHCin] in 0.01 M NaCl.

Such a reduction process taking place at the steel surface could cause the observed fluctuations in OCP and form a protective film, that provides better protection than if [4-OHCin]⁻ was simply adsorbed to the surface. The imidazolium cations facilitate this process, and may also adsorb to the surface, to synergistically enhance inhibition. On their own, however, they are largely ineffective without any bulky substituents.

A cathodic overpotential, such as that applied during the polarisation test, could increase the rate of the reaction, enhancing the surface film. This could explain the anodic shift in E_{corr} and the reduction in i_{corr} that was induced in the 4 mM dual-active inhibitor solutions. If the conditions are changed to allow better film formation prior to the measurement, for instance a longer immersion time, or increased inhibitor concentration, then the cathodic enhancement may not be noticeable.

From a corrosion protection perspective, the synergistic effects of any film-forming behaviour could be beneficial, provided controls can be put in place to manage unwanted precipitation of the inhibitor. From a testing perspective, however, the methods used in this research were not entirely compatible with the inhibitors' behaviour.

Although the OCP fluctuations are unavoidable in electrochemical tests, there are a number of ways in which the experimental procedure could be adjusted to remove the cathodic overpotential effect. As seen in Table 5, increasing the OCP rest period, or increasing the concentration eliminated ΔE_{corr} . Drawbacks to these methods, however, include the increased testing time and greater inhibitor quantities required.

Measuring the cathodic and anodic arms in separate tests removed the cathodic overpotential changes to E_{corr} (Figure 22). After OCP for 30 min, the electrode was scanned in the cathodic or anodic direction. For each test, i_{corr} was determined to be the intercept between E_{corr} and the slope of the single anodic or cathodic curve in the Tafel regions (10 mV to 25 mV).¹ This method produced a value twice as large as the single polarisation measurement, suggesting that the excursion in the cathodic directions before starting the polarisation scan modifies the surface and leads to a more protective surface compared to simply scanning anodically or cathodically from OCP. The uncertainty on this value is increased by the separation of the Tafel slopes. Starting the polarisation scan at OCP can make it difficult to determine where E_{corr} is; particularly in this situation, where the OCP is unstable, the scan may not pass through the actual E_{corr} . It is also not possible to match the intercept of the two slopes to each other, and so the calculations rely on the assumption that they will be the same at E_{corr} . In this analysis, it was found that the anodic scans predicted a higher i_{corr} than the cathodic scans. Because of these uncertainties, there is an error of over 30 % associated with the value.

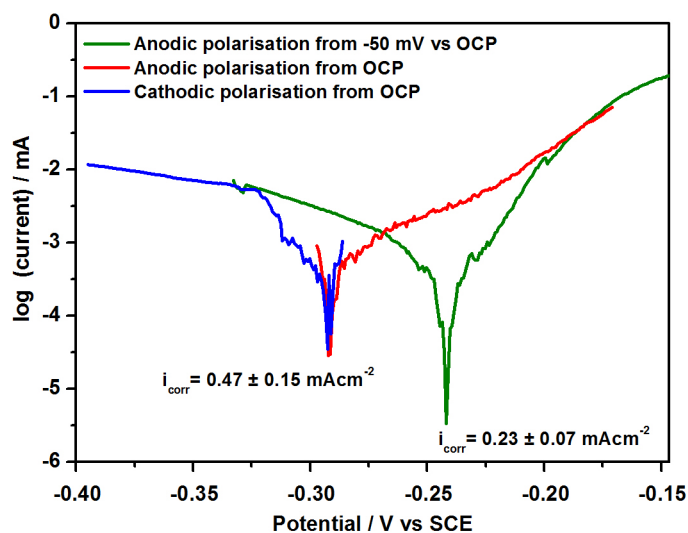


Figure 22. Measurement of the anodic and cathodic arms separately resulted in an increased estimation of i_{corr} .

In many cases, a relatively small cathodic overpotential does not impact upon the results of the test, and previous studies of cinnamate complexes have started the anodic polarisation measurement from -100 mV or -200 mV vs. OCP without encountering issues.²⁰⁻²² The reactivity of the salts presented in this study, and the impact that this had on the polarisation measurements, is a reminder of the importance of using a well-rounded

approach to inhibitor evaluation by combining electrochemical experiments with long-term immersion testing.

3.3 Alkylated Imidazoliums

This section discusses the synthetic route used to produce [triMeImn][4-OHCin] and a suite of similar *N*-substituted imidazolium compounds.

3.3.1 Synthetic Routes

While a number of different methods have been described in the literature for the preparation of *N*-substituted imidazolium salts, the most popular approach exploits alkylation of diamines. In this manner, a diamine is reacted with an orthoester (as the C1 building-block) in the presence of an appropriate acid to effect cyclisation (Figure 23, eq. 1).²³⁻²⁷ This method was used to synthesise the unsubstituted salts reported in Chapter 2. Another complementary route is to use the substituted formamidine with a reactant that provides the C4-C5 building block (i.e. dihaloalkenes²⁸ or cyclic sulfates²⁹ (Figure 23, eq. 2). Gruseck and Heuschmann³⁰ and Ye et al.³¹ further developed methods for the *N*-substitution of 2-methylimidazoline (2-MeImn), by first deprotonating with a strong base (NaH, BuLi) and subsequently alkylating with the desired haloalkane (Figure 23, eq. 3).

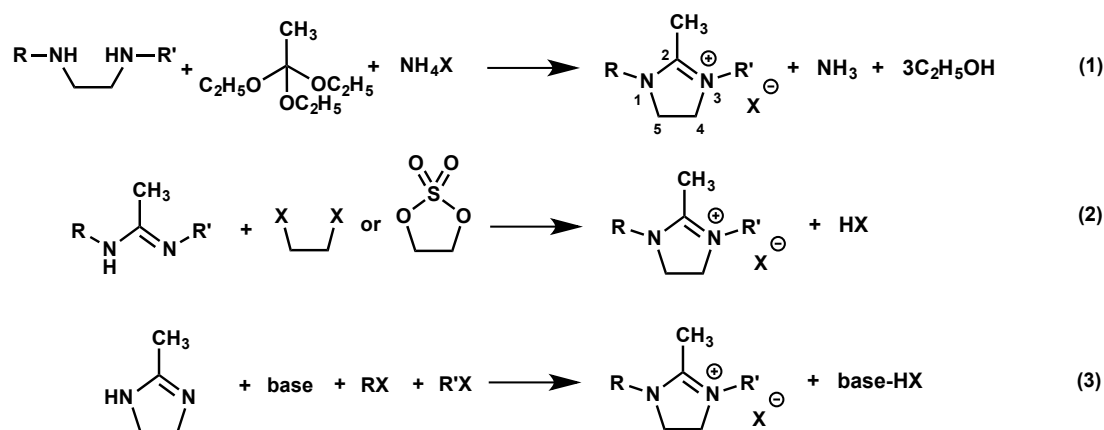


Figure 23. Reaction scheme for synthesis of *N*-substituted 2-methylimidazolium salts.

1,2,3-Trimethylimidazolium tetrafluoroborate, [triMeImn][BF₄], was synthesised following the orthoester exchange method described by Saba et al.²⁷ A flask charged with *N,N'*-dimethylethylenediamine, ammonium tetrafluoroborate and excess triethylorthoacetate was heated, neat, to 120 °C for 3 hours (Table 6, entry 1). Upon completion, the reaction mixture was cooled and the solvent removed under reduced pressure, with the resulting

compound recrystallisation from DCM and ethyl acetate. This was carried out with an isolated yield of 80 %.

Some modifications to the experimental conditions were investigated, as suggested by Alder et al.²³ (Table 6). The authors suggested using 1.5 equivalents of the anion source (Table 1, entry 2), as well as one equivalent of orthoester with ethanol as a solvent (Table 1, entry 3). These adjustments gave similar yields; increasing the amount of NH_4BF_4 gave a slightly reduced yield, while introducing ethanol as a solvent slightly increased the yield. In subsequent syntheses, the latter method employing ethanol as solvent was utilised due to the milder reaction temperatures minimising potential loss of diamine through evaporation (b.p. = 110 °C).

An advantage of the orthoester exchange protocol is that the anion source (as an ammonium salt or acid) can be altered to give a range of salts in a one-pot reaction. However, the range of *N*-substituents is dependent on the availability of the appropriate diamine.

Table 6. Optimisation of reaction conditions for synthesis of [triMeImn][BF₄].

Entry	X equiv.	Y equiv.	Solvent	Temp. / °C	Time / h	yield / %
1	excess	1.03	–	120	3	84
2	excess	1.4	–	120	3	75
3	1.04	1.06	EtOH	90	16	80

Alkylation of 2-MeImn was also explored. Following a procedure from Ye et al.,³¹ 1,3-diethyl, 2-methylimidazolium iodide, [diEtMeImn][I], was obtained via lithiation at the N1 position and stepwise addition of iodoethane (EtI, Figure 24). The initial alkylation installing a substituent at N1 of the imidazoline proved challenging, with over-alkylation at N3 constituting a major side-product when the more reactive iodomethane was employed in this transformation. When EtI was utilised in this synthesis sequence, it was possible to isolate mono-alkylated 1-ethyl, 2-methylimidazoline, which was directly used in the second alkylation step, delivering the desired salt. After recrystallisation from acetonitrile and ethyl acetate, the product was obtained in an 18 % yield.

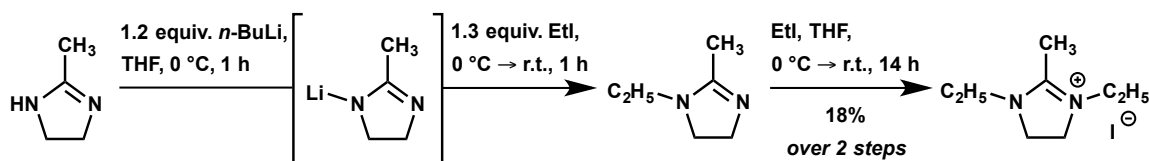


Figure 24. Reaction scheme for synthesis of 1,3-diethyl,2-methylimidazolium iodide via lithiation and alkylation with iodoethane.

Due to the inefficient nature of this synthetic sequence compared to the orthoester route (i.e. Table 6) for the synthesis of small alkyl chain imidazolium cations, further investigations were abandoned. In instances where the appropriate diamine can be purchased or readily synthesised, the simpler route was employed.

However, step-wise alkylation could prove useful for the synthesis of larger or asymmetric cations. It should be noted that Jones and Dimopoulos³² have reported the use of common protecting group *tert*-butoxycarbonyl (Boc), to access *N*-unsubstituted, 2-substituted imidazolines from 2-MeImn following a similar metallation and alkylation of the C-2 α -carbon. A combination of these approaches could provide a method for selectively alkylating 2-MeImn from the N1, N3 or C2 positions.

3.3.2 A Family of Alkylated Imidazolium Cations

Using the method adapted from Alder et al.²³ (Table 6, entry 3), a number of alkylated 2-methylimidazolium salts were synthesised, predominantly with a bromide counter anion (Figure 25). A summary of these salts is presented in Table 7. Where the ammonium salt was not available, the acid was used as an anion source. The [triMeImn]⁺ salts bearing the tetrafluoroborate and salicylate counter ion have been reported previously.^{27, 30, 33}

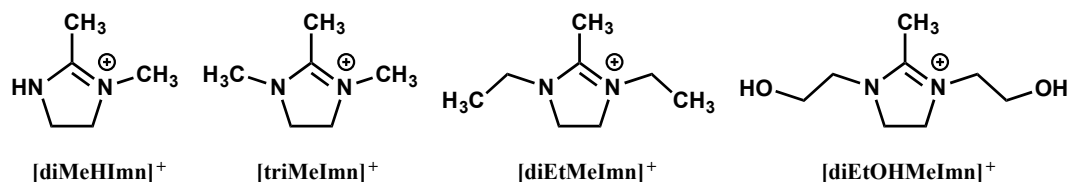


Figure 25. A selection of imidazolium cations synthesised via the orthoester route (l to r): 1,2-dimethylimidazolium, 1,2,3-trimethylimidazolium, 1,3-diethyl,2-methylimidazolium and 1,3-bis(hydroxyethyl),2-methylimidazolium.

Table 7. Alkylated imidazolinium salts synthesised by orthoester exchange (Figure 23, eq. 1).

Sample	R	R'	Anion source	Yield / %	T _m / °C	T _d / °C
[triMeImn][BF ₄]	Me	Me	NH ₄ BF ₄	84	206	366
[triMeImn][Br]*	Me	Me	NH ₄ Br	86	188	365
[triMeImn][Sal]	Me	Me	SalH	30	100	299
[triMeImn][4-OHCin]*	Me	Me	4-OHCinH	90	145 ^d	160
[diMeHImn][BF ₄]*	Me	H	NH ₄ BF ₄	52	110	343
[diMeHImn][Br]*	Me	H	NH ₄ Br	57	140	345
[diMeHImn][4-OHCin]*	Me	H	4-OHCinH	91	125 ^d	144
[diEtMeImn][Br]*	Et	Et	NH ₄ Br	18	155	351
[diEtOHMeImn][Br]*	EtOH	EtOH	NH ₄ Br	16	138	276

*First reported synthesis; ^d decomposition

Although it should be noted that the yields were not optimised, generally it was found that the [triMeImn]⁺ salts were obtained in the highest yields. The yield for [triMeImn][BF₄] was lower than that obtained by Saba et al.²⁷ but comparable to Gruseck and Heuschmann.³⁰ The melting points were also consistent. The particularly low yields obtained for the larger salts [diEtMeImn][Br] and [diEtOHMeImn][Br] are related to difficulties in purification. It was found that as a co-solvent ethyl acetate aided the recrystallisation, however when it was subsequently used to wash the filtered crystals, an oily residue was generated, resulting in loss of product. Cold acetone was found to be a superior solvent for this purpose.

Observing the series of bromide salts, a general trend emerged in the thermal data. Compared to the unsubstituted [2-MeHImn][Br] (T_m = 148 °C), [triMeImn][Br] is more symmetrical, and hence had a higher melting point. However, as the length of the alkyl substituents was increased with [diEtMeImn][Br] and [diEtMeImn][Br], the melting point decreased. This was due to the increased bulk disrupting effective crystal packing. [diMeHImn][Br] had the lowest melting point, due to the asymmetry of the compound.

It would be interesting to compare the cinnamate salts of these cations to the protic [2-MeHImn][4-OHCin], and aprotic [triMeImn][4-OHCin] compounds. In terms of inhibition, it could be expected that the addition of hydroxyethyl functional groups would improve the adsorption of [diEtOHMeImn]⁺ to the steel surface. [diMeHImn]⁺ is also an interesting potential inhibitor. Computational DFT calculations and electrochemical studies by Turcio-Ortega et al.³⁴ showed that this compound was a better inhibitor than

[2-MeHImn]⁺ for mild steel in aqueous HCl. They suggested this was related to the preferred binding mechanisms of the compounds with iron. While the most stable conformation of [2-MeHImn]⁺ involved binding with the ring perpendicular to the surface, [diMeHImn]⁺ was predicted to approach with the ring face parallel to the surface. This would provide greater coverage and protection from corrosive species.

3.4 Conclusions

[2-MeHImn][4-OHCin] showed excellent inhibition on mild steel at high concentrations, but was also effective at concentrations as low as 1 mM. Long-term immersion testing, however, did show that at these lower concentrations, the imidazolium promoted the formation of substantial pits that could not be repassivated.

In an unusual result for organic inhibitors, [2-MeHImn][4-OHCin] was found to inhibit corrosion at both elevated and reduced pH levels. At pH 8, the combined inhibitor performed similarly to [Na][4-OHCin], likely due to adsorption of the anion to the surface. Most carboxylate inhibitors would protonate in acidic environments, making them less effective at migrating to the surface and adsorbing, and [Na][4-OHCin] showed this behaviour, with low inhibition at pH 2. However, the combined inhibitor had an inhibition efficiency of 72 %, and immersion testing showed a dramatic decrease in corrosive attack compared to the control. This indicates that some interaction between the imidazolium and cinnamate species causes a synergistic effect.

This synergy was supported by measurements carried out with a mixture of the two component salts, as well as the imidazolium analogue. In both cases, neither showed performance that matched [2-MeHImn][4-OHCin]. The similarity between [2-MeHImn][4-OHCin] and [triMeImn][4-OHCin], showed that the inhibition mechanism common to imidazolium salts, and not specific to the protic cation.

A proposed explanation for the observed synergy, is the imidazolium-assisted formation of a reduced cinnamate species that forms a protective film on the surface. This model could explain both the unexpected inhibition at low pH, as well as unusual behaviour observed in the electrochemical measurements of the combined inhibitor.

Based on the high level of inhibition observed for cinnamate salts of both [2-MeHImn]⁺ and [triMeImn]⁺, there is great potential for improvement by further modifying the imidazolium cation. A number of synthetic paths for achieving this were identified and a selection of novel salts were presented as proof-of-concept.

3.5 Experimental Methods

3.5.1 Materials

All chemicals were purchased from Sigma and were >98 % pure. They were used without further purification. Solvents were purchased from Sigma Aldrich, Merck and Fluka. Methanol (MeOH) was distilled from sodium metal and stored over 4A molecular sieves. Tetrahydrofuran (THF) was distilled over sodium with benzophenone and stored over 4A molecular sieves. Acetone, ethanol (EtOH), acetonitrile (MeCN), ethyl acetate (EtOAc) and dichloromethane (DCM) were all dried over 4A molecular sieves.

3.5.2 Synthesis

3.5.2.1 2-Methylimidazolium 4-hydroxycinnamate

2-methylimidazole (1.4 g, 16.4 mmol) and 4-hydroxycinnamic acid (2.6 g, 16.4 mmol) were dissolved in a 1:1 mixture of methanol and acetonitrile. The mixture was stirred at room temperature under nitrogen overnight. The solvent was removed via rotary evaporation and the product dried under high vacuum at 60 °C to yield a pale brown solid (4.0 g, 100%). ¹H NMR (400 MHz, DMSO-*d*₆) δ (ppm): 2.26 (s, 3H, CH₃), 6.26-6.30 (d, *J* = 16.0, 1H, CH), 6.78-6.80 (d, *J* = 8.7, 2H, 2x aromatic CH), 3.63 (s, 2H, imidazolium CH=CH) 7.46-7.50 (d, *J* = 16.0, 1H, CH), 7.49-7.51 (d, *J* = 8.6, 2H, 2x aromatic CH). ¹³C NMR (400 MHz, DMSO-*d*₆) δ (ppm): 13.5 (CH₃), 115.8 (2 x aromatic), 115.9 (2 x C=C), 121.1 (2 4° aromatic), 125.3 (C=C), 130.0 (2 x aromatic), 143.6 (N-C=N), 143.8 (C=C), 159.7 (4° aromatic), 166.1, 171.0 (C=O). MS: ES⁺ *m/z* 83.0 [2-MeHIm]⁺; ES⁻ *m/z* 119.0 [C₆H₄CCHOH]⁻, 163.0 [4-OHCin]⁻.

3.5.2.2 1,2,3-Trimethylimidazolium tetrafluoroborate, [triMeImn][BF₄]

Neat synthesis: *N,N'*-dimethylethylenediamine (0.9 g, 9.7 mmol), triethylorthoacetate (4.2 g, excess) and ammonium tetrafluoroborate (1.4 g, 13.7 mmol) were added to a flask. The mixture was stirred at 120 °C for 3 h with a reflux condenser attached. Upon completion, the reaction mixture was cooled and the resulting precipitate was filtered. The solid was dissolved in a minimum volume of DCM and filtered to remove excess ammonium tetrafluoroborate. The desired product was triturated through addition of hot EtOAc to yield fine white needles (1.2 g, 80 %).

Ethanol synthesis: *N,N'*-dimethylethylenediamine (1.0 g, 11.5 mmol), triethylorthoacetate (1.9 g, 12.0 mmol) and ammonium tetrafluoroborate (1.3 g, 13.7 mmol) were added to a flask charged with ethanol (10 mL). The mixture was stirred at

reflux (90 °C) overnight. Upon completion, the reaction mixture was cooled and concentrated under reduced pressure. The resulting orange precipitate was dissolved in a minimum volume of DCM and filtered to remove excess ammonium tetrafluoroborate. The desired product was triturated through addition of hot EtOAc to yield fine white needles (1.9 g, 84 %). ¹H NMR (400 MHz, DMSO-*d*₆) δ (ppm): 2.20 (s, 3H, CH₃), 3.03 (s, 6H, 2 x CH₃), 3.76 (s, 4H, 2 x CH₂). ¹³C NMR (400 MHz, DMSO-*d*₆) δ (ppm): 10.0 (CH₃), 33.3 (2 x CH₃), 49.3 (2 x CH₂), 166.2 (N-C=N). MS: ES⁺ m/z 113.2 [triMeImn]⁺, 313.2 2[triMeImn]⁺[BF₄]⁻; ES⁻ m/z 87.1 [BF₄]⁻.

3.5.2.3 1,2,3-Trimethylimidazolinium Bromide, [triMeImn][Br]

N,N'-dimethylethylenediamine (3.3 g, 37.0 mmol), triethylorthoacetate (6.4 g, 39.1 mmol) and ammonium bromide (3.9 g, 39.3 mmol) were reacted using the ethanol synthesis route and recrystallised from DCM/ EtOAc to yield hygroscopic white needles (6.2 g, 86 %). ¹H NMR (400 MHz, DMSO-*d*₆) δ (ppm): 2.22 (s, 3H, CH₃), 3.04 (s, 6H, 2 x CH₃), 3.77 (s, 4H, 2 x CH₂). ¹³C NMR (400 MHz, DMSO-*d*₆) δ (ppm): 10.1 (CH₃), 33.4 (2 x CH₃), 49.4 (2 x CH₂), 166.2 (N-C=N). MS: ES⁺ m/z 113.2 [triMeImn]⁺.

3.5.2.4 1,2,3-Trimethylimidazolinium Salicylate, [triMeImn][Sal]

N,N'-dimethylethylenediamine (0.4 g, 5.0 mmol), triethylorthoacetate (0.9 g, 5.5 mmol) and salicylic acid (0.7 g, 5.3 mmol) were reacted using the ethanol synthesis route and recrystallised from acetone to yield hygroscopic white needles (0.4 g, 30 %). ¹H NMR (400 MHz, DMSO-*d*₆) δ (ppm): 2.20 (s, 3H, CH₃), 3.03 (s, 6H, 2 x CH₃), 3.76 (s, 4H, 2 x CH₂), 6.52 - 6.58 (m, 2H, 2 x aromatic), 7.07 - 7.11 (td, *J* = 1.6 Hz, 7.6 Hz, 1H, aromatic), 7.61 - 7.63 (dd, *J* = 1.6 Hz, 7.6 Hz, 1H, aromatic). ¹³C NMR (400 MHz, DMSO-*d*₆) δ (ppm): 10.0 (CH₃), 33.3 (2 x CH₃), 49.3 (2 x CH₂), 115.5 (4° aromatic), 115.7 (aromatic), 129.8 (aromatic), 131.0 (aromatic), 163.2 (4° aromatic), 166.1 (N-C=N), 171.0 (C=O). MS: ES⁺ m/z 113.2 [triMeImn]⁺; ES⁻ m/z 137.1 [Sal]⁻.

3.5.2.5 1,2,3-Trimethylimidazolinium 4-hydroxycinnamate, [triMeImn][4-OHCin]

N,N'-dimethylethylenediamine (1.3 g, 14.4 mmol), triethylorthoacetate (2.6 g, 15.8 mmol) and 4-hydroxycinnamic acid (2.5 g, 15.7 mmol) were reacted using the ethanol synthesis route. The precipitate was washed with EtOAc to remove excess acid (3.6 g, 90 %). ¹H NMR (400 MHz, DMSO-*d*₆) δ (ppm): 2.18 (s, 3H, CH₃), 3.01 (s, 6H, 2 x CH₃), 3.73 (s, 4H, 2 x CH₂), 6.13 - 6.17 (d, *J* = 15.8, 1H, CH), 6.76 - 6.78 (d, *J* = 8.6 Hz, 2H, 2 x aromatic), 7.00 - 7.04 (d, *J* = 15.8 Hz, 1H, CH), 7.22 - 7.24 (d, *J* = 8.6 Hz, 2H, 2 x aromatic). ¹³C NMR (400 MHz, DMSO-*d*₆) δ (ppm): 10.0 (CH₃), 33.3 (2 x CH₃), 49.3 (2 x

CH₂), 115.5 (2 x aromatic), 125.7 (C=C), 126.4 (4° aromatic), 128.2 (2 x aromatic), 136.0 (C=C), 163.2 (4° aromatic), 166.1 (N-C=N), 171.0 (C=O). MS: ES⁺ m/z 113.2 [triMeImn]⁺; ES⁻ m/z 163.1 [4-OHCin]⁻.

3.5.2.6 1,2-Dimethylimidazolinium tetrafluoroborate, [diMeHImn][BF₄]

N-methylethylenediamine (0.6 g, 7.9 mmol), triethylorthoacetate (1.4 g, 8.4 mmol) and ammonium tetrafluoroborate (0.9 g, 8.3 mmol) were reacted using the ethanol synthesis route and recrystallised from DCM/ EtOAc to yield pale yellow plates (0.8 g, 52 %). ¹H NMR (400 MHz, DMSO-*d*6) δ (ppm): 2.16 (s, 3H, CH₃), 3.00 (s, 3H, CH₃), 3.69 – 3.84 (m, 4H, 2 x CH₂). ¹³C NMR (400 MHz, DMSO-*d*6) δ (ppm): 11.8 (CH₃), 32.9 (CH₃), 42.9 (CH₂) 51.6 (CH₂), 167.5 (N-C=N). MS: ES⁺ m/z 99.1 [diMeHImn]⁺; ES⁻ m/z 87.1 [BF₄]⁻.

3.5.2.7 1,2-Dimethylimidazolinium bromide, [diMeHImn][Br]

N-methylethylenediamine (1.0 g, 14.0 mmol), triethylorthoacetate (2.4 g, 15.0 mmol) and ammonium bromide (1.5 g, 15.7 mmol) were reacted using the ethanol synthesis route and recrystallised from DCM/ acetone to yield white needles (1.4 g, 57 %). ¹H NMR (400 MHz, DMSO-*d*6) δ (ppm): 2.20 (s, 3H, CH₃), 3.01 (s, 3H, CH₃), 3.70 – 3.86 (m, 4H, 2 x CH₂). ¹³C NMR (400 MHz, DMSO-*d*6) δ (ppm): 11.4 (CH₃), 32.5 (CH₃), 42.2 (CH₂) 51.1 (CH₂), 167.0 (N-C=N). MS: ES⁺ m/z 99.1 [diMeHImn]⁺.

3.5.2.8 1,2-Dimethylimidazolinium 4-hydroxycinnamate, [diMeHImn][4-OHCin]

N-methylethylenediamine (0.4 g, 4.5 mmol), triethylorthoacetate (0.8 g, 4.7 mmol) and 4-hydroxycinnamic acid (0.8 g, 4.7 mmol) were reacted using the ethanol synthesis route. The precipitate was washed with EtOAc to remove excess acid (1.7 g, 91 %). ¹H NMR (400 MHz, DMSO-*d*6) δ (ppm): 1.94 (s, 3H, CH₃), 2.81 (s, 3H, CH₃), 3.35 – 3.39 (t, *J* = 9.6 Hz, 2H, CH₂), 3.51 – 3.55 (t, *J* = 9.6, 2H, CH₂) 6.22 - 6.23 (d, *J* = 16.0 Hz, 1H, CH), 6.75 – 6.77 (d, *J* = 8.4 Hz, 2H, 2 x aromatic), 7.26 – 7.30 (d, *J* = 16.0 Hz, 1H, CH), 7.38 – 7.41 (d, *J* = 8.4 Hz, 2H, 2 x aromatic). ¹³C NMR (400 MHz, DMSO-*d*6) δ (ppm): 11.8 (CH₃), 32.6 (CH₃), 44.8 (CH₂) 51.4 (CH₂), 115.7 (2 x aromatic), 121.7 (C=C), 126.2 (4° aromatic), 129.0 (2 x aromatic), 139.3 (C=C), 159.1 (4° aromatic), 166.4 (N-C=N), 170.2 (C=O). MS: ES⁺ m/z 99.2 [diMeHImn]⁺; ES⁻ m/z 163.1 [4-OHCin]⁻.

3.5.2.9 1,3-Diethyl, 2-methylimidazolinium bromide, [diEtMeImn][Br]

N,N'-diethylethylenediamine (0.9 g, 7.7 mmol), triethylorthoacetate (1.3 g, 8.1 mmol) and ammonium bromide (0.8 g, 8.1 mmol) were reacted using the ethanol synthesis

route and recrystallised from MeCN/ acetone to yield white needles (0.3 g, 18 %). ^1H NMR (400 MHz, DMSO-*d*₆) δ (ppm): 1.12 - 1.16 (t, $J = 7.2$, 6H, 2 x CH₃), 2.27 (s, 3H, CH₃), 3.44 – 3.49 (q, $J = 7.2$, 4H, 2 x CH₂), 3.81 (s, 4H, 2 x CH₂). ^{13}C NMR (400 MHz, DMSO-*d*₆) δ (ppm): 10.0 (CH₃), 12.3 (2 x CH₃), 41.0 (2 x CH₂), 46.4 (2 x CH₂), 165.0 (N-C=N). MS: ES⁺ m/z 141.1 [diEtMeImn]⁺.

3.5.2.10 1,3-Bis(hydroxyethyl), 2-methylimidazolium bromide, [diEtOHMeImn][Br]

N,N'-bis(hydroxyethyl)ethylenediamine (1.2 g, 7.8 mmol), triethyl-orthoacetate (1.3 g, 8.3 mmol) and ammonium bromide (0.9 g, 8.7 mmol) were reacted using the ethanol synthesis route and recrystallised from hot EtOH to yield white needles (0.3 g, 16 %). ^1H NMR (400 MHz, DMSO-*d*₆) δ (ppm): 2.26 (s, 3H, CH₃), 3.34 – 3.52 (m, 4H, 2 x CH₂), 3.56 – 3.60 (m, 4H, 2 x CH₂), 3.87 (s, 4H, 2 x CH₂), 5.00 – 5.02 (t, $J = 5.6$ Hz, 2H, OH) . ^{13}C NMR (400 MHz, DMSO-*d*₆) δ (ppm): 10.8 (CH₃), 47.4 (2 x CH₂), 48.8 (2 x CH₂), 57.3 (2 x CH₂), 166.7 (N-C=N). MS: ES⁺ m/z 173.1 [diEtOHMeImn]⁺.

3.5.2.11 1,3-Diethyl, 2-methylimidazolium iodide, [diEtMeImn][I]

Under N₂ gas flow, 2-methylimidazoline (1.5 g, 18.1 mmol) was added to a flask with 60 mL THF and cooled to 0 °C in an ice bath. *n*-BuLi (31 mL of a 1.6 M solution in hexane, 24.3 mmol) was added dropwise and a white precipitate formed. The ice bath was removed and the mixture stirred at ambient temperature for 30 min. The mixture was again cooled to 0 °C and iodoethane (1.9 mL, 23.5 mmol) was added dropwise. The mixture was stirred for 30 min at 0 °C and a further 30 min at ambient temperature, during which time the precipitate disappeared. Upon completion, the solvent was removed under reduced pressure and the mixture treated with 10 mL of 1 M NaOH aqueous solution, and 10 mL water. The product (*N*-ethyl, 2-methylimidazoline) was extracted into DCM. The organic layer was separated, concentrated under reduced pressure and the crude residue dissolved in 60 mL THF. The solution was cooled to 0 °C and a second equivalent of iodoethane (1.5 mL, 18.1 mmol) was added dropwise. The mixture was stirred overnight yielding a separated phase that subsequently solidified upon standing. This product was filtered and recrystallised from MeCN and EtOAc (0.86 g, 18 %). ^1H NMR (400 MHz, DMSO-*d*₆) δ (ppm): 1.30 – 1.33 (t, $J = 7.3$ Hz, 6H, 2 x CH₃), 2.38 (s, 3H, CH₃), 3.55 – 3.61 (q, $J = 7.3$ Hz, 4H, 2 x CH₂), 4.01 (s, 4H, 2 x CH₂). MS: ES⁺ m/z 141.1 [diEMeImn]⁺, 409.2 2[diEMeImn][I]⁺.

3.5.3 Characterisation

NMR spectra were recorded in DMSO-*d*₆ (Merck) using a Bruker Avance 400 (9.4 T magnet) fitted with a BACS 60 tube autosampler, operating at 400 MHz. Low resolution ESI mass spectra were recorded on a Micromass Platform II QMS with a cone voltage of 35 V, using methanol as the mobile phase.

DSC was carried out using a Perkin Elmer DSC 8000 with liquid nitrogen cryo cooler. Scans were run at a heating/cooling rate of 10 °C /min over a temperature range of -80 – 250 °C. Transition temperatures were reported using the peak maximum of the thermal transition. TGA was undertaken on a Mettler Toledo TGA/DSC 1 STARe System. Samples were heated at 10 °C /min over a temperature range of 25 – 550 °C.

3.5.4 Electrochemistry

All electrochemical measurements were carried out using a multi-channel potentiostat (VMP2, Princeton Applied Research). Experiments were carried out in a Faraday cage to prevent electrical interference. For cyclic voltammetry samples were dissolved in acetonitrile and used as the electrolyte in a three-electrode system with platinum working and counter electrodes and an aqueous Ag/ Ag⁺ reference. Measurements were carried out at a scan rate 20 mVs.⁻¹.

For the potentiodynamic polarisation experiments, AS1020 steel electrodes (Composition: 0.26 % C, 0.45 % Mn, 0.14 % Cr, 0.19 % Si, 0.18 % Al, 0.35 % Other, and balance Fe) with a 1.0 cm diameter (0.78 cm²) set in epoxy resin were used. They were abraded with silicon carbide paper to P1200 grit. The electrodes were washed with distilled water, dried and stored in a desiccator under vacuum. Potentiodynamic polarisation experiments were carried out one hour after electrode preparation.

4 mM, 0.01 M or 0.05 M test solutions were prepared by dissolving appropriate masses of each compound in 1L of 0.01 M sodium chloride solution (made with milliQ water). The pH of these solutions ranged from 6.5 – 7.0.

All polarisation experiments were carried out in an open-to-air, standard three-electrode system consisting of a SCE reference electrode with luggin attachment, a titanium mesh counter electrode, and the working electrode with 150 mL of test solution as the electrolyte.

After immersion the OCP was monitored for 30 min (or in some cases 24 h), and then the potentiodynamic polarisation experiment was carried out at a scanning rate of 0.167 mV s⁻¹. An initial scan from -10 to +10 mV vs. OCP was measured, and the

electrode rested for 5 min. Following this, scans started at 50 mV more negative than OCP and continued through OCP for a range of 250 mV in the positive direction. Replicate measurements were carried out. The i_{corr} values were calculated using Tafel extrapolation methods. Where anodic and cathodic curves were near linear within 25 mV from E_{corr} , both Tafel slopes were extrapolated until the lines intersected at E_{corr} .

Individual cathodic and anodic scans were measured directly after the OCP hold, for 250 mV in either direction from OCP. i_{corr} was calculated to be the intersect between E_{corr} and the Tafel slope extrapolated from the linear region within 25 mV from E_{corr} . From i_{corr} , the inhibitor efficiency (IE) was calculated according to Equation 1 (Section 3.1).

3.5.5 Surface Analysis

Steel coupons (1.0 cm² AS1020 steel coupons set in epoxy resin) were prepared in the same way as the electrodes for the immersion experiments. The coupons were immersed in 4 mM, 0.01 M or 0.05 M solutions of inhibitor in 0.01M NaCl for 24 hours or 7 days. The coupons were observed using a Leica MZ6 optical microscope at a magnification of x 0.8. The samples then had the corrosion product removed from the surface by immersion in a solution containing hydrochloric acid and hexamethylene tetramine, as detailed in ASTM G1-03 (2011).³⁵

For SEM analysis a JEOL NeoScope JCM-5000 benchtop scanning electron microscope was used at an accelerating voltage of 10kV. 3D surface profilometry was performed on a Bruker Contour GT-K1 3D optical microscope. Using the image analysis software, Vision 64, the number of pits deeper than 1 μm was detected for each of the 950 x 1267 μm scans. At least five representative areas for each sample were recorded and the number of pits per square mm were calculated. The average pit depth, maximum pit depth and the surface roughness, S_a were also calculated.

The IR spectrum of the precipitate formed in the 0.05 M [2-MeHImn][4-OHCIn] solution was obtained via diamond crystal ATR FTIR using a Perkin Elmer Frontier. 16 scans were co-added at a resolution of 4cm⁻¹.

3.6 References

1. R. G. Kelly, J. R. Scully, D. Shoesmith and R. G. Buchheit, *Electrochemical Techniques in Corrosion Science and Engineering*, Marcel Dekker, New York, 2002.
2. Y. Tan, M. Mocerino and T. Paterson, *Corros. Sci.*, 2011, **53**, 2041-2045.
3. M. W. Ranney, *Corrosion Inhibitors*, Noyes Data Corporation, New Jersey, 1976.
4. A. L. Chong, J. I. Mardel, D. R. MacFarlane, M. Forsyth and A. E. Somers, *ACS Sustainable Chem. Eng.*, 2016, **4**, 1746-1755.
5. A. L. Chong, M. Forsyth and D. R. MacFarlane, *Electrochim. Acta*, 2015, **159**, 219-226.

6. M. R. Ortega Vega, S. R. Kunst, J. A. T. da Silva, S. Mattedi and C. de Fraga Malfatti, *Corros. Eng. Sci. Techn.*, 2015, **50**, 547-558.
7. A. Yousefi, S. Javadian, N. Dalir, J. Kakemam and J. Akbari, *RSC Adv.*, 2015, **5**, 11697-11713.
8. M. A. M. Ibrahim, M. Messali, Z. Moussa, A. Y. Alzahrani, S. N. Alamry and B. Hammouti, *Port. Electrochim. Acta*, 2011, **29**, 375-389.
9. S. K. Shukla, L. C. Murulana and E. E. Ebenso, *Int. J. Electrochem. Sci.*, 2011, **6**, 4286-4295.
10. D. Bajpai and V. K. Tyagi, *J. Oleo Sci.*, 2006, **55**, 319-329.
11. A. Edwards, C. Osborne, S. Webster, D. Klenerman, M. Joseph, P. Ostovar and M. Doyle, *Corros. Sci.*, 1994, **36**, 315-325.
12. A. J. McMahon, *Colloids Surf.*, 1991, **59**, 187-208.
13. D. A. Jones, *Principles and Prevention of Corrosion*, Prentice-Hall, New Jersey, 1996.
14. C. L. Wilson and K. B. Wilson, *Trans. Electrochem. Soc.*, 1943, **84**, 153-163.
15. I. Nishiguchi and T. Hirashima, *Angew. Chem. Int. Ed.*, 1983, **22**, 52-53.
16. O. Shin-ichi and H. Tadao, *Bull. Chem. Soc. Jpn.*, 1953, **26**, 11-15.
17. L. M. Korotaeva, T. Y. Rubinskaya, L. V. Mikhal'chenko, I. A. Rybakova and V. P. Gul'tyai, *Russ. J. Electrochem.*, 2011, **47**, 1139.
18. I. B. Il'chibaeva, E. S. Kagan and A. P. Tomilov, *Russ. J. Electrochem.*, 2002, **38**, 1045-1046.
19. F. Beck, *Angew. Chem. Int. Ed.*, 1972, **11**, 760-781.
20. F. Blin, S. G. Leary, K. Wilson, G. B. Deacon, P. C. Junk and M. Forsyth, *J. Appl. Electrochem.*, 2004, **34**, 591-599.
21. M. Seter, B. Hinton and M. Forsyth, *J. Electrochem. Soc.*, 2012, **159**, C181-C189.
22. P. V. Hien, N. S. H. Vu, V. T. H. Thu, A. Somers and N. D. Nam, *Appl. Surf. Sci.*, 2017, **412**, 464-474.
23. R. W. Alder, M. E. Blake, S. Bufali, C. P. Butts, A. G. Orpen, J. Schutz and S. J. Williams, *J. Chem. Soc., Perkin Trans. 1*, 2001, 1586-1593.
24. A. Alexakis, C. L. Winn, F. Guillen, J. Pytkowicz, S. Roland and P. Mangeney, *Adv. Synth. Catal.*, 2003, **345**, 345-348.
25. A. Cornia, F. Felluga, V. Frenna, F. Ghelfi, A. F. Parsons, M. Pattarozzi, F. Roncaglia and D. Spinelli, *Tetrahedron*, 2012, **68**, 5863-5881.
26. A. J. Arduengo III, R. Krafczyk, R. Schmutzler, H. A. Craig, J. R. Goerlich, W. J. Marshall and M. Unverzagt, *Tetrahedron*, 1999, **55**, 14523-14534.
27. S. Saba, A. Brescia and M. K. Kaloustian, *Tetrahedron Lett.*, 1991, **32**, 5031-5034.
28. K. M. Kuhn and R. H. Grubbs, *Org. Lett.*, 2008, **10**, 2075-2077.
29. R. Jazzar, H. Liang, B. Donnadieu and G. Bertrand, *J. Organomet. Chem.*, 2006, **691**, 3201-3205.
30. U. Gruseck and M. Heuschmann, *Chem. Ber.*, 1987, **120**, 2053-2064.
31. G. Ye, W. P. Henry, C. Chen, A. Zhou and C. U. Pittman Jr, *Tetrahedron Lett.*, 2009, **50**, 2135-2139.
32. R. C. F. Jones and P. Dimopoulos, *Tetrahedron*, 2000, **56**, 2061-2074.
33. F. Takahashi and H. Yoshimura, *Japan Pat.*, JP2003313170A, 2003.
34. D. Turcio-Ortega, T. Pandiyan, J. Cruz and E. Garcia-Ochoa, *J. Phys. Chem. C*, 2007, **111**, 9853-9866.
35. ASTM, G1-03(2011), West Conshohocken, PA, 2011.

4 PROTIC SUGAR ACID SALTS FOR THE CORROSION INHIBITION OF MILD STEEL

In keeping with the design of dual-functional salts, chapter 4 explores a new family of anions to be paired with the imidazolinium cations. It was hoped that this would help in understanding the behaviour of the cation. While [2-MeHImn][4-OHCin] is a highly effective inhibitor for mild steel in chloride solutions, [2-MeHImn][Br] is ineffective. This chapter provides some perspective on whether the synergistic effects of the [2-MeHImn]⁺ cation extend to pairings with other anions. Section 4.1 is a manuscript prepared for publication, with accompanying supplementary information in section 4.2.

The anions explored in this chapter are uronic acids. These acids are sugars where the C6 carbon has been oxidised to a carboxylic acid. The glucose derivative, glucuronic acid, plays an important role in metabolic processes in both plants and animals. Uronic acids pose no toxicity threat and, if found to be viable inhibitors, would be a ‘green’ choice. It was hoped that the heteroatom functionality of the sugar derivatives, including the carboxylate moiety, would lead to good surface adsorption and protection of the steel surface. This is the case for another sugar acid derivative, gluconic acid, salts of which are commonly used as corrosion inhibitors in water-cooling systems.

A modified synthetic route was employed in this chapter. Preparation similar to the synthesis in chapter 2 was used to prepare 2-methylimidazoline. This base was titrated to the equivalence point with an aqueous solution of acid, and the water subsequently removed to yield the desired salt. This method was adopted to achieve a salt formulation as close to stoichiometry as possible. Due to the nature of acid-base chemistry, even slight excesses can cause substantial changes in pH. However, unlike with aprotic salts, the equilibrium nature of proton transfer, and limited differences in solubility between the contributing acid and base and the respective salt, made post-synthetic purification to remove any impurities (i.e. recrystallisation or phase separation) ineffective.

4.1 Protic sugar acid salts for the corrosion inhibition of mild steel

Alison L. Chong,^a Maria Forsyth^b and Douglas R. MacFarlane^{a*}

^aSchool of Chemistry, Monash University, Clayton, Victoria 3800, Australia.

^bInstitute for Frontier Materials, Deakin University, Burwood, Victoria 3125, Australia.

* Corresponding author. Email: douglas.macfarlane@monash.edu

Abstract

Environmentally friendly organic inhibitors are keenly sought after to provide safe corrosion protection for mild steel, a material that is widely used but, if left untreated, can suffer from corrosive attack. Sugars and their derivatives provide a class of safe and renewable chemicals which feature heteroatom functionality that is advantageous in organic inhibitors. In this work novel protic salts were synthesised from glucuronic acid and galacturonic acid combined with a selection of heterocyclic amines. The corrosion inhibition of these materials has been investigated through potentiodynamic polarisation and immersion studies. The salts were found to act as anodic inhibitors, although they were unable to suppress pitting corrosion at the concentrations tested. Subtle changes in the cation and anion structure were found to affect the corrosion mechanisms.

Introduction

Steel, and in particular mild steel, is one of the most widely used materials in modern infrastructure. And yet, if left exposed to the environment, it is prone to corrosive attack.¹ This can result in significant shortening of operating lifetimes, and it is estimated that worldwide, corrosion causes trillions of dollars' worth of damage each year.² Hence, it is highly important to adequately protect structures and mitigate the effects of corrosion.

One such method of protection is the use of corrosion inhibitors. Chromate corrosion inhibitors have been known to be the state of the art for a long time.³ However, they are highly toxic and harmful to the environment, and this has resulted in strict controls on their use.^{4, 5} As such, there is significant motivation to develop highly efficient and yet environmentally friendly inhibitors.^{3, 6, 7} Inorganic compounds containing zinc and rare earth metals have been developed,⁸⁻¹⁰ as well as compounds featuring nitrates, phosphates and carboxylates.¹¹⁻¹³ It is the heteroatom (O, N, P, S) and conjugation functionality that make these effective organic inhibitors.

Naturally derived compounds are good candidates for green corrosion inhibitors; they feature heteroatom functionality, are generally non-toxic and can be cheaply and renewably sourced. Dating back to the early twentieth century, studies have investigated the use of a wide variety of extracts from plants,¹⁴⁻¹⁶ fruits,^{17, 18} herbs and spices^{19, 20} for the protection of steel, particularly in acidic environments. In many of these cases, however, the active ingredient of these extracts has not been identified and isolated.²¹

Drugs and pharmaceuticals have also been identified as potential inhibitors due to their well understood toxicity and environmental effects.²² Examples include compound families isolated from natural sources such as penicillins^{23, 24} and quinolones.²⁵⁻²⁷ These pharmaceuticals, in addition to inhibiting general corrosion, could also be excellent choices for combating microbiologically influenced corrosion.²⁸ Possible drawbacks with the use of drugs as inhibitors are their expense and fears of enhancing microbial resistance.

Sugars and carbohydrates present an abundant and cost effective class of natural materials. Some success has been had in the use of sugars as inhibitors in their native form; Ostovari et al.²⁹ showed corrosion inhibition of steel with D-glucose (as a component of henna dye) and Muller et al.³⁰ demonstrated inhibition of aluminium and zinc corrosion with fructose and maltose. Molasses and other sugar-based agricultural by-products have also been shown to be good vapour phase inhibitors on carbon steel.³¹

More common is the use of species derived from sugars, such as aldonic and aldaric acids. Gluconic acid, and its simple salts such as sodium and calcium gluconate have been widely studied for use as inhibitors for steel under a range of conditions and are commercially used in water cooling systems.³²⁻³⁴ It has been observed that gluconic acid in low concentrations can suppress the anodic corrosion reaction. However, it can also form soluble iron complexes, resulting in accelerated anodic dissolution at higher inhibitor concentrations.³⁴ A number of patents cover the incorporation of sugar acids into inhibitor formulations for corrosion inhibition under a variety of conditions.³⁵⁻³⁷

This paper utilises uronic acid anions to develop non-toxic corrosion inhibitors. D-glucuronic acid and D-galacturonic acid are epimeric uronic acids obtained from the oxidation of glucose and galactose respectively. In the human body, these acids participate in a key metabolic pathway for removing drugs and other pollutants, by binding to them to increase their water solubility.³⁸ In nature, they can be found as constituents of polysaccharides such as pectin.³⁹ Prebakaran et al.⁴⁰ demonstrated successful corrosion inhibition of carbon steel using pectin as part of a synergistic ternary mixture with Zn²⁺

and propyl phosphonic acid, in which they suggested the formation of a complex at the anodic sites.

To our knowledge, this work is the first study on the inhibitive effects of uronic acids; the large number of hydroxyl groups, in addition to the carboxylate functionality, could allow these compounds to coordinate to a metal surface (e.g. iron in steel), creating a protective layer as has been observed with many other carboxylate inhibitors.⁴¹

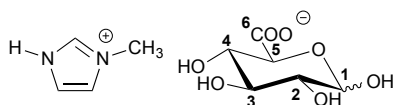
In prior studies, natural organic inhibitors have been used in combination with other compounds to produce synergistic effects, however, they are typically added in their neutral form or as simple salts (where the sodium or halide counter ion is merely a spectator). In this work, we neutralise the uronic acids with amines to form salts that have both a functional anion and cation. This is drawn from a key aspect of the synthetic design of ionic liquids (ILs), in which combinations of organic ions are assembled such that both ions contribute useful properties. The literature includes an example of uronic acid ILs which behaved as low toxicity hydrogenation catalysts.⁴² In this study the uronic acids were paired with a selection of common IL cations (imidazolium, pyrrolidinium) and cations previously shown to have synergistic corrosion inhibiting effects (imidazolium).⁴³

Experimental

Synthesis

All chemicals were purchased from Sigma and were > 98 % pure. They were used without further purification.

1-methylimidazolium glucuronate, [HMIm][Glu]



1-methylimidazole (0.37 g, 4.5 mmol) was dissolved in water and titrated with 0.1 M glucuronic acid (0.90 g, 4.6 mmol) to the equivalence pH 5.15. The mixture was stirred at room temperature for an hour and the solvent removed to yield an off-white solid (1.2 g, 98 %) Anomeric ratio 37 % α and 63 % β . ¹H NMR (400 MHz, D₂O) δ (ppm): 3.29 – 3.33 (dd, $J_{1\beta-2\beta}=10.0$ Hz, $J_{2\beta-3\beta}=9.4$ Hz, 1H, H-2 β), 3.52 – 3.55 (m, 3H, H-4 α , H-3 β , H-5 β), 3.58-3.62 (dd, $J_{1\alpha-2\alpha}=3.8$ Hz, $J_{2\alpha-3\alpha}=5.8$ Hz, 1H, H-2 α), 3.73 – 3.78 (m, 2H, H-3 α , H-4 β), 3.95 (s, 3H, CH₃), 4.10 – 4.12 (d, $J_{4\alpha-5\alpha}=10.0$ Hz, 1H, H-5 α), 4.66 – 4.68 (d, $J_{1\beta-2\beta}=8.0$ Hz, 1H, H-1 β), 5.26 – 5.27 (d, $J_{1\alpha-2\alpha}=3.8$ Hz, 1H, H-1 α), 7.46 – 7.47 (d, $J=1.2$ Hz, 2H, 2 x

CH), 8.76 (s, H, CH). ^{13}C NMR (400 MHz, D_2O) δ (ppm): 35.4 (CH_3), 71.3 (CH), 71.8 (CH), 71.9 (CH), 72.1 (CH), 72.6 (CH), 74.0 (CH), 75.8 (CH), 76.5 (CH), 92.1 (C-1 α), 95.9 (C-1 β), 119.5 (C=C), 122.9 (C=C), 139.8 (N-C=N), 174.8 (C-6 α), 179.3 (C-6 β). MS: ES^+ m/z 83.1 [HMIm] $^+$.

Further syntheses are described in the supplementary information (SI).

Characterisation

The compounds were characterised using NMR spectroscopy and mass spectrometry. NMR spectra were recorded in $\text{DMSO-}d_6$ (Merck) using a Bruker Avance 400 (9.4 T magnet) fitted with a BACS 60 tube autosampler, operating at 400 MHz. Low resolution ESI mass spectra were recorded on a Micromass Platform II QMS with a cone voltage of 35 V, using methanol as the mobile phase.

Differential scanning calorimetry (DSC) was carried out using a Perkin Elmer DSC 8000 with liquid nitrogen cryo cooler. Scans were run at a heating/cooling rate of 10 $^\circ\text{C}/\text{min}$ over a temperature range of -80 – 150 $^\circ\text{C}$. Thermogravimetric analysis (TGA) was undertaken on a Mettler Toledo TGA/DSC 1 STARE System. Samples were heated at 10 $^\circ\text{C}/\text{min}$ over a temperature range of 25 – 450 $^\circ\text{C}$.

Electrochemical Testing

For potentiodynamic polarisation experiments AS1020 steel electrodes (Composition: 0.26 % C, 0.45 % Mn, 0.14 % Cr, 0.19 % Si, 0.18 % Al, 0.35 % Other, and balance Fe) with a 1.0 cm diameter (0.78 cm^2) set in epoxy resin were used. They were abraded with silicon carbide paper to P1200 grit from P240 grit. The electrodes were washed with distilled water, dried with N_2 and stored in a desiccator. Potentiodynamic polarisation experiments were carried out an hour after electrode preparation.

The test solutions were prepared by dissolving appropriate masses of each compound in 500 mL of 0.01 M sodium chloride solution (made with milliQ water) to make concentrations of 4 mM or 0.01 M. The pH of these solutions ranged from 5.5- 6.5.

All polarisation experiments were carried out using a Princeton Applied Research VMP2 multichannel potentiostat in an open-to-air, standard three-electrode system consisting of a saturated calomel reference electrode (SCE) with a luggin capillary, a titanium mesh counter electrode, and the working electrode with 150mL of test solution as the electrolyte. After immersion the open circuit potential (OCP) was monitored for 30 minutes, and then the potentiodynamic polarisation experiment was carried out at a scanning rate of 0.167 mV s^{-1} . The scans started at 50 mV more negative than OCP and

continued through OCP for a range of 250 mV in the positive direction. Measurements were carried out in triplicate. The i_{corr} values were calculated using Tafel extrapolation methods. Where anodic and cathodic curves were near linear and symmetrical within 25 mV from E_{corr} , both Tafel slopes were interpolated until the lines intersected at E_{corr} . Inhibitor efficiencies were calculated according to Equation 1.

$$IE = \frac{i_{\text{corr}}(\text{control}) - i_{\text{corr}}(\text{inhibitor})}{i_{\text{corr}}(\text{control})} \quad (1)$$

Immersion Testing

For immersion experiments, steel coupons (1.0 cm² AS1020 steel coupons set in epoxy resin) were prepared in the same way as the electrodes. The coupons were immersed in 4 mM or 0.01 M solutions of inhibitor in 0.01M NaCl for 24 hours. The coupons were observed using a Leica MZ6 optical microscope at a magnification of x0.8 and then washed with distilled water and blown dry with nitrogen. The samples then had the corrosion product removed from the surface by immersion for four minutes in a solution containing hydrochloric acid and hexamethylene tetramine, as detailed in ASTM G1-03 (2011).⁴⁴ The surfaces were then observed with SEM and optical profilometry.

For SEM analysis a JEOL NeoScope JCM-5000 benchtop scanning electron microscope was used at an accelerating voltage of 10kV. 3D surface profilometry was performed on a Bruker Contour GT-K1 3D optical microscope. Using the image analysis software, Vision 64, the number of pits deeper than 1 μm was detected for each of the 950 x 1267 μm scans. At least five representative areas for each sample were recorded and the number of pits per square mm were calculated. The average pit depth, maximum pit depth and the surface roughness, S_a were also calculated.

Results and Discussion

Synthesis

D-glucuronic acid and D-galacturonic acid were reacted with a selection of secondary amines in a simple acid – base reaction to form protic salts (Figure 1). In order to ensure a one-to-one ratio of components, the bases were added to an aqueous mixture of the acid via titration. After stirring at room temperature and evaporation of the solvent, this produced a series of amorphous, hygroscopic salts in quantitative yields (Table 1). The final products include a mixture of α - and β -pyranose anomers due to mutarotation at the C1 position in the sugar acids. Most were found to be in keeping with the 36 % α to 64 % β ratio expected for glucose-based structures. A number of minor by-products, likely

furanose isomers, were carried through from the galacturonic acid into the final salts.⁴⁵ Characterisation and anomer ratios as determined by ¹H NMR spectroscopy are provided in the SI.

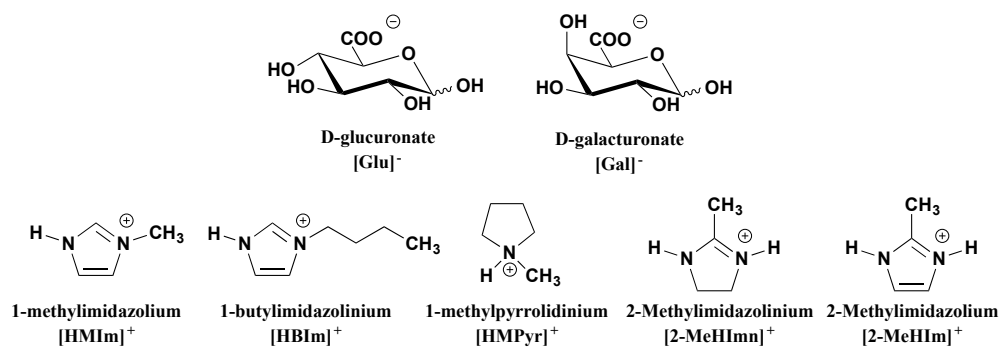


Figure 1. Selection of uronic acid anions and protic ammonium cations.

Thermogravimetric analysis (Table 1) shows that most of the glucuronate salts had decomposition temperatures (T_d) just over 130 °C, lower than that of the pure acid. Poor thermal stability can be a problem with protic carboxylates due to facile amide decomposition pathways.⁴⁶ Interestingly, [2-MeHIm][Glu] showed similar thermal stability to the acid, while [2-MeHImn][Glu] showed the lowest thermal stability, decomposing at 99 °C. The low thermal stability of the [2-MeHImn]⁺ cation can be attributed to the lack of aromaticity, which in turn leads to reduced stability in the ring.

With the exception of [2-MeHIm][Gal], the galacturonate salts were found to be more stable than their glucuronate counterparts. They were also all more stable than the pure GluH, which showed a T_d of 91 °C, substantially lower than GalH. [Na][Gal] was the most stable galacturonate salt, decomposing at 176 °C.

While no melting points were observed for these materials, many displayed glass transitions (T_g) above 0 °C, the highest of which was [2-MeHImn][Glu] at 33 °C. These unusually high temperature glass transitions are consistent with those observed for the tetrabutylammonium salts with the same anions synthesised by Ferlin et al.⁴²

Table 1. Thermal transitions of glucuronate and galacturonate salts.

Compound	T _d / °C ± 5	T _g / °C ± 0.5
[HMIm][Glu]	165	–
[HBIm][Glu]	130	21.4
[HMPyr][Glu]	137	18.1
[2-MeHImn][Glu]	99	30.5
[2-MeHIm][Glu]	132	33.0
[Na][Glu]	132	–
GluH*	165	–
[HMIm][Gal]	140	3.9
[HBIm][Gal]	142	8.8
[2-MeHImn][Gal]	107	14.2
[Na][Gal]*	176	–
GalH*	91	–

*Purchased commercially

Short Term Corrosion Inhibition

The salts containing the [2-MeHImn]⁺ cation were selected for corrosion testing due to its successful synergistic corrosion inhibition observed with other carboxylates.⁴³ [Na][Glu] and [2-MeHIm][Glu] were tested for comparison.

Figure 2 shows polarisation curves for mild steel electrodes in an electrolyte solution of 4 mM inhibitor in 0.01 M NaCl. The calculated corrosion potentials, E_{corr}, and corrosion current densities, i_{corr}, are shown in Table 2. [Na][Glu] modestly reduced i_{corr} relative to the control, with no shift in E_{corr}. This performance is poorer than sodium gluconate, which generally shows a substantial anodic shift from the control and can show inhibition efficiencies greater than 80% at similar concentrations.³³

The combined organic salts showed clear anodic effects and better inhibition than the sodium salt. 4 mM [2-MeHImn][Glu] caused a more anodic shift in E_{corr} than 4 mM [2-MeHImn][Gal], although both produced similar current densities. They were approximately twice as effective as the sodium salt. The performance of these salts is comparable to simple aromatic carboxylates with the same cation.⁴⁷ Under similar experimental conditions, 2-methylimidazolium salicylate, [2-MeHImn][Sal], and 2-methylimidazolium gentisate, [2-MeHImn][Gen], showed similar shifts in E_{corr} and produced inhibition efficiencies of 13 % and 49 % respectively. These salts did not show the same extent of synergy displayed by 2-methylimidazolium 4-hydroxycinnamate,

[2-MeHImn][4-OHCin], thought to be derived from the particular reactivity of the α,β -unsaturated carbonyl (ref. this thesis, Section 3.2).

Although the addition of 4 mM [2-MeHIm][Glu] resulted in inhibition efficiencies comparable to the other uronic acid salts, it caused an unexpected 100 mV anodic shift relative to [2-MeHImn][Glu]. The presence of the [2-MeHIm]⁺ cation also appeared to alter the anodic arm, suggesting more rapid dissolution of the metal under anodic overpotentials.

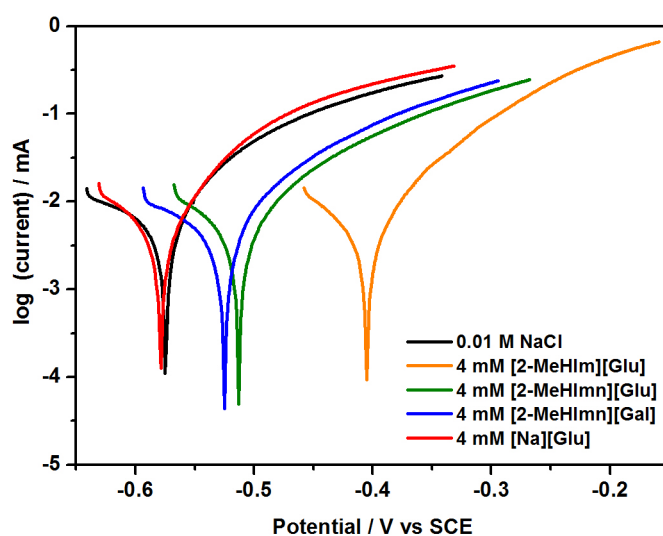


Figure 2. Polarisation curves for mild steel electrodes in neutral aqueous electrolytes with 0.01 M NaCl and 4 mM inhibitor.

Table 2. Corrosion potential, E_{corr} , corrosion current density, i_{corr} and inhibition efficiency.

Inhibitor	$E_{\text{corr}} / \text{mV}$	$i_{\text{corr}} / \text{mAcm}^{-2}$	% IE
0.01 M NaCl control	-571 ± 5	2.2 ± 0.3	–
4 mM [2-MeHImn][Glu]	-500 ± 20	1.6 ± 0.3	29
0.01 M [2-MeHImn][Glu]	-482 ± 9	1.39 ± 0.06	37
4 mM [2-MeHIm][Glu]	-399 ± 7	1.7 ± 0.2	25
4 mM [2-MeHImn][Gal]	-531 ± 6	1.5 ± 0.1	33
4 mM [Na][Glu]	-577 ± 6	1.9 ± 0.1	15

To investigate the effect of concentration, 0.01 M [2-MeHImn][Glu] was tested (Figure 3). Increasing the concentration of inhibitor caused a 20 mV anodic shift and slight decrease in i_{corr} . This differs from the observation by Refaey³⁴ that increasing the concentration of sodium gluconate causes a negative shift in E_{corr} . Interestingly, Tourir et

al.³³ also noted a trend of negative shifts in E_{corr} as the concentration of sodium gluconate was increased (in simulated cooling water), however, they observed a cathodic shift when the concentration was increased from 0.005 M to 0.01 M. In those experiments, 0.01M was the optimal concentration, as above this the corrosion current densities began to increase.

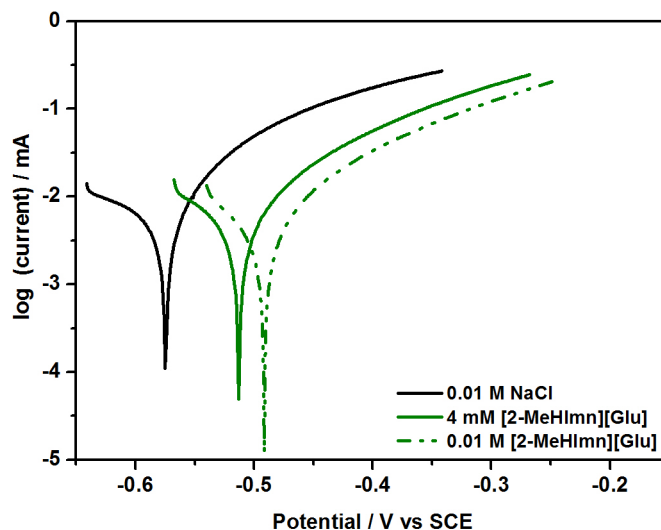


Figure 3. Polarisation curves comparing effects of concentration on [2-MeHImn][Glu] inhibition.

Immersion Testing

24 h immersion tests were undertaken to observe the long-term behaviour of the inhibitors. These provide more information about the mechanism of corrosion taking place. Mild steel coupons were immersed in solutions containing 0.01 M NaCl and 4 mM or 0.01 M of each inhibitor under ambient conditions. After 24 h the samples were imaged using an optical microscope. The corrosion product was then removed using hexamethylenetetramine and hydrochloric acid as per ASTM G1-03 (2011)⁴⁴ and the etched surface analysed by SEM. Figure 4 shows microscope images of the immersed coupons accompanied by an SEM image representative of the corroded regions on each surface. Comparative SEM images of uncorroded regions of the coupons can be found in the SI.

In all cases there was a substantial decrease in the amount of corrosion product present compared to the control (containing only 0.01 M NaCl), however, localised pitting behaviour was observed. Immersion in 4 mM [2-MeHImn][Glu] (Figure 4a) showed contrasting areas of near pristine steel and clusters of pits. The minimal amount of visual corrosion product suggests the formation of soluble iron-gluconate complexes as observed for similar work with gluconates.³⁴ Increasing the concentration to 0.01 M

inhibitor (Figure 4c) appeared to enhance the growth of selected pits, suggesting that even at this concentration the ions do not form a complete protective film on the surface of the steel. The coupon immersed in 4 mM [2-MeHIm][Glu] (Figure 4e) showed some general corrosion in addition to the appearance of pitting. Figure 4g shows the coupon immersed in 4 mM [2-MeHImn][Gal] displaying a region with corrosion product similar to the control. This suggests that the corrosion product is not as soluble in the presence of the [Gal].

Compared to the control, that features a rough surface and small evenly distributed pits (Figure 4j), the addition of 4 mM [2-MeHImn][Glu] resulted in a smoother surface but the formation of large pits clustered together as observed by SEM (Figure 4b). Figure 4d showed that this behaviour is exacerbated when the inhibitor concentration is increased. A rough surface, indicating general corrosion as seen in the control, was observed for 4 mM [2-MeHIm][Glu] in addition to the large pits that formed in the presence of [2-MeHImn][Glu] (Figure 4f). Figure 4h shows corrosion in the presence of 4 mM [2-MeHImn][Gal] formed a finer pit structure than the glucuronate salts.

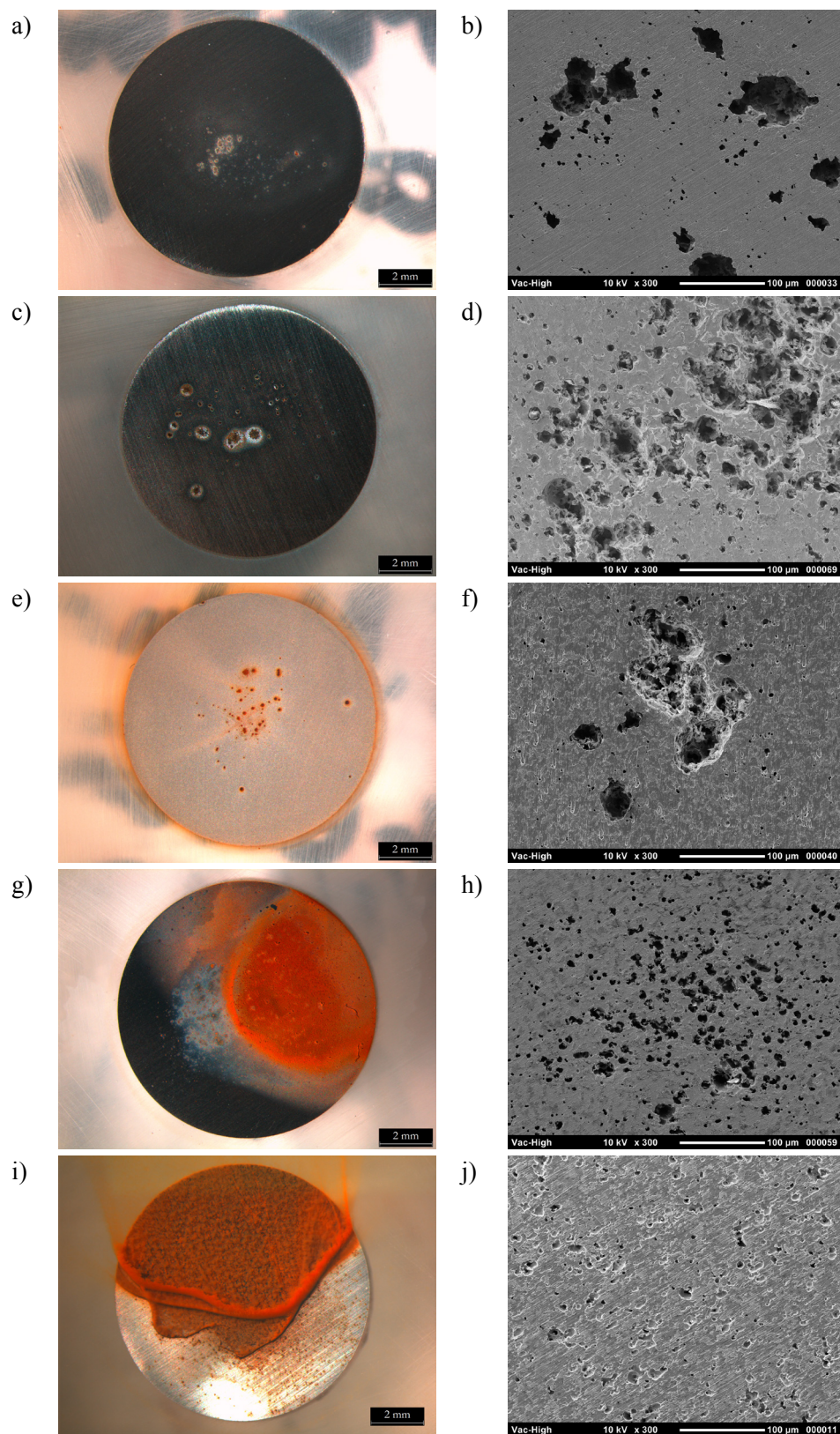


Figure 4. Optical images (x 0.8) with corrosion product and SEM images (x 300) after removal of corrosion product of mild steel after immersion for 24 h in 0.01 M NaCl and a) and b) 4 mM [2-MeHImn][Glu]; c) and d) 0.01 M [2-MeHImn][Glu]; e) and f) 4 mM [2-MeHIm][Glu]; g) and h) 4 mM [2-MeHImn][Gal]; i and j) control – no inhibitor.

3D optical profilometry was also carried out on the etched samples. Analysis of different sites on the surface was used to determine the number of pits per square millimetre and the average and maximum depth of these pits. The surface roughness (S_a) was also determined, with the results shown in Table 3.

Table 3. Pit analysis from optical profilometry.

Sample	pits / mm ²	Average pit depth / μm	Maximum pit depth / μm	Surface roughness / μm
As polished steel	0	-	-	0.081 ± 0.013
0.01 M NaCl control	350 ± 80	7.8 ± 0.8	36	0.42 ± 0.03
4 mM [2-MeHImn][Glu]	13 ± 8	39 ± 15	82	0.4 ± 0.2
0.01 M [2-MeHImn][Glu]	22 ± 12	27 ± 11	94	0.8 ± 0.05
4 mM [2-MeHIm][Glu]	140 ± 50	7 ± 5	76	0.39 ± 0.10
4 mM [2-MeHImn][Gal]	80 ± 30	13 ± 4	79	0.16 ± 0.03

Pits deeper than 1 μm counted. Pit analysis reported for corroded regions of coupons.

The use of 4 mM [2-MeHImn][Glu] inhibitor resulted in a substantial reduction in the number of pits per square millimetre, however, there was a dramatic increase in the depth of these pits. This is shown in Figure 5, where the surface of the sample immersed in the control solution shows an even distribution of shallow pits, but the surface of the sample immersed in the solution containing the inhibitor shows the formation of several deep pits. This suggests that although the inhibitor can successfully reduce general corrosion and the formation of pits, it does not provide full surface coverage at the tested concentration, and once a pit is established, it is ineffective at stopping further growth. Increasing the inhibitor concentration did result in a decrease in the average pit depth but, as corroborated by the SEM data, stable pitting still takes place.

The sample immersed in 4 mM [2-MeHIm][Glu] showed a much larger number of pits with a smaller average depth, reflecting the appearance of general corrosion and shallow pitting observed in the microscope and SEM images. Deeper pitting was still observed, with a maximum pit depth of 76 μm . These differences between the analogous cations are consistent with similar studies using the [4-OHCin]⁻ anion (ref. this thesis Section 3.2). [2-MeHImn][Gal] also showed a larger number of pits in comparison to [2-MeHImn][Glu].

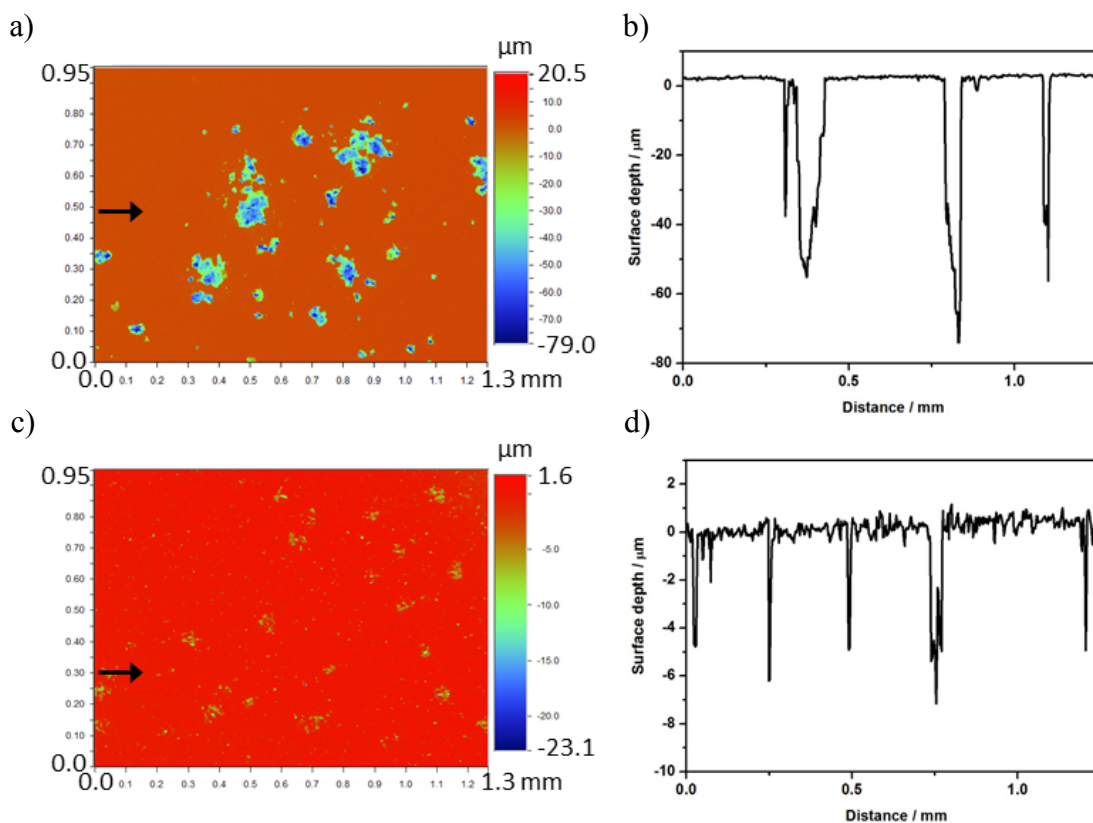


Figure 5. a) Optical profilometry image of 4 mM [2-MeHImn][Glu] sample; b) cross-section of surface depth across 4 mM [2-MeHImn][Glu] sample; c) optical profilometry image of 0.01 M NaCl control sample; d) cross-section of surface depth across 0.01 M NaCl control sample. Note change in depth scale. The cross-section position is marked by the black arrows.

Pitting corrosion has been observed on steel in the presence of similar inhibitors. Tan et al.⁴⁸ determined that imidazolines can aggravate localised corrosion by forming small numbers of anodic sites that corrode rapidly. Previous work in our group has observed this behaviour on mild steel immersed in [2-MeHImn][4-OHCin] and 0.01 M NaCl, although the extent of the pitting was less severe than in the current study (ref. this thesis, Chapter 3). Sodium gluconate inhibitors can also cause pitting on steel.^{33, 34}

Localised corrosion is a known issue with anodic inhibitors. Typically an anodic organic inhibitor will adsorb to the metal surface, preventing the approach of chlorides and other aggressive species. While this can greatly reduce general corrosion, any gaps in the coverage are vulnerable to corrosive attack. If the surrounding protected areas can support cathodic processes (i.e. oxygen reduction) the resulting large cathode – small anode system can lead to high current densities concentrated at the pit sites and rapid metal dissolution. For this reason it is important that anodic inhibitors are used in sufficient quantities.

A problem may arise, however, if the uronic acid anions act similarly to the related gluconate anion. It has been found that gluconates can form soluble metal complexes, and

Refaey³⁴ suggests that increasing the inhibitor concentration may enhance the complexes' solubility and lead to active metal dissolution. This complexation process is useful for preventing calcium deposits, and makes gluconates a popular combined corrosion and scale inhibitor.^{32, 33} While studies on the aqueous complexation of copper have shown uronic acids to be weaker ligands than their aldonic acid counterparts, stable metal – ligand complexes do form.⁴¹

If $[\text{Glu}]^-$ does solubilise iron, as is suggested by the lack of visible corrosion products on the immersed coupons (Figure 4), then it may explain the enhanced pitting corrosion compared to other carboxylate inhibitors. Further increasing the concentration may exacerbate pitting rather than reduce it. It is possible that the combination of $[\text{2-MeHImn}]^+$, that limits the number of anodic sites, and $[\text{Glu}]^-$, that can encourage anodic dissolution, resulted in the severity of localised attack that was observed in the immersion tests. As the polarisation curves do not indicate that the uronic acid salts have any inhibitory effect on cathodic processes, these anions may be best used in conjunction with a cathodic inhibitor or oxygen scavenger. The imidazolium cation could be replaced with alternative corrosion inhibiting amines, such as aliphatic amines or pyridine, that have shown effective cathodic inhibition.

Conclusions

Organic salts can be readily formed through the neutralisation of uronic acids with secondary amines, many of which show ambient temperature glass transitions. Polarisation measurements show that the uronic acid salts can inhibit corrosion at relatively low concentrations on mild steel in the presence of 0.01 M NaCl. The anodic behaviour and overall reduction in current densities is enhanced with the incorporation of heterocyclic cations $[\text{2-MeHImn}]^+$ and $[\text{2-MeHIm}]^+$, increasing efficiency from 15 % to 30% compared to the sodium salt. Longer-term immersion testing showed that subtle changes in the structure of the inhibitor such as conformation ($[\text{Glu}]^-$ vs. $[\text{Gal}]^-$) or bond saturation ($[\text{2-MeHImn}]^+$ vs. $[\text{2-MeHIm}]^+$) affect the corrosion mechanisms. The tested inhibitors provided some surface protection from corrosive attack, although they were not able to stop the occurrence of stable pitting at the concentrations tested. With further optimisation, uronic acid salts could be potential environmentally friendly corrosion inhibitors.

References

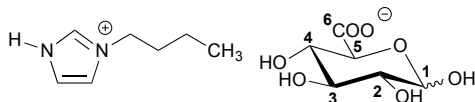
1. E. Mattsson, *Basic Corrosion Technology for Scientists and Engineers*, 2nd edition edn., The Institute of Materials, London, 2001.
2. G. Schmitt, M. Schütze, G. F. Hays, W. Burns, E.-H. Han, A. Pourbaix and G. Jacobson, *Global Needs for Knowledge Dissemination, Research, and Development in Materials Deterioration and Corrosion Control*, The World Corrosion Organization, 2009.
3. J. Sinko, *Prog. Org. Coat.*, 2001, **42**, 267-282.
4. S. Wilbur, H. Abadin, M. Fay, D. Yu, B. Tencza, L. Ingerman, J. Klotzbach and S. James, *Toxicological Profile for Chromium*, US Department of Public Health and Human Services, Atlanta, 2012.
5. J. Guertin, in *Chromium (VI) handbook*, CRC Press, Boca Raton, 2004, pp. 215-230.
6. R. L. Twite and G. P. Bierwagen, *Prog. Org. Coat.*, 1998, **33**, 91-100.
7. G. B. Deacon, P. C. Junk, M. Forsyth and W. W. Lee, *Chem. Aust.*, 2008, **75**, 18-21.
8. R. Naderi, M. Mahdavian and M. M. Attar, *Electrochim. Acta*, 2009, **54**, 6892-6895.
9. B. R. W. Hinton and L. Wilson, *Corros. Sci.*, 1989, **29**, 967-985.
10. M. Forsyth, M. Seter, B. Hinton, G. Deacon and P. Junk, *Aust. J. Chem.*, 2011, **64**, 812-819.
11. M. J. Pryor and M. Cohen, *J. Electrochem. Soc.*, 1953, **100**, 203-215.
12. A. M. Shams El Din and L. Wang, *Desalination*, 1996, **107**, 29-43.
13. P. Saura, E. Zornoza, C. Andrade and P. Garcés, *Corrosion*, 2011, **67**, D1-D15.
14. M. S. Al-Otaibi, A. M. Al-Mayouf, M. Khan, A. A. Mousa, S. A. Al-Mazroa and H. Z. Alkhatlan, *Arab. J. Chem.*, 2014, **7**, 340-346.
15. S. A. Verma and G. Mehta, *Bull. Electrochem.*, 1999, **15**, 67-70.
16. A. F. Gualdrón, E. N. Becerra, D. Y. Peña, J. C. Gutiérrez and H. Q. Becerra, *J. Mater. Environ. Sci.*, 2013, **4**, 143-158.
17. R. M. Saleh, A. A. Ismail and A. A. El Hosary, *Br. Corros. J.*, 1982, **17**, 131-135.
18. S. Umoren, I. B. Obot, Z. Gasem and N. A. Odewunmi, *J. Dispersion Sci. Technol.*, 2015, **36**, 789-802.
19. K. Srivastav and P. Srivastava, *Br. Corros. J.*, 1981, **16**, 221-223.
20. E. Khamis and N. AlAndis, *Materialwiss. Werkstofftech.*, 2002, **33**, 550-554.
21. P. B. Raja and M. G. Sethuraman, *Mater. Lett.*, 2008, **62**, 113-116.
22. G. Gece, *Corros. Sci.*, 2011, **53**, 3873-3898.
23. N. O. Eddy, S. A. Odoemelam and P. Ekwumemgbo, *Sci. Res. Essays*, 2009, **4**, 033-038.
24. N. O. Eddy and S. A. Odoemelam, *Advances in Natural and Applied Sciences*, 2008, **2**, 225-233.
25. E. E. Ebenso, I. B. Obot and L. Murulana, *Int. J. Electrochem. Sci.*, 2010, **5**, 1574-1586.
26. S. Acharya and S. Upadhyay, *T. Indian. I. Metals*, 2004, **57**, 297-306.
27. M. Seter, M. J. Thomson, A. Chong, D. R. MacFarlane and M. Forsyth, *Aust. J. Chem.*, 2013, **66**, 921-929.
28. M. Seter, M. J. Thomson, J. Stoimenovski, D. R. MacFarlane and M. Forsyth, *Chem. Commun.*, 2012, **48**, 5983-5985.
29. A. Ostovari, S. M. Hoseinie, M. Peikari, S. R. Shadizadeh and S. J. Hashemi, *Corros. Sci.*, 2009, **51**, 1935-1949.
30. B. Müller, *Corros. Sci.*, 2002, **44**, 1583-1591.
31. M. Kharshan, A. Furman, M. Shen, R. Kean, K. Gillette and L. Austin, *Mater. Performance*, 2012, 17-22.
32. R. Tourir, N. Dkhireche, M. E. Touhami, M. E. Bakri, A. H. Rochdi and R. A. Belakhmima, *J. Saudi Chem. Soc.*, 2014, **18**, 873-881.
33. R. Tourir, M. Cenoui, M. El Bakri and M. Ebn Touhami, *Corros. Sci.*, 2008, **50**, 1530-1537.
34. S. A. M. Refaey, *Appl. Surf. Sci.*, 2000, **157**, 199-206.
35. K. R. Smith, E. C. Olson and S. E. Lentsch, *USA Pat.*, US 8114344 B1, 2012.
36. R. S. Koefod, *United States Pat.*, US 20070278446 A1, 2010.
37. B. A. Miksic, C. Chandler, M. Kharshan, A. Furman, B. Rudman and L. Gelner, *United States Pat.*, US 5597514 A, 1998.
38. G. J. Dutton, in *Glucuronic Acid Free and Combined*, Academic Press, 1966, pp. 185-299.

39. T. Mehtiö, M. Toivari, M. G. Wiebe, A. Harlin, M. Penttilä and A. Koivula, *Crit. Rev. Biotechnol.*, 2016, **36**, 904-916.
40. M. Prabakaran, S. Ramesh, V. Periasamy and B. Sreedhar, *Res. Chem. Intermed.*, 2015, **41**, 4649-4671.
41. G. M. Escandar and L. F. Sala, *Can. J. Chem.*, 1992, **70**, 2053-2057.
42. N. Ferlin, M. Courty, S. Gatard, M. Spulak, B. Quilty, I. Beadham, M. Ghavre, A. Haiß, K. Kümmerer, N. Gathergood and S. Bouquillon, *Tetrahedron*, 2013, **69**, 6150-6161.
43. A. L. Chong, J. I. Mardel, D. R. MacFarlane, M. Forsyth and A. E. Somers, *ACS Sustainable Chem. Eng.*, 2016, **4**, 1746-1755.
44. ASTM International, ASTM G1-03(2011), West Conshohocken, PA, 2011.
45. T. E. Acree, R. S. Shallenberger and L. R. Mattick, *Carbohydr. Res.*, 1968, **6**, 498-502.
46. T. L. Greaves, A. Weerawardena, C. Fong, I. Krodkiewska and C. J. Drummond, *J. Phys. Chem. B*, 2006, **110**, 22479-22487.
47. A. L. Chong, M. Forsyth and D. R. MacFarlane, *Electrochim. Acta*, 2015, **159**, 219-226.
48. Y. Tan, M. Mocerino and T. Paterson, *Corros. Sci.*, 2011, **53**, 2041-2045.

4.2 Supplementary Information

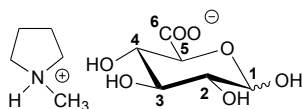
Synthesis

1-Butylimidazolium glucuronate, [HBIIm][Glu]



1-butylimidazole (0.61 g, 4.9 mmol) was dissolved in water and titrated with 0.1 M glucuronic acid (0.96 g, 4.9 mmol) to the equivalence pH 5.1. The mixture was stirred at room temperature for an hour and the solvent removed to yield an off-white solid (1.5 g, 96 %). Anomeric ratio: 36 % α and 64 % β . ^1H NMR (400 MHz, D_2O) δ (ppm): 0.93 – 0.97 (t, $J=7.4$ Hz, 3H, CH_3), 1.30 – 1.40 (m, 1H, CH_2), 1.86 – 1.93 (m, 2H, CH_2), 3.29 – 3.33 (dd, $J_{1\beta-2\beta}=8.0$ Hz, $J_{2\beta-3\beta}=9.2$ Hz, 1H, H-2 β), 3.50 – 3.55 (m, 3H, H-4 α , H-3 β , H-5 β), 3.58-3.62 (dd, $J_{1\alpha-2\alpha}=3.8$ Hz, $J_{2\alpha-3\alpha}=6.2$ Hz, 1H, H-2 α), 3.73 – 3.78 (m, 2H, H-3 α , H-4 β), 4.10 – 4.12 (d, $J_{4\alpha-5\alpha}=1.6$ Hz, 1H, H-5 α), 4.25 – 4.28 (t, $J=3.2$ Hz, 2H, CH_2), 4.66 – 4.68 (d, $J_{1\beta-2\beta}=8.0$ Hz, 1H, H-1 β), 5.26 – 5.27 (d, $J_{1\alpha-2\alpha}=3.8$ Hz, 1H, H-1 α), 7.48 – 7.49 (dt, $J=1.6$ Hz, $J=9.6$ Hz, 2H, 2 x CH), 8.73 (s, 1H, CH). ^{13}C NMR (400 MHz, D_2O) δ (ppm): 12.6 (CH_3), 18.8 (CH_2), 31.3 (CH_2), 49.1 (CH_2), 71.3 (CH), 71.8 (CH), 71.9 (CH), 72.1 (CH), 72.6 (CH), 74.0 (CH), 75.6 (CH), 76.2 (CH), 89.7 (C-1 α), 95.9 (C-1 β), 119.7 (C=C), 121.7 (C=C), 134.3 (N-C=N), 170.8 (C-6 α), 172.4 (C-6 β). MS: ES^+ m/z 125.2 [HBIIm] $^+$; ES^- m/z 193.1 [Glu] $^-$.

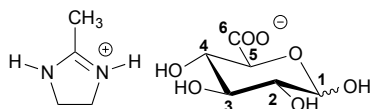
1-Methylpyrrolidinium glucuronate, [HMPyr][Glu]



1-methylpyrrolidine (0.37 g, 4.3 mmol) was dissolved in water (0.37 g, 4.3 mmol) and titrated with 0.1 M glucuronic acid (0.81 g, 4.2 mmol) to the equivalence pH 6.8. The mixture was stirred at room temperature for an hour and the solvent removed to yield an off-white solid (1.1 g, 95 %). Anomeric ratio: 34 % α and 66 % β . ^1H NMR (400 MHz, D_2O) δ (ppm): 0.931 – 0.968 (t, 2H, CH_2), 2.01 – 2.10 (m, 2H, CH_2), 2.15 – 2.24 (m, 2H, CH_2), 2.95 (m, 2H, CH_2), 2.95 (s, 3H, CH_3), 3.06 – 3.13 (m, 2H, CH_2), 3.30 – 3.34 (dd, $J_{1\beta-2\beta}=8.0$ Hz, $J_{2\beta-3\beta}=9.2$ Hz, 1H, H-2 β), 3.53 – 3.56 (m, 3H, H-4 α , H-3 β , H-5 β), 3.59 – 3.62 (dd, $J_{1\alpha-2\alpha}=3.6$ Hz, $J_{2\alpha-3\alpha}=5.8$ Hz, 1H, H-2 α), 3.65 – 3.71 (m, 2H, CH_2), 3.74 – 3.79 (m, 2H, H-3 α , H-4 β), 4.12 – 4.15 (d, $J_{4\alpha-5\alpha}=10.0$ Hz, 1H, H-5 α), 4.67 – 4.69 (d, $J_{1\beta-2\beta}=8.0$ Hz, 1H, H-1 β), 5.27 – 5.28 (d, $J_{1\alpha-2\alpha}=3.6$ Hz, 1H, H-1 α). ^{13}C NMR (400 MHz, D_2O) δ

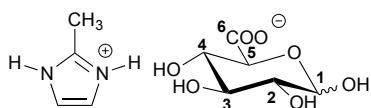
(ppm): 23.4 (2 x CH₂), 55.1 (2 x CH₂), 70.8 (CH), 72.5 (CH), 72.7 (CH), 73.0 (CH), 73.3 (CH), 74.9 (CH), 75.1 (CH), 76.9 (CH), 92.9 (C-1 α), 97.4 (C-1 β), 173.8 (C-6 β). 174.3 (C-6 α), MS: ES⁺ m/z 86.1 [HMPyr]⁺.

2-Methylimidazolium glucuronate, [2-MeHImn][Glu]

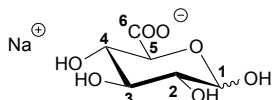


2-methylimidazoline (0.77 g, 9.2 mmol) was dissolved in water and titrated with 0.1 M glucuronic acid (1.7 g, 8.9 mmol) to the equivalence pH 6.5. The mixture was stirred at room temperature for an hour and the solvent removed to yield an off-white solid (2.3 g, 94 %). Anomeric ratio: 39 % α and 61 % β . ¹H NMR (400 MHz, D₂O) δ (ppm): 2.23 (s, 3H, CH₃) 3.29 – 3.33 (dd, $J_{1\beta-2\beta}$ =8.0 Hz, $J_{2\beta-3\beta}$ =9.2 Hz, 1H, H-2 β), 3.50 – 3.55 (m, 3H, H-4 α , H-3 β , H-5 β), 3.58 – 3.61 (dd, $J_{1\alpha-2\alpha}$ =4.0 Hz, $J_{2\alpha-3\alpha}$ =9.8 Hz, 1H, H-2 α), 3.73 – 3.78 (m, 2H, H-3 α , H-4 β), 3.92 (s, 4H, 2x CH₂), 4.10 – 4.12 (d, $J_{4\alpha-5\alpha}$ =10.0 Hz, 1H, H-5 α), 4.66 – 4.68 (d, $J_{1\beta-2\beta}$ =8.0 Hz, 1H, H-1 β), 5.26 – 5.27 (d, $J_{1\alpha-2\alpha}$ =4.0 Hz, 1H, H-1 α). ¹³C NMR (400 MHz, D₂O) δ (ppm): 11.7 (CH₃), 44.4 (2 x CH₂), 71.3 (CH), 71.9 (CH), 71.9 (CH), 72.1 (CH), 72.6 (CH), 74.0 (CH), 75.6 (CH), 76.2 (CH), 92.1 (C-1 α), 95.9 (C-1 β), 168.6 (N-C=N), 175.8 (C-6 α), 176.8 (C-6 β). MS: ES⁺ m/z 85.1 [2-MeHImn]⁺; ES⁻ m/z 193.0 [Glu]⁻.

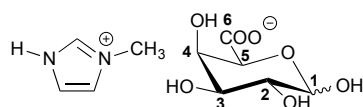
2-Methylimidazolium glucuronate, [2-MeHIm][Glu]



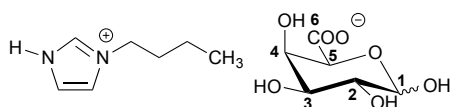
2-methylimidazole (0.72 g, 8.4 mmol) was dissolved in water and titrated with 0.1 M glucuronic acid (1.8 g, 9.1 mmol) to the equivalence pH 5.6. The mixture was stirred at room temperature for an hour and the solvent removed to yield an off-white solid (2.2 g, 94 %). Anomeric ratio: 40 % α and 60 % β . ¹H NMR (400 MHz, D₂O) δ (ppm): 2.55 (s, 3H, CH₃), 3.19 – 3.23 (dd, $J_{1\beta-2\beta}$ =8.0 Hz, $J_{2\beta-3\beta}$ =9.2 Hz, 1H, H-2 β), 3.41 – 3.45 (m, 3H, H-4 α , H-3 β , H-5 β), 3.48 – 3.52 (m, 1H, H-2 α), 3.63 – 3.68 (m, 2H, H-3 α , H-4 β), 4.00 – 4.02 (d, $J_{4\alpha-5\alpha}$ =10.0 Hz, 1H, H-5 α), 4.56 – 4.58 (d, $J_{1\beta-2\beta}$ =8.0 Hz, 1H, H-1 β), 5.16 – 5.17 (d, $J_{1\alpha-2\alpha}$ =3.6 Hz, 1H, H-1 α), 7.22 (s, 2H, 2 x CH). ¹³C NMR (400 MHz, D₂O) δ (ppm): 13.2 (CH₃), 71.6 (CH), 72.4 (CH), 72.5 (CH), 72.7 (CH), 73.2 (CH), 75.1 (CH), 75.8 (CH), 76.8 (CH), 93.2 (C-1 α), 97.7 (C-1 β), 120.8 (2 x C=C), 160.9 (N-C=N), 170.1 (C-6 α), 172.9 (C-6 β). MS: ES⁺ m/z 83.1 [2-MeHIm]⁺.

Sodium glucuronate, [Na][Glu]

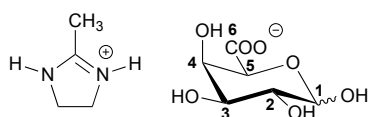
Sodium hydroxide (0.36 g, 9.1 mmol) was dissolved in water and titrated with 0.1 M glucuronic acid (1.8 g, 9.1 mmol) to the equivalence pH 7.5. The mixture was stirred at room temperature for an hour and the solvent removed to yield a white solid (2.0 g, 99 %). Anomeric ratio: 39 % α and 61 % β . ^1H NMR (400 MHz, D_2O) δ (ppm): 3.31 – 3.35 (dd, $J_{1\beta-2\beta}=8.0$ Hz, $J_{2\beta-3\beta}=9.6$ Hz, 1H, H-2 β), 3.52 – 3.59 (m, 3H, H-4 α , H-3 β , H-3 β), 3.60 – 3.64 (dd, $J_{1\alpha-2\alpha}=4.0$ Hz, $J_{2\alpha-3\alpha}=10$ Hz, 1H, H-2 α), 3.75 – 3.80 (m, 2H, H-3 α , H-4 β), 4.11 – 4.14 (d, $J_{4\alpha-5\alpha}=10.0$ Hz, 1H, H-5 α), 4.68 – 4.70 (d, $J_{1\beta-2\beta}=8.0$ Hz, 1H, H-1 β), 5.28 – 5.29 (d, $J_{1\alpha-2\alpha}=4.0$ Hz, 1H, H-1 α). ^{13}C NMR (400 MHz, D_2O) δ (ppm): 71.3 (CH), 71.8 (CH), 71.9 (CH), 72.1 (CH), 72.6 (CH), 74.0 (CH), 75.6 (CH), 76.2 (CH), 92.1 (C-1 α), 95.9 (C-1 β), 176.0 (C-6 β), 176.9 (C-6 α). MS: ES^+ m/z 239.1 $2[\text{Na}]^+ [\text{Glu}]^-$; ES^- m/z 193.1 $[\text{Glu}]^-$, 409.0 $[\text{Na}]^+ 2[\text{Glu}]^-$.

1-Methylimidazolium galacturonate, [HMIm][Gal]

1-methylimidazole (0.32 g, 3.9 mmol) was dissolved in water and titrated with 0.1 M galacturonic acid monohydrate (0.87 g, 4.4 mmol) to the equivalence pH 5.15. The mixture was stirred at room temperature for an hour and the solvent removed to yield a white solid (1.1 g, 99 %). Anomeric ratio: 36 % α and 64 % β . ^1H NMR (400 MHz, D_2O) δ (ppm): 2.23 (s, 3H, CH_3), 3.50 – 3.55 (dd, $J_{1\beta-2\beta}=8.0$ Hz, $J_{2\beta-3\beta}=10$ Hz, 1H, H-2 β), 3.70-3.73 (dd, $J_{3\beta-4\beta}=3.6$ Hz, $J_{2\beta-3\beta}=10$ Hz, 1H, H-3 β), 3.83 – 3.86 (dd, $J_{1\alpha-2\alpha}=4.0$ Hz, $J_{2\alpha-3\alpha}=10$ Hz, 1H, H-2 α), 3.92 – 3.95 (dd, $J_{3\alpha-4\alpha}=3.4$ Hz, $J_{2\alpha-3\alpha}=10$ Hz, 1H, H-3 α), 3.95 (s, 3H, CH_3), 4.08 – 4.09 (d, $J_{4\beta-5\beta}=1.2$ Hz, 1H, H-5 β), 4.24 – 4.25 (dd, $J_{4\beta-5\beta}=1.2$ Hz, $J_{3\beta-4\beta}=3.6$ Hz, 1H, H-4 β), 4.30 – 4.31 (dd, $J_{4\alpha-5\alpha}=1.2$ Hz, $J_{3\alpha-4\alpha}=3.4$ Hz, 1H, H-4 α), 4.43 – 4.44 (d, $J_{4\alpha-5\alpha}=1.2$ Hz, 1H, H-5 α), 4.58 – 4.60 (d, $J_{1\beta-2\beta}=8.0$ Hz, 1H, H-1 β), 5.31 – 5.32 (d, $J_{1\alpha-2\alpha}=4.0$ Hz, 1H, H-1 α), 7.47 (s, 2H, 2xCH), 8.68 (s, 1H, CH). ^{13}C NMR (400 MHz, D_2O) δ (ppm): 35.4 (CH_3), 68.1 (C-2 α), 69.4 (C-3 α), 70.4 (C-4 α), 70.8 (C-4 β), 71.3 (C-5 α), 71.6 (C-2 β), 72.9 (C-3 β), 75.5 (C-5 β), 92.2 (C-1 α), 96.1 (C-1 β), 119.5 (C=C), 123.0 (C=C), 134.9 (N-C=N), 174.1 (C-6 α), 175.0 (C-6 β). MS: ES^+ m/z 83.1 $[\text{HMIm}]^+$.

1-Butylimidazolium galacturonate, [BMIm][Gal]

1-butylimidazole (0.51 g, 4.1 mmol) was dissolved in water and titrated with 0.1 M galacturonic acid monohydrate (0.89 g, 4.6 mmol) to the equivalence pH 5.25. The mixture was stirred at room temperature for an hour and the solvent removed to yield a white solid (1.3 g, 98 %). Anomeric ratio: 36 % α and 64 % β . ^1H NMR (400 MHz, D_2O) δ (ppm): 0.93 – 0.96 (t, $J=7.6$ Hz, 3H, CH_3), 1.30 – 1.39 (m, 1H, CH_2), 1.85 – 1.93 (m, 2H, CH_2), 3.50 – 3.55 (dd, $J_{1\beta-2\beta}=8.0$ Hz, $J_{2\beta-3\beta}=10$ Hz, 1H, H-2 β), 3.70 – 3.73 (dd, $J_{3\beta-4\beta}=3.6$ Hz, $J_{2\beta-3\beta}=10$ Hz, 1H, H-3 β), 3.83 – 3.86 (dd, $J_{1\alpha-2\alpha}=3.6$ Hz, $J_{2\alpha-3\alpha}=10$ Hz, 1H, H-2 α), 3.92 – 3.95 (dd, $J_{3\alpha-4\alpha}=3.3$ Hz, $J_{2\alpha-3\alpha}=10$ Hz, 1H, H-3 α), 4.08 (d, $J_{4\beta-5\beta}=1.2$ Hz, 1H, H-5 β), 4.24 – 4.28 (m, $J_{4\beta-5\beta}=1.6$ Hz, $J_{\text{CH}_2}=7.2$ Hz, 3H, H-4 β , CH_2), 4.30 – 4.31 (dd, $J_{4\alpha-5\alpha}=1.4$ Hz, $J_{3\alpha-4\alpha}=3.3$ Hz, 1H, H-4 α), 4.43 (d, $J_{4\alpha-5\alpha}=1.4$ Hz, 1H, H-5 α), 4.58 – 4.60 (d, $J_{1\beta-2\beta}=8.0$ Hz, 1H, H-1 β), 5.31 – 5.32 (d, $J_{1\alpha-2\alpha}=3.6$ Hz, 1H, H-1 α), 7.48 (s, 2H, 2xCH), 8.74 (s, 1H, CH). ^{13}C NMR (400 MHz, D_2O) δ (ppm): 12.6 (CH_3), 18.8 (CH_2), 31.3 (CH_2), 49.1 (CH_2), 68.1 (C-2 α), 69.4 (C-3 α), 70.4 (C-4 α), 70.8 (C-4 β), 71.3 (C-5 α), 71.6 (C-2 β), 72.9 (C-3 β), 75.5 (C-5 β), 92.2 (C-1 α), 96.1 (C-1 β), 119.6 (C=C), 121.7 (C=C), 134.3 (N-C=N), 175.0 (C-6 α), 175.9 (C-6 β). MS: ES^+ m/z 125.2 [$\text{HBIm}]^+$.

2-Methylimidazolium galacturonate, [2-MeHImn][Gal]

2-methylimidazole (0.65 g, 7.7 mmol) was dissolved in water and titrated with 0.1 M galacturonic acid monohydrate (1.8 g, 9.1 mmol) to the equivalence pH 7.5. The mixture was stirred at room temperature for an hour and the solvent removed to yield a white solid (2.1 g, 99 %). Anomeric ratio: 36 % α and 64 % β . ^1H NMR (400 MHz, D_2O) δ (ppm): 2.23 (s, 3H, CH_3), 3.50 – 3.55 (dd, $J_{1\beta-2\beta}=7.8$ Hz, $J_{2\beta-3\beta}=10$ Hz, 1H, H-2 β), 3.70 – 3.73 (dd, $J_{3\beta-4\beta}=3.6$ Hz, $J_{2\beta-3\beta}=10$ Hz, 1H, H-3 β), 3.83 – 3.86 (dd, $J_{1\alpha-2\alpha}=3.6$ Hz, $J_{2\alpha-3\alpha}=10$ Hz, 1H, H-2 α), 3.92 – 3.95 (m, $J_{3\alpha-4\alpha}=3.4$ Hz, 5H, H-3 α , 2x CH_2), 4.07 (d, $J_{4\beta-5\beta}=0.8$ Hz, 1H, H-5 β), 4.23 – 4.24 (dd, $J_{4\beta-5\beta}=0.8$ Hz, $J_{3\beta-4\beta}=3.6$ Hz, 1H, H-4 β), 4.30 – 4.31 (dd, $J_{4\alpha-5\alpha}=1.2$ Hz, $J_{3\alpha-4\alpha}=3.4$ Hz, 1H, H-4 α), 4.42 (d, $J_{4\alpha-5\alpha}=1.2$ Hz, 1H, H-5 α), 4.58 – 4.60 (d, $J_{1\beta-2\beta}=7.8$ Hz, 1H, H-1 β), 5.31 – 5.32 (d, $J_{1\alpha-2\alpha}=3.6$ Hz, 1H, H-1 α). ^{13}C NMR (400 MHz, D_2O) δ (ppm): 11.7 (CH_3), 44.4 (2x CH_2), 68.1 (C-2 α), 69.4 (C-3 α), 70.4 (C-4 α), 70.8 (C-4 β), 71.4 (C-5 α), 71.6 (C-2 β), 72.9 (C-3 β), 75.5 (C-5 β), 92.2 (C-1 α), 96.1 (C-1 β), 168.6

(N-C=N), 175.1 (C-6 α), 175.9 (C-6 β) MS: ES⁺ m/z 85.1 [2-MeHImn]⁺; ES⁻ m/z 193.1 [Gal]⁻.

Thermal Properties

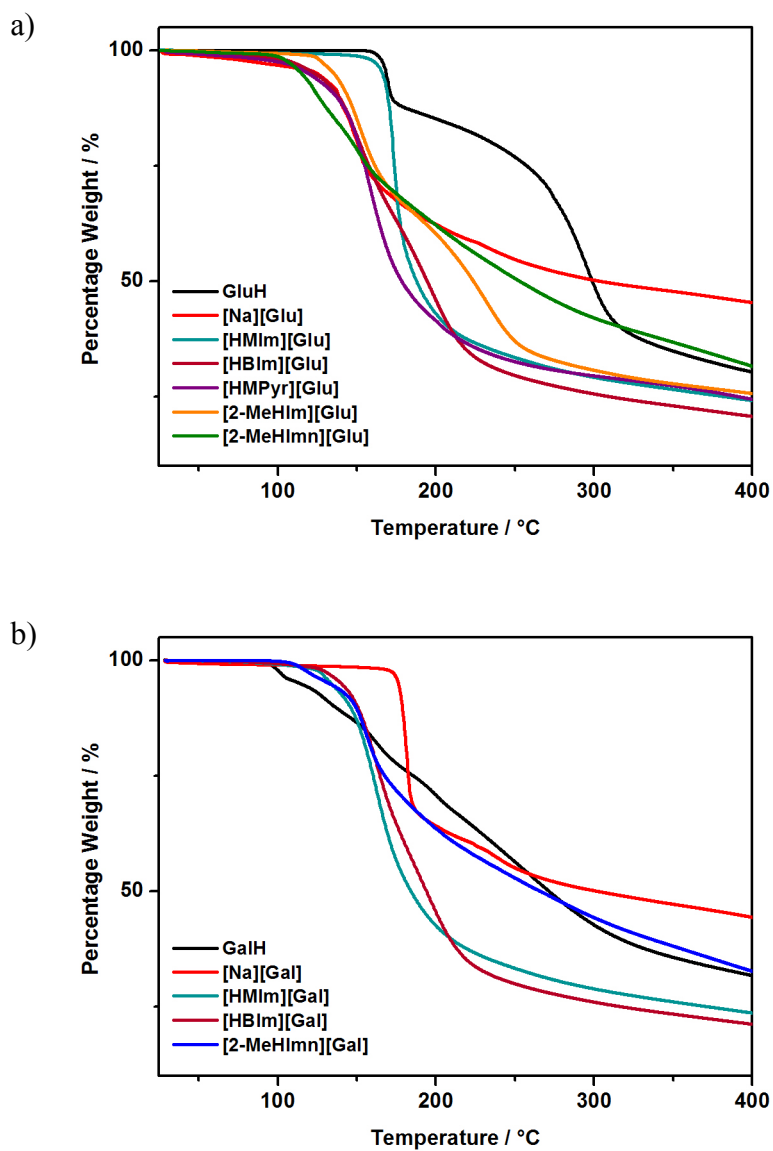


Figure S1. TGA curves for a) glucuronate salts and b) galacturonate salts.

Corrosion Inhibition

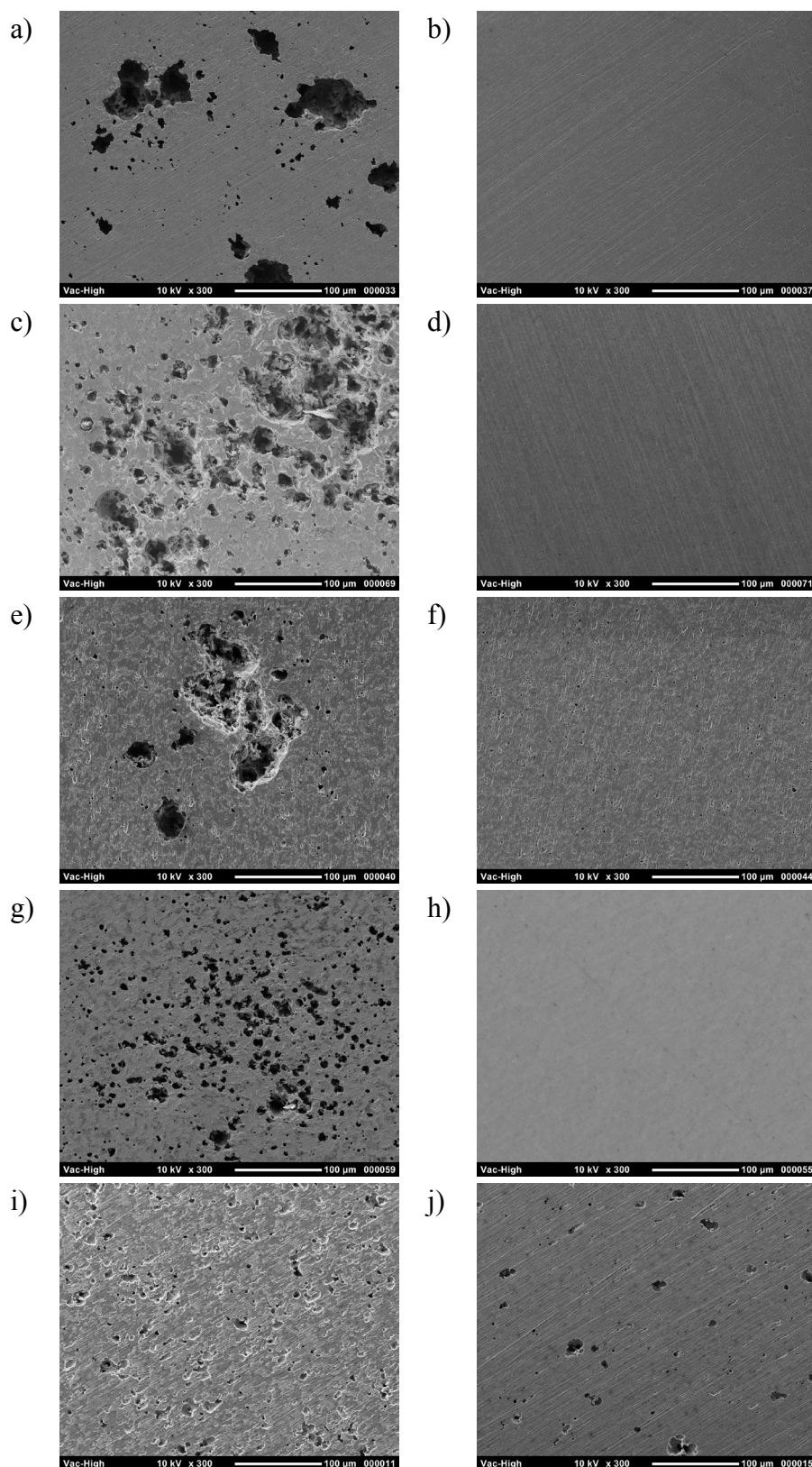


Figure S2. SEM images (x 300) of corroded (left) and uncorroded (right) regions after removal of corrosion product from mild steel immersed for 24 h in 0.01 M NaCl and: a) and b) 4 mM [2-MeHImn][Glu]; c) and d) 10 mM [2-MeHImn][Glu]; e) and f) 4 mM [2-MeHIm][Glu]; g) and h) 4 mM [2-MeHImn][Gal]; i) and j) control – no inhibitor.

5 SOLID-STATE CONDUCTIVITY IN PROTIC IMIDAZOLIUM AND IMIDAZOLINIUM SALTS

Leaving behind the corrosion applications discussed in the previous chapters, this chapter explores the potential for protic salts to be used as solid electrolytes. Chapter 2 provided physical characterisation of 2-methylimidazolinium triflate, [2-MeHImn][TfO], and 2-methylimidazolium triflate [2-MeHIm][TfO]; two protic ILs. During this characterisation, [2-MeHImn][TfO] displayed high ionicity and [2-MeHIm][TfO] good conductivity. In addition to this, Kudo et al.¹ identified [2-MeHIm][TfO] as a proton-conducting material during their study of the liquid-state electrochemical properties at elevated temperatures. This work sought to further investigate the conducting behaviour of these materials in the solid-state, at room temperature.

This study took its cues from prior work on similarly structured salts, classified as protic organic ionic plastic crystals (OIPCs). This family of materials are closely related to ILs, as many of the features that can generate room-temperature ILs (i.e. charge delocalisation, asymmetry and bulk) can also create salts that, at room temperature, are highly disordered solids. In fact, many OIPCs have been discovered alongside IL exploration. The disordered crystal structures in OIPCs can allow for fast ion transport, and they are often studied for solid electrolyte applications. This includes batteries, thermocells and fuel cells.

Solid-state NMR spectroscopy is a powerful tool for understanding the structure and transport behaviours of these materials. Analysing individual nuclei environments provides information about distinct species in the solid and by bringing together a selection of techniques it is possible to building up a picture of how the OIPC behaves. In this chapter, static solid-state and diffusion experiments are used to elucidate the mechanism behind the observed thermal behaviours and conductivities.

Single pulse static spectra (wide line NMR) of the sample can provide information about the rigidity of the structure. In a NMR measurement, the magnetic moment or ‘spin’ of each nucleus is affected not only by the external magnetic field, but also by neighbouring spins. The most common interactions are dipole-dipole interactions and chemical shift anisotropy. In solution, a species can move freely and averaging largely eliminates these effects, resulting in a sharp, well-defined peak for each different nucleus environment on a molecule. However, in a polycrystalline lattice, the individual nuclei cannot move so readily, and their slightly differing environments generate a broad distribution of frequencies. The broadness of these peaks (extracted as the linewidth at half the maximum peak height) is influenced by the extent of molecular motion within the crystal structure.² If the exact dimensions of the crystal structure are known, the linewidths can be modelled to specific rotational processes.^{3,4}

A static NMR experiment will also indicate the presence of any highly mobile, liquid-type phase that may exist in the system. Previous solid-state NMR studies of OIPCs have observed liquid-type behaviour, where a narrow peak is observed superimposed on a broad peak.⁵⁻⁸ Deconvolution of these components provides information about the populations of these mobile and immobile components.

Self-diffusion coefficients can be used to further elucidate the transport behaviour of any mobile nuclei within the solid. First described by Hahn,⁹ pulsed-gradient spin echo or stimulated echo methods (PGSE or PGSTE) can be used to perform NMR diffusion measurements. In this work PGSTE was used. Briefly, a series of radio frequency (RF) pulses and magnetic field gradients are applied to the sample, resulting in an echoed FID signal being detected at a time, τ , after the final RF pulse, equivalent to the time between RF pulses. In these sequences, the first gradient pulse dephases the magnetisation of the spins, while the second pulse rephases them, to generate the echoed signal. However, any nuclei that diffuse during the interval, τ , between pulses cannot be rephased, causing a drop in FID signal intensity. The rate of this signal decay correlates to the diffusivity of the species as described by the Stejskal-Tanner Equation (Equation 1).¹⁰

$$\ln(I/I_0) = -D\gamma^2 G^2 \delta^2 (\Delta - \delta/3) \quad (8)$$

where I is the NMR signal strength and I_0 the signal strength without gradient effects. D is the diffusion coefficient, γ is the gyromagnetic ratio of the nuclei, G is the strength of the magnetic field gradient, δ is the gradient pulse length and Δ is the diffusion time. As γ , δ and Δ are all set constants for the measurement, D can be extracted by measuring across a range of G and plotting I as a function of G .

In the following prepared manuscript, the described solid-state NMR techniques are used, in conjunction with thermal characterisation and impedance spectroscopy, to investigate the differences in structure and conductivity between [2-MeHImn][TfO] and [2-MeHIm][TfO], as well as the influence of doping the salts with either excess acid (anion source) or base (cation source).

1. K. Kudo, S. Mitsushima, N. Kamiya and K.-i. Ota, *Electrochemistry*, 2005, **73**, 668-674.
2. M. H. Levitt, *Spin dynamics : basics of nuclear magnetic resonance*, 2nd ed edn., John Wiley & Sons, Chichester, 2008.
3. J. H. Van Vleck, *Physical Review*, 1948, **74**, 1168-1183.
4. H. S. Gutowsky and G. E. Pake, *J. Chem. Phys.*, 1950, **18**, 162-170.
5. L. Jin, K. M. Nairn, C. M. Forsyth, A. J. Seeber, D. R. MacFarlane, P. C. Howlett, M. Forsyth and J. M. Pringle, *J. Am. Chem. Soc.*, 2012, **134**, 9688-9697.
6. U. A. Rana, R. Vijayaraghavan, D. R. MacFarlane and M. Forsyth, *Chem. Commun.*, 2011, **47**, 6401-6403.
7. J. Rao, R. Vijayaraghavan, F. Chen, H. Zhu, P. C. Howlett, D. R. MacFarlane and M. Forsyth, *Chem. Commun.*, 2016.
8. H. Zhu, D. MacFarlane and M. Forsyth, *J. Phys. Chem. C*, 2014, **118**, 28520-28526.
9. E. L. Hahn, *Physical Review*, 1950, **80**, 580-594.
10. E. O. Stejskal and J. E. Tanner, *J. Chem. Phys.*, 1965, **42**, 288-292.

5.1 Enhancing solid-state conductivity through acid or base doping of protic imidazolium and imidazolinium triflate salts

Alison L. Chong^a, Haijin Zhu^b, Kate M. Nairn^a, Maria Forsyth^b, Douglas R. MacFarlane^{a*}

^aSchool of Chemistry, Monash University, Clayton, Victoria 3800, Australia.

^bInstitute for Frontier Materials, Deakin University, Burwood, Victoria 3125, Australia.

* Corresponding author. Email: douglas.macfarlane@monash.edu

Abstract

Protic salts, including those showing plastic crystal behaviour, are an interesting family of materials being rediscovered for use as solid conducting materials. This work compares two such compounds, 2-methylimidazolium triflate, [2-MeHIm][TfO], and 2-methylimidazolinium triflate [2-MeHIImn][TfO]. The subtle change in structure resulted in substantial differences in thermal behaviour; [2-MeHIm][TfO] shows two solid – solid phase transitions while none were observed for [2-MeHIImn][TfO]. However, both compounds are in a disordered solid state ($\Delta S_f < 40 \text{ JK}^{-1}\text{mol}^{-1}$) resulting in relatively high room temperature conductivities. Neat [2-MeHIImn][TfO] had a conductivity above 10^{-5} Scm^{-1} , but the addition of either the component acid or base as dopants resulted in a substantial increase in conductivity, to over 10^{-4} Scm^{-1} at 30 °C. Solid-state ^1H and ^{19}F NMR spectroscopy suggests that the dopants enhance the conduction primarily by increasing the proportion of mobile ions in the solid matrix. However, [2-MeHIm][TfO] also displays evidence of proton-hopping on the cation.

Introduction

Protic organic ionic plastic crystals (OIPCs) are a class of materials that are of growing interest in the search for solid-state proton conducting materials. Protic OIPCs, and OIPCs generally, signal a move towards the use in electrochemical devices of highly conductive solid-state electrolytes and membranes which avoid many of the limitations introduced by aqueous and organic liquids. These include issues of leakage, solvent evaporation, flammability, and constraints on cell design and operating temperatures.

OIPCs are salts composed of an anion and cation that feature at least one solid phase in which the crystal structure is maintained, but one or both ions is able to move, usually due to a degree of orientational or rotational freedom. This long range order, but short

range disorder, can predispose these materials to slip-plane deformation under mechanical stress, producing plastic properties and hence the term plastic crystal.¹⁻³

OIPCs present an attractive alternative to other types of solid-state conductors. A large number of polymer electrolytes have been developed, but they can suffer from limited conductivities due to the associations between the mobile ions and the relatively immobile backbone of the polymer. In contrast, ceramic materials can support fast ion transport through the crystal lattice, however, they are often quite brittle. OIPCs present a middle ground, whereby they have a defined lattice structure that can support ion transport, but more flexible material properties.^{1,4,5}

Progressing from molecular plastic crystals such as cyclohexane and succinonitrile,^{6,7} the last decades have seen a rise in the number of reports of salts that display plastic crystalline phases. The most common families of OIPCs contain pyrrolidinium, imidazolium or quaternary ammonium cations, paired with anions such as dicyanamide, tetrafluoroborate, hexafluorophosphate or bis(trifluoromethylsulfonyl)imide.^{8,9} Many of these species are found in ionic liquids – a closely related family of low melting salts, and in some cases there is overlap between the two families. A key feature of these ions is their bulky or charge diffuse nature that disrupts the formation of a rigid crystalline structure. All of these early salts feature a fully quaternised or aprotic cation.

The last few years have seen the emergence of a subclass of OIPCs that feature a proton on the cation, rather than a quaternary charged centre. These protic materials can be synthesised through neutralisation of a Brønsted acid and base. This process involves fewer synthetic steps and by-products than the quaternisation and anion metathesis processes that are commonly employed to make aprotic OIPCs.

Protic OIPCs have been proposed in particular for use in proton exchange membrane fuel cells (PEMFCs), energy storage devices which use a membrane to separate two electrolyte reservoirs that only allows protons to permeate.^{10,11} The most common material in commercial use is a hydrated Nafion polymer membrane; however, the operating conditions of these membranes are limited by the need for hydration of the membrane to provide high conductivity.¹² It is proposed that protic OIPCs could provide an entirely solid alternative.

The studies on protic OIPCs for use as proton conductors have largely focused on a select range of anions and cations that are particularly geared towards promoting proton transport. The most commonly studied anion is the triflate anion.¹³⁻¹⁵ As one of the strongest molecular acids ($\text{pK}_a \approx -12$),¹⁶ triflic acid has a very weak conjugate base. Such a

weakly coordinating anion helps to ensure that the released proton is truly decoupled from the matrix. This mimics the commercial Nafion conducting polymer, which features the chemically similar $-\text{CF}_3\text{SO}_3\text{H}$ terminal group.¹² The strength of this acid comes from the combination of both the sulfonate moiety and the electron withdrawing fluorinated methyl group. A number of protic OIPCs have incorporated the closely related nonaflate anion,^{13, 17, 18} or incorporated anions that featured a sulfonate moiety (methanesulfonate,¹⁹ *p*-toluenesulfonate¹³) or fluorination (trifluoroacetate¹³).

The choice of cation has thus far been limited to small nitrogen-based species. Zhu¹⁴ and Chen¹⁷ synthesised protic OIPCs with guanidinium, a symmetrical, charge delocalised cation with six dissociable protons. A contrasting approach is to use imidazolium and similar heterocycles such as benzimidazolium and triazolium. Tricoli et al.¹³ suggest that such a selection is motivated by the amphoteric nature of the nitrogens, which may encourage a Grotthuss-type proton-hopping mechanism through the breaking and formation of N-H bonds. This concept has been studied computationally through the use of molecular dynamics simulations which show that in the presence of a defect such as a proton or hole dopant, proton hopping via rearrangement of N-H bonds is a favourable process.²⁰⁻²²

While some of these protic OIPCs show high intrinsic conductivity, existence of a plastic phase does not guarantee this. One method of improving the conductivity is through the addition of dopants. Previous research into doping plastic crystals has largely focused on the addition of excess acid, usually the anion source. In most cases, the acid used is triflic acid (TfOH). For example, Zhu et al.¹⁴ showed a several orders of magnitude increase in conductivity up to 10^{-3} Scm^{-1} upon the addition of TfOH to guanidinium triflate. Methanesulfonic acid and phosphoric acid have also been used to enhance the conductivity of aprotic OIPC and molecular plastic crystals.^{23, 24} In each of these cases, the acid introduces extra, potentially mobile, protons.

Despite optimising protic OIPC systems for proton conduction, there is evidence that this is not the only mechanism by which these materials show high solid-state conductivities. In-depth solid-state NMR studies of the guanidinium triflate system showed that the predominant mechanism is the percolation of ions through liquid-like regions at the grain boundaries of the crystals.^{14, 25} Disruption to the solid matrix was enhanced by the addition of TfOH as a dopant, resulting in observed increases in conductivity.

What has not been explored in protic OIPCs is the use of the cation source as a base dopant. Computational studies suggest, however, that the introduction of vacancies, such

as an unprotonated nitrogen, could promote a chain of bond rearrangements, in the same way that an excess proton would.^{20, 22} Additionally, the introduction of base molecules could also disrupt the crystal lattice to increase conductivity via a percolation-type model. There is strong interest in membranes for use under “alkaline” conditions, in both water electrolysis and also the nitrogen reduction reaction, both of which are optimal at low proton activity.²⁶⁻²⁸

There is some precedent elsewhere for the use of bases, particularly imidazole, to enhance conductivity. Hamit et al.²⁹ have developed an ionic polymer incorporating imidazolium into the backbone, and Zhao et al.³⁰ propose an imidazole-functionalised cellulose membrane for use in fuel cells.

Herein, we present a study of two analogous triflate organic salts as protic OIPCs, featuring an aromatic 2-methylimidazolium cation and a non-aromatic 2-methylimidazolinium cation. To our knowledge, this is the first study of base doping in a protic OIPC, as well as the first comparative study of the effects of doping with the acid versus the base of an OIPC.

Experimental

Materials

All reagents were purchased from Sigma Aldrich and used without further purification. Tetrahydrofuran (THF) was dried over sodium wire with benzophenone and stored over molecular sieves. Other solvents were dried and stored over 4A molecular sieves.

Synthesis

2-Methylimidazoline, 2-MeImn

Triethylorthoacetate (26.6 g, 0.16 mol) and a catalytic amount of concentrated hydrochloric acid were added to a three-necked flask charged with acetonitrile. Ethylenediamine (9.4 g, 0.156 mol) was added dropwise, resulting in formation of a white precipitate. The mixture was heated to reflux (100 °C) and stirred for 12 hours. The solvent was removed to give a pale yellow solid. Purification by cold-finger recrystallisation yielded white needles (10.8 g, 83 %). ¹H NMR (400 MHz, DMSO-*d*₆) δ (ppm): 1.73 (s, 3H, CH₃), 3.35 (unresolved d, 4H, 2x CH₂), 5.50 (broad s, 2H, 2x NH). ¹³C NMR (400 MHz, DMSO-*d*₆) δ (ppm): 14.7(CH₃), 49.4(2x CH₂), 163.5 (N-C=N). Mass spectrum: ES⁺ m/z 85.0 [2-MeHImn]⁺.

2-Methylimidazolinium triflate, [2-MeHImn][TfO]

2-methylimidazoline (6.9 g, 0.08 mol) was dissolved in deionised water. Triflic acid (12.0 g, 0.08 mol), diluted in water, was added until the solution was neutralised (~pH 6) (Figure S1). The mixture was stirred overnight and the solvent removed to yield an off-white solid. Recrystallisation from hot THF and toluene gave white crystals (14.1 g, 73%). ^1H NMR (400 MHz, DMSO-*d*6) δ (ppm): 2.14 (s, 3H, CH₃), 3.79 (unresolved d, 4H, 2x CH₂), 9.75 (s, 2H, 2x NH). ^{13}C NMR (400 MHz, DMSO-*d*6) δ (ppm): 12.1(CH₃), 44.2 (2x CH₂), 119.07, 122.3 (CF₃) 168.0 (N-C=N). ^{19}F NMR (400 MHz, DMSO-*d*6) δ (ppm): 77.77 (CF₃). Mass spectrum: ES⁺ m/z 85.1 [2-MeHImn]⁺, 319.1 2[2-HMeHImn]⁺[TfO]⁻; ES⁻ m/z 148.9 [TfO]⁻, 383.0 [2-MeHImn]⁺2[TfO]⁻.

2-Methylimidazolium triflate, [2-MeHIm][TfO]

2-methylimidazole (5.5 g, 0.07 mol) was dissolved in deionised water. Triflic acid (10.0 g, 0.07 mol), diluted in water, was added until the solution was neutralised (~pH 5) (Figure S1). The mixture was stirred overnight and the solvent removed to yield an off-white solid (15.1 g, 97%). ^1H NMR (400 MHz, DMSO-*d*6) δ (ppm): 2.55 (s, 3H, CH₃), 7.52 (s, 2H, 2x CH), 13.75 (s, 2H, 2x NH). ^{13}C NMR (400 MHz, DMSO-*d*6) δ (ppm): 11.1 (CH₃), 118.6 (2x CH), 119.1, 122.3 (CF₃) 144.2 (N-C=N). ^{19}F NMR (400 MHz, DMSO-*d*6) δ (ppm): 77.77 (CF₃). Mass spectrum: ES⁺ m/z 83.1 [2-MeHIm]⁺, 315.1 2[2-HMeHIm]⁺[TfO]⁻; ES⁻ m/z 148.9 [TfO]⁻, 380.9 [2-MeHIm]⁺2[TfO]⁻.

Doping

[2-MeHImn][TfO] and [2-MeHIm][TfO] were dissolved in deionised water and 1, 2.5 or 5 mol% of either TfOH, 2-MeImn or 2-MeIm was added from stock solutions. After stirring for at least one hour the solvent was removed and the samples dried under high vacuum at 50 °C for three days. Samples were stored under an inert atmosphere. The water content of the samples was measured using coulometric Karl Fischer titration of methanol solutions with a Metrohm 831 KF Coulometer. Samples were found to contain less than 0.5 wt% water. The dopant levels were measured by titration of aqueous samples with either hydrochloric acid or sodium hydroxide standard solutions (Table S1). The determined doping amounts are used throughout.

Characterisation

^1H , ^{13}C and ^{19}F solution-state NMR spectra were recorded in DMSO-*d*6 (Merck) using a Bruker Avance 400 (9.4 T magnet) fitted with a BACS 60 tube autosampler, operating at 400 MHz (^1H frequency). Low resolution ESI mass spectra were recorded on a

Micromass Platform II QMS with a cone voltage of 35 V, using methanol as the mobile phase.

Differential scanning calorimetry (DSC) was carried out using a Perkin Elmer DSC 8000 with liquid nitrogen cryo cooler. Scans were run at a heating/cooling rate of 10 °C/min over a temperature range of -80 to 100 °C. Transition temperatures were reported using the peak maximum of the thermal transition. Thermogravimetric analysis (TGA) was undertaken on a Mettler Toledo TGA/DSC 1 STARe System. Samples were heated at 10 °C/min over a temperature range of 25 to 550 °C.

Impedance Spectroscopy

The conductivity was evaluated using AC impedance spectroscopy over a range of 10 Hz to 10 MHz. Measurements were carried out using a Biologic MTZ35 meter equipped with a Eurotherm 2204e temperature controller. A probe with two platinum pin electrodes was inserted into the liquid samples, which were allowed to solidify prior to measurements from -10 °C to 75 °C. Resistance values for conductivity calculations were taken to be the low frequency data point closest to the x-axis on the Nyquist plot.

Solid-state NMR Spectroscopy

The samples were ground to a fine powder and sealed into 4 mm solid-state magic angle spinning (MAS) rotors in an inert atmosphere prior to measurement. All variable temperature solid-state ^1H and ^{19}F experiments were performed on a Bruker Avance III 300 MHz wide-bore NMR spectrometer (^1H Larmor frequency of 300.13 MHz). A 4 mm double-resonance MAS probe head was used to record the spectra from stationary powder samples. For both ^1H and ^{19}F experiments, the 90° pulse lengths were 2.0 μs , and the recycle delays were 10 s to allow the system time to recover to equilibrium. Samples were equilibrated for 300 s at each temperature prior to measurement.

For diffusion measurements, the 4 mm rotors were inserted into a standard 5 mm glass tube and a 5 mm diff50 pulse-field gradient probe fitted to the spectrometer. The pulsed gradient stimulated echo (PGSTE) sequence³¹ was used to obtain diffusion coefficients for the cation and anion, based on integration of the ^1H and ^{19}F signals.

Results and Discussion

Thermal Properties and Phase Behaviour

Figure 1 demonstrates the high thermal stability of these salts, with the pure [2-MeHImn][TfO] and [2-MeHIm][TfO] compounds showing decomposition onsets (T_d)

at 385 °C and 393 °C respectively. This stability can be attributed to the stability of the fluorinated anion, and is consistent with decomposition data for other protic triflate ILs.³²

In the case of the imidazolium IL, the addition of the acid or base dopants had a minimal effect on the stability, with only a slight decrease in T_d at the highest doping concentration. The dopants appear to be well incorporated into the ionic mixture, as there was no appreciable weight loss observed at the boiling points of either triflic acid (162 °C) or 2-methylimidazole (270 °C).

This was not the case with the 2-methylimidazolium IL, where it appears that some of the additional acid or base may not be fully incorporated. The addition of 2-MeImn resulted in a loss of up to 1.5 wt% from 190 °C, the boiling point of the base. The addition of acid caused an earlier onset of weight loss from 100 °C, resulting in less than 1 wt% loss. These amounts, however, are smaller than the total doping amount, indicating the dopants are at least partially incorporated into the mixture. This material thus serves as a demonstration of the effect of incomplete solubility of the dopant in the matrix material.

It is possible that the failure of the dopants to fully incorporate into the [2-MeHImn][TfO] solution could be related to a decrease in the strength of the hydrogen bonds to the surrounding ions. As 2-methylimidazoline is a stronger base than 2-methylimidazole, it could be expected that the transferred proton from the triflic acid would be more attached to the imidazolium and less available to form a hydrogen bond network. Hence, some of the unprotonated base is more readily vaporised at its expected boiling temperature.

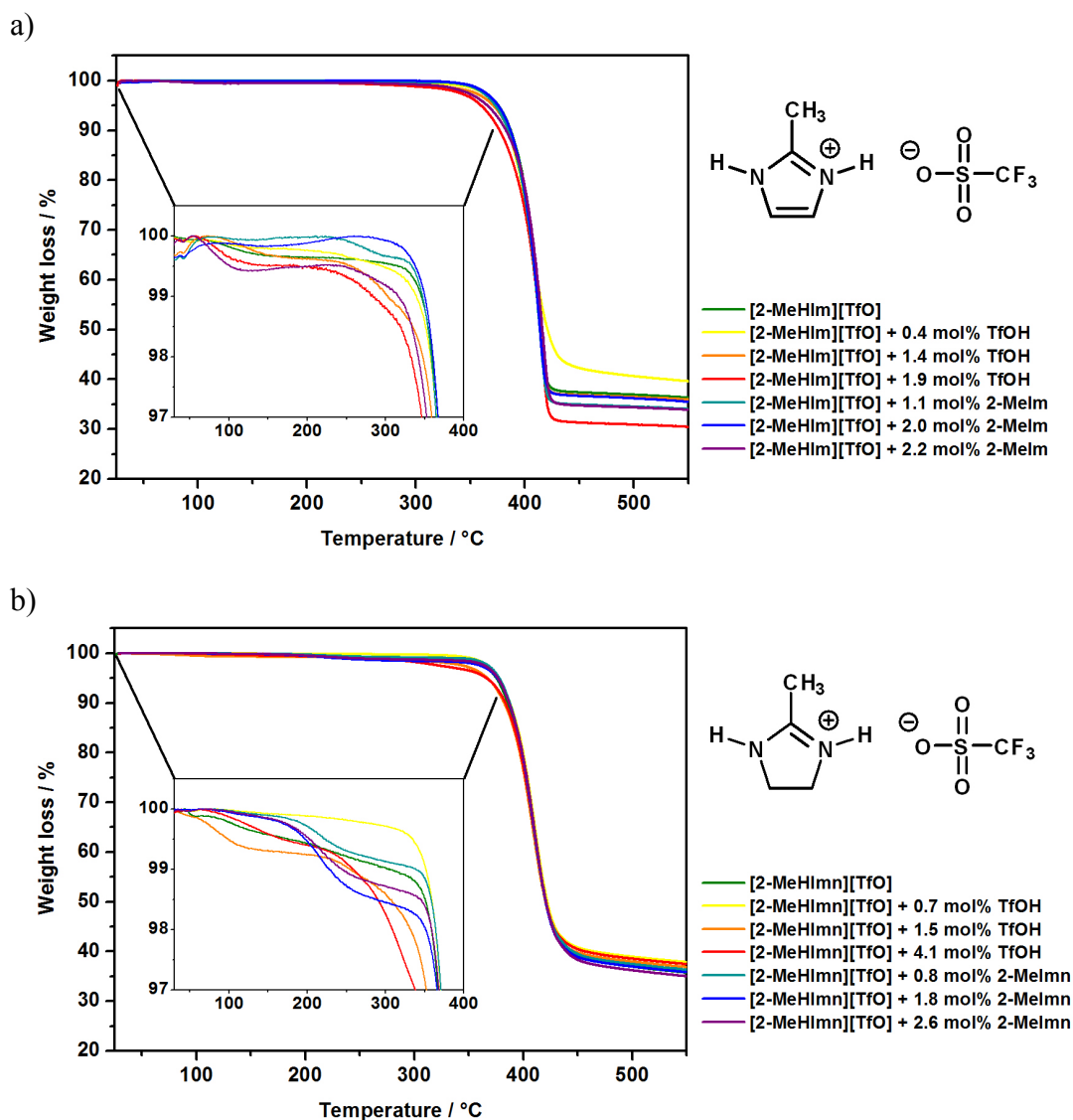


Figure 1. Structure and TGA data for a) [2-MeHIm][TfO] and b) [2-MeHImn][TfO] with acid or base doping.

The thermal transitions of the two compounds are remarkably different. While [2-MeHImn][TfO] shows a simple melt at 65 °C (Figure 2), switching to 2-MeHIm⁺ results in a series of more complex phase changes before an eventual melt at 61 °C (Figure 3).

The addition of either the acid or base to [2-MeHImn][TfO] resulted in a lowering of the melting point and broadening of the transition, behaviour that is consistent with the introduction of impurities into the crystal lattice. Increasing the amount of acid gradually decreased the melting point, whereas less than 1 mol% 2-MeImn was sufficient to depress the melt by 7 °C, similar to the effect of higher base doping levels.

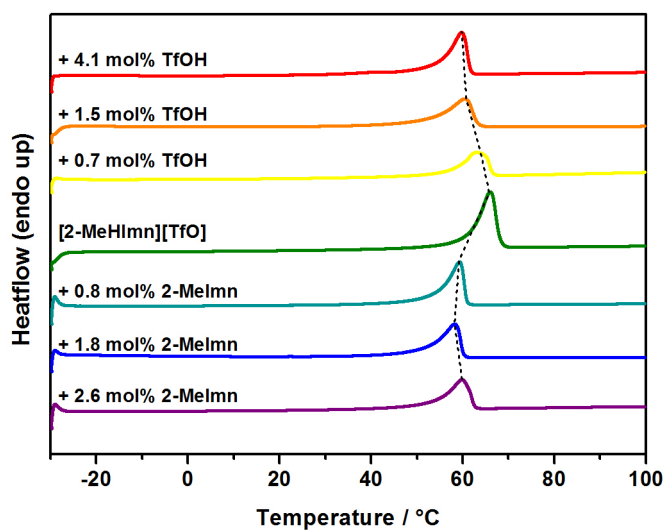


Figure 2. DSC thermograms of [2-MeHIm][TfO] with acid or base doping into the pure salt (green trace, centre diagram). Trend lines are added as a guide.

Instead of a simple melt, [2-MeHIm][TfO] showed endothermic transitions around 13 °C and 30 °C prior to melting at 61 °C (Figure 3). As observed for [2-MeHIm][TfO], doping lowered the melting point, with increasing dopant concentrations depressing the transition by up to 11 °C at the highest TfOH composition.

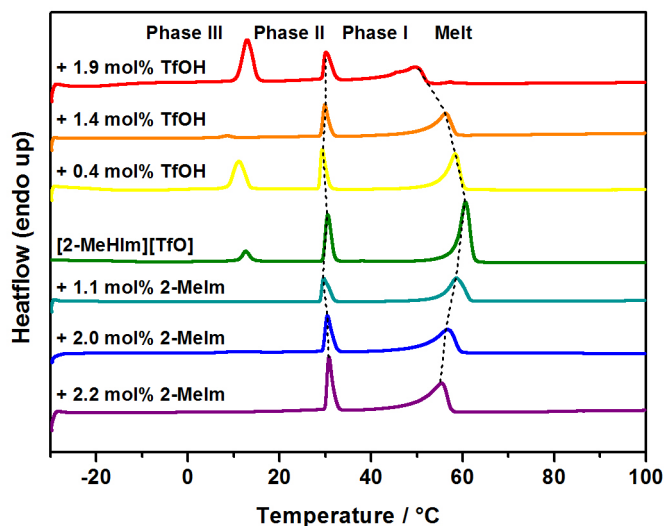


Figure 3. DSC thermograms of [2-MeHIm][TfO] with acid or base doping into the pure salt (green trace, centre diagram). Trend lines are added as a guide.

The I-II solid-solid transition around 30 °C does not show any dependence on the doping level. This suggests that this transition to a more entropically-free crystal lattice is

not affected by the introduction of impurities. The lower temperature transition sees some change in temperature with the introduction of excess TfOH and is completely suppressed in the presence of excess 2-MeIm. It is hypothesised that such behaviour may indicate an eutectic transition, involving generation of a new liquid phase.³³

An important consideration when dealing with multi-phase, potentially plastic materials is Timmermans' criterion, which states that an organic plastic crystal will have an entropy of melting below $20 \text{ JK}^{-1}\text{mol}^{-1}$.² This is because the rotational or translational motion introduced in the preceding transitions reduces the entropy, ΔS_f , required to introduce all degrees of freedom upon melting. The entropy for a more conventional crystal lattice is generally closer to $70 \text{ JK}^{-1}\text{mol}^{-1}$. Table 1 shows the entropy for each transition observed in the two pure salts. In the case of [2-MeHIm][TfO], the entropy of fusion was calculated to be $37 \text{ JK}^{-1}\text{mol}^{-1}$. While this is higher than Timmermans' requirement, it is still around half that typically observed for a fully ordered crystalline salt. Pringle et al.¹ have previously shown that some OIPCs have higher than expected ΔS_f values often as high as $40 \text{ JK}^{-1}\text{mol}^{-1}$, usually when the plastic phase involves rotation of only one ion species and not the other.

It must be noted that ΔS_f of [2-MeHImn][TfO] is similarly low. This suggests that the observed solid state in this material is also quite disordered, implying the presence of a more rigid crystal phase at a lower temperature (outside the measured temperature range), or not easily formed under DSC conditions. It is possible that the disordered nature of the two salts may be a source of lattice defects to enable fast transport of protons in the solid state.

Table 1. Entropies (ΔS) of transitions observed in [2-MeHIm][TfO] and [2-MeHImn][TfO].

Sample	Entropy of Transition / $\text{JK}^{-1}\text{mol}^{-1}$		
	$\Delta S(\text{III-II})$	$\Delta S(\text{II-I})$	$\Delta S_f(\text{melt})$
[2-MeHIm][TfO]	6	15	37
[2-MeHImn][TfO]	-	-	36

Solid-state Conductivity

Figure 4 shows the conductivity of the doped and pure [2-MeHIm][TfO] and [2-MeHImn][TfO] samples measured from $-10 \text{ }^\circ\text{C}$ to above the melt. Due to the nature of the setup, some samples solidified such that there was a poor connection between the electrodes at low temperatures, and thus conductivities at these temperatures could not be

recorded. These materials show comparable conductivity to other un-doped plastic crystals and organic salts.^{14, 17, 34} Of the two neat materials, [2-MeHImn][TfO] showed an order of magnitude greater conductivity at 30 °C. While some studies have demonstrated a clear dependence of the conductivity on the material's phase,^{19, 34} this was not seen for [2-MeHIm][TfO], as there were no observed jumps in conductivity across the two identified transition temperatures at 13 °C and 30 °C. Instead, both salts showed a high and fairly linear change with temperature until they begin to melt.

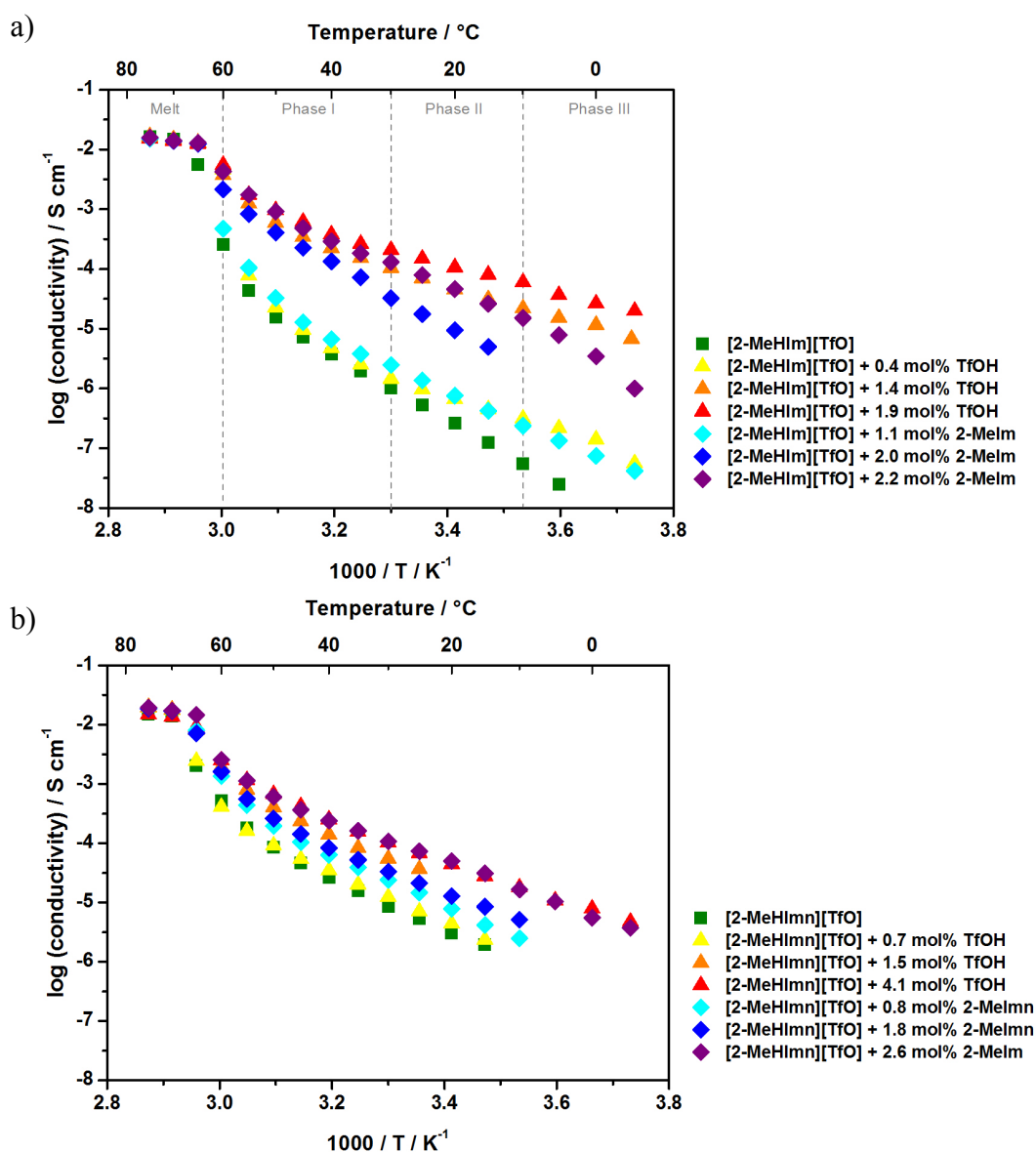


Figure 4. Conductivity of the pure and doped a) [2-MeHIm][TfO] and b) [2-MeHImn][TfO] samples as a function of inverse temperature. Grey lines indicate the phase transitions in [2-MeHIm][TfO] as identified by DSC.

In the [2-MeHIm][TfO] samples there was a clear distinction between the low-doped samples and higher loadings. The addition of a small amount of TfOH resulted in only a modest increase in conductivity, but there was a substantial jump as the dopant concentration was increased, resulting in conductivities $>10^{-4} \text{ Scm}^{-1}$ at 30 °C. This is a technologically significant level of conductivity for a solid electrolyte. Further increasing the amount of TfOH only slightly improved the conductivity. Such a threshold is consistent with work by Zhu et al.¹⁴ that determined conductivity in the guanidinium triflate system was greatly enhanced above a threshold of 1.8 mol% TfOH. A very similar trend can be seen for the base-doped samples, although the conductivity values were lower, particularly as the temperature decreased.

In [2-MeHImn][TfO] doping had a less pronounced effect, with gradual increase in conductivity. At the highest loading, however, both acid and base dopants had the same effect. The overall symmetry of the doping effects can be seen in Figure 5. The addition of large amounts of 2-MeIm and 2-MeImn as dopants led to very similar increases in conductivity to TfOH. This suggests that the conduction mechanisms do not rely solely on the addition of excess protons.

Figure 5 also highlights the effects of doping on each salt. Although the imidazolinium salt was more conductive than the imidazolium salt in its pure state, it did not see as large an increase in conductivity upon doping. Although the pure and low-level doped [2-MeHImn][TfO] samples showed substantially higher conductivities than their imidazolium counterparts, this deficit was made up, with the [2-MeHIm][TfO] samples even showing greater conductivities. It appears as though higher-level doping does not have a fixed additive effect on the two salts, but rather increases conductivity towards a limit, such that at the highest level of loading, the results were somewhat similar across both compounds and across acid and base dopants.

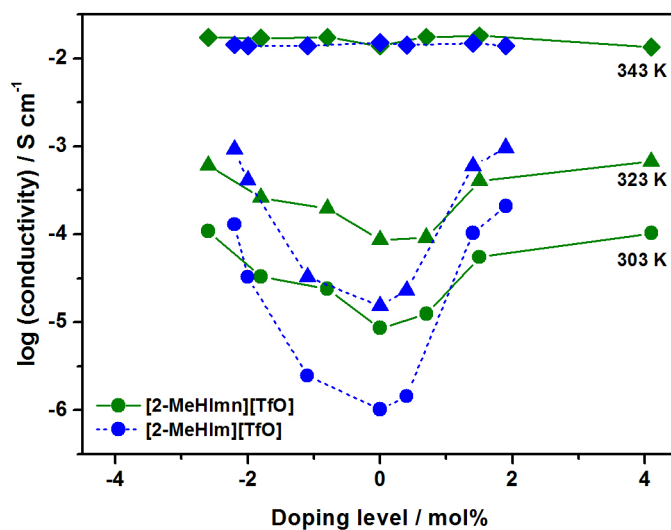


Figure 5. Dependence of conductivity of [2-MeHImn][TfO] and [2-MeHIm][TfO] on mole fraction of dopant at selected temperatures. Added TfOH is considered as a positive proton doping percentage, therefore base doping is “negative” in terms of proton doping. Lines are a guide only.

The conductivities of both neat salts displayed quite strong temperature dependence, which was reduced upon the addition of a dopant. This behaviour is directly related to the energy profile of the conduction process. Using Equation 1, the slope of the Arrhenius plot can be used to calculate the activation energy of conduction, E_a .

$$\sigma = \sigma^0 e^{-E_a/RT} \quad (1)$$

Where σ is the conductivity, and σ^0 the pre-exponential term that represents the conductivity at infinite temperature. In Table 2, it can be seen that at 30 °C, the addition of a dopant substantially decreased E_a . At the highest level of doping, the addition of TfOH more than halved E_a compared to pure [2-MeHIm][TfO]. In [2-MeHImn][TfO], the 2-MeImn dopant had the greater effect. It is clear that both acid and base dopants can effectively reduce the energy barrier required for conduction to take place.

Table 2. Activation energies for conductivity for [2-MeHIm][TfO] and [2-MeHImn][TfO] with highest doping level at 30 °C.

Sample	Activation energy E_a / kJmol ⁻¹ ±5%		
	Neat	+ TfOH	+ base
[2-MeHIm][TfO]	101	47	69
[2-MeHImn][TfO]	83	67	60

Solid State NMR Spectroscopy

Solid-state NMR experiments can provide a better understanding of the conduction mechanisms related to the observed increases in conductivity. As with similar studies, the dynamics of each ion can be tracked separately through the protons on the cation and fluorines on the anion.^{25, 34}

Static spectra across a range of temperatures can be used to evaluate the proportion of mobile species in the solid structure. Figure 6 shows spectra obtained from the pure [2-MeHIm][TfO] and [2-MeHImn][TfO] samples at a selection of temperatures below the melt. The spectra have a broad peak, indicative of immobile nuclei within the crystalline matrix, and sharp peaks (more akin to a solution state spectrum), representing nuclei that have some degree of mobility.³⁵ For both samples, three mobile ^1H peaks are observed, showing chemical shifts and integrations consistent with the number of proton environments in the cations. At any given temperature, [2-MeHImn][TfO] appears to have a greater proportion of mobile cation (^1H) and anion (^{19}F) species. The ^1H [2-MeHIm][TfO] spectra show that the broad peak noticeably narrows at 30 °C. This is paired with the appearance of a shoulder in the ^{19}F spectra at the same temperature, likely due to increased prominence of chemical shift anisotropy (CSA) broadening at these temperatures.

Similar spectra for the highest doped samples can be found in the supplementary information (Figure S3 – Figure S6).

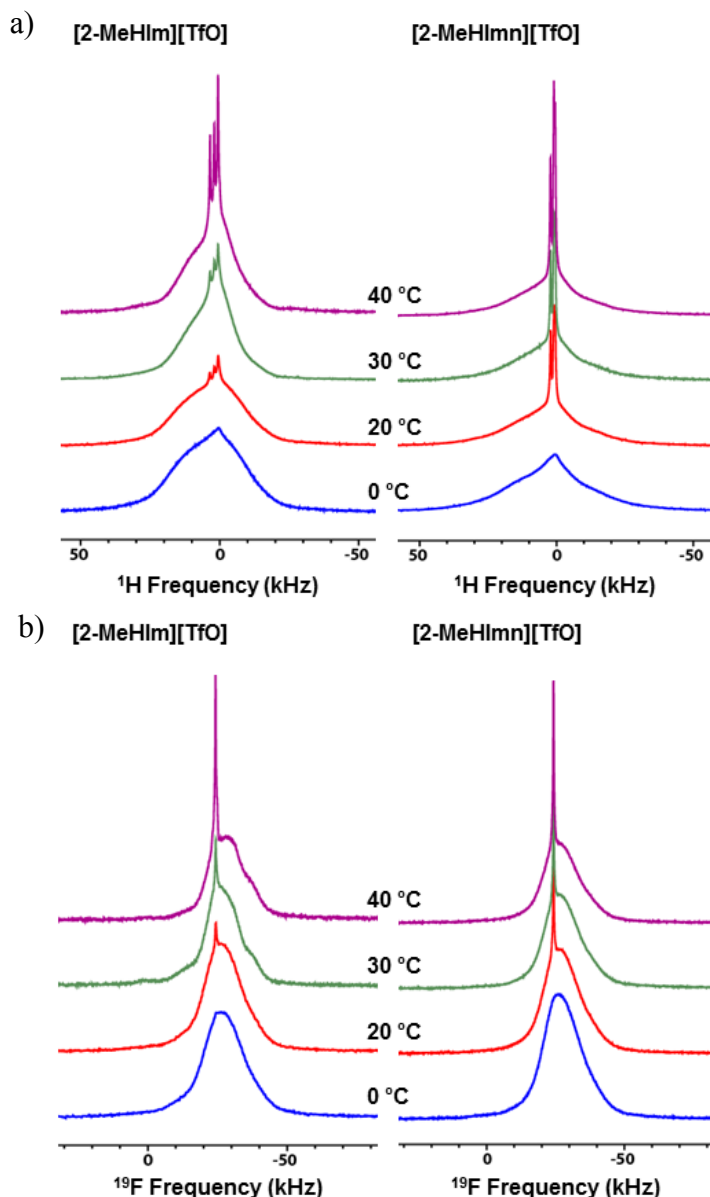


Figure 6. Static solid-state a) ^1H NMR and b) ^{19}F NMR spectra of [2-MeHIm][TfO] and [2-MeHImn][TfO] at selected temperatures.

Area fractions of the narrow peaks, calculated using Gauss-Lorentz and CSA fitting of the spectra are shown in Figure 7.³⁶ An example fit is shown in Figure S8. As expected, all samples show increases in the mobile phase content as the temperature increases. Interestingly, all samples except pure [2-MeHImn][TfO] show 100 % mobile phase at temperatures above 50 °C, below the determined melting point. Due to the broad nature of the transition, the onset of melting may already have occurred at 50 °C, and because the sample is held at the temperature long enough to equilibrate and completely melt.

The area fractions in Figure 7a, confirm that pure [2-MeHImn][TfO] has a larger proportion of mobile cations than [2-MeHIm][TfO] in the solid state. The addition of

dopants, however, substantially increases the area fraction for both samples. In [2-MeHIm][TfO], the acid-doped sample has a greater fraction of mobile cations than the pure or base-doped samples. In contrast, the doped [2-MeHImn][TfO] samples show very similar proportions of cation mobility, regardless of whether the dopant was TfOH or 2-Melm, particularly at lower temperatures. The mobile fraction of cations was quite high for the doped samples, with 20 % of the [2-MeHImn]⁺ cations mobile at 0 °C, well below the melting point.

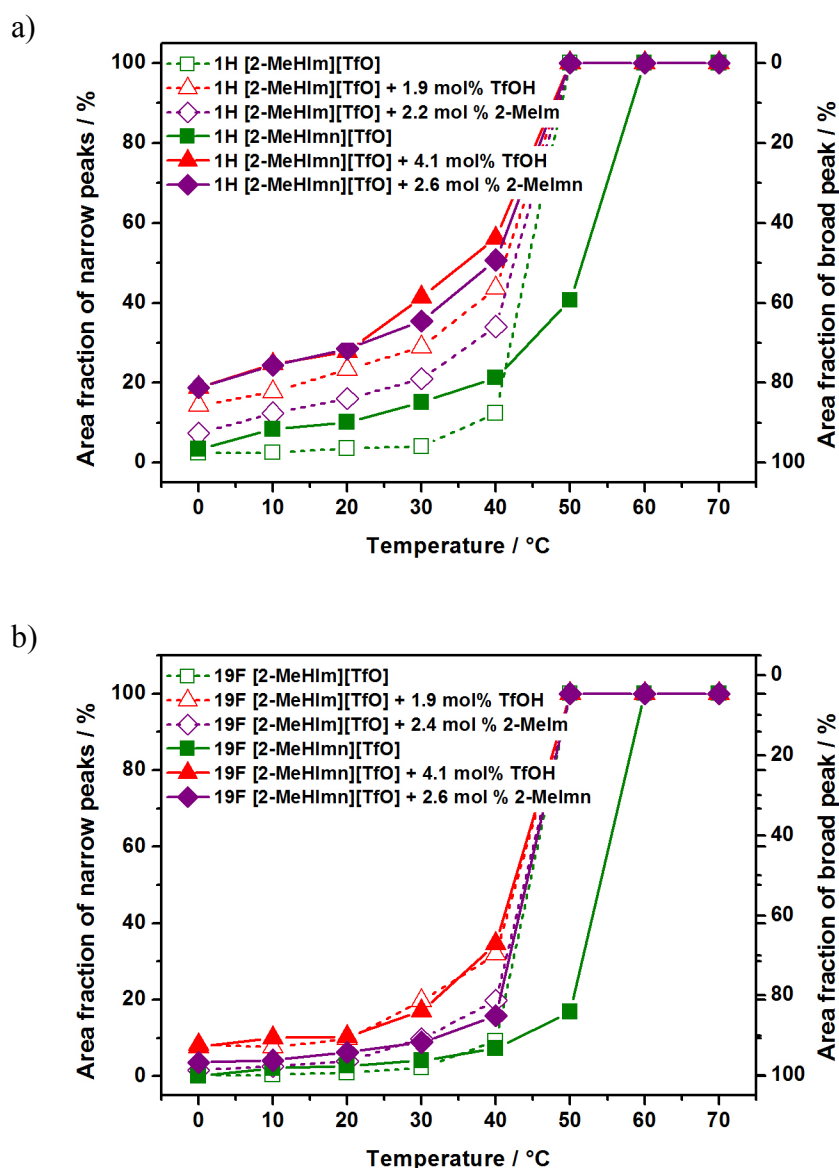


Figure 7. Area fraction of narrow peaks, indicating mobile species in a) ¹H and b) ¹⁹F static NMR spectra. Lines are a guide only.

Figure 7b shows that the anions have a lower mobile fraction than the cations, prior to melting, although it is still quite substantial. Interestingly, the results for the pure and

doped samples are very similar between the two salts. This suggests that the triflate anion behaves in a common way in both structures. In each case the addition of TfOH resulted in a greater proportion of mobile anions than for either the pure or base-doped samples.

The line width at half maximum was calculated for the broad peaks of each static spectrum (Figure 8). The broadness of the solid-state peaks provides an indication of how readily the ions in the matrix can move without diffusing (i.e. rotation of specific groups or tumbling of the whole molecule). The proton peaks were analysed as a single peak, providing an averaged view of the behaviour of the cation in the solid matrix (Figure 8a). The [2-MeHIm][TfO] linewidths were remarkably similar with or without doping, indicating that the dopants do not create additional motion within the solid structure. There is very little change in the linewidths as the temperature is increased, other than a noticeable narrowing of the peaks at 30 °C from 7.1 kHz to 5.1 kHz, corresponding to a relaxation in the cation. This change in motion explains the I-II phase transition observed at the same temperature in the DSC thermograms in Figure 3. Previous studies have also shown a strong correlation between phase transitions and line widths.³⁴ In contrast, the [2-MeHImn][TfO] linewidths display much greater temperature dependence across the whole range, indicative of a steady increase in disorder with increasing temperature. The addition of TfOH dopant resulted in much narrower linewidths than observed for the pure or base-doped [2-MeHImn][TfO].

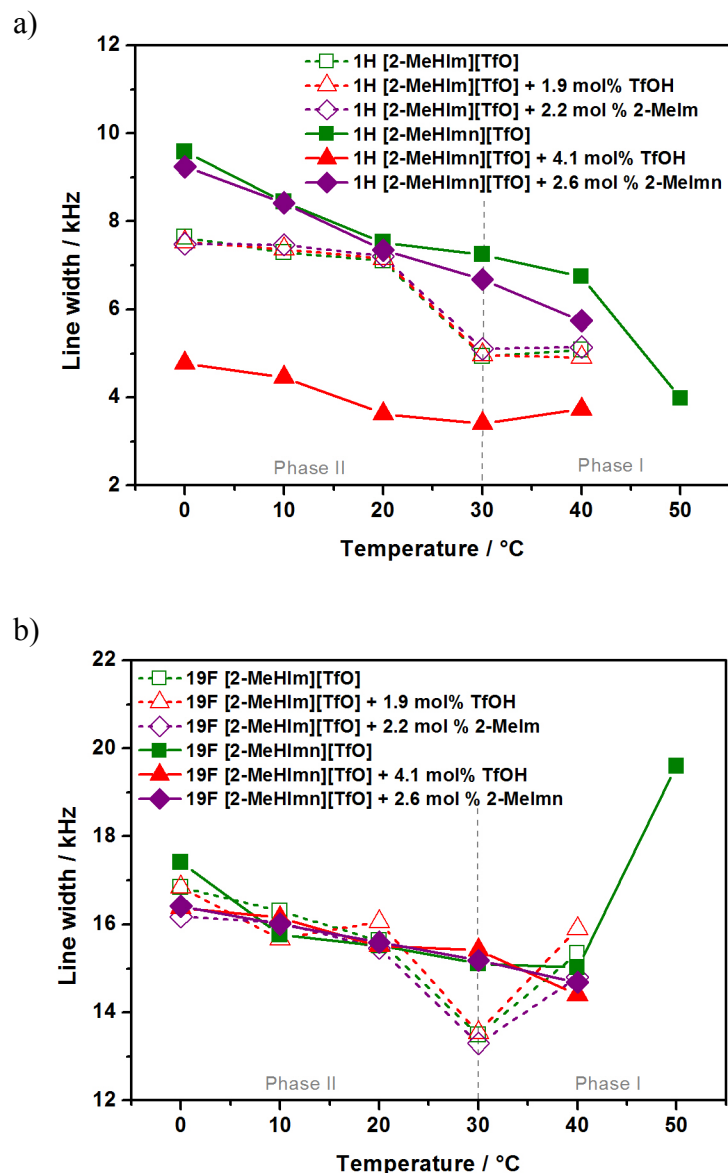


Figure 8. Line widths for broad peaks in a) ^1H and b) ^{19}F static NMR spectra. Lines are a guide only. Grey line indicates phase transition as determined by DSC.

At 0 °C, all of the broad peak linewidths from the ^{19}F spectra were similar (Figure 8b). This suggests that the triflate motions, likely rotation of the CF_3 group, are similar in [2-MeHIm][TfO] and [2-MeHImn][TfO], and that doping the samples does not add any additional motion. However, as observed for the cations, at 30 °C there is a reduction in the linewidths of the [2-MeHIm][TfO] samples from 15.5 kHz to 13.5 kHz. This accompanies the change in the shape of the peaks, notable in Figure 6b, and indicates that the I-II phase transition involves increased dynamics of both the cation and anion. The apparent increase in the [2-MeHIm][TfO] linewidths at 40 °C is due to the method of calculating the width at

half the maximum peak height; at 30 °C the width is measured across the narrowed section of the peak, however, at 40 °C it is measured at the peak shoulder.

While the static solid-state NMR spectra provide some information about the immobile phase, to further investigate the transport properties of the mobile phase, PGSTE diffusion NMR spectroscopy was carried out to calculate the self-diffusion coefficients (D) for ^1H and ^{19}F at selected temperatures. Figure 9a shows a comparison of the cation self-diffusion (D^+), measured based on the integration of the heterocycle ring peaks in the ^1H spectra. In the mobile phase, the addition of either TfOH or 2-MeImn to [2-MeHImn][TfO] resulted in an increase in cation diffusivity. This difference was most obvious at 20 °C, with the diffusion coefficients converging at the melt (60 °C).

Cation diffusion in pure [2-MeHIm][TfO] was observed to be faster than in the doped samples. However, it is possible that this is due to the very small proportion of mobile phase (<4 %) present in the sample at these temperatures. The small peak size makes it difficult to integrate, particularly as the gradient is increased, and can result in overestimation of D . It is unlikely that the addition of dopants slows the ion diffusivity as much as is implied by the data.

Similar trends were observed in the anion self-diffusion (D^-) values, calculated from integration of the ^{19}F peak (Figure 9b). At 20 °C, acid or base-doping [2-MeHImn][TfO] increased the diffusivity of the anion. For [2-MeHIm][TfO], the addition of either acid or base resulted in similar anion diffusivity. This contrasts with Figure 9a, where acid-doping of [2-MeHIm][TfO] gave much higher D^+ values than base-doping.

In both pure compounds the cation and anion diffusion coefficients were closely correlated, while in the doped samples there were differences between D^+ and D^- for each ion (Figure S9). This suggests, along with the reduced melting points, that there is an extensive hydrogen-bonding network in the pure salts that is disrupted by the addition of dopants. The cations diffused faster than the anions in samples where TfOH or 2-MeImn were added as dopants. However, doping [2-MeHIm][TfO] with 2-MeIm had the opposite effect, resulting in the faster motion of the anion. This could be caused by the development of hydrogen bonding networks between the [2-MeHIm] $^+$ cations and base restricting their mobility.

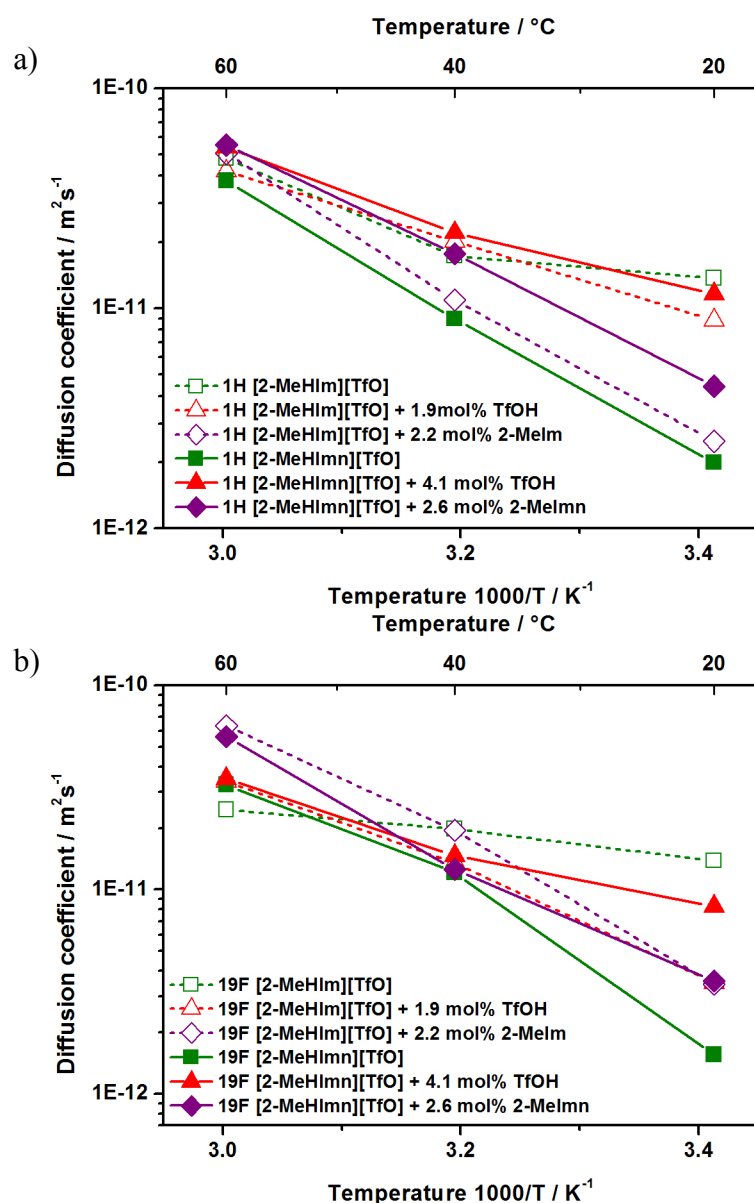


Figure 9. Comparison of [2-MeHIm][TfO] and [2-MeHImn][TfO] a) ^1H cation diffusion coefficients; b) ^{19}F anion diffusion coefficients.

Figure 10 shows the ^1H self-diffusion coefficients for [2-MeHIm][TfO] calculated based on individual integration of the C-H and N-H peaks. At 20°C , the N-H protons exhibited faster diffusion than the C-H protons, however, the values converged towards the melt at 60°C . This behaviour suggests that at lower temperatures the imidazolium cations in the mobile phase may be exhibiting proton-hopping behaviour that contributes to the overall increase in diffusivity of the N-H protons. Such differences between the C-H and N-H diffusivity were not observed for the [2-MeHImn][TfO] samples (Figure S10).

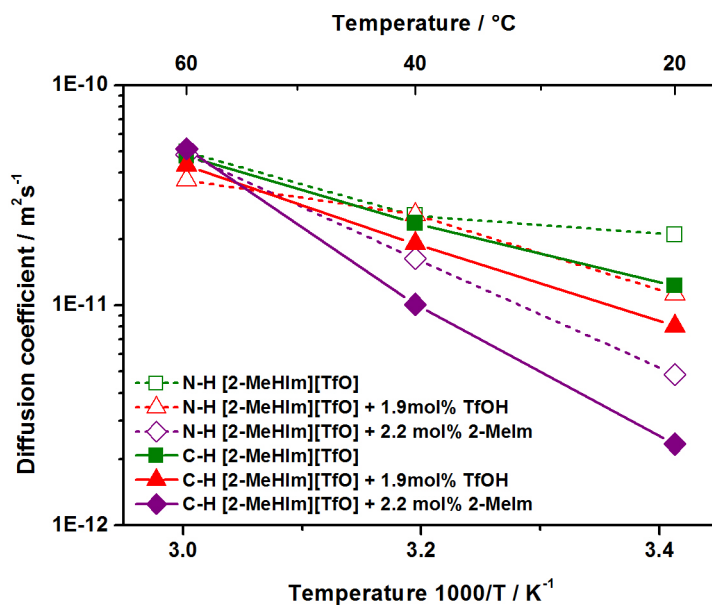


Figure 10. Comparison of diffusion coefficients for the C-H and N-H protons for [2-MeHIm][TfO] with TfOH or 2-MeIm doping. Lines are a guide only.

From the static NMR measurements, it is clear that there is a highly mobile liquid-type phase present. Such a phase has been seen previously at grain boundaries and defects of the crystalline matrix. This is likely the primary reason for the substantial increases in conductivity upon doping. Similar results have been observed for other triflate OIPCs.^{14, 15, 25} The solid-state NMR spectra revealed that the proportion of mobile cations is significant, particularly for [2-MeHImn][TfO], where 4.1 mol % of dopant produces a material with over 25 % mobile cations at room temperature.

The conductivities of the doped and undoped [2-MeHImn][TfO] samples are correlated with the amount of mobile phase. The highly doped samples had very similar mobile cation fractions, much higher than in the pure sample, and this was reflected in their similar conductivities. Although the diffusivity of the cations in the acid-doped mobile phase was higher than in the base-doped sample, the difference was not great enough to be observed in the conductivity measurements. Similarly, [2-MeHIm][TfO] + 1.9 mol% TfOH had a higher fraction of mobile cations than [2-MeHIm][TfO] + 2.2 mol% 2-MeHIm, and greater conductivities.

However, comparing the two different compounds, [2-MeHIm][TfO] showed similarly high conductivities to [2-MeHImn][TfO] when doped, despite the samples having lower fractions of mobile cations with slightly lower D^+ . This could be due to the slightly increased solid phase motions and the influence of proton-hopping in the [2-MeHIm][TfO] systems. Noda et al.³⁷ suggested that [2-MeHIm][TfO] was proton-conducting in their

discussion of the liquid-state conductivity. This outcome, however, is not consistent with the previously observed higher ionicity in the liquid state for [2-MeHImn][TfO] which was suggestive of additional conduction mechanisms.³⁸

In the search for solid-state proton conductors, 2-methylimidazolium triflate appears to be the better candidate, when doped with either excess acid or base. The efficacy of both materials when doped with a base has the potential to broaden the operational range of protic OIPCs to include alkaline conditions, where previously only acids have been investigated for enhancing protic OIPC conductivity. They could be useful as membranes in alkaline fuel cells or electrolysis.

Conclusions

The small change in cation structure between [2-MeHIm][TfO] and [2-MeHImn][TfO] resulted in changes in the physical properties of these salts. Most notably, solid-solid transitions were observed only in [2-MeHIm][TfO], and neat [2-MeHImn][TfO] displayed substantially higher conductivities, although this difference was largely erased upon doping.

The conductivity of the protic salts was effectively increased to greater than 10^{-4} Scm^{-1} close to room temperature through the addition of both the acid and base used to form the component ions. In the case of [2-MeHIm][TfO], TfOH doping had a greater effect, but in [2-MeHImn][TfO] high-level doping with either the acid or base components had a similar effect. Using excess base could be an option for improving protic OIPC conductivities in applications where a highly acidic material is not viable.

Solid-state NMR experiments suggest that the observed increases in conductivity are due to the high proportion of mobile ions, particularly cations, within the solid matrix. The addition of impurities, in the form of acid or base doping, promotes the formation of a highly conductive liquid-like phase. However, in [2-MeHIm][TfO] this is enhanced by additional proton-hopping.

References

1. J. M. Pringle, P. C. Howlett, D. R. MacFarlane and M. Forsyth, *J. Mater. Chem.*, 2010, **20**, 2056-2062.
2. J. Timmermans, *J. Phys. Chem. Solids*, 1961, **18**, 1-8.
3. L. A. K. Staveley, *Annu. Rev. Phys. Chem.*, 1962, **13**, 351-368.
4. J. W. Fergus, *J. Power Sources*, 2010, **195**, 4554-4569.
5. K.-D. Kreuer, S. J. Paddison, E. Spohr and M. Schuster, *Chem. Rev.*, 2004, **104**, 4637-4678.
6. P.-J. Alarco, Y. Abu-Lebdeh, A. Abouimrane and M. Armand, *Nat. Mat.*, 2004, **3**, 476-481.

7. H. Farman, F. M. Coveney and J. C. Dore, *Physica B*, 1992, **180**, 857-860.
8. D. R. MacFarlane, P. Meakin, N. Amini and M. Forsyth, *J. Phys.: Condens. Matter*, 2001, **13**, 8257.
9. V. Armel, M. Forsyth, D. R. MacFarlane and J. M. Pringle, *Energ. Environ. Sci*, 2011, **4**, 2234-2239.
10. V. M. Vishnyakov, *Vacuum*, 2006, **80**, 1053-1065.
11. S. J. Peighambardoust, S. Rowshanzamir and M. Amjadi, *Int. J. Hydrogen Energy*, 2010, **35**, 9349-9384.
12. C. Heitner-Wirguin, *J. Membr. Sci.*, 1996, **120**, 1-33.
13. V. Tricoli, G. Orsini and M. Anselmi, *Phys. Chem. Chem. Phys.*, 2012, **14**, 10979-10986.
14. H. Zhu, U. A. Rana, V. Ranganathan, L. Jin, L. A. O'Dell, D. R. MacFarlane and M. Forsyth, *J. Mater. Chem. A*, 2014, **2**, 681-691.
15. J. Rao, R. Vijayaraghavan, F. Chen, H. Zhu, P. C. Howlett, D. R. MacFarlane and M. Forsyth, *Chem. Commun.*, 2016.
16. E. Raamat, K. Kaupmees, G. Ovsjannikov, A. Trummal, A. Kütt, J. Saame, I. Koppel, I. Kaljurand, L. Lipping, T. Rodima, V. Pihl, I. A. Koppel and I. Leito, *J. Phys. Org. Chem.*, 2013, **26**, 162-170.
17. X. Chen, H. Tang, T. Putzeys, J. Sniekers, M. Wubbenhorst, K. Binnemans, J. Fransaer, D. E. De Vos, Q. Li and J. Luo, *J. Mater. Chem. A*, 2016, **4**, 12241-12252.
18. J. Luo, A. H. Jensen, N. R. Brooks, J. Sniekers, M. Knipper, D. Aili, Q. Li, B. Vanroy, M. Wubbenhorst, F. Yan, L. Van Meervelt, Z. Shao, J. Fang, Z.-H. Luo, D. E. De Vos, K. Binnemans and J. Fransaer, *Energ. Environ. Sci*, 2015, **8**, 1276-1291.
19. J. Luo, O. Conrad and I. F. J. Vankelecom, *J. Mater. Chem. A*, 2013, **1**, 2238-2247.
20. M. Iannuzzi, *J. Chem. Phys.*, 2006, **124**, 204710.
21. J. Thisuwan and K. Sagarik, *RSC Adv.*, 2014, **4**, 61992-62008.
22. A. Mondal and S. Balasubramanian, *J. Phys. Chem. C*, 2016, **120**, 22903-22909.
23. S. Long, P. C. Howlett, D. R. MacFarlane and M. Forsyth, *Solid State Ionics*, 2006, **177**, 647-652.
24. U. A. Rana, R. Vijayaraghavan, D. R. MacFarlane and M. Forsyth, *Chem. Commun.*, 2011, **47**, 6401-6403.
25. H. Zhu, D. MacFarlane and M. Forsyth, *J. Phys. Chem. C*, 2014, **118**, 28520-28526.
26. M. Paidar, V. Fateev and K. Bouzek, *Electrochim. Acta*, 2016, **209**, 737-756.
27. Y. Leng, G. Chen, A. J. Mendoza, T. B. Tighe, M. A. Hickner and C.-Y. Wang, *J. Am. Chem. Soc.*, 2012, **134**, 9054-9057.
28. G. Merle, M. Wessling and K. Nijmeijer, *J. Membr. Sci.*, 2011, **377**, 1-35.
29. H. Erdemi, Ü. Akbey and W. H. Meyer, *Solid State Ionics*, 2010, **181**, 1586-1595.
30. L. Zhao, I. Smolarkiewicz, H. H. Limbach, H. Breitzke, K. Pogorzelec-Glaser, R. Pankiewicz, J. Tritt-Goc, T. Gutmann and G. Buntkowsky, *J. Phys. Chem. C*, 2016, **120**, 19574-19585.
31. R. M. Cotts, M. J. R. Hoch, T. Sun and J. T. Markert, *J. Magn. Reson.*, 1989, **83**, 252-266.
32. T. L. Greaves and C. J. Drummond, *Chem. Rev.*, 2008, **108**, 206-237.
33. IUPAC, *Compendium of Chemical Terminology*, 2nd edn., Oxford, 1997.
34. L. Jin, K. M. Nairn, C. M. Forsyth, A. J. Seeber, D. R. MacFarlane, P. C. Howlett, M. Forsyth and J. M. Pringle, *J. Am. Chem. Soc.*, 2012, **134**, 9688-9697.
35. D. C. Apperley, R. K. Harris and P. Hodgkinson, *Solid-State NMR: Basic Principles & Practice*, Momentum Press, New York, 2012.
36. D. Massiot, F. Fayon, M. Capron, I. King, S. Le Calvé, B. Alonso, J.-O. Durand, B. Bujoli, Z. Gan and G. Hoatson, *Magn. Reson. Chem.*, 2002, **40**, 70-76.
37. A. Noda, M. A. B. H. Susan, K. Kudo, S. Mitsushima, K. Hayamizu and M. Watanabe, *J. Phys. Chem. B*, 2003, **107**, 4024-4033.
38. A. L. Chong, M. Forsyth and D. R. MacFarlane, *Electrochim. Acta*, 2015, **159**, 219-226.

5.2 Supplementary Information

Synthesis

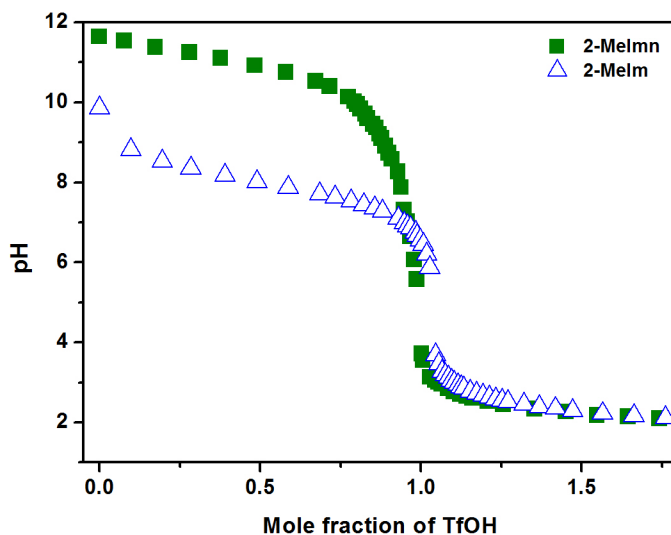


Figure S1. Titrations of 2-MeImn and 2-MeIm with 0.1 M TfOH.

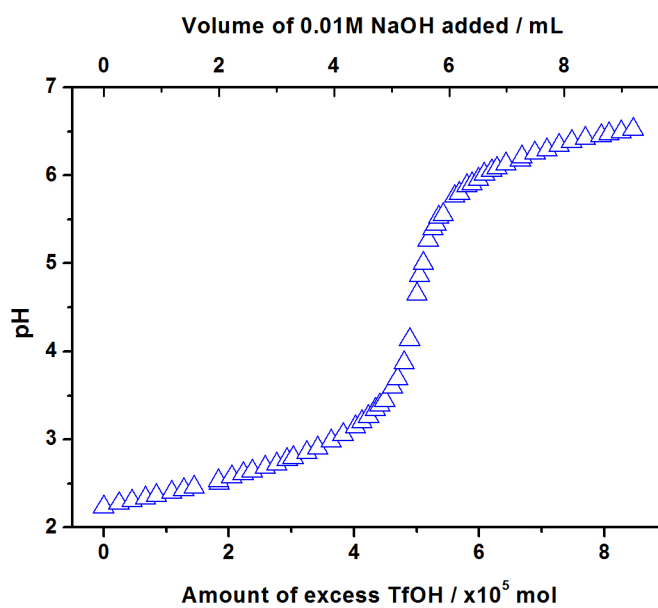


Figure S2. Titration of [2-MeHImn][TfO] + 4.1 mol% TfOH with 0.009 M NaOH.

Table S1. Dopant level determined by titration with HCl or NaOH standard solutions.

Sample	Amount added / mol%	Amount measured / mol%
[2-MeHIm][TfO] + 0.4 mol% TfOH	1	0.4 ± 0.1
[2-MeHIm][TfO] + 1.4 mol% TfOH	2.5	1.4 ± 0.1
[2-MeHIm][TfO] + 1.9 mol% TfOH	5	1.9 ± 0.2
[2-MeHIm][TfO] + 1.1 mol% 2MeIm	1	1.1 ± 0.2
[2-MeHIm][TfO] + 2.0 mol% 2MeIm	2.5	2.0 ± 0.1
[2-MeHIm][TfO] + 2.2 mol% 2MeIm	5	2.2 ± 0.2
[2-MeHImn][TfO] + 0.7 mol% TfOH	1	0.7 ± 0.1
[2-MeHImn][TfO] + 1.5 mol% TfOH	2.5	1.5 ± 0.1
[2-MeHImn][TfO] + 4.2 mol% TfOH	5	4.1 ± 0.3
[2-MeHImn][TfO] + 0.8 mol% 2MeImn	1	0.8 ± 0.1
[2-MeHImn][TfO] + 1.8 mol% 2MeImn	2.5	1.8 ± 0.3
[2-MeHImn][TfO] + 2.6 mol% 2MeImn	5	2.6 ± 0.1

The differences in doping amounts, as determined by titration, reflect the difficulty in accurately doping materials with small amounts of volatile components. The loss of acid dopant during sample preparation has been previously observed¹ and it is important to determine the actual levels, rather than rely on the nominal doping value. The substantial loss of dopant when 5 mol% was added suggests that high doping concentrations may not be stable. Despite the losses, however, increasing amounts of dopant were retained, such that a trend is maintained across each doping system. Due to the differences in dopant levels, direct comparison of samples (i.e. [2-MeHImn][TfO] + 5 mol % TfOH vs. [2-MeHImn][TfO] + 5 mol% 2-MeImn) has been largely avoided, with discussion focused on the general trends.

Static Solid-state NMR Spectra

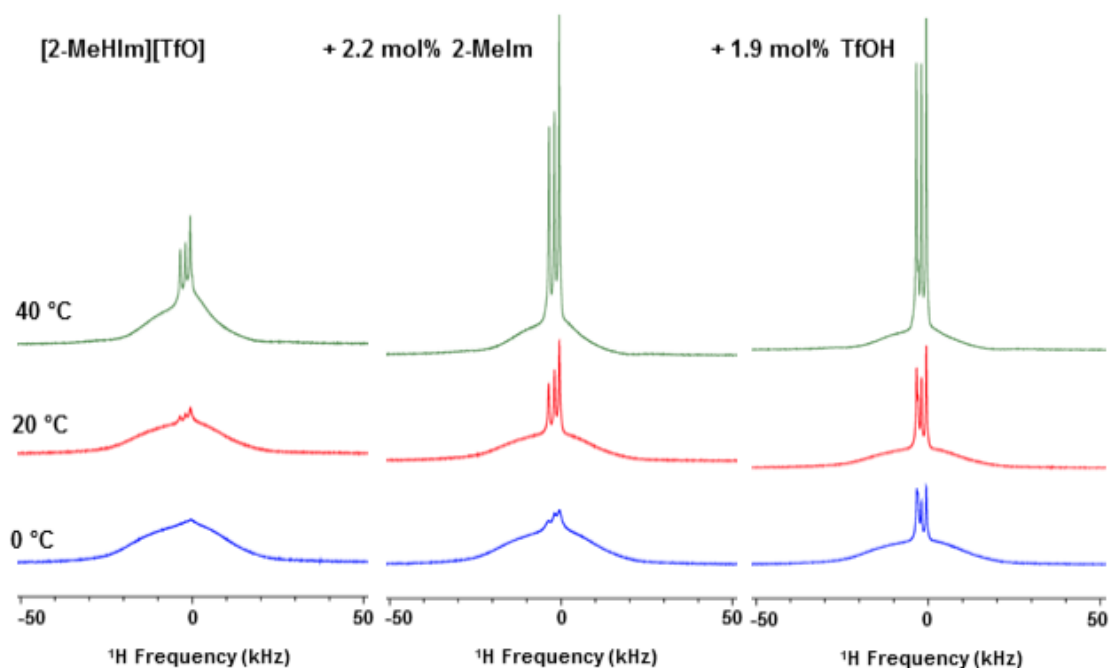


Figure S3. Static solid-state ^1H NMR spectra of [2-MeHIm][TfO] with doping at selected temperatures.

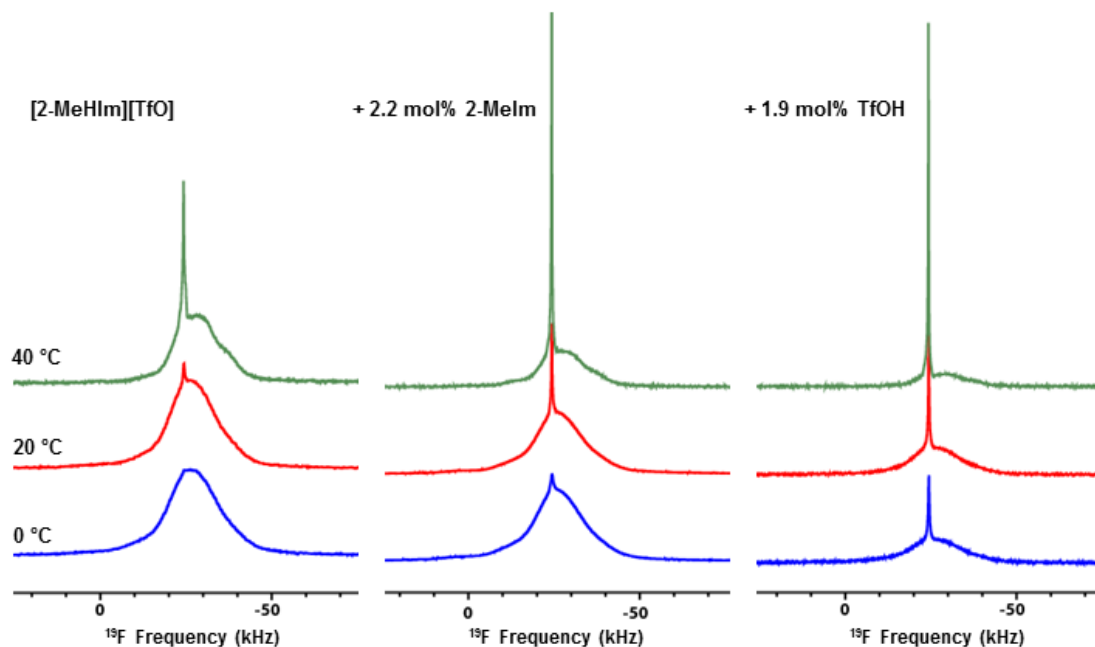


Figure S4. Static solid-state ^{19}F NMR spectra of [2-MeHIm][TfO] with doping at selected temperatures.

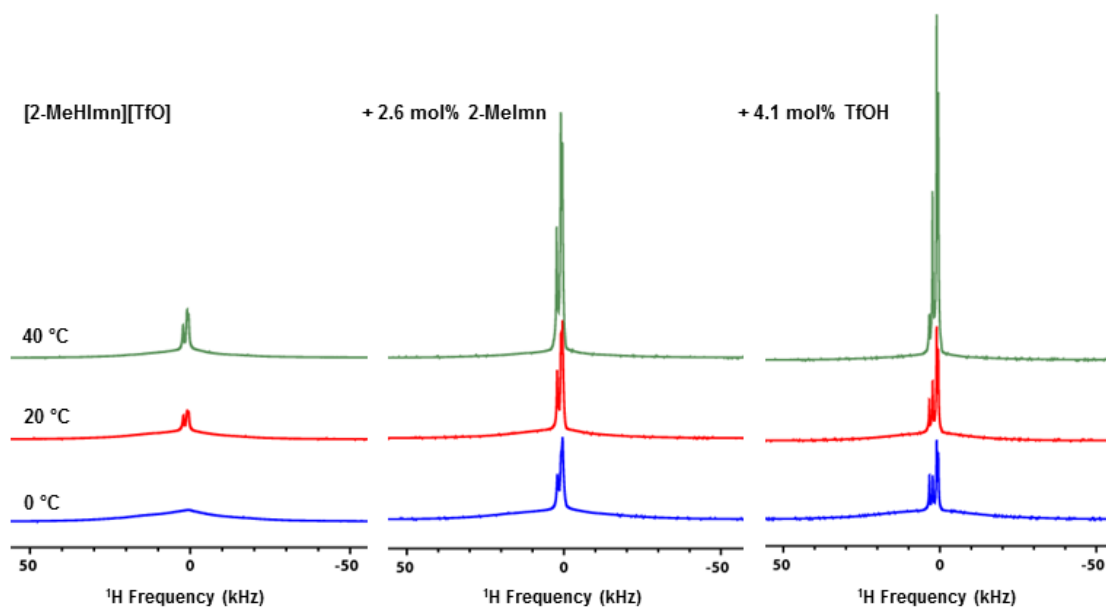


Figure S5. Static solid-state ^1H NMR spectra of [2-MeHImn][TfO] with doping at selected temperatures.

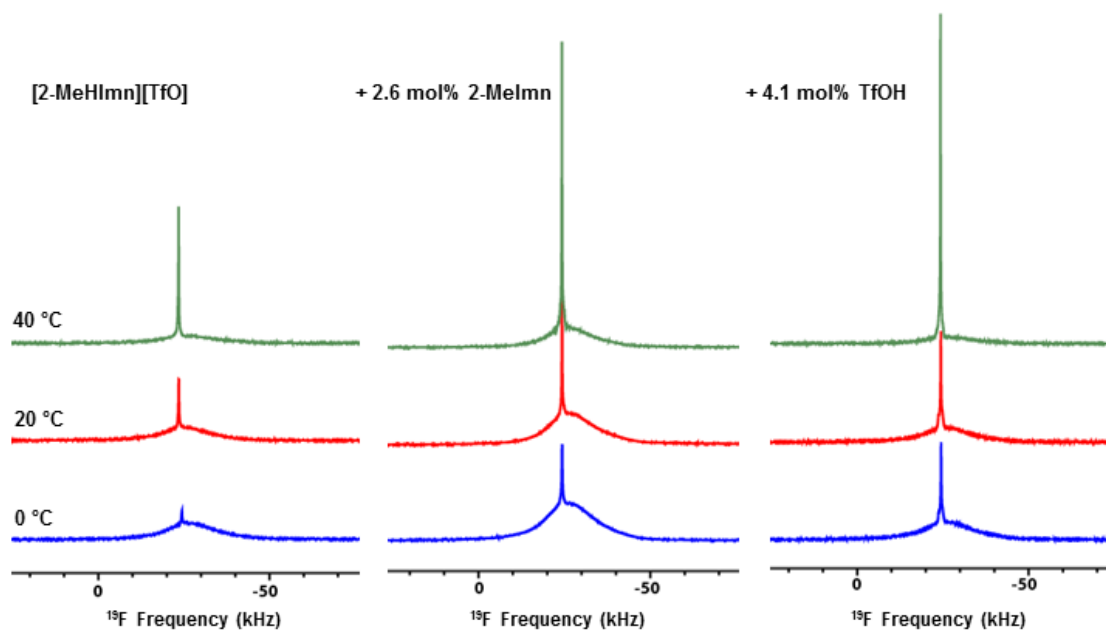


Figure S6. Static solid-state ^{19}F NMR spectra of [2-MeHImn][TfO] with doping at selected temperatures.

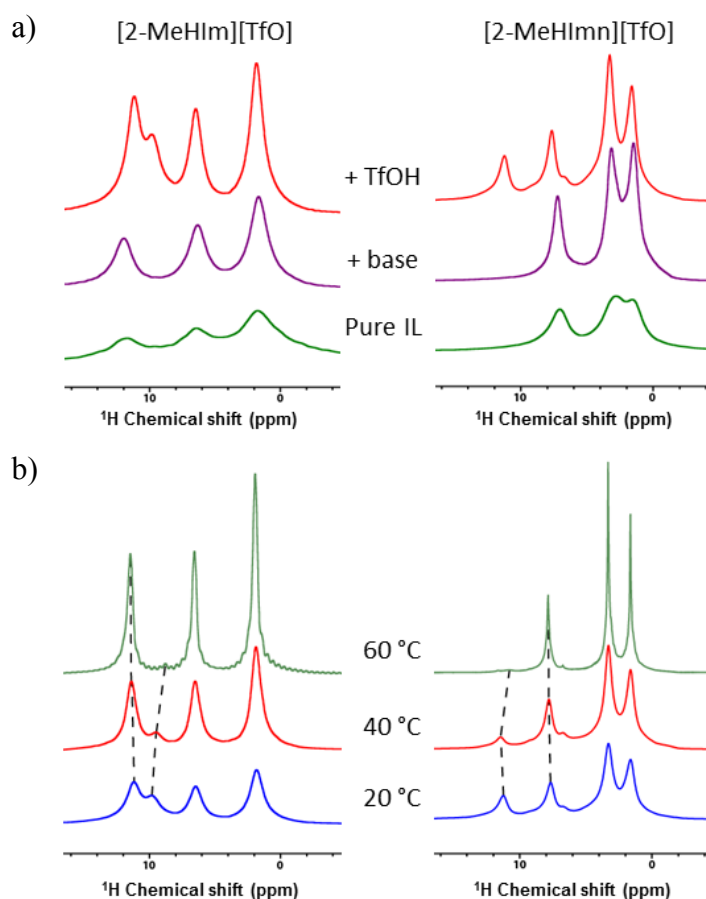


Figure S7. Comparison of the narrow ^1H peaks for a) [2-MeHIm][TfO] and [2-MeHImn][TfO] with doping at 273 K; b) TfOH doped samples showing shift in N-H and TfOH peaks with increasing temperature.

An additional narrow peak was observed in the ^1H spectra for both of the TfOH doped samples. This has been attributed to the hydroxyl protons from the doped TfOH. As the temperature is increased, the magnitude of this peak decreases, as exchange with the more dominant N-H peak increases.

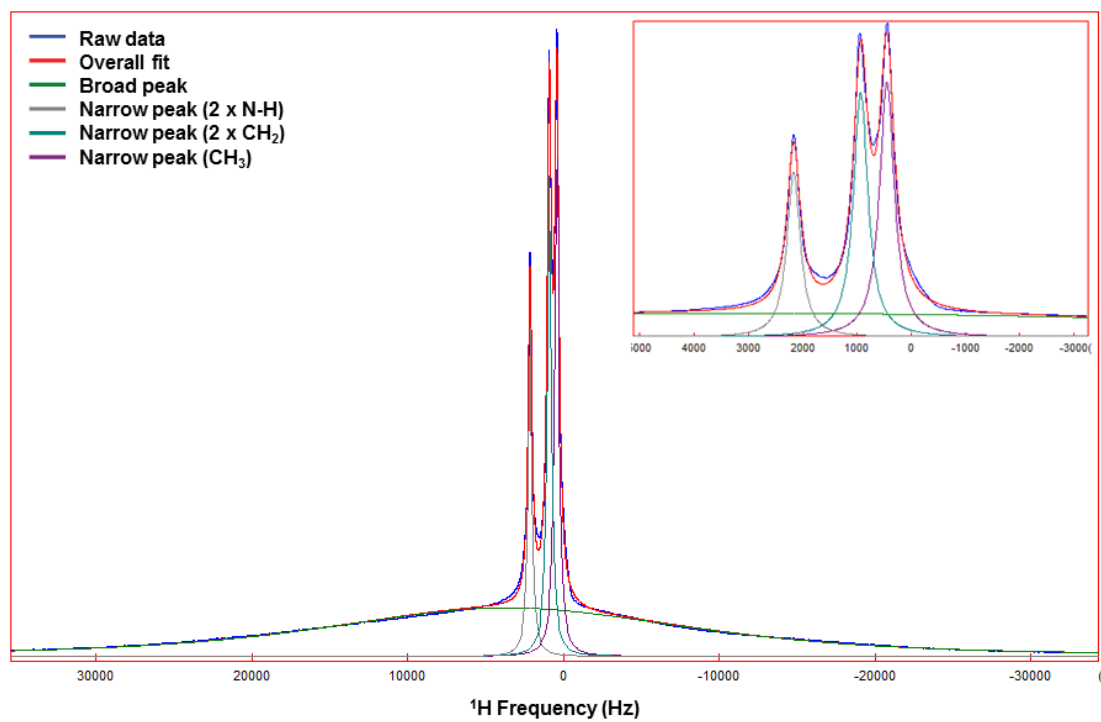


Figure S8. Line fitting for [2-MeHImn][TfO] + 2.6 mol% 2-MeImn at 20 °C using dmfit software.²

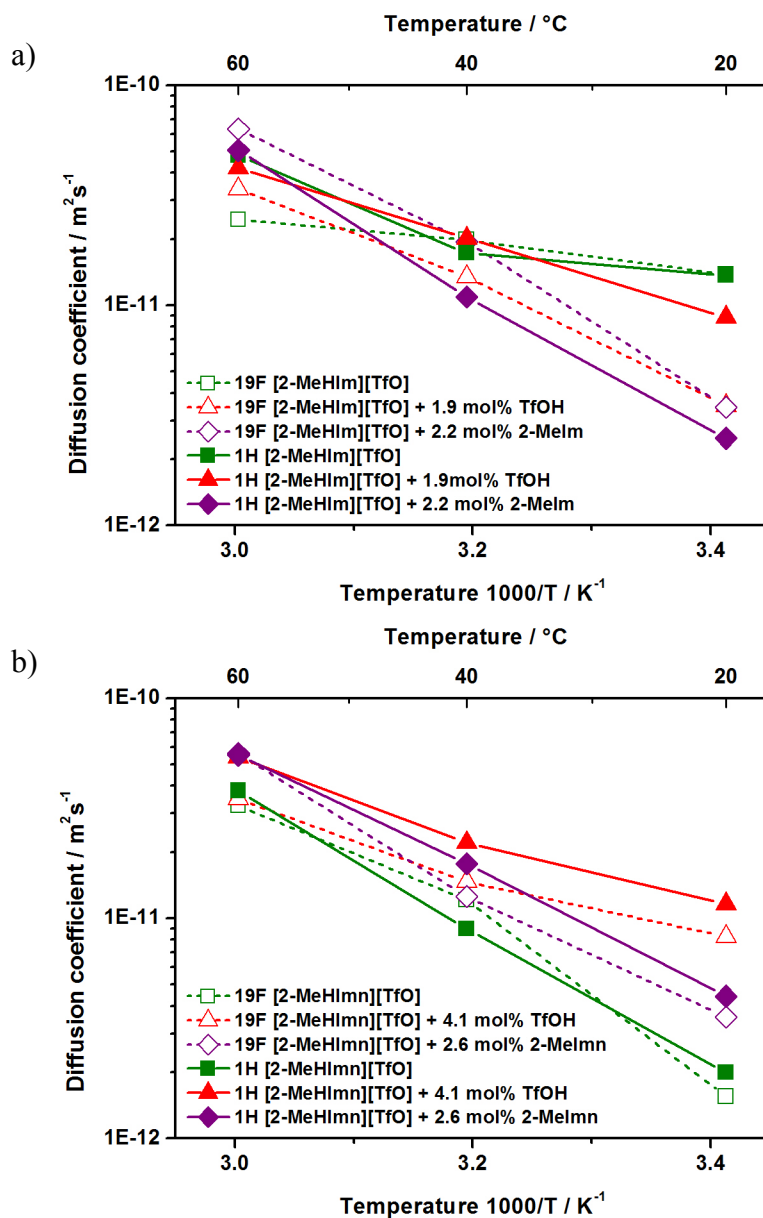


Figure S9. Comparison of cation and anion diffusion coefficients for a) [2-MeHIm][TfO] and b) [2-MeHImn][TfO] with TfOH and base doping. Lines are a guide only.

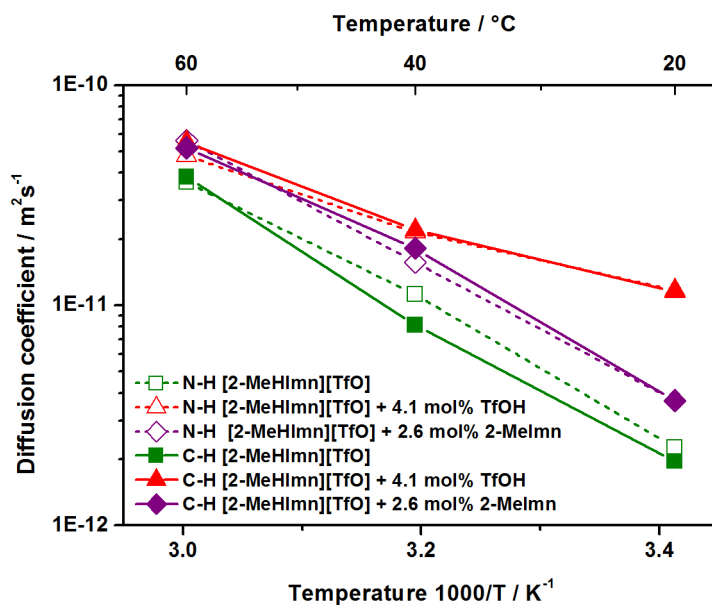


Figure S10. Comparison of diffusion coefficients for C-H and N-H protons in $[2\text{-MeHImn}]^+$. The similarity in values suggests the protons in both environments diffuse together as part of the whole cation.

1. K. Kudo, S. Mitsushima, N. Kamiya and K.-i. Ota, *Electrochemistry*, 2005, **73**, 668-674.
2. D. Massiot, F. Fayon, M. Capron, I. King, S. Le Calvé, B. Alonso, J.-O. Durand, B. Bujoli, Z. Gan and G. Hoatson, *Magn. Reson. Chem.*, 2002, **40**, 70-76.

6 CONCLUSIONS AND FUTURE WORK

6.1 Conclusions

This thesis has explored the synthesis of a number of novel organic imidazolium salts. They have been shown to behave in unique ways compared to their imidazolium counterparts, and showed promise for use in applications as corrosion inhibitors and solid electrolytes.

In Chapter 2, a series of protic 2-methylimidazolium salts were synthesised. These were found to mostly have melting points close to, or less than, 100 °C. [2-MeHImn][TfO] and [2-MeHImn][Sal] were liquid over a sufficient temperature range for the measurement of liquid-state physical properties. In comparison to the analogous imidazolium cation, [2-MeHImn]⁺ was found to make less fragile ILs, likely due to the less charge-diffuse nature of the non-aromatic ring. Although [2-MeHImn][TfO] was more viscous and less conductive than [2-MeHIm][TfO], the imidazolium IL showed high ionicity – reflective of the conductivity being higher than expected based on ion conduction alone. This suggested the contribution of additional conduction mechanisms such as proton-hopping.

A comparison of the aromatic carboxylate salts in the same chapter showed that all compounds acted as anodic inhibitors to minimise corrosion on mild steel under aqueous chloride conditions. [2-MeHImn][4-OHCin] had a particularly strong inhibiting effect. As a combined salt, this inhibitor performed better than salts of the component ions, [Na][4-OHCin] and [2-MeHImn][Br], in both electrochemical and longer-term immersion testing.

Further study of the corrosion inhibition of [2-MeHImn][4-OHCin] was presented in Chapter 3. This salt was found to benefit from a synergistic effect that resulted in high levels of inhibition under both mildly basic (pH 8) and acidic (pH 2) conditions. At pH 8, inhibition of the combined salt was similar to [Na][4-OHCin], suggesting that adsorption of the cinnamate was the key mechanism. However, under acidic conditions, both

component ions provided very little protection for the steel and only the combined salt was an effective inhibitor. The level of protection was such that after immersion in the pH 2 solution with [2-MeHImn][4-OHCin] for 24 hours, no significant pitting was observed on the steel. IR spectroscopy was able to identify bands corresponding to an Fe – [4-OHCin]⁻ complex on the surface of the immersed coupons, but evidence of the cation was inconclusive.

In addition to outperforming the component salts individually, [2-MeHImn][4-OHCin] was found to be more effective than a mixture of the component salts. The combined inhibitor was also substantially more effective than the analogous [2-MeHIm][4-OHCin]. A number of modified imidazolium salts were synthesised and the aprotic [triMeImn][4-OHCin] salt showed similar levels of inhibition as [2-MeHImn][4-OHCin]. It was apparent that the synergistic effect was specific to the combination of imidazolium and cinnamate. A possible explanation for this effect is reactivity of the α,β -unsaturated carbonyl in the presence of the imidazolium. This could lead to precipitation of oligomeric species as a protective surface film.

Chapter 4 confirmed the importance of the combination of anion and cation in generating a synergistic effect. A new series of protic salts was synthesised using two uronic acid anions: glucuronate, [Glu]⁻, and galacturonate, [Gal]⁻. It was found that pairing these anions with [2-MeHImn]⁺ resulted in modest levels of inhibition relative to [Na][Glu]. The inhibition efficiencies were similar to those of the imidazolium carboxylates investigated in Chapter 2, however, the new compounds did not match the inhibition levels of [2-MeHImn][4-OHCin]. Immersion testing of the inhibitors revealed that this combination of ions may in fact have an antagonistic relationship, as imidazolines can concentrate the number of pits that are formed, while sugar acids can solubilise Fe²⁺, accelerating pit growth. This led to the formation of substantial pits in some areas, while other parts of the coupon were protected. These ions could be effective inhibitors, but not as a combined salt.

The final chapter of this thesis examined the conductivity of the triflate ILs that were introduced in Chapter 2. These compounds showed good conductivity as solids at room temperature. The conductivity could be enhanced by up to two orders of magnitude through the addition of dopant quantities of the anion source (TfOH) or cation source (2-MeImn or 2-MeIm). This was the first example of base-doping in solid protic salts. It was found that the addition of base was as effective as using an acid dopant. Solid-state NMR studies determined that the primary mode of conduction in these samples was ion

transport through liquid-like regions within the solid. The proportion of mobile ions increased with the addition of the dopants, particularly for [2-MeHImn][TfO], where over a quarter of the cations within the solid were highly mobile at room temperature. Measurement of the diffusion coefficients of the mobile fraction suggested that there may be some additional proton conduction in [2-MeHIm][TfO]. Although both doped systems showed high levels of conductivity, for proton-conducting applications, [2-MeHIm][TfO] would be the preferred salt.

6.2 Future Work

There are a number of ways in which this work could be progressed to more fully understand the nature of the studied imidazolium salts, as well as to optimise their use as corrosion inhibitors and solid electrolytes.

Further mechanistic studies are required to fully understand the nature of the reactivity between the imidazolium and cinnamate species. This could include characterisation of the electrolyte precipitate with techniques such as NMR spectroscopy, as well as *in situ* IR spectroscopy studies to monitor any changes in solution, or at the steel surface, over time. Further electrochemical probing of the reduction process could also be informative. By increasing the scope of the project to include corrosion testing of the additional synthesised cations, as well as cations featuring longer alkyl chains, it would be possible to determine the level of alkylation required for the imidazoline to inhibit in its own right, and ascertain whether this additional bulk still permits reactivity with the cinnamate. Similarly, one could explore the effects of substitutions to the cinnamate anion on the synergistic relationship.

It was found that the inhibition of these salts was anodic in nature, but, as seen with the uronic acid salts, this can lead to substantial localised corrosion if the surface protection is insufficient and cathodic reactions can proceed unchecked. This could be addressed through the use of complementary inhibitors. Work is being carried out in our group to investigate the effects of partnering [2-MeHImn][4-OHCin] with rare-earth cinnamate salts such as $\text{La}(4\text{-OHCin})_3$. As a cathodic precipitator, La^{3+} could minimise the cathodic rate of reaction, resulting in mixed inhibition.

More broadly, this work has shown the promise of task-specific salts and ILs for use as corrosion inhibitors. There is great scope to explore the use of other corrosion inhibiting ions, such as benzimidazolium, or even to incorporate antimicrobial ions for combined anti-corrosion – biocidal action. However, for these compounds to be put forward as

'green' replacements for current corrosion inhibitors it is important to support the exploration of novel salt formations with environmental assessment such as toxicity and biodegradability testing.

The comparative study of [2-MeHImn][TfO] and [2-MeHIm][TfO] provided an interesting insight into the differences introduced by removing the aromaticity from the imidazolium ring. If single crystals can be obtained, single crystal x-ray diffraction could provide information about the non-planar chemical structure that is adopted due to the C4-C5 saturation in the imidazolinium ring. The crystal structure data could also be used to calculate theoretical linewidths based on molecular motions that could be compared to the measured solid-state linewidths. This could help to clarify the specific motions related to the phases of [2-MeHIm][TfO] that were not observed in [2-MeHImn][TfO].

More practically, while [2-MeHImn][TfO] and [2-MeHIm][TfO] showed good conductivity, they are yet to be trialled within a complete battery or fuel cell system. This could provide a better indication of their viability as electrolytes. These materials could be considered for PEMFCs, as well as alkaline fuel cells in the case of the base-doped samples. Some factors that would have to be taken into consideration when using these materials are their hygroscopic nature and control of the dopant level. Another concern that has been observed in other OIPCs is that these materials may be too mechanically soft to use as pure solid-state electrolytes. One way that this can be improved is by incorporating the OIPCs into polymer membranes.

BIBLIOGRAPHY

- T. J. Abraham, D. R. MacFarlane and J. M. Pringle, *Energ. Environ. Sci.*, 2013, **6**, 2639-2645.
- Y. Abu-Lebdeh, A. Abouimrane, P.-J. Alarco and M. Armand, *J. Power Sources*, 2006, **154**, 255-261.
- S. Acharya and S. Upadhyay, *T. Indian. I. Metals*, 2004, **57**, 297-306.
- A. Acidi, M. Hasib-ur-Rahman, F. Larachi and A. Abbaci, *Korean J. Chem. Eng.*, 2014, **31**, 1043-1048.
- T. E. Acree, R. S. Shallenberger and L. R. Mattick, *Carbohydr. Res.*, 1968, **6**, 498-502.
- J. Adebahr, M. Grimsley, N. M. Rocher, D. R. MacFarlane and M. Forsyth, *Solid State Ionics*, 2008, **178**, 1798-1803.
- J. Adebahr, A. J. Seeber, D. R. MacFarlane and M. Forsyth, *J. Phys. Chem. B*, 2005, **109**, 20087-20092.
- Z. Ahmad, in *Principles of Corrosion Engineering and Corrosion Control*, Butterworth-Heinemann, Oxford, 2006, pp. 9-56.
- I. Aiad, A. A. Hafiz, M. Y. El-Awady and A. O. Habib, *J. Surfactants Deterg.*, 2010, **13**, 247-254.
- M. S. Al-Otaibi, A. M. Al-Mayouf, M. Khan, A. A. Mousa, S. A. Al-Mazroa and H. Z. Alkhatlan, *Arab. J. Chem.*, 2014, **7**, 340-346.
- P.-J. Alarco, Y. Abu-Lebdeh, A. Abouimrane and M. Armand, *Nat. Mat.*, 2004, **3**, 476-481.
- R. W. Alder, M. E. Blake, S. Bufali, C. P. Butts, A. G. Orpen, J. Schutz and S. J. Williams, *J. Chem. Soc., Perkin Trans. 1*, 2001, 1586-1593.
- A. Alexakis, C. L. Winn, F. Guillen, J. Pytkowicz, S. Roland and P. Mangeney, *Adv. Synth. Catal.*, 2003, **345**, 345-348.
- E. H. B. Anari, M. Romano, W. Teh, J. Black, E. Jiang, J. Chen, T. To, J. Panchompoo and L. Aldous, *Chem. Commun.*, 2016, **52**, 745-748.
- C. A. Angell, *Chem. Rev.*, 2002, **102**, 2627-2650.
- G. Annat, J. Adebahr, I. R. McKinnon, D. R. MacFarlane and M. Forsyth, *Solid State Ionics*, 2007, **178**, 1065-1071.
- D. C. Apperley, R. K. Harris and P. Hodgkinson, *Solid-State NMR: Basic Principles & Practice*, Momentum Press, New York, 2012.
- A. J. Arduengo III, R. Krafczyk, R. Schmutzler, H. A. Craig, J. R. Goerlich, W. J. Marshall and M. Unverzagt, *Tetrahedron*, 1999, **55**, 14523-14534.
- M. Armand, F. Endres, D. R. MacFarlane, H. Ohno and B. Scrosati, *Nat. Mat.*, 2009, **8**, 621-629.
- V. Armel, M. Forsyth, D. R. MacFarlane and J. M. Pringle, *Energ. Environ. Sci.*, 2011, **4**, 2234-2239.
- ASTM International, ASTM G1-03(2011), West Conshohocken, PA, 2011.
- A. Atta, G. El-Mahdy, H. Al-Lohedan and A. Ezzat, *Molecules*, 2015, **20**, 11131.
- M. A. Azaroual, E. F. El Harrak, R. Touir, A. Rochdi and M. E. Touhami, *J. Mol. Liq.*, 2016, **220**, 549-557.
- Y. Bai, J. Zhang, Y. Wang, M. Zhang and P. Wang, *Langmuir*, 2011, **27**, 4749-4755.
- D. Bajpai and V. K. Tyagi, *J. Oleo Sci.*, 2006, **55**, 319-329.
- A. Basile, A. I. Bhatt and A. P. O'Mullane, *Nat. Commun.*, 2016, **7**, ncomms11794.
- D. M. Bastidas, E. Cano and E. M. Mora, *Anti Corros. Method. M.*, 2005, **52**, 71-77.
- J. M. Bastidas and E. M. Mora, *Can. Metall. Q.*, 1998, **37**, 57-65.
- J. M. Bastidas, E. M. Mora and S. Feliu, *Mater. Corros.*, 1990, **41**, 343-347.
- F. Beck, *Angew. Chem. Int. Ed.*, 1972, **11**, 760-781.
- T. Behrsing, G. B. Deacon and P. C. Junk, in *Rare Earth-Based Corrosion Inhibitors*, Woodhead Publishing, Cambridge, 2014, pp. 1-37.
- A. S. Ben, *Int. J. Electrochem. Sci.*, 2013, **8**, 10788-10804.
- A. I. Bhatt, I. May, V. A. Volkovich, M. E. Hetherington, B. Lewin, R. C. Thied and N. Ertok, *J. Chem. Soc., Dalton Trans.*, 2002, 4532-4534.
- K. Binnemans, *Chem. Rev.*, 2005, **105**, 4148-4204.
- J. J. Black, T. Murphy, R. Atkin, A. Dolan and L. Aldous, *Phys. Chem. Chem. Phys.*, 2016, **18**, 20768-20777.

- F. Blin, S. G. Leary, G. B. Deacon, P. C. Junk and M. Forsyth, *Corros. Sci.*, 2006, **48**, 404-419.
- F. Blin, S. G. Leary, K. Wilson, G. B. Deacon, P. C. Junk and M. Forsyth, *J. Appl. Electrochem.*, 2004, **34**, 591-599.
- M. Bouklah, B. Hammouti, A. Aouniti, M. Benkaddour and A. Bouyanzer, *Appl. Surf. Sci.*, 2006, **252**, 6236-6242.
- A. Brandt, J. Grasvik, J. P. Hallett and T. Welton, *Green Chem.*, 2013, **15**, 550-583.
- A. Brandt, J. Pires, M. Anouti and A. Balducci, *Electrochim. Acta*, 2013, **108**, 226-231.
- X. Chen, H. Tang, T. Putzeys, J. Sniekers, M. Wubbenhorst, K. Binnemans, J. Fransaer, D. E. De Vos, Q. Li and J. Luo, *J. Mater. Chem. A*, 2016, **4**, 12241-12252.
- Y. F. Cheng and J. L. Luo, *J. Electrochem. Soc.*, 1999, **146**, 970-976.
- A. L. Chong, M. Forsyth and D. R. MacFarlane, *Electrochim. Acta*, 2015, **159**, 219-226.
- A. L. Chong, J. I. Mardel, D. R. MacFarlane, M. Forsyth and A. E. Somers, *ACS Sustainable Chem. Eng.*, 2016, **4**, 1746-1755.
- E. I. Cooper and C. A. Angell, *Solid State Ionics*, 1986, **18**, 570-576.
- A. Cornia, F. Felluga, V. Frenna, F. Ghelfi, A. F. Parsons, M. Pattarozzi, F. Roncaglia and D. Spinelli, *Tetrahedron*, 2012, **68**, 5863-5881.
- R. M. Cotts, M. J. R. Hoch, T. Sun and J. T. Markert, *J. Magn. Reson.*, 1989, **83**, 252-266.
- S. Cukierman, *Biochim. Biophys. Acta Bioenergetics*, 2006, **1757**, 876-885.
- D. M. D'Alessandro, B. Smit and J. R. Long, *Angew. Chem. Int. Ed.*, 2010, **49**, 6058-6082.
- H. Danneel, *Z. Elektrochem. Angew. P.*, 1905, **11**, 249-252.
- C. G. Dariva and A. F. Galio, in *Developments in Corrosion Protection*, ed. M. Aliofkhaezrai, InTech, 2014.
- J. de Damborenea, A. Conde and M. A. Arenas, in *Rare Earth-Based Corrosion Inhibitors*, Woodhead Publishing, Cambridge, 2014, pp. 84-116.
- G. B. Deacon, P. C. Junk, M. Forsyth and W. W. Lee, *Chem. Aust.*, 2008, **75**, 18-21.
- J.-D. Decoppet, S. B. Khan, M. S. A. Al-Ghamdi, B. G. Alhogbi, A. M. Asiri, S. M. Zakeeruddin and M. Grätzel, *Energy Technol.*, 2017, **5**, 321-326.
- M. Deetlefs, K. R. Seddon and M. Shara, *Phys. Chem. Chem. Phys.*, 2006, **8**, 642-649.
- J. Ding and D. W. Armstrong, *Chirality*, 2005, **17**, 281-292.
- T. Du, J. Chen and D. Cao, *Br. Corros. J.*, 2000, **35**, 229-231.
- G. J. Dutton, in *Glucuronic Acid Free and Combined*, Academic Press, 1966, pp. 185-299.
- E. E. Ebenso, I. B. Obot and L. Murulana, *Int. J. Electrochem. Sci.*, 2010, **5**, 1574-1586.
- N. O. Eddy and S. A. Odoemelam, *Advances in Natural and Applied Sciences*, 2008, **2**, 225-233.
- N. O. Eddy, S. A. Odoemelam and P. Ekwumemgbo, *Sci. Res. Essays*, 2009, **4**, 033-038.
- A. Edwards, C. Osborne, S. Webster, D. Klenerman, M. Joseph, P. Ostovar and M. Doyle, *Corros. Sci.*, 1994, **36**, 315-325.
- J. Efthimiadis, W. C. Neil, A. Bunter, P. C. Howlett, B. R. Hinton, D. R. MacFarlane and M. Forsyth, *ACS Appl. Mater. Interfaces*, 2010, **2**, 1317-1323.
- M. Egashira, M. Tanaka-Nakagawa, I. Watanabe, S. Okada and J.-i. Yamaki, *J. Power Sources*, 2006, **160**, 1387-1390.
- A. M. El-Shamy, K. Zakaria, M. A. Abbas and S. Zein El Abedin, *J. Mol. Liq.*, 2015, **211**, 363-369.
- M. S. Elsaesser, I. Kohl, E. Mayer and T. Loerting, *J. Phys. Chem. B*, 2007, **111**, 8038-8044.
- F. Endres, D. MacFarlane and A. Abbott, *Electrodeposition from Ionic liquids*, Wiley-VCH, Weinheim, 2008.
- H. Erdemi, Ü. Akbey and W. H. Meyer, *Solid State Ionics*, 2010, **181**, 1586-1595.
- G. M. Escandar and L. F. Sala, *Can. J. Chem.*, 1992, **70**, 2053-2057.
- U. Evans and B. F. Brown, *Localised corrosion*, National Association of Corrosion Engineers, Houston, Tex, 1974.
- H. Farman, F. M. Coveney and J. C. Dore, *Physica B*, 1992, **180**, 857-860.
- F.-I. Fei, J. Hu, J.-x. Wei, Q.-j. Yu and Z.-s. Chen, *Constr. Build. Mater.*, 2014, **70**, 43-53.
- J. W. Fergus, *J. Power Sources*, 2010, **195**, 4554-4569.
- N. Ferlin, M. Courty, S. Gatard, M. Spulak, B. Quilty, I. Beadham, M. Ghavre, A. Haiß, K. Kümmerer, N. Gathergood and S. Bouquillon, *Tetrahedron*, 2013, **69**, 6150-6161.
- M. Forsyth, C. M. Forsyth, K. Wilson, T. Behrsing and G. B. Deacon, *Corros. Sci.*, 2002, **44**, 2651-2656.
- M. Forsyth, M. Seter, B. Hinton, G. Deacon and P. Junk, *Aust. J. Chem.*, 2011, **64**, 812-819.

Bibliography

- M. Forsyth, K. Wilson, T. Behrsing, C. Forsyth, G. B. Deacon and A. Phanasgaonkar, *Corrosion*, 2002, **58**, 953-960.
- M. G. Freire, C. M. S. S. Neves, I. M. Marrucho, J. A. P. Coutinho and A. M. Fernandes, *J. Phys. Chem. A*, 2010, **114**, 3744-3749.
- R. Fuchs-Godec and M. G. Pavlović, *Corros. Sci.*, 2012, **58**, 192-201.
- M. T. Garcia, E. Campos, A. Marsal and I. Ribosa, *Environ. Int.*, 2008, **34**, 1001-1005.
- G. Gece, *Corros. Sci.*, 2011, **53**, 3873-3898.
- M. Gong, C. Jiang, X. Zheng, X. Zeng and X. Lin, *Adv. Mater. Res.*, 2012, **476-478**, 1434-1440.
- T. L. Greaves and C. J. Drummond, *Chem. Rev.*, 2008, **108**, 206-237.
- T. L. Greaves, A. Weerawardena, C. Fong, I. Krodkiewska and C. J. Drummond, *J. Phys. Chem. B*, 2006, **110**, 22479-22487.
- C. J. T. Grothuss, *Ann. Chim. - Sci. Mat.*, 1806, **58**, 54 - 73.
- U. Gruseck and M. Heuschmann, *Chem. Ber.*, 1987, **120**, 2053-2064.
- A. F. Gualdrón, E. N. Becerra, D. Y. Peña, J. C. Gutiérrez and H. Q. Becerra, *J. Mater. Environ. Sci.*, 2013, **4**, 143-158.
- J. Guertin, in *Chromium (VI) handbook*, CRC Press, Boca Raton, 2004, pp. 215-230.
- K. E. Gutowski, J. D. Holbrey, R. D. Rogers and D. A. Dixon, *J. Phys. Chem. B*, 2005, **109**, 23196-23208.
- H. S. Gutowsky and G. E. Pake, *J. Chem. Phys.*, 1950, **18**, 162-170.
- D. Guzmán-Lucero, O. Olivares-Xometl, R. Martínez-Palou, N. V. Likhanova, M. A. Domínguez-Aguilar and V. Garibay-Febles, *Ind. Eng. Chem. Res.*, 2011, **50**, 7129-7140.
- E. L. Hahn, *Physical Review*, 1950, **80**, 580-594.
- M. Hajime, Y. Masahiro, T. Kazumi, N. Masakatsu, K. Yukiko and M. Yoshinori, *Chem. Lett.*, 2000, **29**, 922-923.
- C. Heitner-Wirguin, *J. Membr. Sci.*, 1996, **120**, 1-33.
- W. A. Henderson, D. M. Seo, Q. Zhou, P. D. Boyle, J.-H. Shin, H. C. De Long, P. C. Trulove and S. Passerini, *Adv. Energy Mat.*, 2012, **2**, 1343-1350.
- P. V. Hien, N. S. H. Vu, V. T. H. Thu, A. Somers and N. D. Nam, *Appl. Surf. Sci.*, 2017, **412**, 464-474.
- B. R. W. Hinton and L. Wilson, *Corros. Sci.*, 1989, **29**, 967-985.
- C. C. Ho, J. W. Evans and P. K. Wright, *J. Micromech. Microeng.*, 2010, **20**, 104009.
- T. P. Hoar and W. R. Jacob, *Nature*, 1967, **216**, 1299-1301.
- T. P. Hoar, D. C. Mears and G. P. Rothwell, *Corros. Sci.*, 1965, **5**, 279-289.
- M. Hosseini, S. F. L. Mertens and M. R. Arshadi, *Corros. Sci.*, 2003, **45**, 1473-1489.
- W. L. Hough, M. Smiglak, H. Rodriguez, R. P. Swatloski, S. K. Spear, D. T. Daly, J. Pernak, J. E. Grisel, R. D. Carliss, M. D. Soutullo, J. J. H. Davis and R. D. Rogers, *New J. Chem.*, 2007, **31**, 1429-1436.
- P. C. Howlett, T. Khoo, G. Mooketsi, J. Efthimiadis, D. R. MacFarlane and M. Forsyth, *Electrochim. Acta*, 2010, **55**, 2377-2383.
- P. C. Howlett, F. Ponzio, J. Fang, T. Lin, L. Jin, N. Iranipour and J. Efthimiadis, *Phys. Chem. Chem. Phys.*, 2013, **15**, 13784-13789.
- P. Huang, J.-A. Latham, D. R. MacFarlane, P. C. Howlett and M. Forsyth, *Electrochim. Acta*, 2013, **110**, 501-510.
- M. Iannuzzi, *J. Chem. Phys.*, 2006, **124**, 204710.
- M. A. M. Ibrahim, M. Messali, Z. Moussa, A. Y. Alzahrani, S. N. Alamry and B. Hammouti, *Port. Electrochim. Acta*, 2011, **29**, 375-389.
- I. B. Il'chibaeva, E. S. Kagan and A. P. Tomilov, *Russ. J. Electrochem.*, 2002, **38**, 1045-1046.
- IUPAC, *Compendium of Chemical Terminology*, 2nd edn., Oxford, 1997.
- A. Izgorodin, E. Izgorodina and D. R. MacFarlane, *Energ. Environ. Sci.*, 2012, **5**, 9496-9501.
- E. I. Izgorodina, J. Rigby and D. R. MacFarlane, *Chem. Commun.*, 2012, **48**, 1493-1495.
- E. I. Izgorodina, Z. L. Seeger, D. L. A. Scarborough and S. Y. S. Tan, *Chem. Rev.*, 2017, **117**, 6696-6754.
- M. J. Earle, P. B. McCormac and K. R. Seddon, *Green Chem.*, 1999, **1**, 23-25.
- S. Javadian, A. Yousefi and J. Neshati, *Appl. Surf. Sci.*, 2013, **285**, Part B, 674-681.
- R. Jazzar, H. Liang, B. Donnadieu and G. Bertrand, *J. Organomet. Chem.*, 2006, **691**, 3201-3205.

- L. Jin, S. de Leeuw, M. V. Koudriachova, J. M. Pringle, P. C. Howlett, F. Chen and M. Forsyth, *Phys. Chem. Chem. Phys.*, 2013, **15**, 19570-19574.
- L. Jin, K. M. Nairn, C. M. Forsyth, A. J. Seeber, D. R. MacFarlane, P. C. Howlett, M. Forsyth and J. M. Pringle, *J. Am. Chem. Soc.*, 2012, **134**, 9688-9697.
- D. A. Jones, *Principles and Prevention of Corrosion*, Prentice-Hall, New Jersey, 1996.
- R. C. F. Jones and P. Dimopoulos, *Tetrahedron*, 2000, **56**, 2061-2074.
- V. Jovancicevic and J. O. M. Bockris, *J. Electrochem. Soc.*, 1986, **133**, 1797-1807.
- M. Kar, B. Winther-Jensen, M. Armand, T. J. Simons, O. Winther-Jensen, M. Forsyth and D. R. MacFarlane, *Electrochim. Acta*, 2016, **188**, 461-471.
- M. Kar, B. Winther-Jensen, M. Forsyth and D. R. MacFarlane, *Phys. Chem. Chem. Phys.*, 2013, **15**, 7191-7197.
- R. G. Kelly, J. R. Scully, D. Shoesmith and R. G. Buchheit, *Electrochemical Techniques in Corrosion Science and Engineering*, Marcel Dekker, New York, 2002.
- E. Khamis and N. AlAndis, *Materialwiss. Werkstofftech.*, 2002, **33**, 550-554.
- M. Kharshan, A. Furman, M. Shen, R. Kean, K. Gillette and L. Austin, *Mater. Performance*, 2012, 17-22.
- T. Khoo, P. C. Howlett, M. Tsagouria, D. R. MacFarlane and M. Forsyth, *Electrochim. Acta*, 2011, **58**, 583-588.
- T. Khoo, A. Somers, A. A. J. Torriero, D. R. MacFarlane, P. C. Howlett and M. Forsyth, *Electrochim. Acta*, 2013, **87**, 701-708.
- R. S. Koefod, *United States Pat.*, US 20070278446 A1, 2010.
- L. M. Korotaeva, T. Y. Rubinskaya, L. V. Mikhal'chenko, I. A. Rybakova and V. P. Gul'tyai, *Russ. J. Electrochem.*, 2011, **47**, 1139.
- E. Kowsari, S. Y. Arman, M. H. Shahini, H. Zandi, A. Ehsani, R. Naderi, A. P. Hanza and M. Mehdipour, *Corros. Sci.*, 2016, **112**, 73-85.
- E. Kowsari, M. Payami, R. Amini, B. Ramezanzadeh and M. Javanbakht, *Appl. Surf. Sci.*, 2014, **289**, 478-486.
- K.-D. Kreuer, S. J. Paddison, E. Spohr and M. Schuster, *Chem. Rev.*, 2004, **104**, 4637-4678.
- K. Kudo, S. Mitsushima, N. Kamiya and K.-i. Ota, *Electrochemistry*, 2005, **73**, 668-674.
- K. M. Kuhn and R. H. Grubbs, *Org. Lett.*, 2008, **10**, 2075-2077.
- G. H. Lane, *Electrochim. Acta*, 2012, **83**, 513-528.
- A. Leema Rose, A. Peter Pascal Regis, S. Rajendran, A. Krishnaveni and F. R. Selvarani, *Arab. J. Sci. Eng.*, 2012, **37**, 1313-1325.
- B. Lenarcik and P. Ojczenasz, *J. Heterocycl. Chem.*, 2002, **39**, 287-290.
- Y. Leng, G. Chen, A. J. Mendoza, T. B. Tighe, M. A. Hickner and C.-Y. Wang, *J. Am. Chem. Soc.*, 2012, **134**, 9054-9057.
- M. H. Levitt, *Spin dynamics : basics of nuclear magnetic resonance*, 2nd ed edn., John Wiley & Sons, Chichester, 2008.
- S. Li, L. Qiu, C. Shi, X. Chen and F. Yan, *Adv. Mater.*, 2014, **26**, 1266-1271.
- X. Li, S. Deng, H. Fu and G. Mu, *Corros. Sci.*, 2009, **51**, 2639-2651.
- X. Li, S. Deng, H. Fu and G. Mu, *Corros. Sci.*, 2010, **52**, 1167-1178.
- X. Li, S. Deng, H. Fu, G. Mu and N. Zhao, *Appl. Surf. Sci.*, 2008, **254**, 5574-5586.
- X. Li, S. Deng, G. Mu and Q. Qu, *Mater. Lett.*, 2007, **61**, 2514-2517.
- N. V. Likhanova, O. Olivares-Xometl, D. Guzmán-Lucero, M. A. Domínguez-Aguilar, N. Nava, M. Corrales-Luna and M. C. Mendoza, *Int. J. Electrochem. Sci.*, 2011, **6**, 4514-4536.
- H. H. Lin, J. D. Peng, V. Suryanarayanan, D. Velayutham and K. C. Ho, *J. Power Sources*, 2016, **311**, 167-174.
- Z. Liu, P. Bertram and F. Endres, *J. Solid State Electrochem.*, 2017, 1-7.
- S. Long, P. C. Howlett, D. R. MacFarlane and M. Forsyth, *Solid State Ionics*, 2006, **177**, 647-652.
- I. Lozano, E. Mazario, C. O. Olivares-Xometl, N. V. Likhanova and P. Herrasti, *Mater. Chem. Phys.*, 2014, **147**, 191-197.
- J. Luo, O. Conrad and I. F. J. Vankelecom, *J. Mater. Chem. A*, 2013, **1**, 2238-2247.
- J. Luo, A. H. Jensen, N. R. Brooks, J. Sniekers, M. Knipper, D. Aili, Q. Li, B. Vanroy, M. Wubbenhorst, F. Yan, L. Van Meervelt, Z. Shao, J. Fang, Z.-H. Luo, D. E. De Vos, K. Binnemans and J. Fransaer, *Energ. Environ. Sci.*, 2015, **8**, 1276-1291.

Bibliography

- D. R. MacFarlane, M. Forsyth, P. C. Howlett, J. M. Pringle, J. Sun, G. Annat, W. Neil and E. I. Izgorodina, *Acc. Chem. Res.*, 2007, **40**, 1165-1173.
- D. R. MacFarlane, M. Forsyth, E. I. Izgorodina, A. P. Abbott, G. Annat and K. Fraser, *Phys. Chem. Chem. Phys.*, 2009, **11**, 4962-4967.
- D. R. MacFarlane, P. Meakin, N. Amini and M. Forsyth, *J. Phys.: Condens. Matter*, 2001, **13**, 8257.
- D. R. MacFarlane, N. Tachikawa, M. Forsyth, J. M. Pringle, P. C. Howlett, G. D. Elliott, J. H. Davis, M. Watanabe, P. Simon and C. A. Angell, *Energ. Environ. Sci.*, 2014, **7**, 232-250.
- J. Maddox, *USA Pat.*, 3629104, 1973.
- E. J. Maginn, *J. Phys.: Condens. Matter*, 2009, **21**, 373101.
- P. Mäki-Arvela, I. Anugwom, P. Virtanen, R. Sjöholm and J. P. Mikkola, *Ind. Crops Prod.*, 2010, **32**, 175-201.
- T. Markley, F. Blin, M. Forsyth and B. Hinton, in *Rare Earth-Based Corrosion Inhibitors*, Woodhead Publishing, Cambridge, 2014, pp. 117-142.
- D. Massiot, F. Fayon, M. Capron, I. King, S. Le Calvé, B. Alonso, J.-O. Durand, B. Bujoli, Z. Gan and G. Hoatson, *Magn. Reson. Chem.*, 2002, **40**, 70-76.
- H. Matsumoto, H. Sakaebe, K. Tatsumi, M. Kikuta, E. Ishiko and M. Kono, *J. Power Sources*, 2006, **160**, 1308-1313.
- E. Mattsson, *Basic Corrosion Technology for Scientists and Engineers*, 2nd edition edn., The Institute of Materials, London, 2001.
- L. Mayrand-Provencher, S. Lin, D. Lazzerini and D. Rochefort, *J. Power Sources*, 2010, **195**, 5114-5121.
- M. McLin and C. A. Angell, *J. Phys. Chem.*, 1988, **92**, 2083-2086.
- A. J. McMahon, *Colloids Surf.*, 1991, **59**, 187-208.
- T. Mehtiö, M. Toivari, M. G. Wiebe, A. Harlin, M. Penttilä and A. Koivula, *Crit. Rev. Biotechnol.*, 2016, **36**, 904-916.
- G. Merle, M. Wessling and K. Nijmeijer, *J. Membr. Sci.*, 2011, **377**, 1-35.
- M. Messali and M. A. M. Asiri, *J. Mater. Environ. Sci.*, 2013, **4**, 770-785.
- T. Migita, N. Tachikawa, Y. Katayama and T. Miura, *Electrochemistry*, 2009, **77**, 639-641.
- B. A. Miksic, C. Chandler, M. Kharshan, A. Furman, B. Rudman and L. Gelner, *United States Pat.*, US 5597514 A, 1998.
- M. S. Miran, T. Yasuda, M. A. B. H. Susan, K. Dokko and M. Watanabe, *J. Phys. Chem. C*, 2014, **118**, 27631-27639.
- S. A. Mohd Noor, P. C. Howlett, D. R. MacFarlane and M. Forsyth, *Electrochim. Acta*, 2013, **114**, 766-771.
- R. Mohtadi, O. Tutusaus and F. Mizuno, *USA Pat.*, US 9455473 B1, 2016.
- A. Mondal and S. Balasubramanian, *J. Phys. Chem. C*, 2016, **120**, 22903-22909.
- D. Monti, E. Jónsson, M. R. Palacín and P. Johansson, *J. Power Sources*, 2014, **245**, 630-636.
- G. N. Mu, T. P. Zhao, M. Liu and T. Gu, *Corrosion*, 1996, **52**, 853-856.
- B. Müller, *Corros. Sci.*, 2002, **44**, 1583-1591.
- L. C. Murulana, A. K. Singh, S. K. Shukla, M. M. Kabanda and E. E. Ebenso, *Ind. Eng. Chem. Res.*, 2012, **51**, 13282-13299.
- R. Naderi, M. Mahdavian and M. M. Attar, *Electrochim. Acta*, 2009, **54**, 6892-6895.
- P. Narmada, M. V. Rao, G. Venkatachari and B. V. A. Rao, *Anti Corros. Method. M.*, 2006, **53**, 310-314.
- I. Nishiguchi and T. Hirashima, *Angew. Chem. Int. Ed.*, 1983, **22**, 52-53.
- A. Noda, M. A. B. H. Susan, K. Kudo, S. Mitsushima, K. Hayamizu and M. Watanabe, *J. Phys. Chem. B*, 2003, **107**, 4024-4033.
- Y. NuLi, J. Yang and R. Wu, *Electrochem. Commun.*, 2005, **7**, 1105-1110.
- E. E. Oguzie, Y. Li and F. H. Wang, *J. Colloid Interface Sci.*, 2007, **310**, 90-98.
- P. C. Okafor, C. B. Liu, X. Liu, Y. G. Zheng, F. Wang, C. Y. Liu and F. Wang, *J. Solid State Electrochem.*, 2010, **14**, 1367-1376.
- P. C. Okafor and Y. Zheng, *Corros. Sci.*, 2009, **51**, 850-859.
- O. Olivares-Xometl, C. López-Aguilar, P. Herrasti-González, N. V. Likhanova, I. Lijanova, R. Martínez-Palou and J. A. Rivera-Márquez, *Ind. Eng. Chem. Res.*, 2014, **53**, 9534-9543.

- M. Ontiveros-Rosales, O. Olivares-Xometl, N. V. Likhanova, I. V. Lijanova, D. Guzman-Lucero and M. Del Consuelo Mendoza-Herrera, *Res. Chem. Intermed.*, 2017, **43**, 641-660.
- M. R. Ortega Vega, S. R. Kunst, J. A. T. da Silva, S. Mattedi and C. de Fraga Malfatti, *Corros. Eng. Sci. Techn.*, 2015, **50**, 547-558.
- A. Ostovari, S. M. Hoseinie, M. Peikari, S. R. Shadizadeh and S. J. Hashemi, *Corros. Sci.*, 2009, **51**, 1935-1949.
- M. Paidar, V. Fateev and K. Bouzek, *Electrochim. Acta*, 2016, **209**, 737-756.
- S. Papavinasam, in *Uhlig's Corrosion Handbook*, ed. R. W. Revie, John Wiley & Sons, Inc., New Jersey, 2011, pp. 1021-1032.
- S. J. Pas, J. Huang, M. Forsyth, D. R. MacFarlane and A. J. Hill, *J. Chem. Phys.*, 2005, **122**, 064704.
- S. J. Peighambardoust, S. Rowshanzamir and M. Amjadi, *Int. J. Hydrogen Energy*, 2010, **35**, 9349-9384.
- M. Pourbaix, *Atlas of electrochemical equilibria in aqueous solutions*, 2nd edn., National Association of Corrosion Engineers, Houston, Tex, 1974.
- M. Prabakaran, S. Ramesh, V. Periasamy and B. Sreedhar, *Res. Chem. Intermed.*, 2015, **41**, 4649-4671.
- J. M. Pringle and V. Armel, *Int. Rev. Phys. Chem.*, 2011, **30**, 371-407.
- J. M. Pringle, P. C. Howlett, D. R. MacFarlane and M. Forsyth, *J. Mater. Chem.*, 2010, **20**, 2056-2062.
- M. J. Pryor and M. Cohen, *J. Electrochem. Soc.*, 1953, **100**, 203-215.
- Y. Qiang, L. Guo, S. Zhang, W. Li, S. Yu and J. Tan, *Sci. Rep.*, 2016, **6**, 33305.
- Q. Qu, S. Jiang, W. Bai and L. Li, *Electrochim. Acta*, 2007, **52**, 6811-6820.
- E. Raamat, K. Kaupmees, G. Ovsjannikov, A. Trummal, A. Kütt, J. Saame, I. Koppel, I. Kaljurand, L. Lipping, T. Rodima, V. Pihl, I. A. Koppel and I. Leito, *J. Phys. Org. Chem.*, 2013, **26**, 162-170.
- P. B. Raja and M. G. Sethuraman, *Mater. Lett.*, 2008, **62**, 113-116.
- S. Rajendran, B. V. Apparao and N. Palaniswamy, *Electrochim. Acta*, 1998, **44**, 533-537.
- S. Ramachandran and V. Jovancevic, *Corros. Sci.*, 1999, **55**, 259 - 267.
- S. Ramachandran, B.-L. Tsai, M. Blanco, H. Chen, Y. Tang and W. A. Goddard, *Langmuir*, 1996, **12**, 6419-6428.
- M. Ramdin, T. W. de Loos and T. J. H. Vlugt, *Ind. Eng. Chem. Res.*, 2012, **51**, 8149-8177.
- U. Rammelt, S. Koehler and G. Reinhard, *Corros. Sci.*, 2008, **50**, 1659-1663.
- U. Rammelt, S. Koehler and G. Reinhard, *Corros. Sci.*, 2009, **51**, 921-925.
- U. Rammelt, S. Koehler and G. Reinhard, *Corrosion*, 2011, **67**, 1-7.
- U. A. Rana, R. Vijayaraghavan, D. R. MacFarlane and M. Forsyth, *Chem. Commun.*, 2011, **47**, 6401-6403.
- M. W. Ranney, *Corrosion Inhibitors*, Noyes Data Corporation, New Jersey, 1976.
- B. Rao, M. Rao, S. Rao and B. Sreedhar, *J. Surf. Eng. Mater. Adv. Technol.*, 2013, **3**, 28-42.
- J. Rao, R. Vijayaraghavan, F. Chen, H. Zhu, P. C. Howlett, D. R. MacFarlane and M. Forsyth, *Chem. Commun.*, 2016.
- S. A. M. Refaey, *Appl. Surf. Sci.*, 2000, **157**, 199-206.
- P. R. Roberge, in *Handbook of Corrosion Engineering, Second Edition*, McGraw Hill Professional, Access Engineering, New York, 2012.
- R. Rogers and K. R. Seddon, *Ionic Liquids: Industrial Applications for Green Chemistry ACS Symposium Series 818*, American Chemical Society, Wash., DC, 2002.
- K. Romanenko, L. Jin, P. Howlett and M. Forsyth, *Chem. Mater.*, 2016, **28**, 2844-2851.
- Z. P. Rosol, N. J. German and S. M. Gross, *Green Chem.*, 2009, **11**, 1453-1457.
- S. Saba, A. Brescia and M. K. Kaloustian, *Tetrahedron Lett.*, 1991, **32**, 5031-5034.
- R. M. Saleh, A. A. Ismail and A. A. El Hosary, *Br. Corros. J.*, 1982, **17**, 131-135.
- Y. Sasikumar, A. S. Adekunle, L. O. Olasunkanmi, I. Bahadur, R. Baskar, M. M. Kabanda, I. B. Obot and E. E. Ebenso, *J. Mol. Liq.*, 2015, **211**, 105-118.
- V. S. Sastri, in *Green Corrosion Inhibitors*, John Wiley & Sons, Inc., 2011, pp. 167-211.
- N. Sato, *Electrochim. Acta*, 1971, **16**, 1683-1692.
- P. Saura, E. Zornoza, C. Andrade and P. Garcés, *Corrosion*, 2011, **67**, D1-D15.

- G. Schmitt, M. Schütze, G. F. Hays, W. Burns, E.-H. Han, A. Pourbaix and G. Jacobson, *Global Needs for Knowledge Dissemination, Research, and Development in Materials Deterioration and Corrosion Control*, The World Corrosion Organization, 2009.
- C. Schreiner, S. Zugmann, R. Hartl and H. J. Gores, *J. Chem. Eng. Data*, 2009, **55**, 1784-1788.
- A. J. Seeber, M. Forsyth, C. M. Forsyth, S. A. Forsyth, G. Annat and D. R. MacFarlane, *Phys. Chem. Chem. Phys.*, 2003, **5**, 2692-2698.
- S. Seki, Y. Kobayashi, H. Miyashiro, Y. Ohno, A. Usami, Y. Mita, N. Kihira, M. Watanabe and N. Terada, *J. Phys. Chem. B*, 2006, **110**, 10228-10230.
- M. Seter, B. Hinton and M. Forsyth, *J. Electrochem. Soc.*, 2012, **159**, C181-C189.
- M. Seter, M. J. Thomson, A. Chong, D. R. MacFarlane and M. Forsyth, *Aust. J. Chem.*, 2013, **66**, 921-929.
- M. Seter, M. J. Thomson, J. Stoimenovski, D. R. MacFarlane and M. Forsyth, *Chem. Commun.*, 2012, **48**, 5983-5985.
- A. M. Shams El Din and L. Wang, *Desalination*, 1996, **107**, 29-43.
- J. L. Shamshina, P. S. Barber and R. D. Rogers, *Expert Opin. Drug Deliv.*, 2013, 1-15.
- S. Shi, P. Yi, C. Cao, X. Wang, J. Su and J. Liu, *CIESC Journal*, 2005, **56**, 1112-1119.
- O. Shin-ichi and H. Tadao, *Bull. Chem. Soc. Jpn.*, 1953, **26**, 11-15.
- S. K. Shukla, L. C. Murulana and E. E. Ebenso, *Int. J. Electrochem. Sci.*, 2011, **6**, 4286-4295.
- J. Sinko, *Prog. Org. Coat.*, 2001, **42**, 267-282.
- K. R. Smith, E. C. Olson and S. E. Lentsch, *USA Pat.*, US 8114344 B1, 2012.
- K. Srivastav and P. Srivastava, *Br. Corros. J.*, 1981, **16**, 221-223.
- L. A. K. Staveley, *Annu. Rev. Phys. Chem.*, 1962, **13**, 351-368.
- E. O. Stejskal and J. E. Tanner, *J. Chem. Phys.*, 1965, **42**, 288-292.
- M. Stern and A. L. Geary, *J. Electrochem. Soc.*, 1957, **104**, 56-63.
- J. Stoimenovski, P. M. Dean, E. I. Izgorodina and D. R. MacFarlane, *Faraday Discuss.*, 2012, **154**.
- J. I. Stoimenovski, Ekaterina I. and D. R. MacFarlane, *Phys. Chem. Chem. Phys.*, 2010, **12**, 10341-10347.
- H.-H. Strehblow, in *Corrosion Mechanisms in Theory and Practice*, ed. P. Marcus, Marcel Dekker, New York, 2nd edn., 2002, vol. 17.
- T. Suzuki, H. Nishihara and K. Aramaki, *Corros. Sci.*, 1996, **38**, 1223-1234.
- R. Świsłocka, M. Kowczyk-Sadowy, M. Kalinowska and W. Lewandowski, *Spectroscopy*, 2012, **27**, 35-48.
- F. Takahashi and H. Yoshimura, *Japan Pat.*, JP2003313170A, 2003.
- Y. Tan, M. Mocerino and T. Paterson, *Corros. Sci.*, 2011, **53**, 2041-2045.
- R. Taniki, K. Matsumoto, T. Nohira and R. Hagiwara, *J. Power Sources*, 2014, **245**, 758-763.
- J. Thisuwan and K. Sagarik, *RSC Adv.*, 2014, **4**, 61992-62008.
- J. Timmermans, *J. Phys. Chem. Solids*, 1961, **18**, 1-8.
- L. Timperman, P. Skowron, A. Boisset, H. Galiano, D. Lemordant, E. Frackowiak, F. Beguin and M. Anouti, *Phys. Chem. Chem. Phys.*, 2012, **14**, 8199-8207.
- R. Touir, M. Cenoui, M. El Bakri and M. Ebn Touhami, *Corros. Sci.*, 2008, **50**, 1530-1537.
- R. Touir, N. Dkhireche, M. E. Touhami, M. E. Bakri, A. H. Rochdi and R. A. Belakhmima, *J. Saudi Chem. Soc.*, 2014, **18**, 873-881.
- V. Tricoli, G. Orsini and M. Anselmi, *Phys. Chem. Chem. Phys.*, 2012, **14**, 10979-10986.
- D. Turcio-Ortega, T. Pandiyan, J. Cruz and E. Garcia-Ochoa, *J. Phys. Chem. C*, 2007, **111**, 9853-9866.
- R. L. Twite and G. P. Bierwagen, *Prog. Org. Coat.*, 1998, **33**, 91-100.
- R. Tyagi, V. K. Tyagi and S. K. Pandey, *J. Oleo Sci.*, 2007, **56**, 211-222.
- S. Umoren, I. B. Obot, Z. Gasem and N. A. Odewunmi, *J. Dispersion Sci. Technol.*, 2015, **36**, 789-802.
- S. A. Umoren, *J. Appl. Polym. Sci.*, 2011, **119**, 2072-2084.
- J. H. Van Vleck, *Physical Review*, 1948, **74**, 1168-1183.
- C. Verma, E. E. Ebenso and M. A. Quraishi, *J. Mol. Liq.*, 2017, **233**, 403-414.
- S. A. Verma and G. Mehta, *Bull. Electrochem.*, 1999, **15**, 67-70.
- V. M. Vishnyakov, *Vacuum*, 2006, **80**, 1053-1065.
- E. Vuorinen and W. Skinner, *Br. Corros. J.*, 2002, **37**, 159-160.
- C. A. Wamser, *J. Am. Chem. Soc.*, 1948, **70**, 1209-1215.

- P. Wang, Q. Dai, S. M. Zakeeruddin, M. Forsyth, D. R. MacFarlane and M. Grätzel, *J. Am. Chem. Soc.*, 2004, **126**, 13590-13591.
- P. Wang, S. M. Zakeeruddin, J.-E. Moser and M. Grätzel, *J. Phys. Chem. B*, 2003, **107**, 13280-13285.
- P. Wasserscheid and T. Welton, in *Ionic Liquids in Synthesis*, Wiley-VCH, Weinheim, 2008.
- T. Welton, *Chem. Rev.*, 1999, **99**, 2071-2084.
- J. M. West, *Electrodeposition and corrosion processes*, Van Nostrand Reinhold, London, 1965.
- S. Wilbur, H. Abadin, M. Fay, D. Yu, B. Tencza, L. Ingerman, J. Klotzbach and S. James, Toxicological Profile for Chromium, US Department of Public Health and Human Services, Atlanta, 2012.
- C. L. Wilson and K. B. Wilson, *Trans. Electrochem. Soc.*, 1943, **84**, 153-163.
- W. Xu, E. I. Cooper and C. A. Angell, *J. Phys. Chem. B*, 2003, **107**, 6170-6178.
- D. Yang, M. Zhang, J. Zheng and H. Castaneda, *RSC Adv.*, 2015, **5**, 95160-95170.
- T. Yasuda and M. Watanabe, *MRS Bull.*, 2013, **38**, 560-566.
- G. Ye, W. P. Henry, C. Chen, A. Zhou and C. U. Pittman Jr, *Tetrahedron Lett.*, 2009, **50**, 2135-2139.
- S. Yesudass, Lukman O. Olasunkanmi, I. Bahadur, M. M. Kabanda, I. B. Obot and Eno E. Ebenso, *J. Taiwan. Inst. Chem. Eng.*, 2016, **64**, 252-268.
- N. Yoshimoto, M. Matsumoto, M. Egashia and M. Morita, *J. Power Sources*, 2010, **195**, 2096-2098.
- M. Yoshizawa, W. Xu and C. A. Angell, *J. Am. Chem. Soc.*, 2003, **125**, 15411-15419.
- M. Yoshizawa-Fujita, K. Fujita, M. Forsyth and D. R. MacFarlane, *Electrochem. Commun.*, 2007, **9**, 1202-1205.
- A. Yousefi, S. Javadian, N. Dalir, J. Kakemam and J. Akbari, *RSC Adv.*, 2015, **5**, 11697-11713.
- J. Zhang, G. Qiao, S. Hu, Y. Yan, Z. Ren and L. Yu, *Corros. Sci.*, 2011, **53**, 147-152.
- L. Zhao, I. Smolarkiewicz, H. H. Limbach, H. Breitzke, K. Pogorzelec-Glaser, R. Pankiewicz, J. Tritt-Goc, T. Gutmann and G. Buntkowsky, *J. Phys. Chem. C*, 2016, **120**, 19574-19585.
- X. Y. Zhao, J. L. Wang, H. Luo, H. R. Yao, C. Y. Ouyang and L. Z. Zhang, *J. Zhejiang Univ. Sci. A*, 2016, **17**, 155-162.
- X. Zheng, S. Zhang, M. Gong and W. Li, *Ind. Eng. Chem. Res.*, 2014, **53**, 16349-16358.
- X. Zheng, S. Zhang, W. Li, M. Gong and L. Yin, *Corros. Sci.*, 2015, **95**, 168-179.
- H. Zhu, D. MacFarlane and M. Forsyth, *J. Phys. Chem. C*, 2014, **118**, 28520-28526.
- H. Zhu, U. A. Rana, V. Ranganathan, L. Jin, L. A. O'Dell, D. R. MacFarlane and M. Forsyth, *J. Mater. Chem. A*, 2014, **2**, 681-691.

Bibliography

This thesis was formatted using a Microsoft Word thesis template adapted from Kayla Friedman and Malcolm Morgan of the Centre for Sustainable Development, University of Cambridge, UK.